Doctoral Thesis ETH No. 17023

EVOLUTION OF THE WESTERN CORDILLERA IN THE ANDES OF ECUADOR (LATE CRETACEOUS-PALEOGENE)

A dissertation submitted to the

SWISS FEDERAL INSTITUTE OF TECHNOLOGY ZÜRICH

for the degree of

Doctor of Natural Sciences

presented by

CRISTIAN VALLEJO CRUZ

Ingeniero Geólogo, Escuela Politécnica Nacional, Quito

born on 01.02.1972

citizen of
Quito, Ecuador

accepted on the recommendation of

Prof. Dr. Wilfried Winkler	ETH Zürich	examiner
Dr. Richard Spikings	University of Geneva	co-examiner
Dr. John Aspden	British Geological Survey	co-examiner
Prof. Dr. Arturo Egüez	EPN Quito	co-examiner
Prof. Dr. Jean Pierre Burg	ETH Zürich	co-examiner

2007

ACKNOWLEDGEMENTS

I should acknowledge first Wilfried Winkler for his continue support during the last ten years, and to encourage me during every step of my pre and postgraduate studies. I am very thankful with Richard Spikings for his enthusiasm during the project and our long and fruitful discussions about the Geology of Ecuador. Thanks to Peter Hochuli for his help before and during my doctoral studies.

Thanks to Eric Reusser from the Mineralogical Institute at ETH for the microprobe analysis; similarly, thanks to Zoltan Zajacz for assist me in the acquisition of the LA-ICPMS trace elements data. Acknowledgements to Francois Bussy from University of Lausanne for helping with the U/Pb LA-ICPMS zircon dating Thanks to Frowin Pirovino for his support in the laboratory work, and for helping me to improve my german skills.

John Aspden, Arturo Egüez, Kevin Burke, Jean Pierre Burg, Andrew Kerr and Ramón Vera are acknowledged for their critical comments to improve this study. My PhD project benefited from the $^{40}Ar/^{39}Ar$ and geochemical analyzes performed at the Mineralogical Department of Geneva University, thanks to Michael Dungan and Urs Schaltegger for allowing me to use the equipment there.

I also have to mention my colleagues in Escuela Politécnica Nacional in Quito, particularly to Edwin León, for his friendship and support during my graduate studies in Ecuador. Thanks to all my colleagues at ETH, people who support me since the very beginning of my stay in Switzerland, Sergio Llana, Geoffrey Ruiz, Alex Kunov, José Esteban, Lorena Jaramillo, Katrin Monecke, Boris Kaus, Thomas Kocher, Freddy Yugsi, Nick Richardson, Jonas von Ruette, Nergui Martin, and all people from the Geological Institute ETH for their support. Danke schön.

Special thanks to Leonard Luzieux for his friendship and the great moments we shared in Ecuador and Switzerland. Thanks to Regula Schaelchli for her support and for making my life and of my family much easier.

Field sampling benefited from the assistance and knowledge of Efraín Montenegro, William Lugo, Diego Villagómez, Ricardo Vargas, Luis Taco and Alex Carrera.

This project was supported by the Swiss National Science Foundation, projects 2-77193-02 and 2-77504-04.

Thanks to Janeth and Esteban, you both made this possible.

INDEX

ABSTRACT **1**

ZUSAMMENFASSUNG **3**

RESUMEN **5**

CHAPTER 1: INTRODUCTION **7**

1.1 SCOPE OF THE STUDY 7

1.3 GEOLOGICAL OVERVIEW OF ECUADOR 10

1.3.1 The Western Cordillera 11

1.4 PREVIOUS WORK IN THE WESTERN CORDILLERA 12

CHAPTER 2 GEOLOGICAL FRAMEWORK **17**

2.1 CRETACEOUS TO OLIGOCENE STRATIGRAPHY 17

2.1.2 Pallatanga Block 17

2.1.2.1 Pallatanga Formation 17

2.1.2.2 San Juan Unit 20

2.1.2.3 The Pujilí Melange and the Pujilí Granite 22

2.1.2.4 Totoras Amphibolite 25

2.1.2.5 The Rio Cala Group 26

La Portada Formation 26

Mulaute Formation. 30

Pilatón Formation. 31

Natividad Formation 33

Rio Cala Formation 36

2.1.2.6 Yunguilla Formation 37

2.1.2.7 Silante Formation 40

2.1.2.8 Pilaló Formation 46

2.1.2.9 Saguangal Formation. 51

2.1.2.10 Angamarca Group 53

Saquisilí Formation 53

Unacota Formation 56

Apagua Formation 57

El Laurel Formation 60

2.1.2.11 San Juan de Lachas Formation 61

2.1.2.12 Macuchi Unit 61

2.1.3 Naranjal Block 66

2.1.3.1 Naranjal Unit 67

CHAPTER 3: PROVENANCE ANALYSIS 72

3.1 INTRODUCTION AND GOALS 72

3.2 HEAVY MINERALS ANALYSIS 72

3.2.1 Rationale of the method 72

3.2.2 Results 75

3.2.2.1 Pilatón Formation 76

3.2.1.2 Mulaute Formation 76

3.2.2.3 Yunguilla Formation 77

3.2.2.4 Silante Formation 78

3.2.2.5 Pilaló Formation 79

3.2.2.6 Saguangal Formation 80

3.2.2.7 Angamarca Group 81

3.2.2.8 Macuchi Unit (Las Juntas Turbidites) 82

3.3 SINGLE GRAIN GEOCHEMISTRY. 84

3.3.1 Rationale of the method 84

3.3.2 Results 85

3.3.2.1 Clinopyroxene geochemistry from the volcanic basement 86

3.3.2.2 Clinopyroxene geochemistry of the sedimentary rocks 89

3.3.2.3 Garnet Geochemistry of the Saquisilí Formation 92

3.4 U/PB DETRITAL ZIRCON DATING 92

3.4.1 Results 92

3.4.1.1 Yunguilla Formation 93

3.4.1.2 Saguangal Formation 94

3.4.1.3 Macuchi Unit 95

3.5 INTERPRETATION 95

3.5.1 The pre-accretionary Rio Cala arc island arc sequence 95

3.5.2 The syn-collisional Yunguilla Formation 96

3.5.3 The post-accretionary formations 97

3.5.3.1 The Silante volcanic arc 97

3.5.3.2 The Angamarca Group 98

3.5.3.3 The Macuchi Unit 99

3.5.4 Age of the source regions 99

CHAPTER 4: RADIOMETRIC AGES OF THE IGNEOUS ROCKS 101

4.1 U/Pb SHRIMP ANALYSES 103

4.1.1 Rationale of the method 103

4.1.2 SHRIMP-Results 105

4.2 $^{40}Ar/^{39}Ar$ ANALYSES 107

4.2.1 Rationale of the method 107

4.2.2 Results 108

4.2.2.1 Basement rocks 110

4.2.2.2 Volcanic cover sequence 110

4.3 INTERPRETATION 119

4.3.1 The age of the basement of the Western Cordillera 119

4.3.2 The age of the Rio Cala Island arc. 120

4.3.3 The latest Maastrichtian to Paleocene Silante continental arc 121

4.3.4 The Middle to Late Eocene volcanic arc 122

4.3.5 The latest Eocene - Oligocene volcanic arc 123

CHAPTER 5: GEOLOGICAL EVOLUTION OF THE WESTERN CORDILLERA 124

5.1 THE CARIBBEAN PLATEAU 124

5.2 AGE AND ORIGIN OF THE CARIBBEAN PLATEAU 125

5.3 THE GREAT ARC OF THE CARIBBEAN 127

5.4 LATE CRETACEOUS OCEANIC PLATEAU AND ISLAND ARC SEQUENCES IN THE NORTHERN ANDES (ECUADOR AND COLOMBIA) 128

5.5 INACCURANCE IN PREVIOUS GEODYNAMIC MODELS OF THE WESTERN CORDILLERA 133

5.6 GEODYNAMIC EVOLUTION OF THE WESTERN CORDILLERA 134

5.6.1 Coniacian (88 Ma): The origin of the crystalline basement. 134

5.6.2 Santonian to Early Campanian (85-83 Ma): Initiation of subduction below the oceanic plateau 136

5.6.3 Campanian to Maastrichtian (83-75 Ma): The Rio Cala island arc 138

5.6.4 Latest Campanian to Maastrichtian (~73-70 Ma): Collision of the Pallatanga Block 139

5.6.5 Latest Maastrichtian: The Silante Arc 140

5.6.6 Paleocene: The Macuchi Arc 140

5.6.7 Early to Middle Eocene 141

5.6.8 Late Eocene 141

5.6.9 Latest Eocene - Oligocene 142

CHAPTER 6 CONCLUSIONS 144

BIBLIOGRAPHY 146

APPENDIX

APPENDIX 1: Analytical procedures of whole-rock geochemistry. 159

APPENDIX 2: Major, trace elements and isotopic composition from selected Western Cordillera samples 160

APPENDIX 3: Analytical procedures for heavy minerals determinations, clinopyroxene chemistry and U/Pb laser ablation ICPMS zircon dating. 161

APPENDIX 4: Samples for Heavy Mineral analysis from the Western Cordillera. 162

APPENDIX 5: Heavy Minerals of the samples from the Western Cordillera. 164

APPENDIX 6: Composition of the clinopyroxenes of samples from the Western Cordillera. 167

APPENDIX 7: Mean chemical composition and structural formula of the clinopyroxene phenocrysts used for this study 170

APPENDIX 8: Trace elements composition of clinopyroxenes from the Western Cordillera. 191

APPENDIX 9 Analytical procedures U/Pb SHRIMP dating and $^{40}Ar/^{39}Ar$ analyses. 197

APPENDIX 10: U-Pb results by the LA-ICPMS method 199

APPENDIX 11: Summary of SHRIMP U-Pb zircon results from rocks of the Western Cordillera. 201

APPENDIX 12: $^{40}Ar/^{39}Ar$ Data 204

LIST OF TABLES

Table 2.1 Reported Ages from the Macuchi Unit. 66

Table 3.1. Summary of the heavy minerals data. 96

Tabla 4.1 Radiometric age reported from the Cretaceous to Oligocene in the Western Cordillera. 102

Table. 4.2 Sumary of U/Pb zircon ages and 40Ar/39Ar plateau ages of igneous rock from the Western Cordillera obtained in this study. 109

Table 5.1. Summary of radiometric (mostly $^{40}Ar/$ Ar) and biostratigraphic ages on oceanic plateau rocks from the Caribbean and Northern South America. 126

ABSTRACT

The subduction of ocean floor at a convergent plate boundary can be regarded as approximating a steady-state process. Interruption or cessation of that process commonly follows the arrival of a buoyant object. Arcs and continents are the familiar kinds of buoyant objects involved in collisions. I here provide a detailed analysis of a less familiar kind of collision, that of an oceanic plateau.

The determination of accurate and precise ages for the timing of collision between oceanic plateaus and continental crust provides an understanding of how the indenting and buttressing plates respond to the collisional event. The volcanic basement of the Ecuadorian Western Cordillera (Pallatanga Formation and San Juan Unit) is made up of mafic and ultramafic rocks with oceanic plateau geochemical affinities. A SHRIMP crystallization age (zircon) of 87.1±1.66 Ma (2σ) and $^{40}Ar/^{39}Ar$ (hornblende) age of 84.69±2.22 Ma (2σ) from an accreted fragment of the plateau, overlap with an $^{40}Ar/^{39}Ar$ age of 88±1.6 Ma age obtained for oceanic plateau basement rocks of the Piñon Formation in coastal Ecuador (Luzieux et al., 2006), and a suite of ~92-88 Ma ages reported for oceanic plateau sequences in Colombia and the Caribbean region. These results are consistent with the idea that the oceanic plateau rocks of the Western Cordillera and coastal Ecuador are derived from the Late Cretaceous Caribbean Colombia Oceanic Plateau (CCOP).

Intraoceanic island arc sequences (Pujilí Granite, Rio Cala Group, Naranjal Unit) overlie the plateau and yield crystallization ages that range between ~85–72 Ma. The geochemistry and radiometric ages of lavas associated with the Rio Cala Arc, combined with the age range and geochemistry of their turbiditic, volcanoclastic products indicate that the arc initiated by westward subduction beneath the Caribbean Plateau, and are coeval with island arc rocks of coastal Ecuador (Las Orquideas, San Lorenzo and Cayo formations). These island arc units may be related to the Late Cretaceous Great Arc of the Caribbean.

Paleomagnetic analyses of volcanic rocks, of the Piñon and San Lorenzo formations of the southern external forearc (Luzieux, 20067), indicate their pre-collisional extrusion at equatorial or shallow southern latitudes. Furthermore, paleomagnetic declination data from basement and sedimentary cover rocks in the coastal region (Luzieux, 2007) indicate 20–50^{o} of clockwise rotation during the Campanian, which was probably synchronous with the collision of the oceanic plateau and arc sequence with South America.

The initial collision between the South American Plate and the Caribbean Plateau was synchronous with accelerated surface uplift and exhumation (>1km/my) within the buttressing continental margin during the Late Cretaceous (c. 75–65 Ma), in an area extending as far inland as the Eastern Cordillera. The rapid exhumation coincides with the deposition of continental siliciclastic material in both the fore- and backarc environments (Yunguilla and Tena formations respectively).

Collectively, this evidence shows that the initial collision between the Caribbean Plateau and the Ecuadorian margin occurred during the late Campanian–Maastrichtian (73–70 Ma), and resulted in plugging of the subduction zone, the termination of island arc magmatism, and deformation of the continental margin.

Magmatism associated with the Campanian–early Maastrichtian Rio Cala Arc, which erupted through the Pallatanga Formation, ceased during the Maastrichtian and was followed by the initiation of east-dipping subduction beneath the accreted oceanic plateau. The new active margin gave rise to the latest Maastrichtian (ca 65 Ma) Silante volcanic arc, which was deposited in a terrestrial environment.

During the Palaeocene to Eocene, marine conditions were dominant in the area now occupied by the Western Cordillera, and volcanic rocks of the Macuchi Unit were deposited, possibly as a temporal continuation of the Silante volcanic arc. This submarine volcanism was coeval with the deposition of siliciclastic rocks of the Angamarca Group, and the Saguangal Formation, which were mainly derived from the emerging Eastern Cordillera.

Finally, no evidence exists to support previous hypotheses that the Macuchi Arc accreted in the Late Eocene, causing structural inversion of the Angamarca Basin. It is geometrically difficult to suggest that the Macuchi Block accreted in the Late Eocene, and inserted itself between the Piñon and Pallatanga blocks, which accreted during the Late Cretaceous. Furthermore, volcanic rocks of the Macuchi Unit are found to be conformably overlain by turbidites of the Angamarca Group.

ZUSAMMENFASSUNG

Die Subduktion von Ozeankruste an einer konvergenten Plattengrenze kann als annähernd kontinuierlichen Prozess betrachtet werden. Die Unterbrechung dieses Vorganges wird im Allgemein durch die Ankunft eines isostatisch aufschwimmenden, schwer zu subduzierendes Objektes verursacht. Vulkanbögen und Kontinente sind typischerweise solche Elemente, welche sich der Subduktion entziehen. In der vorliegenden Arbeit wird eine ausführliche Analyse einer weniger üblichen Kollision einer ozeanischen Hochebene (Plateau) und ihren assoziiertem intraozeanischen Inselbögen vorgestellt, d.h. die Kollision des ozeanischen Pallatanga-Blockes mit dem nordwestlichen Kontinentalrand von Südamerika.

Die Ermittlung des genauen Zeitablaufes des Zusammenstosses zwischen dem ozeanischen Plateau/Arc-Komplexes mit kontinentaler Kruste liefert ein Verständnis dafür, wie die eindrückende ozeanische und die dagegen drückende kontinentale Platte bei der Kollision reagieren.

Der vulkanische Sockel der Westkordillere (Pallatanga Formation und San Juan Einheit) besteht aus mafischen und ultramafischen Gesteinen mit geochemischen Eigenschaften von ozeanischen Plateaus. Ein daraus gewonnenes U/Pb SHRIMP (Zirkon) Kristallisationsalter von 87.1±1.66 Ma (2σ) und ein $^{40}Ar/^{39}Ar$ Alter (Hornblende) von 84.69±2.22 Ma (2σ) decken sich mit: (1) einem $^{40}Ar/^{39}Ar$ Hornblendealter von 88±1.6 Ma in mafischen Grundgebrirgsgesteinen der Piñon Formation im küstennahen Forearc von Ecuador (Luzieux et al., 2006) und (2) einer Reihe von radiometrischen Datierungen von ähnlichen Gesteinen (~ 92-88 Ma) in der Westkordillere von Kolumbien und in der karibischen Region. Die chronostratigraphische und geochemische Korrelation legt nahe, dass die Vorkommen im ecuadorianischen Forearc vom spätkretazischen Caribbean Colombian Oceanic Plateau (CCOP) herstammen. Bekannte ozeanische Inselbogen-Bildungen (Pujilí Granit, Rio Cala Gruppe, Naranjal Einheit) überlagern die Plateau-Formationen und lieferten Kristallisationalter zwischen ~ 85-72 Ma. Die Summe der geochemischen Resultate und radiometrischen Alter von Laven und assoziierten turbiditischen Sedimenten im Rio Cala Inselbogen zeigt, dass sie durch westgerichtete Subduktion unter das kolumbisch-karibische Plateau (CCOP) gebildet wurden. Sie haben damit einen gleichen Ursprung wie die Inselbogenformationen an der Küste von Ecuador (die Las Orquideas, San Lorenzo und Cayo Formationen), und alle können gleichermassen mit vulkanischen Formationen der späten Kreide im Inselbogen der Grossen Antillen verglichen werden.

Paläomagnetische Analysen der vulkanischen Formationen in den Piñón- und San Lorenzo-Blöcken des südlichen äusseren Forearcs (Luzieux, 2007) beweisen, dass sie vor der Kollision in einer äquatorialen oder leicht südlichen Breiten ausgeflossen sind. Ausserdem zeigen paläomagnetische Deklinationsdaten vom Küstengebiet eine rechtssinnige Rotation der Blöcke von 20-50° um eine vertikale Achse an (Luzieux, 2007). Die Rotation erfolgte mit grösster Wahrscheinlichkeit während der Kollision des Plateau/Inselbogen-Komplexes, die anhand

biostratigraphischer Daten zeitlich mit dem späten Campanian-frühen Maastrichtian genau festgelegt werden kann.

Publizierte thermochronologische Analysen zeigen eine durch die Kollision verursachte schnelle Exhumierung (>1km/my) des Kontinentalrandes während der späten Kreide (~ 75-65 Ma) an, die auch zeitlich mit dem Einsetzen der siliziklastischen Sedimentation im Forearc ihren Niederschlag findet (Yunguilla Formation, spätes Campanian-Maastrichtian). Die Kollision des karibischen Plateaus mit der südamerikanischen Platte äusserte sich im Speziellen auch in einer weit in den Kontinent hinein reichende Hebung und Exhumierung metamorpher Tiefengesteine in der Ostkordillere, wie es aus dem Detritus der altersgleichen Yunguilla Formation im Forearc bzw. der Tena Formation im Retroarc Foreland-Becken abgeleitet werden kann.

Der Magmatismus des Rio Cala Arcs (Campanian-frühes Maastrichtian), der durch die Pallatanga Formation stiess, versiegte während des Maaastrichtians. Gleichzeitig richtete sich unter den im Forearc akkretionierten Plateau-Teilen eine ostgerichtete Subduktionszone ein. Über diesem neuen aktiven Kontinentalrand bildete sich ab dem späten Maastrichtian (ca 65 Ma) der terrestrische Silante-Vulkanbogen aus.

Während des Paleozäns und Eozäns herrschten im Bereich der späteren Westkordillere (dem inneren Forearc) marine Verhältnisse vor, wo sich auch die Vulkanite des Macuchi Arcs ergossen, wahrscheinlich als Nachfolger des Silante Arcs. Der submarine Vulkanismus ereignete sich zeitgleich mit der proximalen siliziklastischen turbiditischen Sedimentation der Angamarca Gruppe und der Saguangal Formation, welche von der aufsteigenden Ostkordillere geschüttet wurden.

Schlussendlich können in der vorliegenden Arbeit keine positiven Beweise erbracht werden, dass der Macuchi Arc erst im späten Eozän mit dem Kontinentalrand kollidiert sein soll, womit frühere Autoren die Inversion des Angamarca-Beckens erklärt haben. Es ist räumlich und zeitlich unvereinbar, dass sich der Macuchi Arc - nach der erwiesenermassen oberkretazischen kollektiven Kollision der Plateau- und intraozeanischen Inselbogen-Blöcke (e.g. Piñon, San Lorenzo, Pallatanga, Rio Cala) mit dem nordwestlichen Rand des südamerikanischen Kontinents - zwischen diese Blöcke geschoben habe. Im Gegenteil, die autochthone Stellung des Macuchi Arcs wird auch durch seine beobachtete normalstratigraphische Überlagerung durch die Angamarca Gruppe bestärkt.

RESUMEN

La subducción de corteza oceánica en un límite convergente de placa se puede mirar como un proceso contínuo. La interrupción o la finalización de este proceso comúnmente se asocian a la llegada de un objeto boyante. Los arcos volcánicos y corteza continental son las clases de objetos comúnmente implicados en colisiones. En este trabajo, se proporciona un análisis detallado de una clase menos familiar de colisión, la de un plateau oceánico.

La determinación precisa de la colisión entre plateaus oceánicos y la corteza continental proporciona una comprensión de como las placas tectónicas responden a eventos colisionales.

El basamento volcánico de la Cordillera Occidental (Formación Pallatanga y Unidad San Juan) se compone de rocas máficas y ultramáficas con afinidades geoquímicas de plateau oceánico. Una edad de cristalización SHRIMP (zircón) de 87.1±1.66 Ma. (2σ) y de $^{40}Ar/^{39}Ar$ (hornblenda) de 84.69±2.22 Ma. (2σ) de fragmentos accrecionados del plateau, se superponen con una edad $^{40}Ar/^{39}Ar$ (hornblenda) de 88±1.6 (2σ) Ma. obtenida para las rocas oceánicas del basamento de la Formación Piñón en la costa de Ecuador (Luzieux et al., 2006), y una serie de edades de ~92-88 Ma. reportadas para las secuencias de plateau oceánico en Colombia y la región del Caribe.

Estos resultados son consistentes con la idea que las rocas de plateau oceánico de la Cordillera Occidental y la Costa de Ecuador se derivan del Plateau Oceánico del Caribe y Colombia (CCOP) de edad Cretácico Tardío.

Las secuencias de arco de isla intraoceánico (Granito de Pujilí, Grupo Río Cala, Unidad Naranjal) sobreyacen a rocas del plateau y tienen edades de cristalización que se extienden entre ~85-72 Ma. La geoquímica y las edades radiométricas de las lavas asociadas al arco de Río Cala, combinado con el rango de edades y la geoquímica de sus productos turbidíticos y volcanoclásticos indican que el arco se inició por subducción hacia el oeste debajo de el CCOP, y son contemporáneas con las rocas del arco de isla de la Costa de Ecuador (Formaciones Las Orquídeas, San Lorenzo y Cayo). Estas unidades del arco de isla se pueden relacionar con el Gran Arco Cretácico del Caribe.

Los análisis paleomagnéticos de rocas volcánicas, de las formaciones Piñon y San Lorenzo de la zona de antearco (Luzieux, 2007), indican su extrusión pre-colisional en latitudes ecuatoriales. Además, los datos paleomagnéticos de la declinación del basamento y de la cobertura sedimentarias de la región costera (Luzieux, 2007) indican 20-50° de rotación en sentido horario cerca de la época de la colisión, durante el Campaniano. La rotación fue probablemente síncrona con la colisión de la secuencia de plateau oceánico y de arco con Sudamérica.

Rápida exhumación (>1km/ma) a lo largo del margen continental durante el Cretácico tardío durante ~75-65 Ma es consistente en tiempo con el inicio de sedimentación clástica derivado del margen continental en el Campaniano Tardío – Maastrichtiano (Formación de Yunguilla). La colisión inicial entre la Placa Sudamericana y el Plateau del Caribe fue síncrona con el levantamiento y la exhumación acelerados dentro del margen continental, en un área

que se extendía tan lejos como la Cordillera Oriental, y con la depositación de material siliciclástico derivado del continente en el antearco y trasarco (las formaciones Yunguilla y Tena respectivamente). Colectivamente, esta evidencia demuestra que la colisión inicial entre el Plateau Caribe y el margen de Ecuador ocurrió durante el Campaniano Tardío - Maastrichtian (73-70 Ma.), y dio lugar al bloqueo de la zona de subdución, a la terminación del magmatismo del arco de isla, y a la deformación del margen continental.

El magmatismo asociado al arco Río Cala (Campaniano - Maastrichtiano Temprano), que se produjo sobre la Formación Pallatanga, cesó durante el Maastrichtiano y fue seguido por la iniciación de subducción hacia el este, debajo del plateau oceánico acrecionado. El nuevo margen activo dio lugar al arco volcánico Silante del Maastrichtiano Tardío (aprox. 65 Ma.), que fue depositado en un ambiente terrestre. Durante el Palaeoceno al Eoceno, las condiciones marinas fueron dominantes en el área ahora ocupada por la Cordillera Occidental, y las rocas volcánicas de la unidad Macuchi fueron depositadas, posiblemente como continuación del arco volcánico de Silante. Este volcanismo submarino fue contemporáneo con la depositación de las rocas siliciclásticas del Grupo Angamarca, y la Formación Saguangal, que fueron derivadas principalmente de la Cordillera Oriental que emergía.

Finalmente, ninguna evidencia existe para apoyar hipótesis anteriores que sugieren que el arco volcánico Macuchi fue acrecionado en el Eocene Tardío, causando la inversión estructural de la Cuenca de Angamarca. Es geométricamente difícil sugerir que el bloque Macuchi se acrecionó en el Eoceno Tardío, e insertó entre los bloques de Piñón y Pallatanga, que fueron acrecionados durante el Cretácico Tardío. Además, turbiditas del Grupo Angamarca sobreyacen conformablemente rocas volcánicas de la Unidad Macuchi..

CHAPTER 1: INTRODUCTION

1.1 SCOPE OF THE STUDY

The Andean mountain chain, located along the western, active margin of South America, can be divided according to distinct along-strike trending features. Documented geological changes include the height and width of the Andean range, changes in 20th century seismicity, the timing of Neogene volcanic activity, and differences in volcanic arc width, and composition. Furthermore, the Northern Andes (i.e. north of 5°S; Fig. 1.1; Ecuador and Colombia) are unique along the plate margin because they are partly formed by oceanic allochthonous blocks, which accreted in the Cretaceous period. Such accretionary events are considered to be responsible for orogenesis, surface uplift, and the composition of arc volcanism in the Northern Andes (Feininger and Bristow, 1980; McCourt et al., 1984; Spikings et al., 2001, 2005; Guillier et al., 2001; Toro et al., 2005).

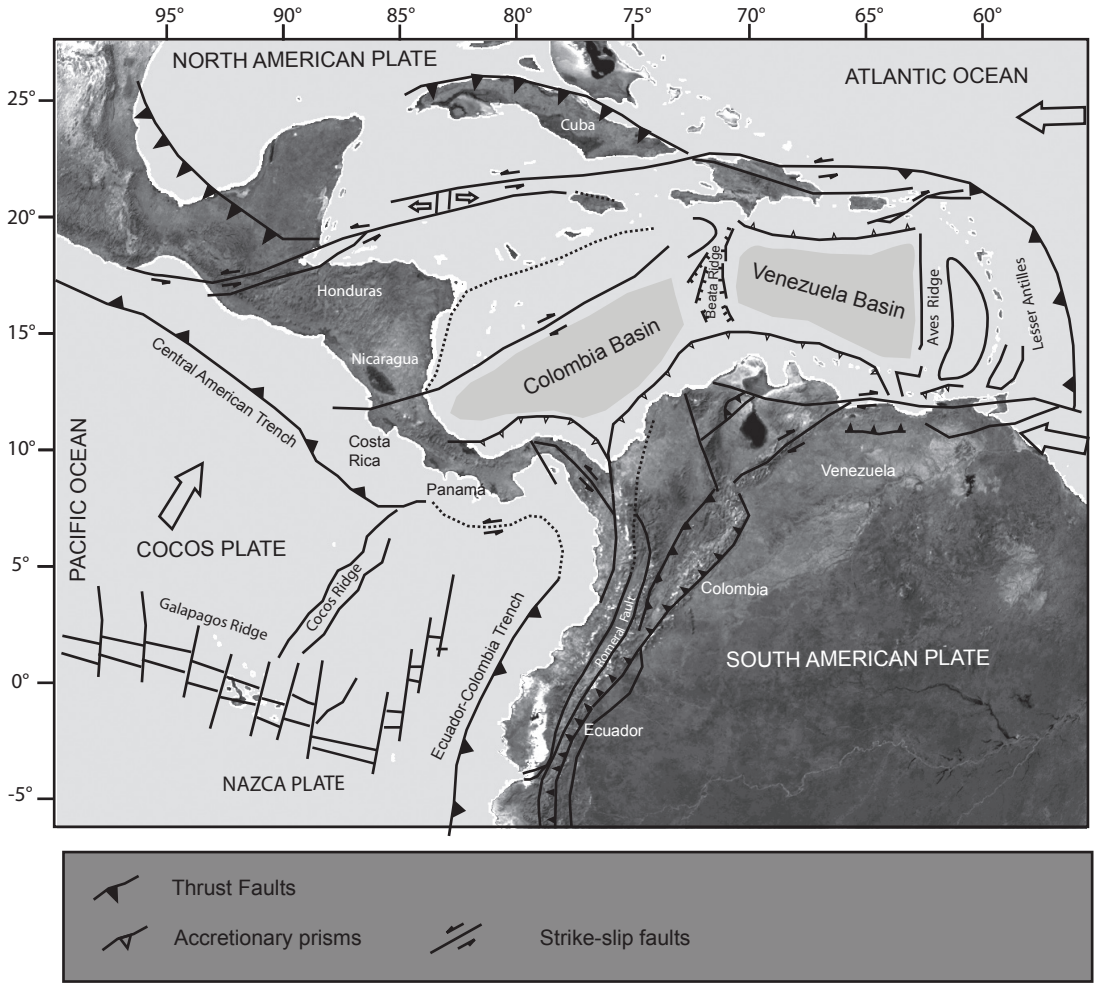

Fig. 1.1. Structural sketch map of the Northern Andes and Caribbean region (Modified from Beccaluva et al., 1996)

The accreted blocks are characterized by a large positive Bouger anomaly within the regions

of the Western Cordilleras and external forearc regions of Colombia and Ecuador (Case et al., 1971; Feininger and Seguin, 1983), indicating they are underlain by a thick sequence (>10km) of mafic crystalline rocks. Consequently, the northwestern margin of the South American Plate represents a region where continental crust grew via accretion processes during the Cretaceous, and hence a quantitative understanding of the evolution of the northern Andes will provide useful information on the mechanisms of the growth of continental crust.

This thesis presents a detailed analysis of the stratigraphy and tectonic evolution of the Western Cordillera of Ecuador (Fig. 1.2) between 1° N (the Colombian border) and 3° South. The data acquired has been used to propose a coherent paleogeographic and tectonic model for the evolution of the Western Cordillera. The model has subsequently been integrated into the plate tectonic context of the Pacific Northern Andean subduction system.

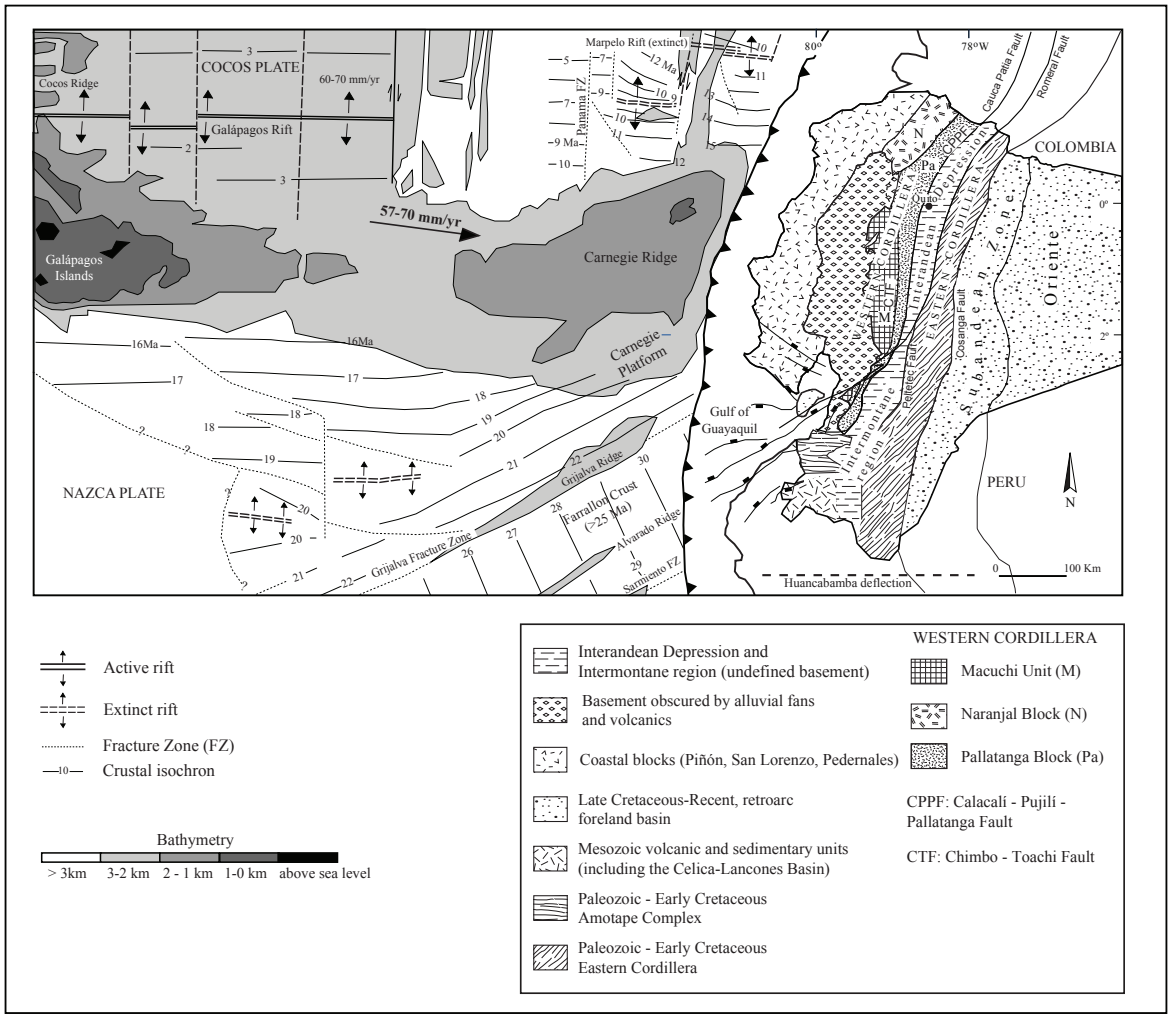

Fig 1.2: Geological setting of Ecuador, simplified bathymetry and magnetic anomalies of the Nazca Plate. Modified from Spikings et al. (2001), Lonsdale (2005) and own results.

Several researchers in the Western Cordillera of Ecuador (e.g. Wolf, 1892; Sauer, 1965; Egüez, 1986; Kerr et al., 2002a; Jaillard et al., 2004; Spikings et al., 2005) have provided useful contributions to understanding the stratigraphic and tectonic evolution of this ocean-continent

accretionary complex. Nevertheless, various geological problems remain unsolved, mainly because of the poor and discontinuous nature of rock exposures, as well as a lack of a coherent chronostratigraphic framework, determined using quantitative data.

Key outstanding questions that require answering, prior to developing a model for the geological evolution of the Western Cordillera, are:

- The age and origin of the allochthonous volcanic basement of the Western Cordillera.
- The time and duration of accretion of the allochthonous blocks.
- The Paleogene history of the Western Cordillera.
- The allochthonous vs. autochthonous origin of the Macuchi Unit (a volcanic arc sequence).

This study addresses these questions by acquiring and interpreting new qualitative (e.g. field study descriptions) and quantitative (e.g. geochemistry and geochronology) data from rocks of the Western Cordillera of Ecuador. Provenance studies of the sedimentary formations in the Western Cordillera, allow to constrain the mineralogical and chemical composition, age and hence approximate location and origin of the source regions, as well as to establish stratigraphic correlations. $^{40}Ar/^{39}Ar$ and U/Pb radiometric analyses have been utilized to provide a temporal framework for the evolution of the basement and volcanic cover sequences. Detailed field studies and rock sampling have been performed along several east – west oriented sections across the Western Cordillera, which intersect the main sedimentary and basement rock units.

1.2 GEOGRAPHICAL SETTING OF THE STUDY AREA

The Andes in Ecuador comprise the north-south trending Eastern and Western cordilleras, which are separated by the topographically low, Interandean Depression. The studied area is located in the Western Cordillera of Ecuador between 0º 20' N to 3º S (Fig.1.2), in an area that was recently mapped by the British Geological Survey (BGS) and the Ecuadorian Geological Survey (CODIGEM, later renamed DINAGE) between 1996 and 2000.

The eastern limit of the study area is defined by a partially concealed, regional-scale fault (Calacalí-Pujilí-Pallatanga Fault) that separates Cretaceous and Tertiary stratigraphic sequences of the Western Cordillera from thick Quaternary volcanic rocks of the Interandean Depression. The western border of the Western Cordillera is a sharp topographic break that marks its limit with a flat coastal plain.

The altitude of the Western Cordillera varies from 1000 to 4000 masl, and the highest peaks are defined by recent volcanoes (e.g. Chimborazo volcano; 6300 masl; Fig. 1.3). The Interandean Depression is connected to the coast via roads, which follow river valleys that cut the Western Cordillera, and provide access to often weathered and poorly exposed outcrops. The studied region hosts several ecologic systems, including coastal tropical forest, pre-montane and montane cloud forest, and paramo (high altitude grasslands) above 3800 masl. Between 200 m and 1700 m the vegetation is dense and consists of primary tropical forest.

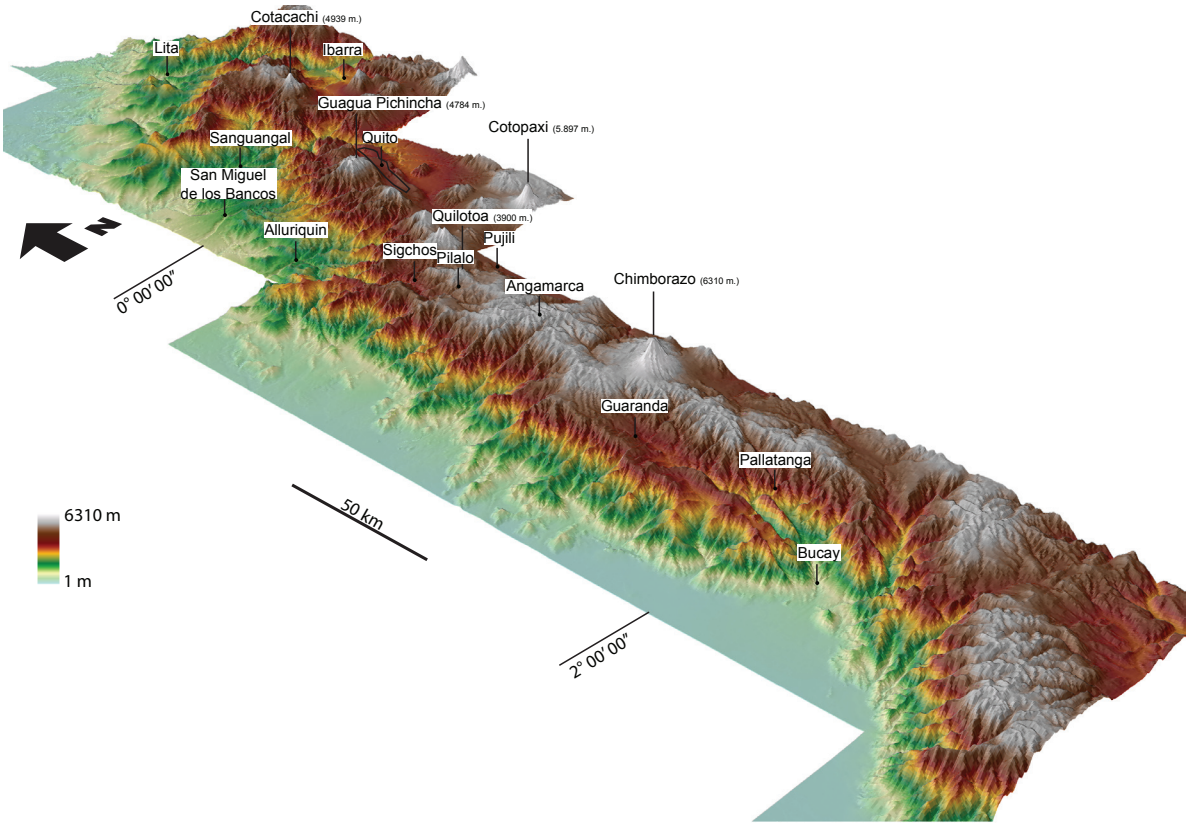

Fig. 1.3. Digital elevation model from the Western Cordillera (Data from Souris, 2001).

1.3 GEOLOGICAL OVERVIEW OF ECUADOR

The active continental margin of Ecuador is characterized by the subduction of the Nazca Plate below the South American Plate, at a mean rate of 58 mm/yr. (Trenkamp et al., 2002). North of the Grijalva fracture zone (Fig. 1.2), young oceanic crust (< 25 Ma) produced at the Cocos-Nazca spreading center is being subducted at an angle of 25-35º (Lonsdale, 1978; Lonsdale and Klitgord, 1978), whereas older oceanic crust (> 25 Ma) is being subducted south of the scarp (e.g. Lavenu et al., 1992).

Ecuador can be subdivided in five distinct morphotectonic regions (Fig. 1.2): (1) The coastal lowlands, with a basement composed of oceanic crust (Feininger and Bristow, 1980; Jaillard et al., 1995; Reynaud et al., 1999) and covered by Paleogene to Neogene forearc deposits, (2) The Western Cordillera, which is composed of mafic and intermediate extrusive and intrusive rocks, tectonically juxtaposed with mostly turbiditic deposits of Late Cretaceous to Oligocene age. (3) The Interandean valley lies to the east of the Western Cordillera, and hosts thick Pliocene to Pleistocene volcanic deposits, which bury its basement. However, small inliers and enclaves in volcanic rocks show that the basement is composed of metamorphic and mafic, crystalline rocks (e.g. Bruet, 1987). The Interandean Depression extends northwards into Colombia, and is bound against the Western Cordillera (Fig. 1.2) of the Northern Andes by the Calacalí – Pujilí Fault (in Ecuador), and the Cauca Patia Fault (in Colombia). These faults define a part of the dismembered, Late Cretaceous suture between the South American continental margin and

mafic allochthonous blocks, which are partly exposed in the Western Cordillera (e.g. Litherland and Aspden, 1992). (4) The Eastern Cordillera is composed of Paleozoic metamorphic rocks and Mesozoic granitoids (Aspden and Litherland, 1992; Litherland et al., 1994), and is separated from the Interandean Valley by the Peltetec Fault, which is a southward continuation of the Romeral Fault of Colombia. The eastern limit of the Eastern Cordillera is represented by the west dipping Cosanga Fault. (5) The Oriente Basin including the Subandean Zone is a Late Cretaceous-Recent foreland basin that developed on the South American Plate margin, in response to the growth of the Eastern Cordillera.

1.3.1 The Western Cordillera

The Western Cordillera of Ecuador consists of allochthonous oceanic blocks, which are commonly thought to have accreted against the South American Plate margin during the Late Cretaceous (Goosens and Rose, 1973, Feininger, 1980; Jaillard et al., 1995). Transcurrent fault displacement along approximately N-S trending faults has resulted in a complicated assemblage of tectono-stratigraphic units (Fig. 1.4), which juxtaposes volcanosedimentary successions of similar lithologies, but different ages.

The Pallatanga Block is exposed along the eastern border of the Western Cordillera, and is separated from the continental margin by a deformed suture zone (the Calacalí - Pujilí - Pallatanga Fault), which represents a part of the Late Cretaceous ocean – continent suture, and is considered to be the southern prolongation of the Cauca - Patia Fault system in Colombia (e.g. Hughes and Bermúdez, 1997; Litherland and Aspden, 1992). The basement of the Pallatanga Block (Pallatanga Formation) has not previously been dated, mainly due to the absence of fresh rock samples. However, geochemical analyses reveal an E-MORB type composition (Lapierre et al., 2000; Hughes and Pilatasig, 2002; Kerr et al., 2002a; Mamberti et al., 2003), suggesting that the Pallatanga Formation erupted from a mantle plume, which may be represented by the present-day Galapagos hotspot. Furthermore, it also has been suggested that the rocks are genetically related to the Caribbean Oceanic Plateau (Lapierre et al. 2000; Spikings et al., 2001; Kerr et al., 2002a).

The Macuchi Unit is located along the western border of the Western Cordillera and its eastern border coincides with the regional-scale, Chimbo Toachi Fault (Hughes and Bermúdez, 1997; Hughes and Pilatasig, 2002). Volcanic and sedimentary rocks of the Macuchi Unit are commonly considered to have been deposited in an intraoceanic island arc setting (e.g. Egüez, 1986; Aguirre and Atherton, 1987), and overlie either rocks of MORB (Boland et al., 2000) or oceanic plateau (Chiaradia and Fontbotè, 2001) affinity. The age of the Macuchi Unit is poorly constrained, but probably ranges from Paleocene to the Late Eocene, as indicated from radiometric and biostratigraphic ages (e.g. Egüez, 1986; Hughes and Pilatasig, 2002; Spikings et al., 2005). The accretion of the Macuchi Unit was previously thought to have occurred during the Late Eocene (Egüez, 1986; Hughes and Pilatasig, 2002; Jaillard et al., 2004), and supporting evidence included: (a) the identification of a regional tectonic overprinting event during the

Eocene (Egüez, 1986; Spikings et al., 2001), (b) elevated cooling and exhumation rates in the Eastern Cordillera during 43-30 Ma (Spikings et al., 2001), and (c) the Macuchi Unit is intruded by undeformed I-type granitoids, which yield K/Ar ages of approximately 20-38 Ma (e.g. Boland et al., 2000; Egüez, 1986). However, the allochthonous origin of the Macuchi Unit is strongly questioned throughout this thesis because the adjacent Piñón Block (Fig. 1.2) accreted to the South American continent during the Late Cretaceous (Luzieux et al., 2006), and it is geometrically challenging to suggest that the Macuchi Block accreted in the Late Eocene, and was inserted between the Piñón and Pallatanga Blocks.

The Naranjal Block is restricted to the northern part of the Western Cordillera (Fig. 1.2), and may extend to the coastal lowlands (Mamberti et al., 2003), and into southern Colombia (Kerr et al., 2002a). Geochemical analyses of the basement of the Naranjal Block yield island arc and oceanic plateau affinities (Boland et al. 2000; Kerr et al., 2002a). Kerr et al. (2002a) suggested that the Naranjal Block accreted to the continental margin during the Eocene.

1.4 PREVIOUS WORK IN THE WESTERN CORDILLERA

The existence of mafic and intermediate extrusive rocks in the Western Cordillera was initially reported by Wolf (1892), who described the volcanic rocks as porphyritic rocks and green schists. Much later, Sauer (1965) referred to the basement basalts of the Western Cordillera as the Formación Diabásica-Porfirítica, and Goosens and Rose (1973) later grouped the Formación Diabásica-Porfirítica with the Piñón Formation of the coastal region, and collectively referred to them as the Basic Igneous Complex, which also extended into Colombia and Central America.

Henderson (1979) re-classified the igneous basement of the Western Cordillera as the Macuchi Formation, distinguished them from the Piñón Formation, due to the presence of both tholeiitic and calc-alkaline lavas, he interpreted them as an island arc suite. Furthermore, Henderson (1979) showed that the volcanic basement of the Western Cordillera is overlain by fine-grained turbidites (Yunguilla Formation) that were deposited over a time period spanning the Late Cretaceous to Eocene. According to Henderson (1979), an accretionary tectonic event, and subsequent deformation of the rocks of the Western Cordillera occurred during the Eocene. Subsequently, Feininger (1980) proposed that the mafic crystalline rocks in the Western Cordillera and coastal region were produced by southwest dipping subduction of an oceanic plate, which gave rise to an intraoceanic arc system that collided against the South American Plate during the Eocene.

Egüez (1986) resolved the Late Cretaceous-Eocene turbiditic rocks into two, distinguishable turbiditic sequences of different age, which he referred to as the Late Cretaceous Yunguilla Formation and the Eocene Apagua Formation. Lebrat et al. (1987) recognized rocks with volcanic-arc affinities, and light rare earth elements (LREE) enriched MORB type (E and T-MORB), within the Macuchi Formation. Rocks with volcanic arc affinities were interpreted as intraoceanic volcanic arc rocks, whereas the T-MORB type rocks were interpreted as slices of the Macuchi Formation basement.

From 1996 to 2001, systematic mapping led by the British Geological Survey (BGS) in collaboration with the Ecuadorian Geological Survey (CODIGEM) produced five large-scale, geological, 1:200.000 scale maps, which cover the whole Western Cordillera (Fig. 1.4). The BGS-CODIGEM work introduced terrane nomenclature to refer to the allochthonous blocks of the Western Cordillera, and redefined the Macuchi Formation by introducing the Pallatanga Unit, which was defined as the ultramafic and mafic basement of the Western Cordillera that has an enriched MORB affinity (the E- and T-MORB of Lebrat et al., 1987). The BGS-CODIGEM mapping program also recognized two sequences of island arc deposits, one of Late Cretaceous age (Naranjal Block) and the other of Tertiary age (Macuchi Unit). The Macuchi Unit was geographically restricted to the island arc volcanic and sedimentary rocks of Eocene age located west of the Chimbo-Toachi Fault (Hughes and Bermúdez, 1997; Hughes and Pilatasig, 2002).

Lapierre et al. (2000) reported an amphibole-plagioclase-whole rock internal Sm/Nd isochron age of 123±13 Ma from a gabbro in the ultramafic complex of the San Juan Formation (Fig. 1.4), which had previously been interpreted as the ultramafic root of the E-MORB type basalts of the Pallatanga Block (e.g. Hughes and Bermúdez, 1997). This interpretation was later supported by Mamberti (2001), who utilized geochemical data to show that the San Juan Unit corresponds to the plutonic roots of an oceanic plateau. Spikings et al. (2001) reported elevated cooling rates in the Eastern Cordillera during 65-55 and 43-30 Ma, which were possibly driven by exhumation in response to the accretion of heterogeneous oceanic crust during collision of the oceanic Pallatanga and Piñón blocks, against northwestern South America.

Kerr et al. (2002) and Hughes and Pilatasig (2002) acquired geochemical data from volcanic rocks of the Western Cordillera, which showed that the Western Cordillera is composed of rocks from a variety of oceanic tectonic settings, including oceanic plateaus (Pallatanga Formation), island arc tholeiites (Naranjal and Macuchi units), back-arc basin basalts (La Portada Formation) and calc-alkaline lavas (Silante Formation). These authors also proposed that the Pallatanga Block accreted to the continental margin during a prolonged accretionary event occurring during the Late Cretaceous, whereas the Late Cretaceous Naranjal and the Eocene Macuchi island arcs may have accreted against the continental margin during the Eocene. The accretion of the Macuchi and Naranjal blocks may have occurred along the Chimbo – Toachi and Mulaute faults, respectively (Fig. 1.4).

Mamberti et al. (2003), Jaillard et al. (2004) and Toro et al. (2005) subdivided the Pallatanga Block in two different oceanic plateau sequences of Albian and Late Cretaceous ages, referred to as the San Juan – Multitud and Guaranda terranes, respectively. According to Jaillard et al. (2004), the San Juan – Multitud Terrane accreted to the continental margin during the Santonian to early Campanian (~85-80 Ma), whereas the Guaranda Terrane accreted during the Late Maastrichtian (68-65 Ma).

Finally, Spikings et al. (2005) presented $^{40}Ar/^{39}Ar$ and fission track data from the Western Cordillera, which record elevated cooling rates during 85 to 60 Ma, with a peak during 85 to 80 Ma. These authors proposed that cooling was a consequence of exhumation that occurred in

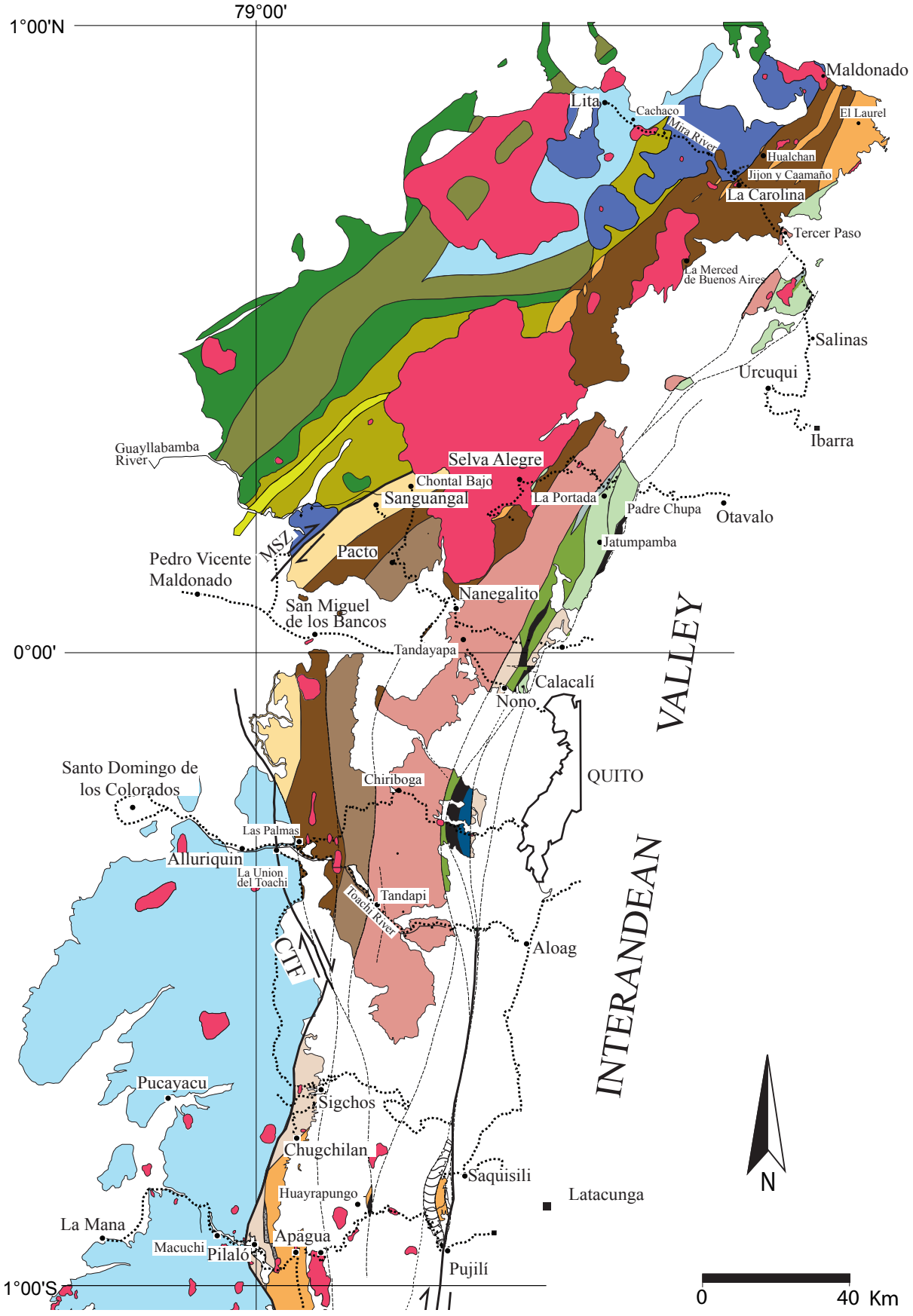

Figure 1.4a. Geological Map of the Western Cordillera from 1° N to 1° S (modified from BGS-CODIGEM, 1996-2000 and own observations)

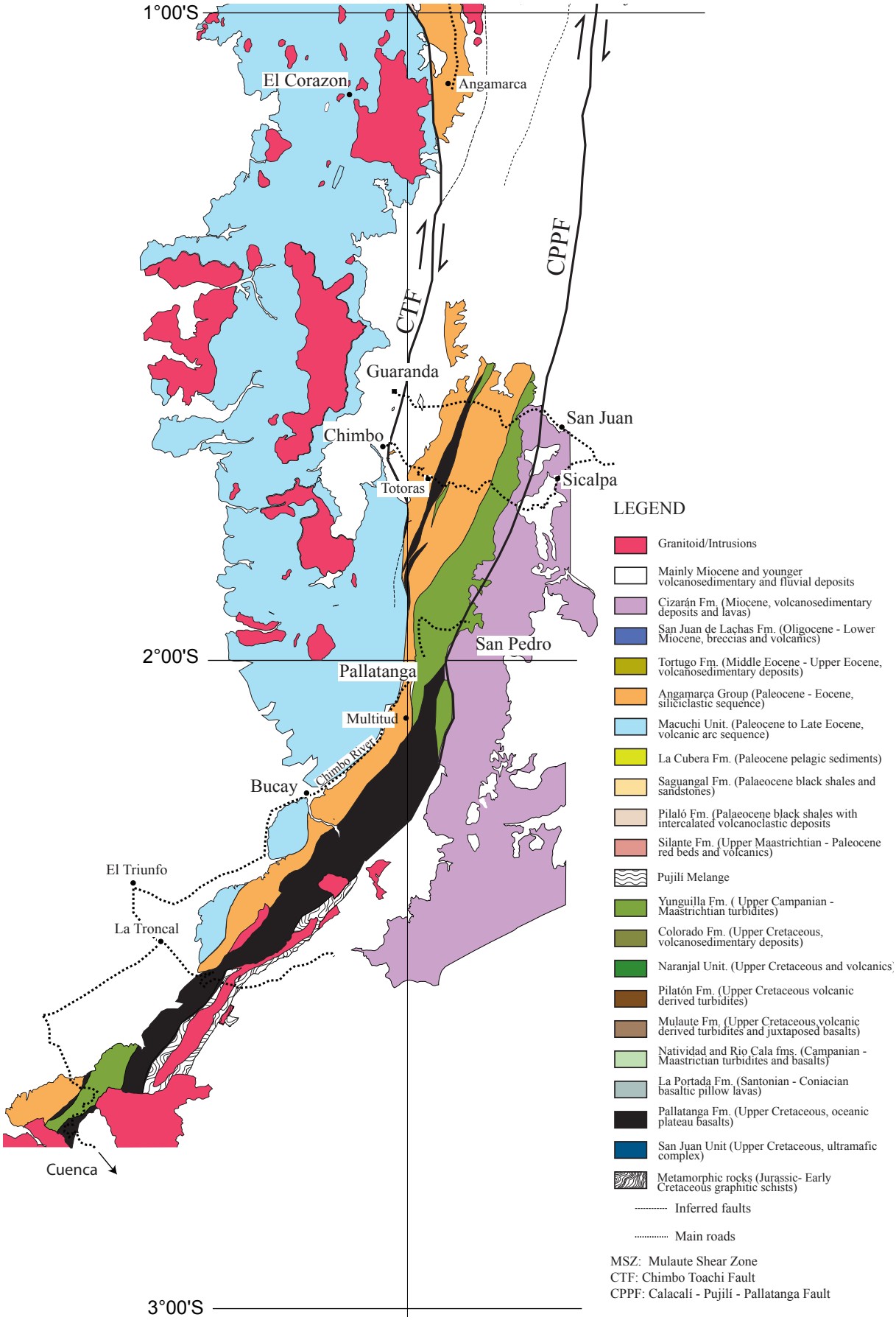

Figure 1.4b. Geological Map of the Western Cordillera from 1° S to 3° S (modified from BGS-CODIGEM, 1996-2000 and own observations)

response to the accretion of the Pallatanga Block at that time, that agrees with a reset peak of K/Ar ages reported by Aspden et al. (2002) in the Eastern Cordillera.

CHAPTER 2 GEOLOGICAL FRAMEWORK

2.1 CRETACEOUS TO OLIGOCENE STRATIGRAPHY

This section presents an overview of the existing, and newly introduced stratigraphic subdivision. To avoid unnecessary confusion, this study tried as much as possible to keep the stratigraphic nomenclature introduced by previous authors, in particularly with the BGS-CODIGEM mapping program. Formal stratigraphic terminology is introduced for the previously informal lithostratigraphic units. These formations are described in this chapter, which presents detailed descriptions of the main lithostratigraphic characteristics that are based on findings during this study, and are accompanied with important geological data obtained from previous authors (e.g. Kehrer and van der Kaaden, 1979; Egüez, 1986; BGS-CODIGEM mapping program, 1996-2000).

2.1.2 Pallatanga Block

The Pallatanga Block hosts the allochthonous, crystalline basement of the Western Cordillera. According to Hughes and Pilatasig (2002), the Pallatanga Block is limited to the west by the Chimbo-Toachi Shear Zone (CTSZ) and to the east by the Calacalí- Pujilí - Pallatanga Fault (CPPF). The CPPF is defined as a suture that separates the Pallatanga Block, which is mainly exposed in the highlands of the Western Cordillera, and is part of a dismembered suture zone, which extends across the basement of the Interandean Valley. The suture zone is exposed as a tectonic melange in the central part of the Western Cordillera (Pujilí Melange), where various exotic blocks are entrained in a foliated serpentinite matrix.

The Pallatanga Block includes several volcanic and sedimentary formations, which can be grouped into: (a) basement rocks of the Pallatanga Formation and the San Juan Unit, (b) Late Cretaceous volcanoclastic rocks with associated basaltic lavas, (c) a sequence of continental red beds and volcanic rocks of latest Maastrichtian to Paleocene age (Silante Fm.), and (d) Paleocene to Eocene sedimentary sequences of the Angamarca Group.

Basement of the Pallatanga Block

2.1.2.1 Pallatanga Formation

Previous work. McCourt et al. (1997) defined the Pallatanga Formation as the volcanic basement of the Western Cordillera, which includes basalts, dolerites and hyaloclastites of N-MORB to oceanic plateau affinity that crop-out along the eastern border of the Western Cordillera. Previous authors used different names to define this sequence, e.g. The Basic Igneous Complex (Goosens and Rose, 1973; Wallrabbe-Adams, 1990), Piñón Formation or the Macuchi Unit (e.g. Henderson, 1979; Bristow and Hoffstetter, 1977; Kennerly, 1980; Baldock, 1982). Lebrat et al. (1985) recognized the enriched MORB nature (E and T-MORB) of some of the volcanic rocks in the Western Cordillera. The E-MORB rocks are mainly located at the eastern border of the Western Cordillera, and their geochemical composition is clearly distinguishable from a

majority of volcanic rocks within the Western Cordillera, which yield arc signatures. Reynaud et al. (1999) demonstrated that the E-MORB rocks of Lebrat et al. (1985), which were subsequently included in the Pallatanga Unit by McCourt et al. (1997) had an oceanic plateau character.

Extensive geochemical analyses across the Western Cordillera, including trace elements and Nd, Sr, U, Pb isotopes (e.g. Cosma et al., 1998; Lapierre et al., 2000; Kerr et al., 2002a; Mamberti; et al., 2003), have established the mantle-plume related nature of the Pallatanga Formation and investigated its possibly genetical relationship with the Caribbean Plateau.

Oceanic plateaus form in deep-ocean basins as broad, flat-topped features lying 2000 m or more above the seafloor (e.g. Mann and Taira, 2004). Condie and Abbot (1999) indicate that globally, approximately one third of the lower crust is composed of mafic rocks derived from mantle plume sources. Oceanic plateaus form by mantle-plume driven eruptions, and characteristically have large aerial extents (>1015 km^2) with anomalously high eruption rates (Saunders et al., 1996). Typically their thickness is greater than 10 km, and locally can exceed 30 km (e.g., the Ontong Java Plateau; Kerr et al., 2003). Oceanic plateaus are not readily subductable because of their inherent buoyancy. Sedimentary rocks that are commonly associated with oceanic plateau rocks include pelagic facies, such as radiolarian cherts and related sedimentary rocks.

Geochemically, oceanic plateaus usually yield primitive mantle normalized La/Nb ratios of ~1 (i.e. no negative Nb anomaly). Normalized to chondrite, REE patterns are typically flat, which is distinctive from arc rocks that show LREE enrichment, or N-MORB, which generally reveal depleted LREE patterns. Plateau basalts are high in MgO (> 8%), with almost no subaerial volcanic deposits, unlike arc related volcanic rocks. Isotopic data, particularly εNd of the oceanic plateaus, typically range between +6 to +8 (Kerr et al., 2003).

Occurrence. The Pallatanga Formation is exposed along the eastern border of the cordillera and is separated from the Interandean Depression by a N-S trending fault (Fig. 1.2; Calacalí–Pujilí-Pallatanga Fault). The type locality lies in the Pallatanga Valley (UTM: 733662/9793241) (Fig. 2.1), and other exposures occur along the Ibarra - Lita, Otavalo - Selva Alegre, Quito - Chiriboga, Calacalí - Pacto, and Guaranda – Riobamba roads, as well as west of Calacalí village (UTM: 770851/10001497), and Huayrapungu (UTM: 743732/9901166).

Lithology. The formation comprises basalts, microgabbros, diabases, peridotites, pillow lavas, massive non-vesicular dolerites and hyaloclastites. The pillow basalts are aphyric, or sometimes contain a few phenocrysts of plagioclase and pyroxene. The textures of the basalts are hypocrystalline to holocrystalline, occasionally glassy with phenocrysts of olivine and pyroxene, and exhibit an intersertal to intergranular texture. The major constituents of the basalts are clinopyroxene, idiomorphic plagioclase, and opaque minerals.

Rocks of the Pallatanga Formation have been subjected to various degrees of ocean-floor hydrothermal alteration under low- to intermediate-green schist facies conditions. This alteration has often resulted in extensive reorganization of the primary igneous phases, resulting in the replacement of plagioclase by albite and/or clay minerals and transformation of clinopyroxene into Fe-actinolite and/or chlorite. In the absence of geochemical analysis or stratigraphic ages,

rocks of the Pallatanga Formation can be easily confused with rocks of the La Portada Formation due to the similar lithology and type of alteration.

Fig. 2.1. Massive pillow basalts of the Pallatanga Fm. in the type locality, the Pallatanga Valley (UTM: 733662/9793241)

Stratigraphic relationships. Along the Western Cordillera, the Pallatanga Formation is found in tectonic slivers separated from adjacent slices by north-south running faults. The Pallatanga Formation is often spatially associated with the Yunguilla Formation, although the contact between these two formations is always tectonic. North of 2°S, the eastern limit of the Pallatanga Formation coincides with the Calacalí – Pallatanga Fault. In southern Ecuador, a faulted contact separates the Pallatanga Formation from graphitic schists within the Western Cordillera, which frequently crop-out within the Eastern Cordillera (Dunkley and Gaibor, 1997; McCourt et al., 1997). Pelagic cherts of Campanian to Maastrichtian age (Jaillard et al., 2004) stratigraphically overlie the Pallatanga Formation, west of Guaranda in central Ecuador.

Geochemistry and environment of formation. Geochemical analyses of rocks of the Pallatanga Formation indicate rock compositions vary between E-MORB and oceanic plateau basalts (Hughes and Bermúdez, 1997; McCourt et al., 1997; Dunkley and Gaibor, 1997; Boland et al., 2000; Kerr et al., 2002a; Hughes and Pilatasig, 2002). Chondrite normalized REE plots yield flat patterns $(La/Yb)_N$ ratios of ~1 (Fig. 2.2). The isotopic composition of the Pallatanga Formation is juvenile, with εNd values ranging from +6 to +10 (Mamberti et al., 2003). The overall geochemical composition of the Pallatanga Formation (e.g. Reynaud et al., 1999; Lapierre, 2000; Hughes and Pilatasig, 2002; Kerr et al., 2002a) indicates an oceanic plateau origin, possibly formed by a mantle plume.

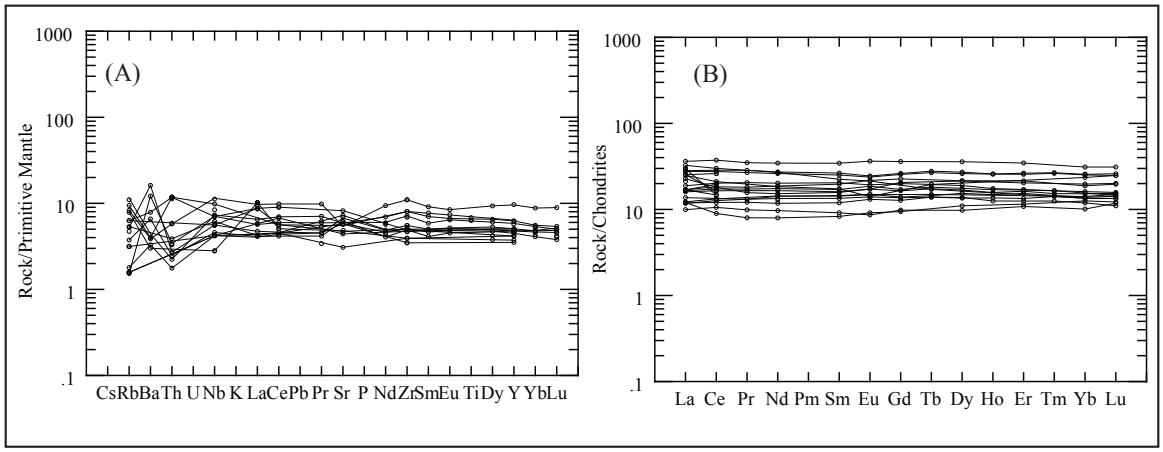

Fig. 2.2. Primitive mantle-normalized multi-element and REE plots (normalizing values from Sun and McDonough 1989) of the Pallatanga Formation. Geochemical data compiled from Van Thournout et al. (1992), Hughes and Pilatasig (2002) and Kerr et al. (2002a).

Age. Until now, the Pallatanga Formation has not been radiometrically dated, due to the high degree of alteration of the rocks. However, previous work suggested the formation is older than Campanian, as it is overlain by Campanian to Maastrichtian radiolarites (Jaillard et al., 2004). Zircons extracted from a layered gabbro of the San Juan Unit (see below), which is interpreted as the ultramafic root zone of the Pallatanga oceanic plateau sequence yielded a weighted mean U/Pb (SHRIMP) age of 87.10±1.66 Ma (2σ). This age is interpreted as the age of crystallization of the mafic basement of the Pallatanga Formation.

2.1.2.2 San Juan Unit

Previous work. These rocks, which crop-out to the southwest of Quito, were first described in detail by Juteau (1977) and were subsequently referred to as the San Juan Unit by Hughes and Bermudez (1997). Hughes and Pilatasig (2002) proposed that the San Juan Unit represents the ultramafic root of the magmatic rocks of the Pallatanga Block, and Mamberti et al. (2004) utilized geochemical data to suggest that the San Juan Unit represents a magmatic chamber that existed within an oceanic plateau setting.

Occurrence. The San Juan Unit is exposed west of the village of San Juan, along the Saloya River, and along the Quito-Chiriboga road (UTM: 758987/9974247), which runs parallel to the river. Isolated exposures of gabbros, lithologically similar to the ones included in the San Juan Unit, can also be observed east of Totoras village, in central Ecuador (UTM: 730472/9809654).

Lithology. At the type locality, the San Juan Unit is an ultramafic sequence, which includes serpentinized peridotites, layered cumulate fine-grained peridotites, dunites, layered cumulate olivine gabbros, fine to coarse-grained amphibole-bearing gabbros (Fig. 2.3), norites, locally

anorthosites and dolerites. The whole sequence dips at 80° to the east, and it is intruded by pegmatitic gabbros, dolerites, and dacitic dykes. Rocks of the San Juan Unit show pervasive hydrothermal alteration, with pyroxene partially or totally replaced by amphibole.

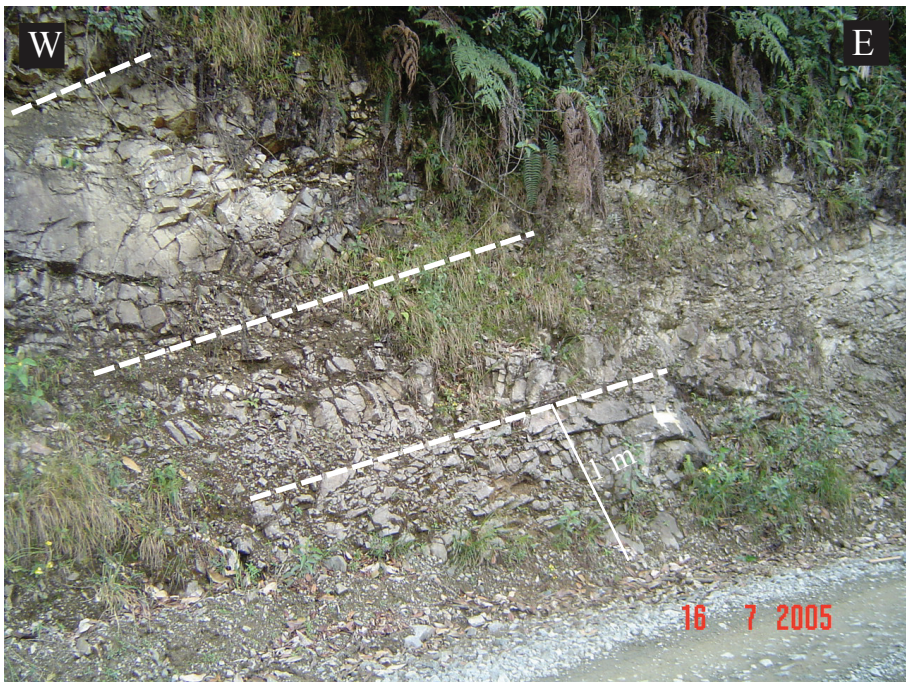

Fig. 2.3. Layered gabbros in the San Juan Formation ultramafic sequence, exposed along the Chiriboga - Las Palmas road (UTM: 758987/9974247). Gabbros at this site yielded a U/Pb SHRIMP zircon age of 87.10±1.66 Ma.

Stratigraphic relationships. The contacts of the San Juan Unit with adjacent formations are faulted. In the type locality, north-south trending faults separate the San Juan Unit from the Yunguilla Formation to the east and the Pallatanga Formation to the west.

Geochemistry and environment of formation. The ultramafic cumulates are depleted in LREEs, whereas the gabbros yield flat or slightly enriched LREE patterns. Their chemical compositions are similar to accreted oceanic plateau basalts, and differentiated sills in western Ecuador (Mamberti et al., 2004). The Unit shows a narrow range of εNd (+8 to +5) and a rather large range of Pb isotopic ratios (Mamberti, 2001; Mamberti et al., 2004). The geochemical evidence suggests that the San Juan Unit represents the plutonic components of an oceanic plateau, in a model similar to that previously proposed by Kerr et al. (1998) for the relationship between the Bolivar Ultramafic Complex and the basaltic Volcanic Fm. in the Western Cordillera of Colombia (Fig. 2.4). The Bolivar ultramafic complex of Colombia includes the same lithologies described in the San Juan Unit, and forms part of the eastern most portion of the Western Cordillera of Colombia, where mantle-plume derived basalts (Volcanic Fm.) have also been identified.

Age. Lapierre et al. (2000) report a Sm/Nd internal isochron age of 123±13 Ma from an amphibole-bearing gabbro of the San Juan Unit. However, amphiboles extracted from the same

sample yield a saddle-shaped $^{40}Ar/^{39}Ar$ age spectrum, which yields a maximum age of 99.2±1.3 Ma (Mamberti et al., 2004).

In the present work, zircons extracted from a layered gabbro of the San Juan Unit yielded a weighted mean U/Pb (SHRIMP) age of 87.10±1.66 Ma (2σ), which we interpret as the time of crystallization of the San Juan Unit (see chapter 4), and hence the oceanic plateau of which they form the ultramafic roots. In the Model of Kerr et al. (1998), the layered gabbros were formed by the accumulation of crystals at the base of magma chambers, within an oceanic plateau (Fig. 2.4).

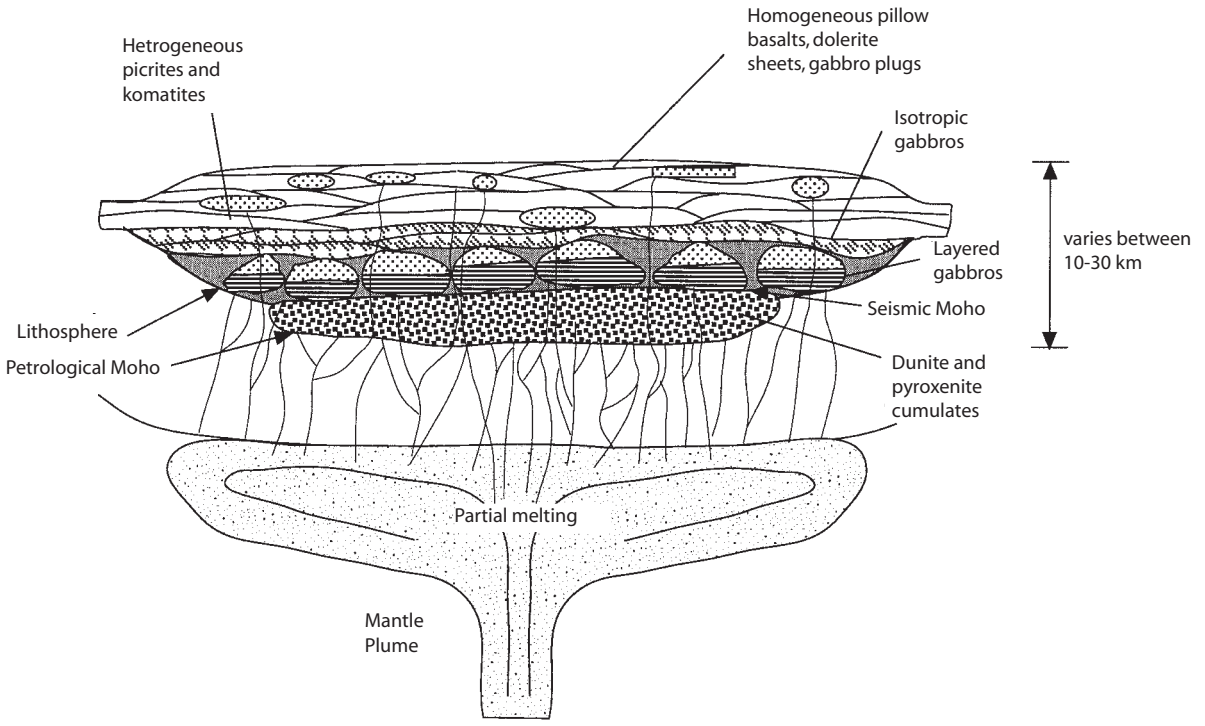

Fig. 2.4. Hypothetical cross-section through an oceanic plateau based on ultramafic sequences in Western Colombia (Kerr et a., 1998)

2.1.2.3 The Pujilí Melange and the Pujilí Granite

Previous work. Hughes and Bermúdez (1997) were the first to name the Pujilí Melange, which refers to the chaotic, and highly mixed assemblage of sheared blocks west of the town of Pujilí.

Occurrence. The best exposures of the Pujilí Melange occur in the area between Pujilí and Saquisilí (Fig. 1.4), in particular along the steeply incised banks of the Quebradas Maca Grande (UTM: 753822/9902945), Pusuchisi and Picisí (UTM: 755300/9898600).

Lithology. The melange comprises blocks of different lithologies, which have widely varying origins, and which are highly deformed displaying a penetrative cleavage. Blocks within the melange include foliated muscovite-rich granitoids, amphibolites, phyllites, grey sandstones, and conglomerates surrounded by a serpentinitic matrix (Fig. 2.5). S-C fabrics in foliated granitoids (Pujilí Granite) indicate dextral shear movement.

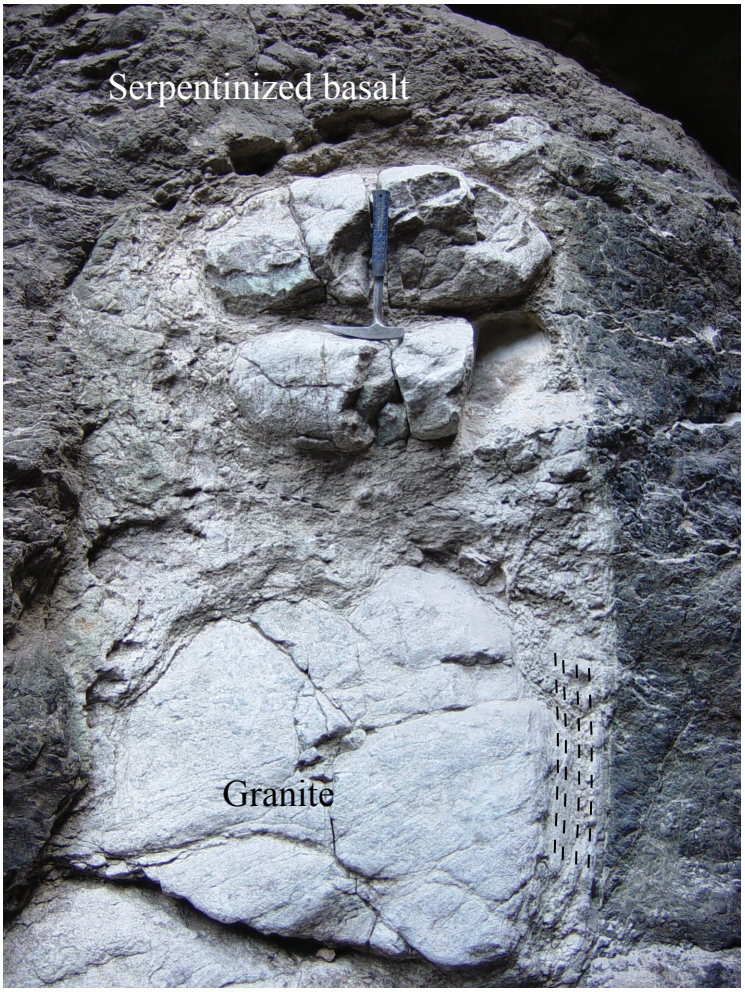

Fig. 2.5. Foliated block of the Pujilí Granite within serpentinized basalts in the quebrada Picisí (UTM: 755300/9898600). S-C structures indicate dextral sense of shearing. Zircon crystals from this block yielded a U/Pb (SHRIMP) age of 85.5 ±1.4 Ma.

Tectonic environment of the Pujilí Melange. The Pujilí Melange is interpreted to be a relic of the suture between the allochthonous oceanic blocks and the continental margin, which formed during terrane accretion in the Late Cretaceous.

Geochemistry and tectonic environment of the Pujilí Granite. The Pujilí Granite as indicated above is part of the blocks included within the Pujilí Melange. Whole rock geochemical data from a sample in the melange, indicates high concentrations of LILE elements, including Ba and Sr (Fig. 2.6), a negative Nb anomaly, strong LREE enrichment ($(La/Yb)_N = 33.7$).

MgO content is 0.21, SiO_2 of 56.92% and Al_2O_3 10.04 %. εNd values of +6 (Fig. 2.7) suggests that the magma was not contaminated with old, continental crust, and lie within the range of values obtained for the Caribbean Oceanic Plateau (Thompson et al., 2003). Negative Nb and Ti anomalies suggest that the Pujilí Granite was formed in a subduction zone setting. The granite is highly depleted in HREE (Fig, 2.6).

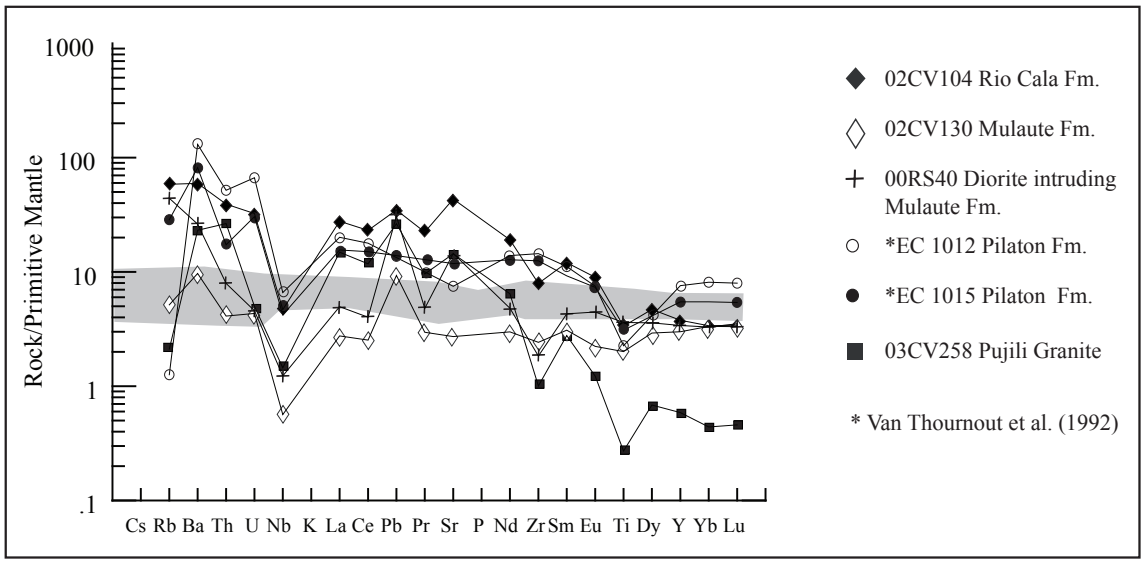

Fig. 2.6. Primitive mantle normalized (Sun and McDonough, 1989) multi-element plot for the Rio Cala, Mulaute, and Pilatón formations and the Pujilí Granite. The subduction nature of these sequences is evident by the relative enrichment in LILE elements and the negative Nb anomaly, the latter not observed in rocks from the Pallatanga Formation (i.e., whole-rock data shown in gray field; Hughes and Pilatasig, 2002).

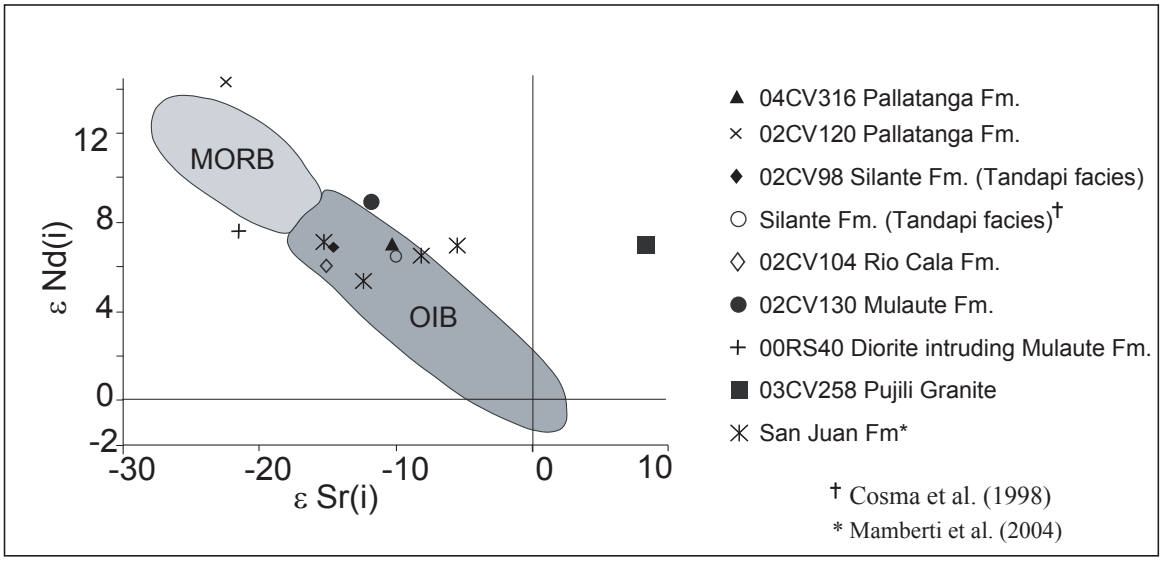

Fig. 2.7. εNdi- εSri correlation diagram for the Rio Cala, Mulaute, San Juan formations and the Pujilí Granite, including data from Cosma et al. (1998) and Mamberti et al. (2004).

The enrichment of LILE and negative Nb and Ti anomalies, in combination with juvenile isotopic ratios suggests the granite crystallized within an intraoceanic island arc setting. The geochemistry of the Pujilí Granite share similarities with Archean TTGs (tonalite-trondhjemite-granodiorite) and the modern analogues, adakites. Adakites are magmas with high SiO_2 (>57%), elevated Al_2O_3, Na_2O, Na_2O/K_2O, LILEs, Sr and low HREE (Drummond and Defant, 1990).

These rocks are inferred to be derived by partial melting of a subducting slab (Kay, 1978). It has been proposed by Sajona et al. (1993) that magmas with adakitic characteristics can be formed during early stages of subduction by partial melting of subducted basaltic oceanic crust below an anomalously hot mantle wedge. Similarly, melting at deep levels of an oceanic plateau sequence could create silicic melts with adakitic geochemical signatures (Condie, 2005).

The association of Late Cretaceous granitic rocks with island arc signatures and Late Cretaceous mafic oceanic plateau rocks is also described on the island of Aruba (White et al., 1999). The Aruba Batholith and the Pujilí Granite have partially adakitic signatures, and yield similar isotopic ratios (εNdi ~7), which, when considering prevailing tectonic reconstructions of the eastern pacific (see later), suggests that they may have crystallized within the same subduction zone, at the same time. In addition, tonalites of the Aruba Batholith yield zircon ion-probe ages of 86±1 Ma (Richard Spikings, pers comm.), which is indistinguishable from the zircon U/Pb SHRIMP crystallization age of 85.5±1.4 Ma for the Pujilí Granite (see below). White et al. (1999) interpreted the Aruba Batholith as being produced by partial melting of the Caribbean Plateau above an incipient subduction zone with an anomalously hot mantle wedge, which may have drove melting at the base of the oceanic plateau. A similar scenario can be proposed for the origin of the Pujilí Granite. However, the HREE depletions of the Pujilí Granite indicate that it was formed below the garnet stability field (~ 60-70 km depth), which indicates that the Pujilí Granite may also have a component derived from melting of a subducted slab, that can account for the adakitic signature.

Age. Spikings et al. (2005) obtained white mica and biotite $^{40}Ar/^{39}Ar$ plateau ages of 86±1 and 82±1 Ma respectively, from foliated granitoids (Pujilí Granite) and a hornblende $^{40}Ar/^{39}Ar$ age of 83±2 Ma for a dacitic block in the melange. According to these authors, the ages represent rapid cooling driven by the accretion of the Pallatanga Block against the South American Plate during the Santonian (~85 Ma). In the present study, a weighted mean U/Pb (SHRIMP) zircon crystallization age of 85.5±0.7 Ma was obtained for the Pujilí Granite. These data therefore refute earlier interpretations, which proposed that the Pujilí Granite represent fragments of Triassic plutons that are currently exposed in the Eastern Cordillera, and became incorporated into the melange zone during ocean-continent collision (e.g. Hughes and Pilatasig, 2002; Spikings et al., 2005).

2.1.2.4 Totoras Amphibolite

Previous work. Jaillard et al. (2004) reported the presence of amphibolites juxtaposed against basalts of oceanic plateau affinity along the Riobamba – Guaranda road section, east of the village of Totoras (Fig. 1.4). Beaudon et al. (2004) presented a detailed geochemical investigation of the amphibolites and associated granulites, and concluded that the Totoras amphibolites and granulites attained peak P-T conditions of 6-9 kbar and 800-850 °C, and were derived from an oceanic plateau protolith. The authors concluded that the amphibolites were produced by metamorphism of the oceanic plateau basement of the Western Cordillera (Pallatanga Fm.)

during the Miocene. However, the $^{40}Ar/^{39}Ar$ ages obtained in this study indicate that cooling from peak metamorphic conditions occurred during the Late Cretaceous (see below), prior to the accretion of rocks of the Pallatanga Fm.

Occurrence. The Totoras amphibolite sequence is located in the central Western Cordillera, east of the locality of Totoras (UTM: 730223/9809289). Amphibolite blocks, which are lithologically similar to the Totoras amphibolite, are also exposed in the Pujilí Melange (Quebrada Maca Grande, UTM: 753822/9902945).

Lithology. The amphibolites are medium to coarse-grained, and are composed of large crystals of green hornblende, plagioclase and white quartz-feldspar vein lets. The vein lets are somewhat younger than the rest of the rock, having filled in fractures in the amphibolite.

Stratigraphic relationships. The amphibolites in the Totoras area are tectonically juxtaposed against unmetamorphosed mafic rocks of the Pallatanga Formation, and the amphibolites were found together with coarse-grained gabbros, lithologically similar to the gabbros of the San Juan Unit, although the Stratigraphic relationship between the amphibolites and the gabbros was not observed in the field. In the Pujilí area, the amphibolites are included as tectonic blocks in the Pujilí Melange.

Geochemistry and environment of formation. Geochemically the amphibolites have oceanic plateau signatures and are believed to have formed during amphibolite facies metamorphism (Jaillard et al., 2004; Beaudon et al., 2005). The estimated thickness of the Caribbean Plateau is c. 20 km (Sinton et al., 1998; Revillon et al., 2000) and with a geothermal gradient of c. 40°C/km then the required P-T conditions to generate such rocks mass well have been achieved towards the base of the plateau.

Age. A hornblende $^{40}Ar/^{39}Ar$ plateau age of 84.69±2.23 (2σ) Ma (see chapter 4) obtained from an amphibolite, collected east of Totoras village (UTM: 0730223/7809289) is interpreted as a cooling age for these rocks following amphibolite facies metamorphism.

Sedimentary and volcanic cover series of the Pallatanga Block

2.1.2.5 The Rio Cala Group

We define the Rio Cala Group as a volcanic and sedimentary sequence deposited in an intraoceanic island arc setting, on top of the Pallatanga Formation. The Group was deposited during the Late Cretaceous, and includes the La Portada, Mulaute, Pilatón, Natividad and Rio Cala formations.

La Portada Formation

Previous work. On purely geochemical grounds, the name Portada Formation was assigned by Kerr et al., (2002a) to a series of pillow basalts exposed in the Otavalo – Selva Alegre road. The basalts yield a geochemical composition compatible with rocks formed in a subduction zone, although they yield unusual low concentrations of LREEs.

Van Thournout at al. (1992) also noted the distinct geochemical character of the basalts, and

interpreted the sequence as boninites, which formed in the forearc region of an island arc. The La Portada Formation has previously been mapped as the Piñón Formation (Egüez et al., 1988), and has also been included within the Pallatanga Formation (Boland et al., 2000).

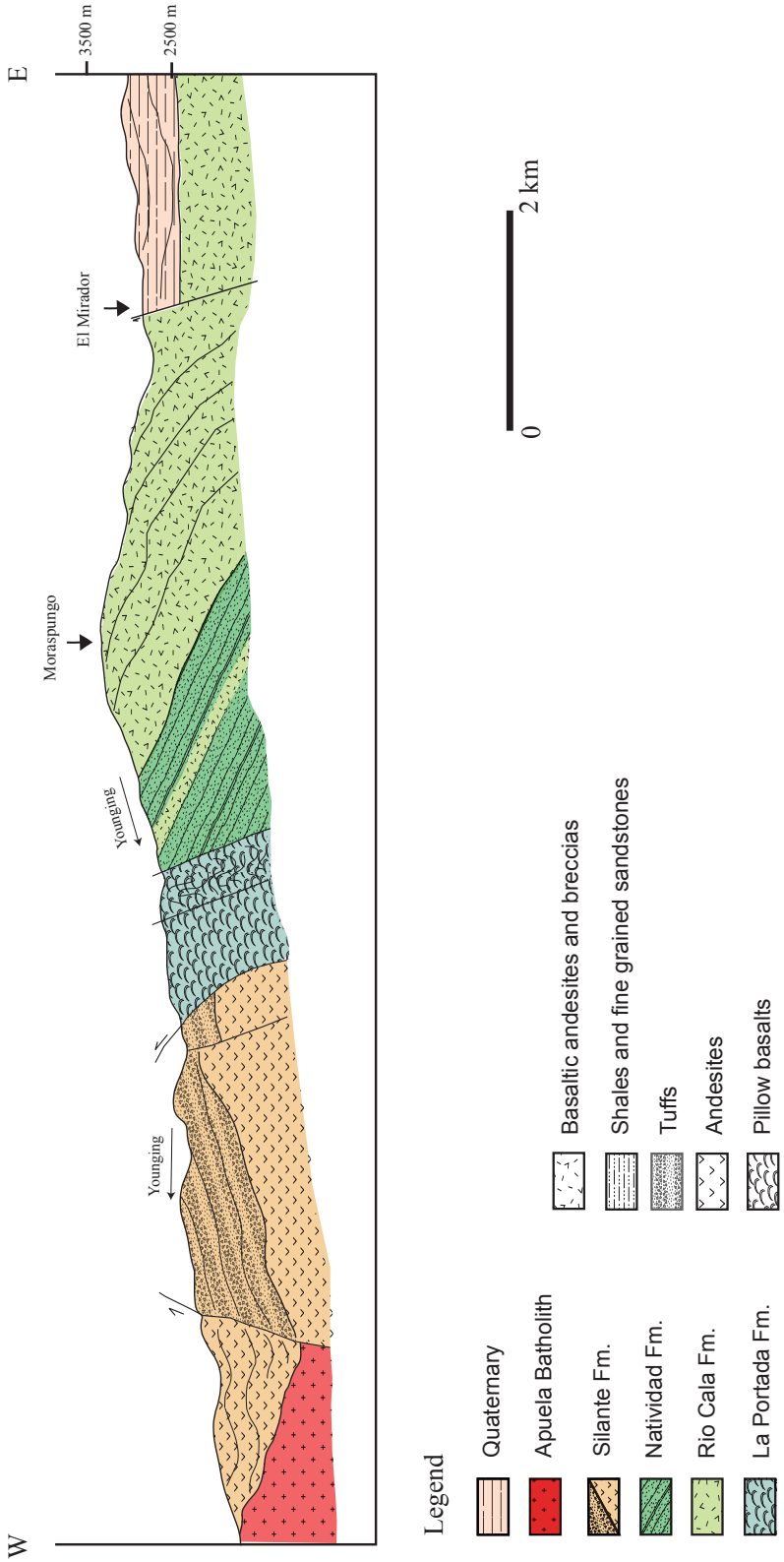

Fig. 2.8. Geological profile along the Otavalo - Selva Alegre road section. (Modified from Egüez et al., 1988).

Occurrence. Basalts of the La Portada and Pallatanga Fms. can only be distinguished by their geochemical compositions, because they are lithologically similar, and all contacts with the juxtaposed rock sequences are tectonic. According to Kerr et al. (2002a), the type section of the La Portada Fm. is exposed in the Quebrada La Portada, along the Otavalo - Selva Alegre road (UTM: 784500/00287). Van Thournout et al. (1992) also reported pillow lavas with chemical compositions similar to the La Portada Formation on the Salinas Lita road, west of the village of La Concepción (UTM: 818623/10064857). Geochemically similar rocks are also reported in the Guayllabamba River (UTM: 741300/10027600), in rocks mapped as the Naranjal Unit by Boland et al. (2000) (see also Kerr et al; 2002a).

Lithology and thickness. The La Portada Formation includes pillowed basalts and string lavas in the Otavalo - Selva Alegre road section. The basalts are aphyric with a glassy matrix, which is partially recrystallized to pumpellyite, chlorite and epidote. The volcanic rocks are strongly oxidized (reddened) and hydrothermally altered. Calcite veining and zeolite filling vacuoles are often observed, and alteration increases towards the contact with the Silante Formation. In the exposures west of La Concepción, the lithologies are similar to the exposures in the Otavalo – Selva Alegre road, although the lavas west of La Concepción village are less oxidized and hydrothermal alteration is manifested by abundant cracks filled with calcite.

Stratigraphic relationships. The pillow basalts of the La Portada Formation that are exposed along the Otavalo - Selva Alegre road, are in tectonic contact with turbidites of the Natividad Formation to the east, and with volcanoclastic rocks of the younger Silante Formation to the west (Fig. 2.8). Close to La Concepción, turbidites of the Natividad Formation are in tectonic contact with deformed volcanic rocks of the La Portada Formation (Fig. 2.9).

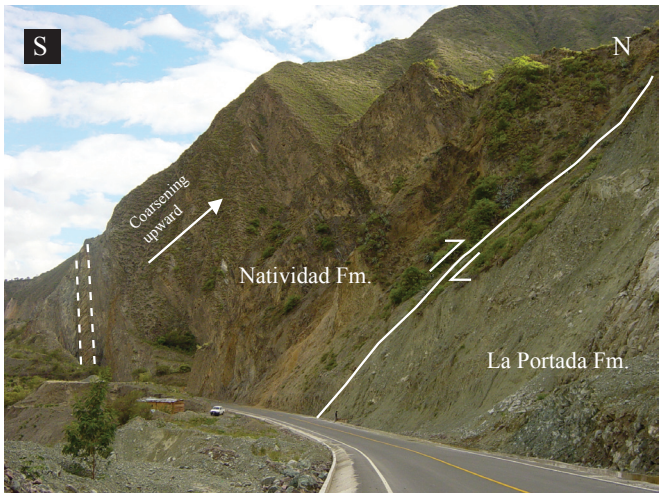

Fig. 2.9. Tectonic contact between turbidites of the Natividad Fm. and basalts of the la Portada Fm. (UTM: 0818623/0064857) along the Ibarra - Lita road.

Geochemistry and environment of formation. Geochemical analyses (Van Thournout, 1991; Kerr et al., 2002a) of basaltic andesites of the La Portada Formation yield arc related signatures

(e.g. negative Nb anomaly). The rocks are slightly depleted in LREEs (Fig. 2.10), with SiO_2 ~49%, CaO_2 of ~15.45% in average, high MgO (>8%), high Cr (>500 ppm), high Al_2O_3 (>23%) and low concentrations of TiO_2 (<0.5%), Zr and Y.

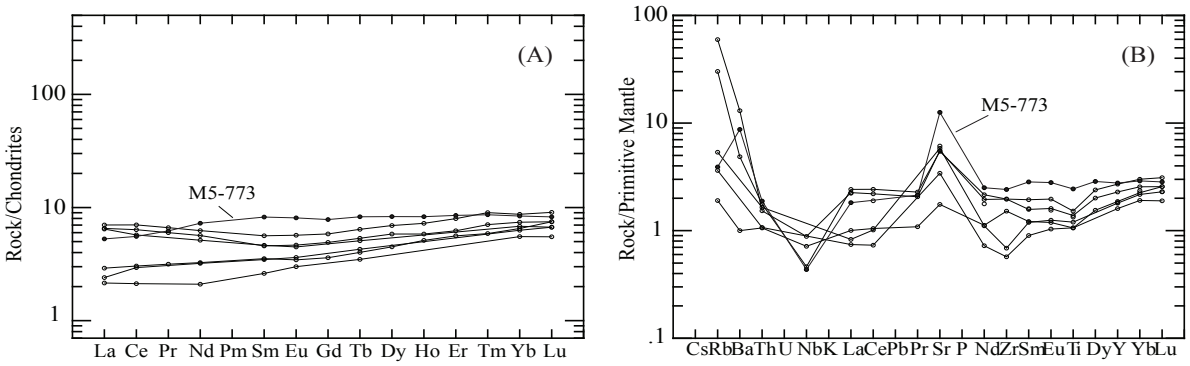

Fig. 2.10. Primitive mantle-normalized multi-element and REE plots (normalizing values from Sun and McDonough 1989) of the La Portada Formation, also showing sample M5-773 of the Naranjal Unit. Geochemical data compiled from Van Thournout et al. (1992) and Kerr et al. (2002a).

The geochemical characteristics are similar to those of boninites (e.g. Crawford et al., 1981). A prevailing interpretation for boninitic rocks is that they define the early stage of island arc volcanic activity (Stern and Bloomer, 1992; Pearce et al., 1992), generated beneath very young and hot oceanic crust (Stern et al., 1991). According to the CaO/Al_2O_3 ratio (1.07 in average) yielded by rocks of the La Portada Formation, they can be classified as High-Ca boninites, whose formation requires the interaction of hot 'dry' residual mantle, which can be associated with plumes, and a subduction-related H_2O-bearing component (Sobolev and Danyushevsky, 1994). It is generally accepted that the high magnesium contents of whole rock and phenocrysts, and the very low HFSE abundance observed in boninites result from melting of highly depleted, refractory mantle peridotite (Crawford et al., 1989). In our opinion, the highly depleted mantle component may be represented by previous melt extraction beneath an oceanic plateau. The enrichment in LILEs and other fluid-mobile elements in boninites results from the involvement of slab-derived, hydrous fluid or hydrous melt, as has been proposed for boninites in other areas (e.g., Crawford et al., 1989; Pearce et al., 1992).

Therefore, rocks of the La Portada Formation may have formed by subduction of oceanic crust, below an oceanic plateau, permitting the interaction of a highly depleted mantle wedge with slab-derived, hydrous fluid. This interpretation is also consistent with the close, present-day spatial association of the La Portada Formation with rocks of the Rio Cala Group, which formed in an island arc setting.

Age. The age of the La Portada Formation is based on foraminifera fossils recovered from mudstones intercalated within the pillow lavas along the Otavalo - Selva Alegre road. The foraminifera *Rugoglobigerina* cf. *pilula* and *Conorbina* sp, and *Valvulineria* cf. *camerata* (sample M5-JX12, in Boland et al., 2000), indicates a Santonian to Early Campanian age

(Wilkinson, 1998).

Mulaute Formation.

Previous work. Hughes and Bermúdez (1997) defined the Mulaute Formation as a mixed volcano-sedimentary sequence cropping out along the Alóag - Santo Domingo road. Previous authors (e.g. Faucher and Savoyat, 1973; Bristow and Hoffstetter, 1977) included sedimentary rocks of the Mulaute Formation into the Cayo de la Sierra Formation, or the Pilatón Beds (Kehrer and Van der Kaaden, 1979). The term Mulaute Formation is used here for basaltic rocks (Toachi Unit of Egüez, 1986), with intercalated turbiditic sediments exposed along the Alóag – Santo Domingo road.

Occurrence. Tectonic slices of the Mulaute Formation are restricted to the northern part of the Western Cordillera (Fig. 1.4). The main outcrops occur along the Alóag – Santo Domingo road, (UTM: 7357588/9962157), which are considered as the type section. Good exposures can also be observed east of the village of Pacto Loma, along the Calacalí – La Independencia road.

Lithology and thickness. The Mulaute Formation along the Alóag – Santo Domingo road section includes thick to medium bedded turbidites (Fig 2.11), with abundant plagioclase, pyroxene and epidote. This facies is lithologically similar to the previously defined Pilatón Formation of Hughes and Bermúdez (1997), and is observed west of La Esperie Batholith (UTM: 738772/9961656). East of this point, primary volcanic rocks, including basaltic andesites, tuffs, and volcanic breccias, dominate the sequence. The volcanic rocks contain abundant epidote, pumpellyite, and chlorite, suggesting they have experienced a low-grade, metamorphic overprint. Previously, this volcanic succession was referred to as the Toachi Unit (e.g. Egüez, 1986; Cosma et al., 1998), and yields island arc geochemical characteristics (Cosma et al., 1998).

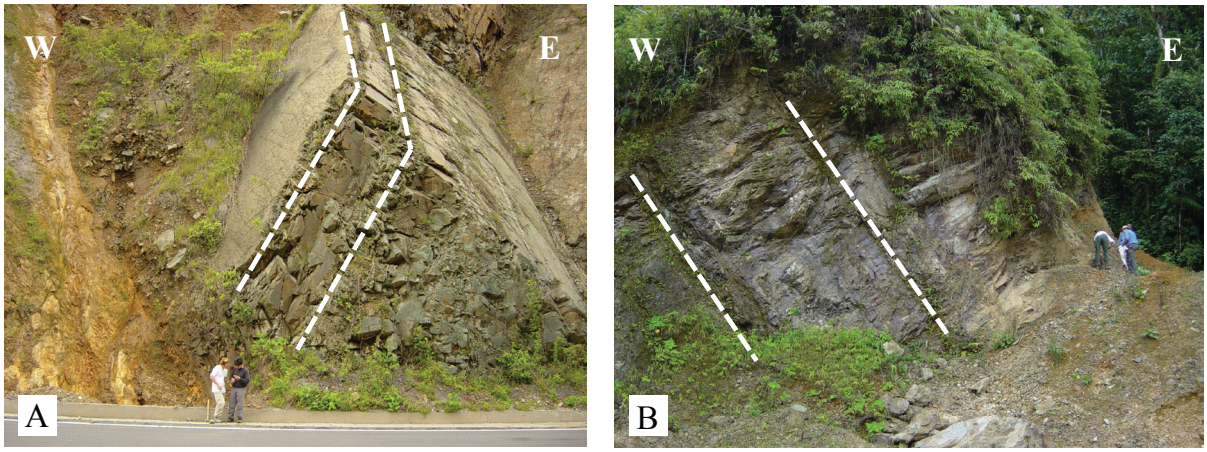

Fig. 2.11. Thick-bedded turbidites of the Pilatón and Mulaute formations. A) Pilatón Fm. exposed along the Ibarra- Lita road (UTM: 0810301/0079791). B) Weathered turbidites of the Mulaute Fm. exposed along the Alóag - Santo Domingo road (UTM: 731253/9965439).

Hughes and Bermúdez (1997) and Boland et al. (2000) included metamorphosed mudstones and siltstones, which underlie and are transitional with volcanic andesitic breccias that can be observed along the Guayllabamba River, east of El Chontal village (UTM: 750957/260297), within the Mulatue Fm. However, new petrographic observations, combined with provenance analyses, suggests these lithologies are unrelated to the Mulaute Formation (see chapter 3), and we classify these deposits as the Saguangal Formation. The remaining total thickness of the Mulaute Formation is estimated to be ~1000 m.

Stratigraphic relationships. The Pilatón Formation overlies the Mulaute Formation along the Alóag – Santo Domingo road section although the nature of the contact is difficult to determine due to the abundant vegetation. A faulted contact with the younger Macuchi Unit is inferred from outcrops along the Alóag – Santo Domingo road section (UTM: 731297/9964928). Tectonic slices of quartz rich turbiditic sandstones, similar to the Yunguilla Formation, can be observed juxtaposed with the Mulaute formation along the Alóag – Santo Domingo road (UTM: 0734827/9962686).

Geochemistry. Cosma et al. (1998) utilized geochemical data acquired from basalts of the Mulaute Formation (Toachi Unit of Egüez, 1986) to assign them an island arc tholeiitic affinity. In this study, we analyzed the whole rock geochemistry of basalts, which are tectonically juxtaposed against turbiditic sandstones along the Alóag - Santo Domingo road. The basalts have slightly enriched REE patterns (Fig. 2.6), with $(La/Yb)_N$ ratios of 1.74 and 1.50, and yield a negative Nb anomaly, which is typical for rocks formed in a subduction zone. εNdi values (Fig. 2.7) of +7 to +9 obtained from basalts (sample 02CV130, UTM: 739370/9962477) and dioritic intrusions (00RS40, UTM: 733130/10001508), indicate a juvenile mantle source, which had not been contaminated by evolved continental crust.

Depositional environment. Sedimentary rocks of the Mulaute Formation were deposited on the proximal to medial part of a submarine turbiditic fan, and were sourced from a contemporary volcanic source of island arc affinity.

Age. The age of the Mulaute Formation is poorly constrained and reliable biostratigraphic ages have not been obtained. Hughes and Bermúdez (1997) report a hornblende K/Ar age of 48.28±0.55 Ma for a diorite, which intrudes the Mulaute Formation north of La Palma village (UTM: 7340/99698), indicating that the Mulaute Formation is pre-Eocene. In addition, the Senonian Pilatón Formation overlies the Mulaute Formation. Although the nature of the contact is unclear, there is no evidence for an unconformity.

We obtained a groundmass $^{40}Ar/^{39}Ar$ plateau age of 20.66±2.2 Ma (see chapter 4) from a basaltic andesite, collected in the La Palma – Chiriboga road section (UTM: 736880/9966987). However, this age is interpreted as being reset, and can not be used to constrain the age of the Mulaute Fm.

Pilatón Formation.

Previous work. Hughes and Bermúdez (1997) defined the Pilatón Formation as a thick-bedded

turbiditic sequence, which crops out along the Alóag – Santo Domingo road. This sedimentary sequence was previously named the Cayo de la Sierra Formation on the National Geological Map of Ecuador (1969), because the sedimentary rocks were correlated with the Cayo Formation of the coastal region (e.g. Savoyat et al., 1970; Faucher and Savoyat, 1973). Kehrer and van der Kaaden (1979) introduced the term Pilatón Beds for these bedded turbidites, whereas the National Geological map of 1982 (Baldock, 1982) included the sediments of the Pilatón Formation in the Chontal Member of the Macuchi Formation.

Occurrence. The Pilatón Formation can be observed along the Alóag - Santo Domingo, Pacto - Gualea, and Pacto - El Paraiso roads. Good exposures are also present along the Ibarra - San Lorenzo, and Quito - Chiriboga roads. The section along the Alóag – Santo Domingo road is the most representative and is considered as the type section (UTM: 741694/9958725).

Lithology and thickness. The Pilatón Formation is composed of thick-bedded, turbiditic sandstones that are rich in volcanic fragments, and microbreccias which contain volcanic, lithic fragments. The sandstones are thick-bedded (Fig. 2.11), and were deposited by high-density turbidite flows, which reworked primary tuffs. Individual beds have a sharp base, and show coarse tail grading, suggesting a proximal source. Along the Alóag – Santo Domingo road, the sedimentary rocks of the Pilatón Formation are east dipping and are isoclinally folded, with north - south oriented fold axes. The turbiditic sandstones are mainly composed of plagioclase, pyroxene and epidote, and mafic minerals are partially replaced by epidote, chlorite and pumpellyite, due to low-grade metamorphism and hydrothermal alteration. The overall mineral composition of the sandstones indicates a volcanic source. The sedimentary rocks are often silicified, and sometimes intercalated with cherts. The Pilatón Formation is strongly weathered at its western border and is indistinguishable from the Mulaute Formation. Facies of the Pilatón Formation in the northern part of the Western Cordillera are very similar to the exposures in the Alóag – Santo Domingo road section, being dominated by thick-bedded, volcanic-derived turbidites, with intercalated cherts. Van Thournout (1991) reported basaltic intercalations within sedimentary rocks of the Pilatón Formation along the Ibarra – Lita road section (UTM: 810863/78904). The Pilatón Formation has an approximate thickness of 2000 m.

Stratigraphic relationships. The contacts of the Pilatón Formation with neighboring formations are mainly tectonic. On the Alóag – Santo Domingo road, turbidites of the Pilatón Formation overlie basaltic rocks (Toachi Unit of Egüez, 1986) of the Mulaute Formation. Kehrer and van der Kaaden (1979) and Egüez (1986) indicate that possibly a hiatus of sedimentation may occur at the base of the Pilatón Formation.

Egüez (1986) indicated that volcanic rocks of the Tandapi volcanic facies of the Silante Formation unconformably overlie the Pilatón Formation. In this study, we were not able to observe this contact, although younging directions along the Alóag – Santo Domingo road section indicate that the Silante Formation is younger than the Pilatón Formation.

Geochemistry. Van Thournout et al. (1992) present geochemical data from a basalt collected on the Salinas – Lita road (sample EC1004). The analyzed sample has a tholeiitic affinity, the

REE chondrite normalized plot of the sample yields a flat profile, and the multi-element plots normalized to primitive mantle show a prominent negative Nb-Ta anomaly. The geochemistry of this sample is consistent with a primitive island arc setting. The chemical composition of detrital clinopyroxenes (see chapter 3) also supports an island arc origin for the turbiditic sediments of the Pilatón Formation.

Depositional environment. The sediments of the Pilatón Formation were deposited on the proximal part of a submarine fan, which was being sourced from a contemporaneous volcanic arc (see chapter 3). Hughes and Bermúdez (1997) interpreted the absence of primary tuffs and accretionary lapilli as evidence of submarine volcanism. The presence of abundant sideromelane in the reworked tuffs also indicates that the volcanic products of the Pilatón Formation erupted in a submarine environment. Therefore, the overall geochemical and petrographic evidence suggests that basalts of the Pilatón Formation erupted in the proximal part of a submarine fan, associated with an intraoceanic island arc.

Age. Sigal (1968) report a foraminifera fauna (*Globotruncana* sp., *Guembelina* sp. and *Globigerina* sp.), which indicates a Senonian age (88.5 to 65.0 Ma). Faucher and Savoyat (1973), and Reynaud et al. (1999) indicated a Turonian to Coniacian age for this Formation, which was interpreted from the unproven existence of an *Inoceramus peruanus* fossil. All the fossils were recovered in the Alóag – Santo Domingo road. A Late Cretaceous age is also supported by the fact that the Paleocene Silante Formation overlies the Pilatón formation in the Alóag – Santo Domingo road. Therefore, we conclude that the Pilatón Formation was deposited during the Late Cretaceous, probably during the Campanian – Maastrichtian period, as indicated by Sigal (1968).

Natividad Formation

Previous work. Boland et al. (2000) applied the name "Natividad Formation" to turbiditic sedimentary rocks that occur along the Ibarra – Lita and the Otavalo – Selva Alegre roads, in the Quebrada Natividad (UTM: 7860/00300). Earlier, Egüez et al. (1988) correlated these sedimentary rocks with turbidites of the Cayo de la Sierra Formation. Van Thournout. (1991) referred to the same turbiditic sedimentary rocks in the northern Western Cordillera as the Mirador and San Jerónimo units, and suggested they were deposited during the Eocene and Cretaceous, respectively. The same authors described exposures the Mirador Unit along the Otavalo – Selva Alegre road in detail, and showed that they were composed of a turbiditic series, interbedded with amygdaloidal lavas and breccias, all intruded by andesitic dykes and sills.

Occurrence. The type section of the Natividad Formation crops-out on the Otavalo – Selva Alegre road (UTM: 0786354/0030440) (Fig. 2.9), and in the Quebrada Natividad (UTM: 786101/30068). There are other extensive outcrops west of Perucho and along the Ibarra – Lita road.

Lithology and thickness. Boland et al. (2000) described the Natividad Formation as a

sedimentary sequence, which includes turbiditic sandstones, mudstones, cherts and intercalated lavas and tuffs of basaltic composition (Fig. 2.12). Lavas and dykes within the Natividad Formation are well exposed at the Otavalo – Selva Alegre road. The volcanic intercalations are basaltic andesites, with milimetric to centimetric crystals of clinopyroxene. The sandstones are strongly silicified and tectonized, and contain abundant epidote produced by low-grade metamorphism of mafic minerals.. A coarsening-upward sequence of turbidites of the Natividad Formation is observed in the Salinas - Lita road section (UTM: 0818623/0064857). At this locality, turbidites of the Natividad Formation are intercalated with primary volcanic rocks, which are petrographically similar to the Rio Cala Formation (see below). This similarity led Boland et al. (2000) to propose that the Rio Cala basalts were the source for the sediments of the Natividad Formation. At the eastern border of the Western Cordillera (e.g. northeast of Nono village), isolated exposures of marine sedimentary rocks with intercalated volcanic rocks were mapped as the Natividad Formation; however, the lithologies and the geochemistry of the volcanic rocks are different to that observed at the type locality. Consequently, some of these exposures may be unrelated to the Natividad Formation.

Fig. 2.12. Fine-grained turbidites intercalated with basaltic tuffs from the Natividad Formation along the Ibarra - Lita road. (UTM: 818653/10064565)

Stratigraphic relationships. A tectonic contact between tectonic slivers of the Natividad Formation turbidites and basalts of the La Portada Formation can be observed on the Salinas – Lita road near to the village of Tres Pasos (UTM: 0818069/0065248). At this locality, a coarsening upward sequence of the Natividad Formation is in tectonic contact with hydrothermally altered and oxidized pillow lavas of the La Portada Formation (Fig. 2.9). On the Otavalo - Selva Alegre road, basaltic andesites and breccias of the Rio Cala Formation overlie and intercalate with turbidites of the Natividad Formation (Fig. 2.13).

Depositional environment. The Natividad Formation was deposited in the medial to distal part of a turbiditic fan, during coeval activity of a volcanic arc.

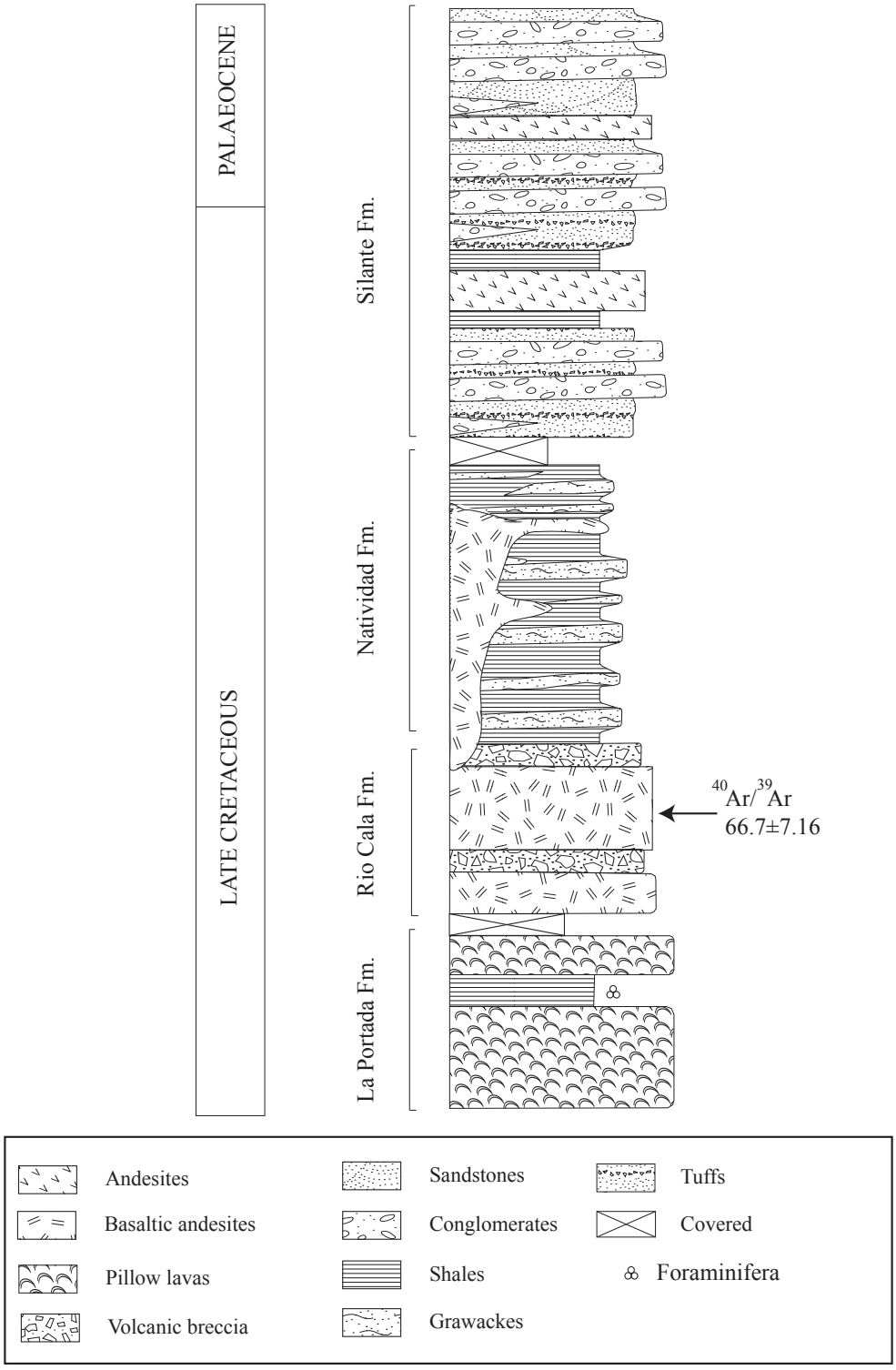

Fig. 2.13. Idealized composite stratigraphic column of the Otavalo - Selva Alegre road section

Age. Based on foraminifera fauna (*Hedbergalla monmouthensis*, *Osangularia navarroana*, *Osangularia cordieriana*), the Natividad Formation was deposited during the Campanian - Maastrichtian (Wilkinson 1998).

Rio Cala Formation

Previous work. Boland et al. (2000) described the Rio Cala Formation as a series of andesite layers, which overlie and are intercalated with volcanoclastic rocks of the Natividad Formation. Previously, lithologies of the Rio Cala Formation were correlated with the Macuchi Unit (Baldock, 1982), although it has now been shown that these formations have contrasting geochemical signatures and ages (Kerr et al., 2002a; Allibon et al., 2005). Kerr et al. (2002a) proposed that volcanic rocks of the Rio Cala Formation were produced by eastward subduction below an already accreted oceanic plateau, in a continental arc setting.

Occurrence. The Rio Cala Formation is restricted to the northern part of the Western Cordillera, between 0° and 1° N. The most representative outcrops occur along the Otavalo – Selva Alegre road section (Fig. 2.13), along the banks of the Río Cala (UTM: 7856/00204). Other exposures can be studied in Jatumpamba village (UTM: 789831/0035681), on the Ibarra – Lita road southwest of La Concepción village (UTM: 819368/0063399), and northwest of the village of Imantág (UTM: 789627/0050845).

Lithology. According to Boland et al., (2000), Kerr et al., (2002a) and our own observations, the Rio Cala Formation consists of massive basaltic to andesitic lavas, volcanic breccias, and minor volcanoclastic sandstones. Under the microscope, the andesites show a porphyritic texture, with plagioclase and clinopyroxene phenocrysts surrounded by a glassy matrix, which is partially altered to chlorite. Typically, pyroxene phenocrysts are up to 2 cm in size. Amygdaloidal andesites and volcanic breccias are also observed in the volcanic succession.

Stratigraphic relationships. Turbidites of the Natividad Formation are conformably overlain and intercalated by basaltic andesites and volcanic breccias of the Rio Cala Formation (UTM: 786350/10030435) in the Otavalo – Selva Alegre road, the contact with any other formations of the Western Cordillera is tectonic (Fig. 2.9).

Geochemistry and formation environment. Basalts of the Rio Cala Formation have both calk-alkaline and tholeiitic affinities (Fig. 2.14). Primitive mantle-normalized multi-element plots of these volcanic rock sequences indicate high concentrations of LILE (Sr and Ba), and a slight enrichment in LREE with a $(La/Yb)_N$ ratio of 8.19. The lavas of the Rio Cala Fm. possess a distinctive negative Nb anomaly, typical of rocks formed in a subduction environment. Isotopic analyses of the Rio Cala Formation yield εNdi values of +6, indicating they derived from a juvenile, mantle source.

Allibon et al. (2005) showed that the lavas of the Rio Cala Formation formed by subduction beneath thickened oceanic crust in an intraoceanic setting, partly because assimilation of oceanic plateau material could account for the LREE enrichment. Similarly, the initial Nd and Pb isotope data indicate that the rocks of the Rio Cala Formation result from mixing a Pacific MORB mantle, subducted pelagic sediments and an oceanic plateau component (Allibon et al., 2005), which is consistent with an intraoceanic, island arc setting.

Age. The Río Cala Formation had not previously been dated by radiometric methods. However, its conformable relationship with the dated Natividad Formation suggests that the Rio

Cala Formation has a Campanian to Maastrichtian age. In this study, we obtained an imprecise plateau $^{40}Ar/^{39}Ar$ age (pyroxene) of 66.7±7.16 Ma (2σ), which we interpret as a crystallization age (see chapter 3).

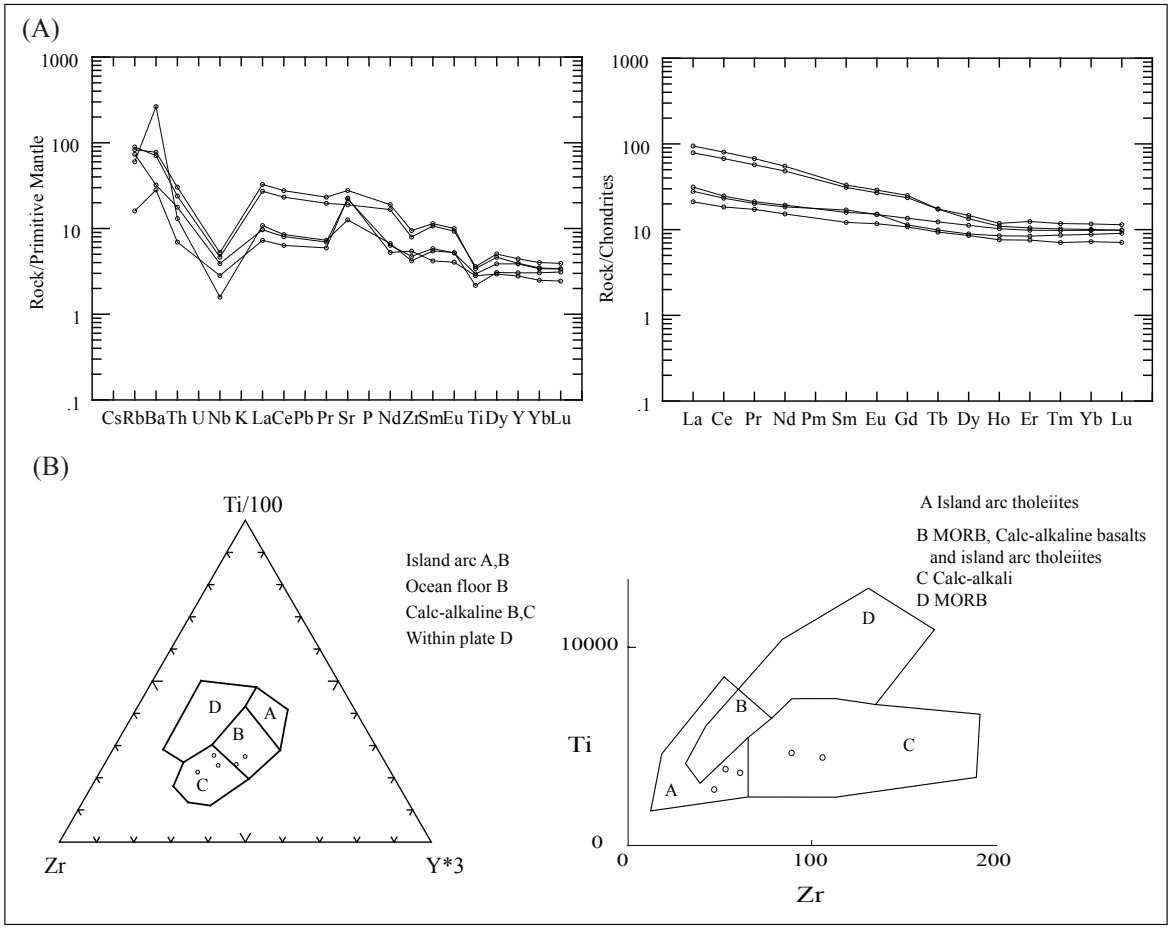

Fig. 2.14. A) Primitive mantle-normalized multi-element and REE plots (normalizing values from Sun and McDonough, 1989) of the Rio Cala Formation, using geochemical data compiled from Kerr et al. (2002a). B) Zr, Ti, Y and Zr vs. Ti discriminatory tectonic plots (Pearce and Cann, 1973) of samples from the Rio Cala Fm.

2.1.2.6 Yunguilla Formation

Previous work. The Yunguilla Formation is a poorly defined and controversial stratigraphic series of strata, mainly because of the absence of stratigraphic contacts with other sedimentary or volcanic formations of the Western Cordillera. Thalmann (1946) defined the Yunguilla Formation as a sedimentary series, composed of dark grey turbiditic siltstones and sandstones exposed west of the Nono village. Bristow and Hoffstetter (1977) and Henderson (1979) correlated this lithology with rocks in the southern part of Ecuador (Cuenca area) and along the Latacunga – La Maná road. However, the sedimentary rocks in the Latacunga – La Maná road were later shown to be Eocene (Egüez, 1986; Hughes and Bermúdez, 1997), and classified as the Apagua Formation.

Occurrence: The real extent of the Yunguilla Formation is still poorly constrained and

confusing. Fine-grained turbiditic rocks of the Angamarca Group (described later) have frequently been mistaken for the Yunguilla Formation (e.g. Henderson, 1979; Baldock, 1982; Lebrat et a., 1985), particularly, when precise biostratigraphic ages were unavailable. However, unlike the turbidites of the Angamarca Group, the Yunguilla Formation shows polyphase deformation. We define the Yunguilla Formation as a fine to medium-grained turbiditic series, which contains a significant modal proportion of material derived from a source rich in granitoid and metamorphic rocks, and with a proven Late Campanian to Maastrichtian age. The Yunguilla Formation is present along the eastern border of the Western Cordillera, between the villages of Nono (northwest of Quito) and Cuenca, in southern Ecuador. Good exposures of the Yunguilla Formation are exposed east of Nono in the Alambi River section (UTM: 768556/9992839), west of Riobamba (San Juan village), in the Cumbe area east of Cuenca, along the Quito – Chiriboga road and in the Río Guayllabamba, between Los Reales and Entables. Other useful outcrops occur along the Calacalí - Nanegalito road (UTM: 772829/1001271).

Lithology and thickness. Lithologies of the Yunguilla Formation are highly variable along-strike of the Western Cordillera. Typical lithologies include dark grey, massive siltstones, pelagic cherts, fine-grained well-sorted sandstones, and calciturbidites. The sandstones contain plagioclase, quartz, amphibole and pyroxenes, and are classified as feldspathic litharenites and lithic arkoses. Grading and cyclicity of bedding suggests that diluted turbidity currents deposited the rocks. The mapped Yunguilla Formation in the Alambi River includes a sequence of strongly folded, fine-grained turbidites in 15 – 20 cm thick beds. Dunkley and Gaibor (1997) reported the presence of volcanic intercalations within the Yunguilla Formation in the southern part of Ecuador.

Sedimentary rocks mapped as the Yunguilla Formation in the Pallatanga Valley host a significant volume of volcanic derived material, and are highly tectonized.

The Yunguilla Formation in the area of Calacalí - Pacto is exposed in two NNE oriented tectonic slices, which are separated by the Pallatanga Formation. The easternmost slice is locally associated with pelagic cherts, which are lithologically similar to Campanian to Maastrichtian cherts described by Jaillard et al. (2004), in central Ecuador. Turbidites of the Yunguilla Formation are general highly deformed (Fig. 2.15) within kink and chevron folds with upright axial planes and NNE oriented fold axes. The main deformation event affecting the Yunguilla Formation most likely occurred during Late Cretaceous accretion (see later).

Stratigraphic relationships. The Yunguilla Formation occurs in tectonic blocks juxtaposed against most other stratigraphic formations identified within the Western Cordillera, and is consistently associated with the Pallatanga Formation along the eastern border of the cordillera; however, the visible contacts are faulted.

.In central Ecuador (Guaranda – Riobamba road), the Yunguilla Formation is in tectonic contact with the Cizarán Formation, and unconformably overlain by the Paleocene Saquisilí Formation, and overlies metamorphic lithologies identical to those found in the Eastern Cordillera, in the southern Western Cordillera, close to the town of Cuenca.

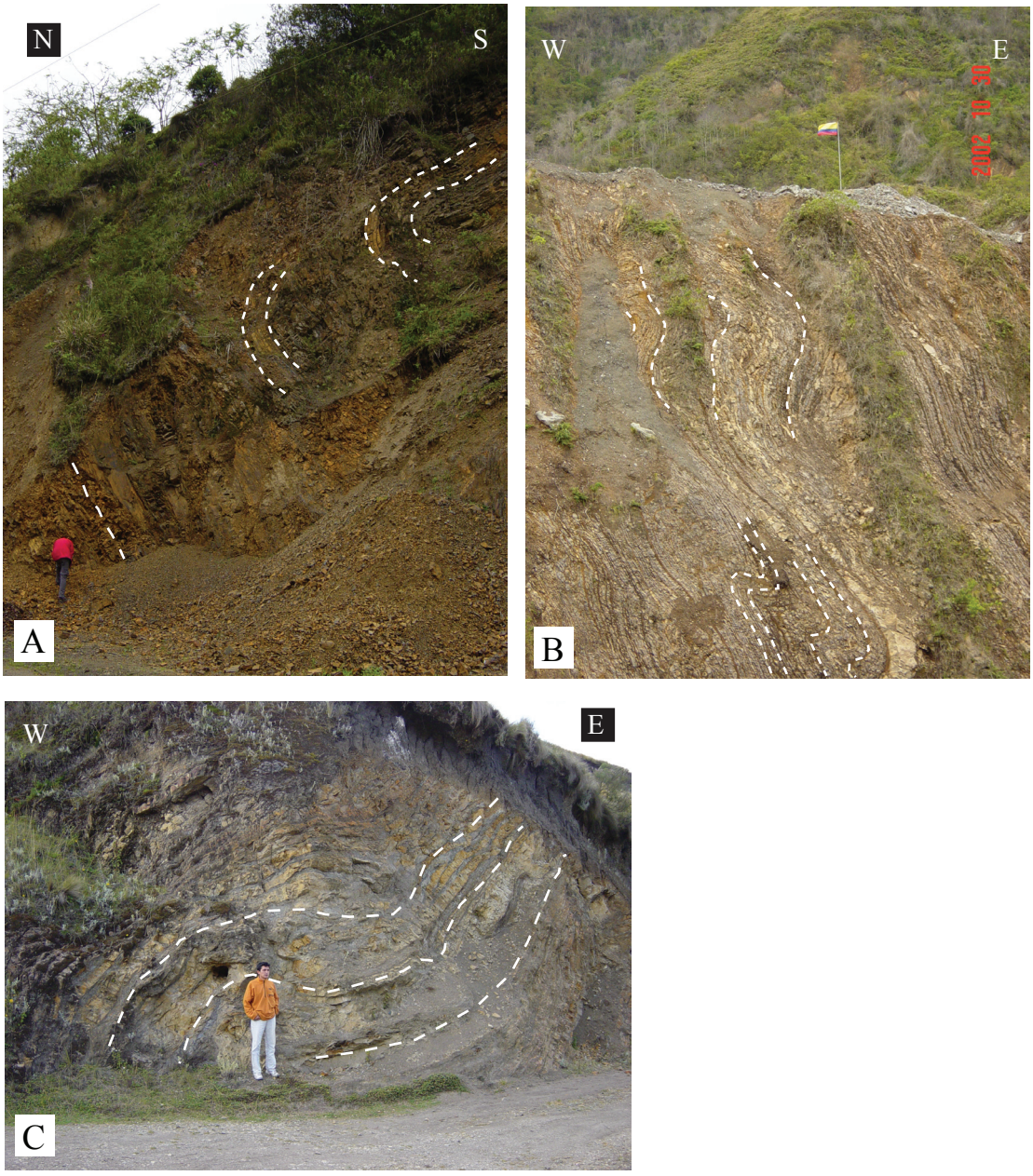

Fig. 2.15. Lithological features of the Yunguilla Fm. A) Chaotic folded turbidites of the Yunguilla Fm. along the Nono - Tandayapa road. B) Folds developed in medium bedded turbidites of the Yunguilla Fm. on the Calacalí - Pacto road (UTM: 768380/00560). C) Folded calciturbidites of the Yunguilla Fm. west of Riobamba (UTM: 741506/9819388)

Previous authors proposed that the Yunguilla Formation is in stratigraphic contact with the Silante Formation (Henderson, 1979; Hughes and Pilatasig, 1997) and the Pallatanga Formation (Jaillard et al., 2004). However, none of these contacts can be verified in the field.

Depositional environment. The Yunguilla Formation represents the medial to distal parts of one or several turbiditic fans, and was likely deposited in a forearc basin. The abundance of quartz and metamorphic minerals indicates that the Yunguilla Formation was probably sourced

from Jurassic (and older) batholiths and Early Cretaceous (and older) metamorphic rocks in the Eastern Cordillera. Jaillard et al. (2005) suggest that the Yunguilla Formation may be correlated with similar deposits in northern Peru (Paita region); these authors proposed that the Yunguilla – Paita Basin was a widespread forearc basin, extending from northern Peru to Quito. Their interpretation is consistent with the actual position of the Yunguilla Formation, east of the accreted oceanic blocks, and being sourced from the Eastern Cordillera

Age. Sigal (1969) obtained a Maastrichtian biostratigraphic age for detrital deposits exposed in the type area (north of Quito), and Bristow and Hoffstetter (1977) reported a Maastrichtian age for the Yunguilla Formation in the southern part of the Western Cordillera. Wilkinson (1996) observed the foraminifera *Heterohelix* sp., *Guembelina globulosa*, *and Rugoglobigerina* aff. *rotundata*, *Rugoglobigerina* aff. *rugosa* and *Globigerinelloides* aff. *prairiehillensis*, which suggest an Early to Middle Maastrichtian age for the Yunguilla Formation collected on the Guaranda - Riobamba road. Boland et al. (2000) found *Bolivinoides decoratus*, *Osangularia* "cordieriana" and *Globerigerinelloides volutos* of Campanian-Maastrichtian age, in the Yunguilla Formation north of Calacalí (UTM: 777000/1001200).

Jaillard et al. (2004) reported the ammonid *Exiteloceras* sp. and *Phylloceras* (*Nophylloceras*) sp., which indicates a Late Campanian to Early Maastrichtian age, west of Sicalpa village (UTM: 73950/98064). The same authors report the foraminifera *Pseudoguembelina excolata* of Late Campanian to Maastrichtian age, from shales intercalated with calciturbidites of the Yunguilla Formation, west of San Juan village (74200/981980).

Savoyat et al. (1970) report foraminifera fauna from the Alambi River, which, according to these authors, indicates a Paleocene age for the Yunguilla Formation. However, these sedimentary rocks conformably overlie the Silante Formation, and contain a significant modal proportion of volcanic derived material, and hence it is likely that they are not part of the Yunguilla Formation. In our view, these sedimentary rocks are correlatable with the Pilaló Formation of central Ecuador (see Pilaló Formation). In conclusion, the Yunguilla Formation has a tightly constrained Late Campanian to Maastrichtian age.

2.1.2.7 Silante Formation

Previous work. The term Silante Formation was used by Baldock (1982) for a continental sequence, which includes red mudstones, crystal-rich tuffs, volcanic conglomerates, and breccias that were previously called the Red Bed Series (e.g. Tschopp, 1948; Kehrer and van der Kaaden, 1979).

Hughes and Bermúdez (1997) and Boland et al. (2000) redefined the Silante Formation by including andesites, dacites and volcanic breccia intercalations of calc-alkaline affinity, into the continental red-bed sequence (Kehrer and Van der Kaaden, 1979; Egüez, 1986; Cosma et al., 1998). This volcanic succession was previously referred to as the Tandapi beds (e.g. Kehrer and Van der Kaaden 1979) or Tandapi Unit (Egüez, 1986). Consequently, in the sense of Hughes and Bermúdez (1997), the Silante Formation was deposited coeval with calc-alkaline, volcanic

arc activity.

Occurrence. The Silante Formation is restricted to the northern area of the Western Cordillera, from the Alóag – Santo Domingo road northward to the Colombian border. The type section is along the Along-Santo-Domingo road. Extensive outcrops are present along the Calacalí – Pacto, (UTM: 768285/1600) Otavalo – Selva Alegre, and Nono – Tandayapa road (UTM: 763379/9995871) sections. Good exposures can also be observed along the Quito-Chiriboga road, west of El Sigsal (UTM: 755142/9969597), and a small outcrop on the Salinas - Lita road (UTM: 814578/10073432).

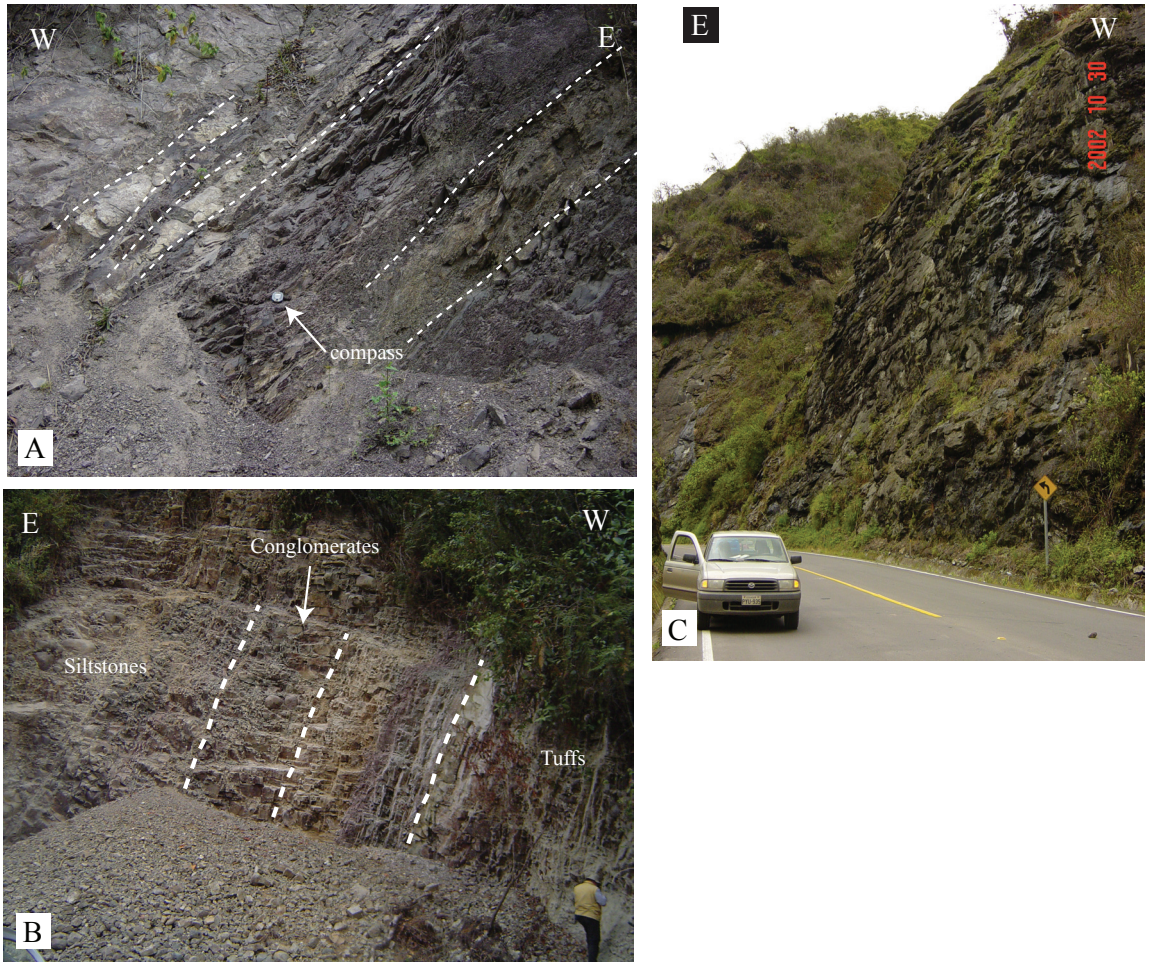

Fig. 2.16. Lithological features of the Silante Fm., northwest of Quito A) Exposure of the red mudstones and siltstones of possible lacustrine origin. B) Fluvial conglomerates intercalated with red mudstones and tuffs, exposed in the Nono - Tandayapa road section (UTM: 762350/9997787). C) Andesitic lavas of the Tandapi volcanic facies near to the faulted contact with the Yunguilla Fm. (UTM: 768022/0001666).

Lithology and thickness. The Silante Formation includes channelized conglomerates and breccias, matrix supported conglomerates deposited by debris flows (lahars), red mudstones and shales, siltstones and violaceous tuffs. Fluvial conglomerates can be observed in the Nono – Tandayapa road (Fig. 2.16), and the matrix of the conglomerates includes crystals of

hornblende, pyroxene, plagioclase, and Fe oxides. The tuffs have a violet colour and contain crystalline fragments of plagioclase, pyroxene, zircon, hornblende and quartz. Sedimentary clasts lithologically similar to the Yunguilla, Pallatanga or Rio Cala formations are found in the conglomerates, indicating reworking of older volcanic and sedimentary formations. Most of the sedimentary rocks of the Silante Formation have experienced very little transport, as revealed by poor sorting and high angularity of the clasts and individual crystal grains.

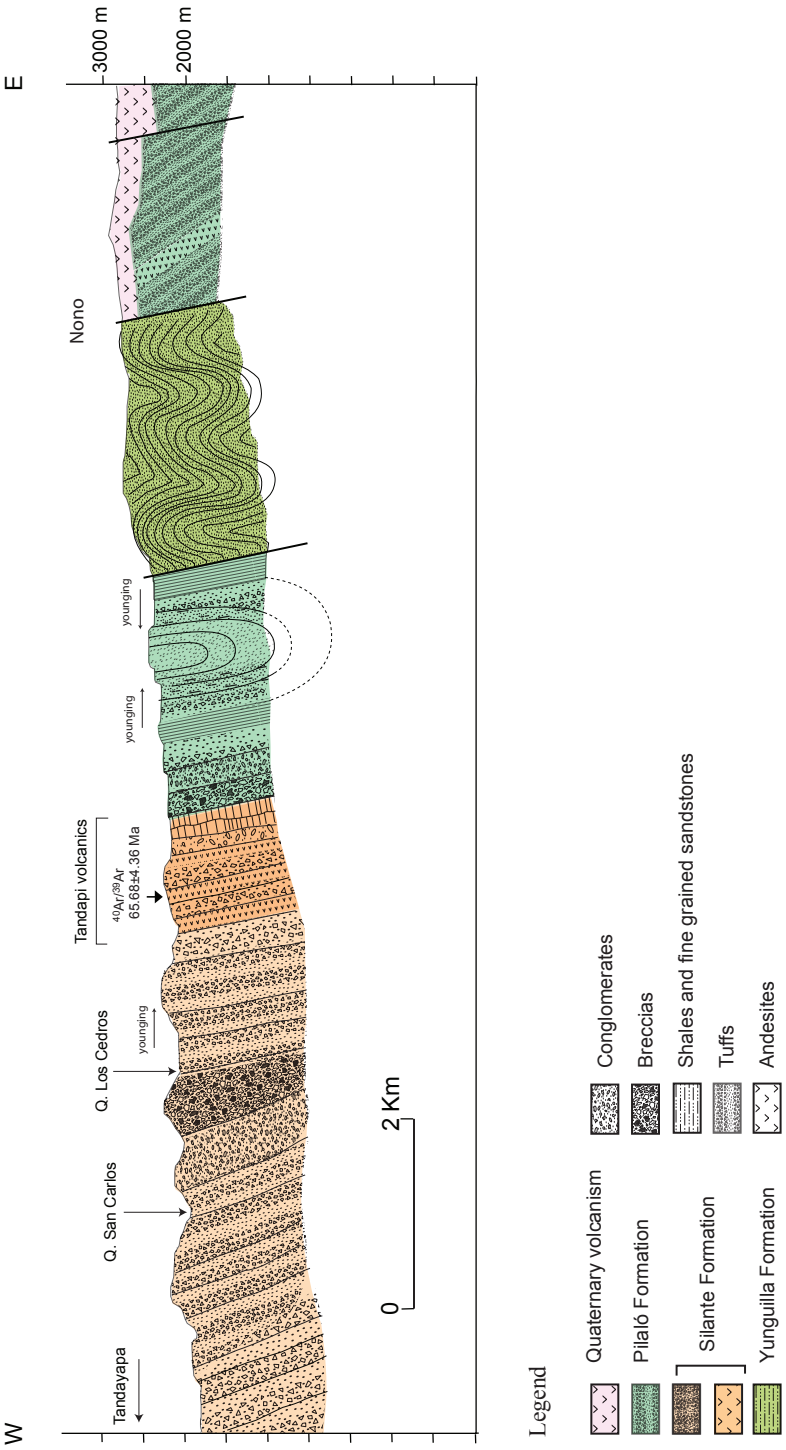

Fig. 2.17. Geological profile along the Tandayapa - Nono road section.

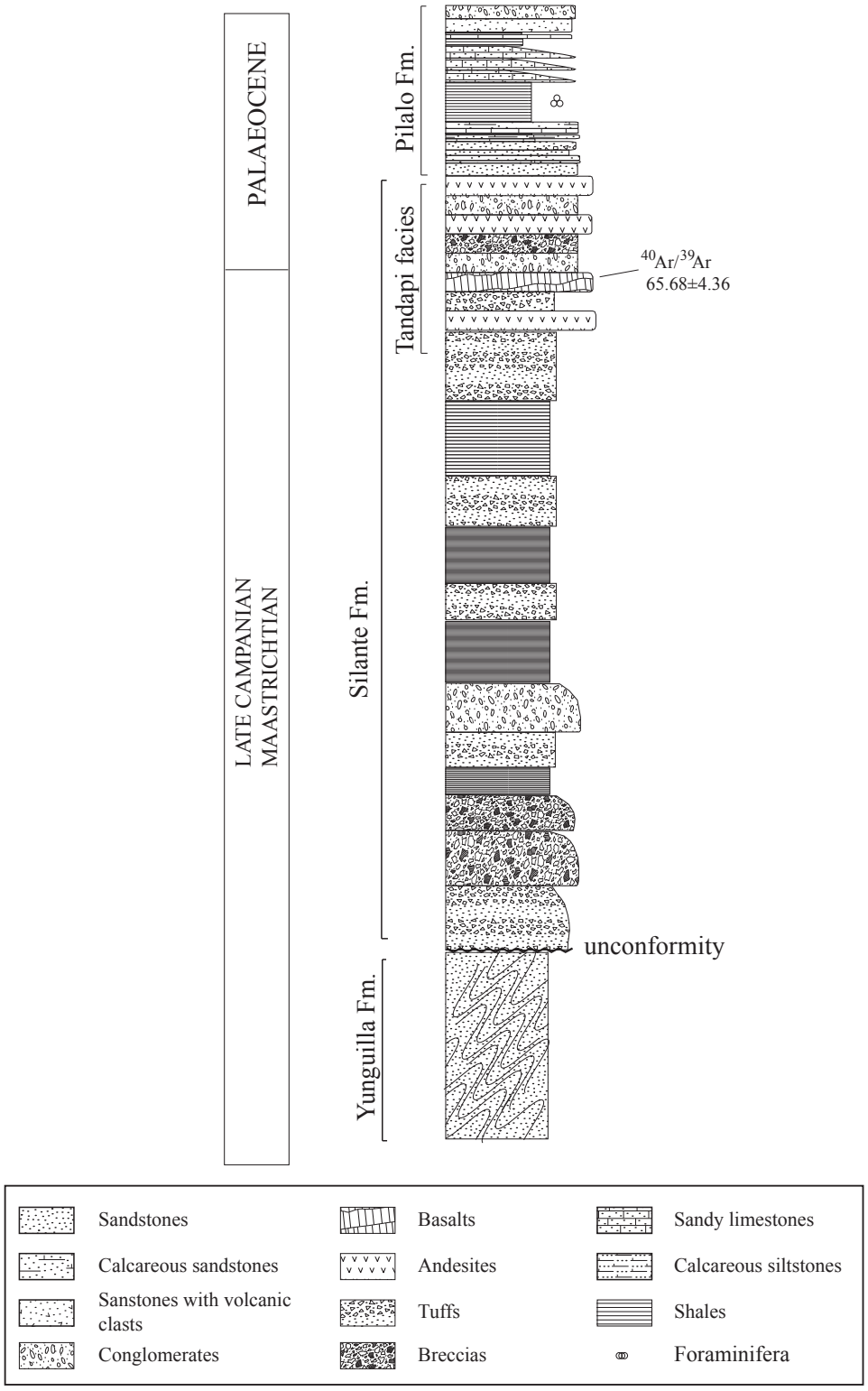

Fig. 2.18. Stratigraphic column along the Nono - Tandayapa road section.

The Tandapi facies (sensu Kehrer and van der Kaaden, 1979) is a primary volcanic sequence within the Silante Formation, which comprises andesites, volcanic conglomerates and volcanic breccias. Hughes and Bermúdez (1997) interpreted the volcanic breccias and conglomerates

with a tuffaceous matrix exposed in the Alóag – Santo Domingo road, as peperites, produced by the intrusion of andesitic rocks into wet sediments. Lithologically, volcanic rocks of the Tandapi facies are porphyritic andesites, with phenocrysts of plagioclase, pyroxenes and hornblende. The Tandapi facies is clearly more geochemically evolved than volcanic rocks of the Late Cretaceous Pallatanga, Mulaute and Pilatón Formations. The absence of pillow structures and sea floor metamorphism in the sequence strongly suggest a terrestrial environment.

Along the Nono - Tandayapa road section (Fig. 2.17), the Tandapi volcanic rocks include fine-grained basaltic lavas, which have an intergranular texture, petrographically similar to the Macuchi Unit. In this section, red mudstones and volcanic conglomerates of the Silante Formation overlie the Tandapi volcanic rocks, which corroborate the presence of Silante-type xenoliths in lavas of the Tandapi volcanics. Consistent eastward younging directions towards the Tandapi facies along the Nono Tandayapa road indicate that the Tandapi volcanic rocks are younger than the local sedimentary sequence of the Silante Formation in this section (Fig. 2.18). Tandapi volcanics containing red xenoliths are also observed further north, in the Yunguilla – El Golan road section (UTM: 771381/10003937).

In the Otavalo – Selva Alegre road section, the Tandapi volcanic facies are located in the middle part of the sequence, whereas in the Alóag –Santo Domingo road, the primary volcanic rocks are at the base of the Silante sequence (Egüez, 1986). Therefore, we suggest that the Tandapi volcanics are the volcanic facies of the Silante Formation.

Henderson (1979) estimates a maximum thickness of the Silante Formation in the range of 5400 m in the Nono – Calacalí road section. Nevertheless, the true thickness of this formation is difficult to determine due to folding of the rocks.

Stratigraphic relationships. The Silante Formation is only found in tectonic contact with mafic, crystalline basement rocks, and most of the sedimentary cover sequence. The nature of the contact with the Yunguilla Formation is controversial as several authors have proposed that the Silante Formation is overlies the Yunguilla Formation (e.g. Hughes and Pilatasig, 2002), whereas other authors report the inverse scenario (e.g. Henderson, 1979; Wallrabe-Adams, 1990). These different interpretations were derived after observing outcrops of the Yunguilla and Silante formations located northwest of Quito (Nono area). According to our field observations from the Nono - Tandayapa road section, andesites of the Tandapi facies are overlain by a sequence of calciturbidites, cherts and black shales of the Paleocene Pilaló Formation.

Geochemistry of the Tandapi volcanic facies. Several investigators have presented geochemical data from primary volcanic rocks within the Silante Formation. Kehrer and van der Kaaden (1979) derived a calc-alkaline affinity for rocks of the Tandapi facies. Similarly, Egüez (1986) and Cosma et al. (1998) published geochemical data from andesites of the Tandapi volcanic facies in the Alóag – Santo Domingo road, which also reveal a calc-alkaline affinity (Fig. 2.19), with an enrichment in LREE, and a negative Nb anomaly, suggesting a continental volcanic arc setting. In this study, we obtained isotopic data (εNd +6.88; εSr -14.7; Fig. 2.7) from an andesite of the Tandapi volcanic facies collected in the Otavalo – Selva Alegre road (sample

02CV98; UTM: 780518/10032317), which suggests that the magmas were not contaminated by continental crust. Cosma et al. (1998) reported similar isotopic data acquired from samples of the Tandapi volcanic facies in the Alóag – Santo Domingo road section, suggesting that the Silante arc erupted through isotopically juvenile rocks.

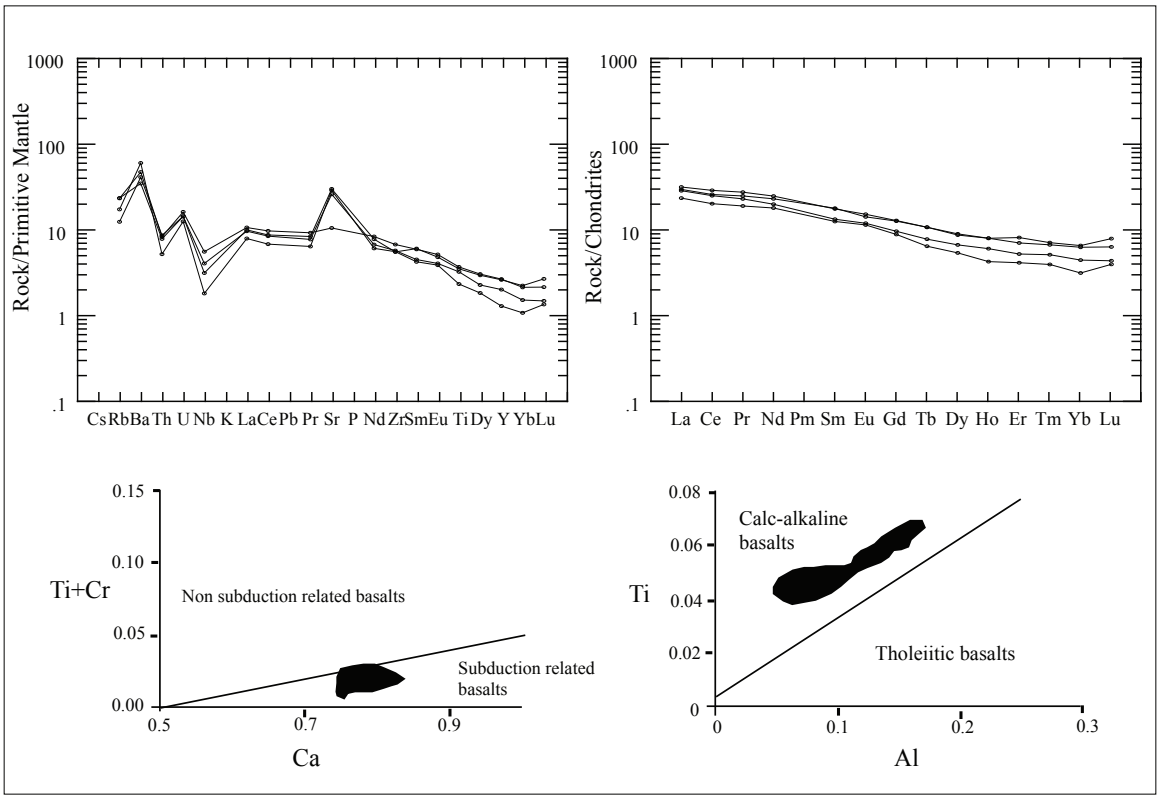

Fig. 2.19. Primitive mantle-normalized multi-element and REE plots (normalizing values from Sun and McDonough, 1989) of the Tandapi volcanic facies of the Silante Formation. Geochemical data compiled from Cosma et al. (1998).

Depositional environment. The mixed presence of red, fluvial plain mudstones and fluvial conglomerates with volcanoclastic rocks and primary andesitic lavas (Fig. 2.16), most commonly occurs during sedimentation in a continental environment, associated with a contemporaneous volcanic arc. The contribution of coeval volcanic arc material is supported by the abundance of primary volcanic rocks observed across the sequence, and the fact that the andesitic lavas of the Tandapi facies seem to occur at different levels within the formation. Isotopic data suggest that the volcanic arc was built on top of juvenile crust, suggesting that it may have erupted through the Pallatanga Fm.

Age and comparisons. Boland et al. (2000) reported the presence of foraminifera fauna in the Silante Fm., including *Bulimina secaensis*, *Globigerina angiporoides*, *Globorotalia munda* and a single specimen of *Neouvigerina chirana*. The fossils were collected from marine sedimentary rocks attributed to the Silante Formation, North of Calacalí, and the assemblage yields a Late Eocene age. However, the samples were collected along a faulted contact between the Silante

Formation and sedimentary rocks that are probably correlatable with the Eocene Angamarca Group, which crops out to the west of the fault. Therefore, the Eocene age of Boland et al. (2000) may be unrelated to the Silante Formation. Zircon fission track data from tuffs intercalated into red-beds yield an age of 16.8±0.8 Ma (Hughes and Bermúdez, 1997). However, zircon fission track ages partially reset at temperatures >~220°C (Tagami et al., 1998), and hence the age only represents a minimum crystallization age.

During the present study, we obtained several $^{40}Ar/^{39}Ar$ ages from magmatic rocks of the Silante Formation. Volcanic rocks of the Tandapi facies, in the Nono – Tandayapa road section, yielded a plateau $^{40}Ar/^{39}Ar$ age of 65.68±4.36 Ma (2σ, groundmass). Similarly, rocks of the Tandapi facies in the Calacalí – Pacto road section yielded plateau ages of 58.1±3.9 Ma (2σ, groundmass), 61.0±1.1 Ma (2σ, groundmass), and 63.96±10.7 Ma (2σ, plagioclase; see chapter 4). These ages indicate that the volcanic rocks within the Silante Formation, and hence the formation itself was deposited during the latest Maastrichtian to Early Paleocene.

According to the lithologies and radiometric ages of the Silante Formation, this sequence correlates with the Sacapalca Formation in southern Ecuador, which includes andesitic volcanic flows, tuffaceous sedimentary rocks, red mudstones, sandstones and volcanic conglomerates. Pratt et al. (1997) and Hungerbühler (2002) described the Sacapalca Formation as an unmetamorphosed volcanic sequence, deposited in a terrestrial environment, which was deposited on continental crust. Hungerbühler et al. (2002) obtained a zircon fission track age of 66.9±5.8 Ma (2σ) from a dacite west of the town of Catacocha (UTM: 646051/9555116), and the sequence is cut by the San Lucas pluton, which yielded a Rb/Sr (isochron) age of 53±2 Ma (Aspden et al., 1992b).

2.1.2.8 Pilaló Formation

Previous work. Egüez and Bourgeois (1986) assigned the term "Pilaló Unit" to a volcano sedimentary sequence exposed close to the Pilaló village, along the Latacunga - La Maná road. Hughes and Bermúdez (1997) proposed that the Pilaló Formation is a lateral equivalent of the Apagua Formation, but with a discrete andesitic volcanic source. However, in the type locality, the Eocene Unacota limestone conformably overlies the Pilaló Formation, whereas the Apagua Formation conformably overlies the Unacota limestone. Therefore, the Pilaló and Apagua formations are not lateral equivalents.

Occurrence. Good exposures of the Pilaló Formation are located east of the village of Pilaló (UTM: 722672/9895844), in the Chilcas - Pilaló river-valley, and along the road from Pilaló to Angamarca (Fig. 2.20). Extensive exposures of the Pilaló Formation can be observed west of Sigchos and along the Sigchos - Chugchilán road. Lithologically similar rocks to the Pilaló Formation can also be observed northwest of Quito, along the Alambi River, west of Nono. Previous authors (e.g. Faucher and Savoyat, 1973; Sigal, 1969) included the sedimentary rocks of the Alambi River section within the Yunguilla Formation. However, our petrographic, radiometric and provenance analyses demonstrate that these exposures are equivalents of the

Pilaló Formation. Egüez (1986) reported lithologically similar sedimentary and volcanic rocks from a locality west of Pilaló (his Santa Ana Unit), although this correlation could not be confirmed during our fieldwork.

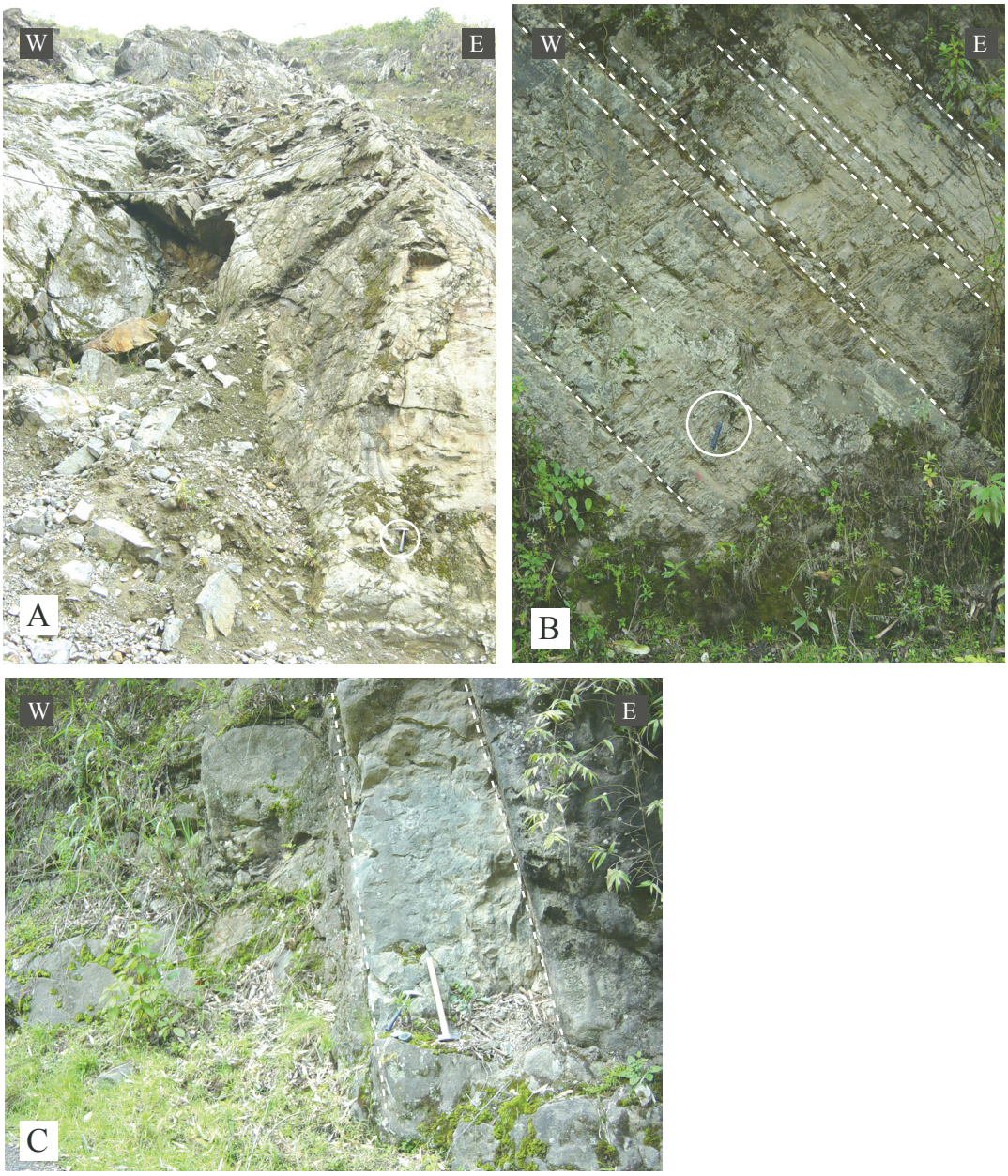

Fig. 2.20. Lithological features of the Pilaló Fm. A) Andesites of the Pilaló Fm. in the Latacunga - La Maná road. B) Calcareous turbidites near to the faulted contact with the Yunguilla Fm. in the Nono Tandayapa road (UTM: 766437/9993801). C) Thick-bedded reworked tuffs at the base of the Pilaló Fm. along the Nono - Tandayapa road (UTM: 765615/9994229).

Lithology and thickness. The Pilaló Formation, in the type locality, contains coarse-grained turbiditic sandstones, black shales, matrix supported breccias with volcanic clasts of andesitic composition, siltstones and reworked tuffs. The volcanic breccias contain fragments of red, oxidized andesites. Egüez (1986) reported the presence of red beds, and therefore suggested a

depositional continental environment, which corroborates the presence of wood fragments in tuff horizons.

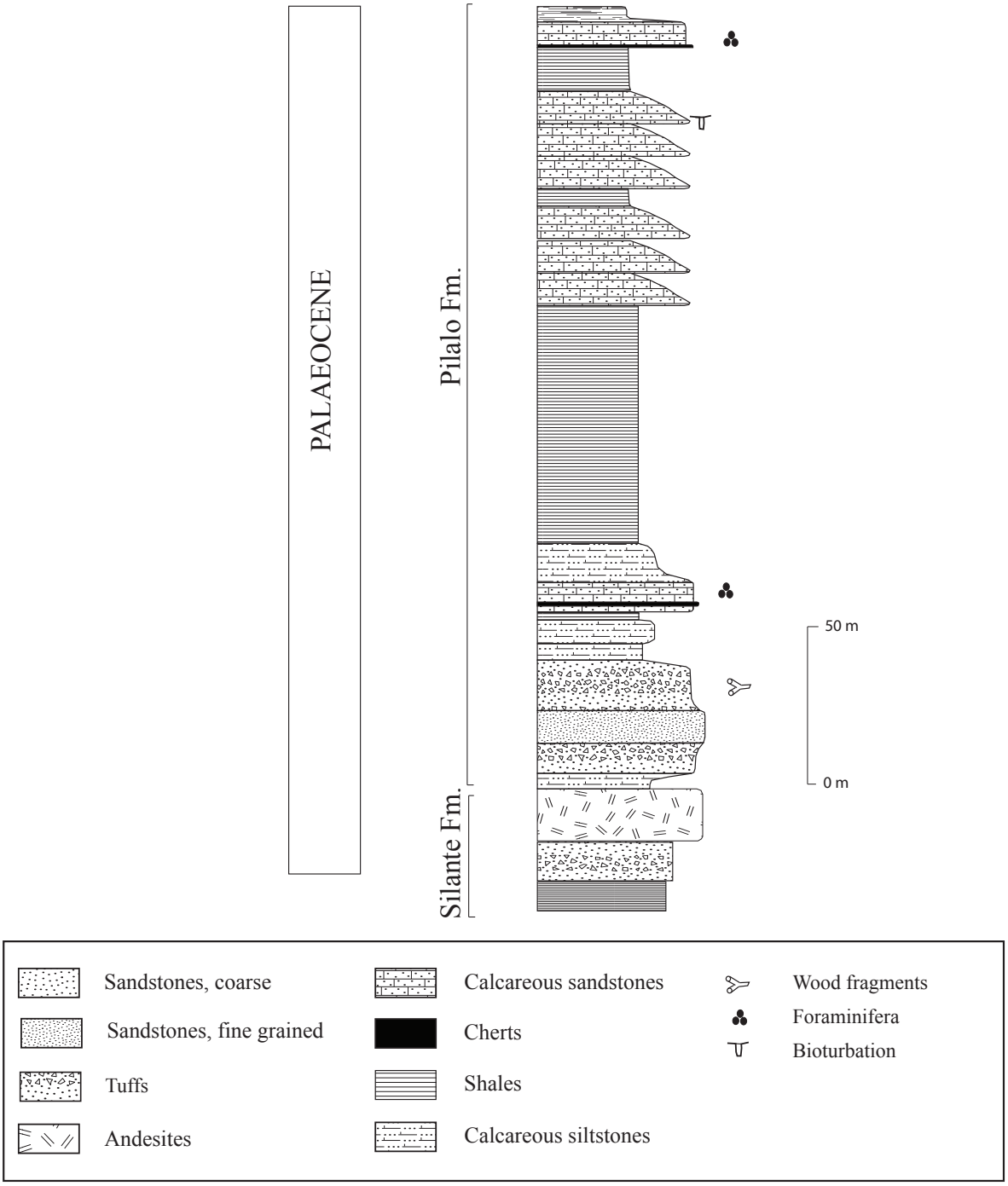

Fig. 2.21. Stratigraphic column of the Pilaló Formation along the Nono - Tandayapa road.

The Alambi River section (Fig. 2.21) hosts bioturbated calciturbidites, black shales, and tuffs. The calciturbidites contain abundant foraminifera fossils, and the tuffs are reworked and contain plagioclase, pyroxene, andesitic clasts, and wood fragments measuring up to 4 cm across (UTM: 766049/9993478). The carbonized wood suggests transport of land plants from continental areas to the marine basin via volcanic eruptions. The tuffs have vesicular glass shards and typically include red oxidized andesitic clasts, similar to the exposures in the Pilaló

area. The proportion of volcanic material increases towards the base of the formation (Fig. 2.21).

Black shales with intercalations of volcanic sandstones, breccias and crystal-rich tuffs that are lithologically correlatable with the Pilaló Formation can be observed south of the village of Sigchos, along the road to Chugchilán village. At this locality, the beds dip to the west, similar to the Alambi River section.

The thickness of the Pilaló Formation is difficult to determine, although Hughes and Bermúdez (1997) report an estimated thickness of 1000 m.

Stratigraphic relationships. The Pilaló Formation in the Alambi River conformably overlies the Tandapi volcanic facies of the Silante Formation. (Fig. 2.18). Along the Latacunga - La Maná road, the Pilaló Formation is in contact with the Macuchi Unit, although the nature of the contact can not be determined. Hughes and Bermúdez (1997) assumed that the contact coincides with the Chimbo - Toachi Fault, which these authors considered to be a suture the between the Macuchi Block and the Pallatanga Block. The contact of the Pilaló Formation with the overlying Unacota Limestone in the Latacunga – La Maná road section (Fig. 2.22) is interpreted to be conformable, and can be observed in the Chilcas River (Hughes and Bermúdez, 1997).

Depositional environment. The Pilaló Formation was deposited on a marine basin plain, as determined by the presence of pelagic chert and black shale layers. Coeval volcanic activity is revealed by the presence of volcanic breccias and tuffs. The active volcanic arc was probably situated in a terrestrial environment, as suggested by the presence of oxidized clasts and carbonized wood fragments observed in the tuffs. The source of the volcanic material was probably the coeval and partially continental Tandapi volcanic facies of the Silante Formation.

Age. Savoyat et al. (1970) recovered foraminifera fauna from two samples in the Alambi River section. The first sample yielded *Rzehakina* (or *Sigmoilina*), *Globigerina* sp*., Haplopragmoides* sp*., Tritaxia* sp*., Globotruncana* gr. *bulloides Vogler, G.* gr. *Arca* (Cushman), *G*. gr. *linnei* (d`Orbigny), *Globigerinella* sp., *Guembelina* sp., *Rugoglobigerina* cf. *hantkeninoides* Brönnimann). According to Savoyat et al. (1970), these assemblages correlate with the Danian. However, the fossil assemblage may be more indicative of a Maastrichtian age (M. Caron, personal communication).

The second sample in the same section yielded the following foraminifera: *Gaudryina* sp., *Marsonella* sp., *Nodosaria* sp., ?*Pseudoparella* sp., *Turborotalia* sp., *Globogerina* sp., *Bolivinopsis* sp., *Haplopragmoides* sp., *Clavulinoides* sp., *Globorotalia* sp., *Lenticulina* sp., *Rzehakina epigona* (Rzehak), *Ceratobulimina* sp., *Robulus* sp., *Trochammina* sp., *Spiroplectammina* sp., *Verneuilina* sp.

The presence of *Rzehakina epigona* suggest that the sample may be of Paleocene age, because this form is known in Paleocene to Early Eocene strata in northern South America (Molinares and Jaramillo, 2005). Similarly, in the Pilaló area, Eocene limestones of the Unacota Formation conformably overlie the Pilaló Formation, corroborating a Paleocene age for the Pilaló Formation, possibly extending to the Early Eocene.

Egüez and Bourgois (1986) obtained a plagioclase K/Ar (whole rock) age of 24±1.2 Ma from a plagioclase phyric andesite, which intrudes the Pilaló Formation in the Pilaló area, which represents a minimum age for the Pilaló Formation. Wallrabe-Adams (1990) obtained a whole rock K/Ar age of 52.7±2.9 Ma from an andesite observed at the base of the Pilaló Formation in the Alambi River, which may represent a crystallization age, although it may also be partially reset.

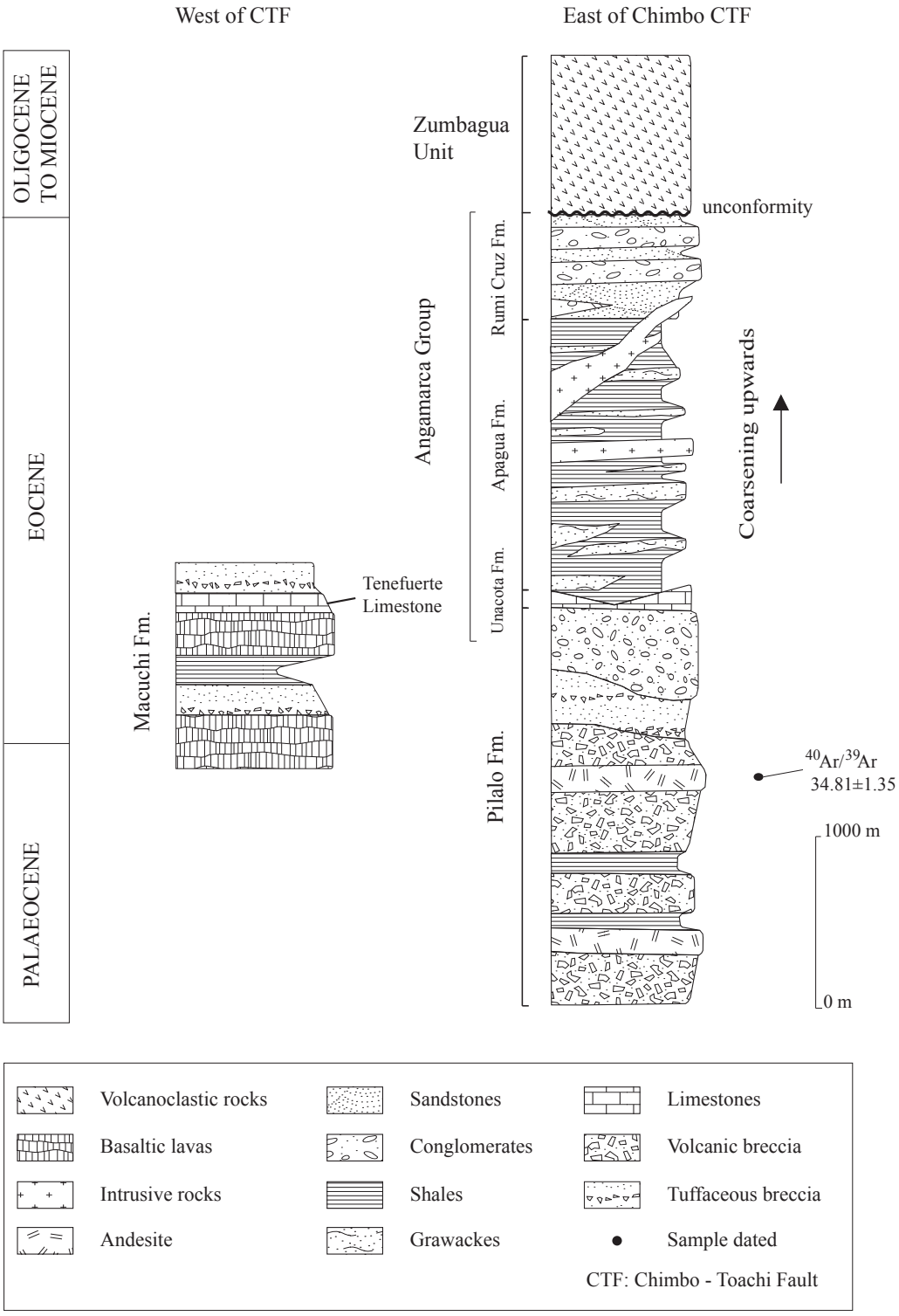

Fig. 2.22. Stratigraphic column of the Latacunga - La Maná section. CTSZ = Chimbo Toachi Shear Zone.

In the present study, an andesitic stock found between the villages of Sigchos and Chugchilán (UTM: 733589/9919408) yielded a plateau $^{40}Ar/^{39}Ar$ age of 34.81±1.35 Ma (2σ, hornblende), which can also be considered as a minimum age for this formation. From an andesite intercalated with marine sedimentary rocks of the Pilaló Formation, we obtained a plateau $^{40}Ar/^{39}Ar$ age of 64.3±0.4 Ma (2σ, pyroxene), which may approximate to the depositional age of the Pilaló Formation. This age is indistinguishable with our $^{40}Ar/^{39}Ar$ ages (~65 Ma) obtained from andesites and basaltic andesites of the Tandapi volcanic facies of the Silante Formation, which directly conformably sedimentary rocks of the Pilaló Formation, west of Nono village (see chapter 4).

Therefore, the evidence indicates that the Pilaló Formation is most likely of Early Paleocene to Early Eocene age.

2.1.2.9 Saguangal Formation.

Previous work. The Saguangal Formation is a new sedimentary sequence, which we define in this study. This Formation was previously included in both the Chontal Formation (Baldock, 1982), and the Mulaute Unit (Hughes and Bermúdez, 1997; Boland et al. 2000). However, provenance and field evidence acquired during the present study strongly suggests that this unit is an independent formation, which is younger than the Mulaute Formation. Baldock (1982) defined the Chontal Formation as the "non-volcanic member" of the Macuchi Unit.

Occurrence. The Saguangal Formation is exposed along the banks of the Guayllabamba River, northwest of the village of Saguangal (UTM: 747194/23517), which is considered as the type locality. Additional outcrops also occur in the Guayllabamba River, at the intersection with the Gualea – El Chontal road (UTM: 751245/0026440), and northeast of Mashpi village (UTM: 737678/0021952), and to the south of San Miguel de los Bancos (726111/9989071).

Lithology and thickness. The Saguangal Formation is an ~1000 m thick sequence of black mudstones and siltstones with intercalated sandstones (Fig. 2.23). The mudstones are metamorphosed, and have developed a slaty cleavage. The lower part of the sequence includes volcanic breccias with volcanic clasts of andesitic composition, abundant crystals of feldspars, pyroxenes and hornblendes, which can be observed south of the town of San Miguel de los Bancos, in the Cocaniguas River (UTM: 726121/9989103). According to younging directions, the volcanosedimentary facies progressively changes to black mudstones intercalated with fine to medium grained quartz rich sandstones, which dominate the upper part of the sequence. The sandstones contain abundant muscovite and plagioclase.

The mudstone dominated sequence is clearly exposed southwest of the Apuela Batholith, along the road from Urcutambo to El Chontal village (UTM: 751245/10026440). At this locality, mudstones of the Saguangal Formation are intensively cleaved, and reveal the growth of metamorphic chloritoid. Hughes and Bermúdez (1997) suggested that the metamorphism was produced by shearing along the Mulaute Shear Zone during an Eocene accretionary event. The cleaved mudstones are overlain by conglomerates in the Guayllabamba River, which

reworked black mudstones of the Saguangal Formation, clasts of basalt and quartz veins. Intense deformation and discontinuity of the exposures renders it difficult to determine the real thickness of the succession, although we estimate it to be ~1000 m.

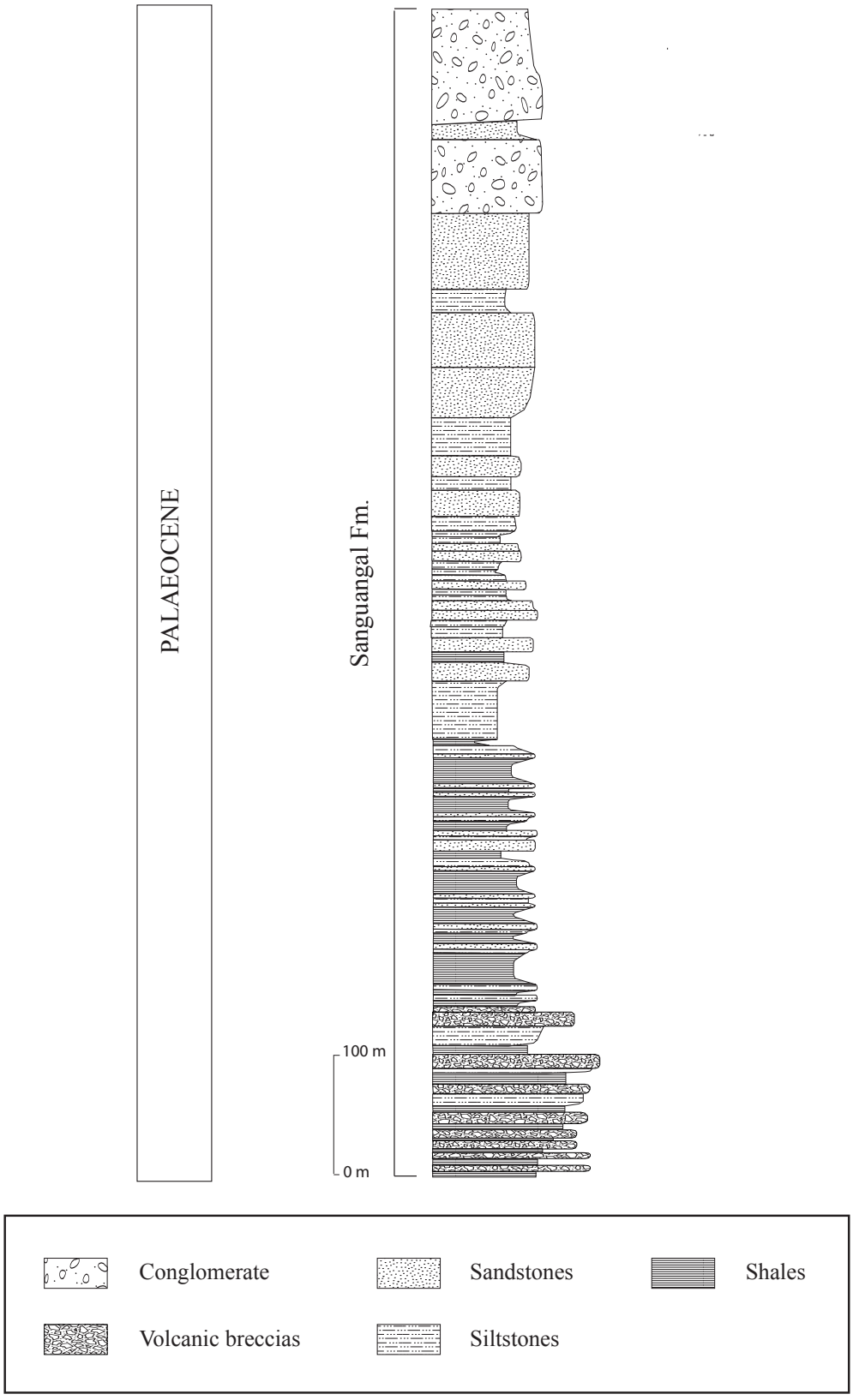

Fig. 2.23. Stratigraphic column of Sanguangal Formation.

Stratigraphic relationships. We did not observe any stratigraphic contacts between the Saguangal Formation and other formations. We assume the Saguangal Formation unconformably overlies the Mulaute Formation, whereas volcanoclastic rocks of the Eocene Tortugo Formation are interpreted to overlie the Saguangal Formation in the Guayllabamba River section.

Depositional environment. Intense deformation of the sedimentary rocks renders it difficult to find sedimentary structures, to indicate the depositional environment. However, the presence of fluvial conglomerates at the top of the formation indicates a shallowing upward sequence, with the black shales and sandstones being deposited in a shallow marine or lacustrian environment.

Age. The age of the Saguangal Formation is not well established. From mudstones located northeast of Saguangal village (UTM: 7472/265). Wilkinson (1998) reported a single specimen of the foraminifera genus *Stensioeina*, indicating Late Cretaceous to Danian age. We have dated detrital zircons from the Saguangal Formation and obtained a U/Pb age of 58.8±8.9 Ma (2σ), which represents a maximum stratigraphic age (see chapter 3). The age of the zircons may also be indicative of coeval volcanism observed at the base of the formation. Consequently, we suggest that the Saguangal Formation was partially derived from the Maastrichtian to earliest Paleocene Silante volcanic arc, which corroborates with the calc-alkaline geochemical composition of the clinopyroxenes of the Saguangal and Silante formations (see chapter 3).

2.1.2.10 Angamarca Group

The Angamarca Group is a siliciclastic sequence, which generally includes turbiditic sandstones and conglomerates, as well as a limestone interval. The Angamarca Group was deposited from the Paleocene to the Oligocene, and is subdivided from base to top into the Saquisilí, Apagua, Unacota and Rumi Cruz formations. Based on lithological and provenance analyses, we have included the El Laurel Formation as a northern extension of the Angamarca Group. Geographically, the outcrops of the Angamarca Group occur east of the Macuchi Unit (Fig. 1.4) and, according to Hughes and Bermúdez (1997), both sequences are separated by the regional dextral Chimbo – Toachi Fault. The Angamarca Group typically contains abundant quartz and metamorphic-derived minerals, which imply that it was sourced from granitoids and metamorphic rocks that are now exposed in the Eastern Cordillera (see chapter 3). The sedimentary rocks of the Angamarca Group were most likely deposited in a large basin, which was subsequently dissected by NNE-SSW trending strike-slip faults. The following sections describe the main characteristics of the formations included in the Angamarca Group

Saquisilí Formation

Previous work. Hughes and Bermúdez (1997) first defined the Saquisilí Formation based on Paleocene ages obtained from turbidite beds in the Saquisilí area. Previous workers correlated these sedimentary rocks with the lithologically similar, Late Cretaceous Yunguilla Formation (see e.g. Baldock, 1982). Jaillard et al. (2004) reported Paleocene turbidites from the Riobamba

to Guaranda road section, which are temporally correlatable with the Saquisilí Formation. The same authors also included into the conglomerates of the Gallo Rumi Member into the Saquisilí Formation, which they interpreted to be part of the same turbidite fan system.

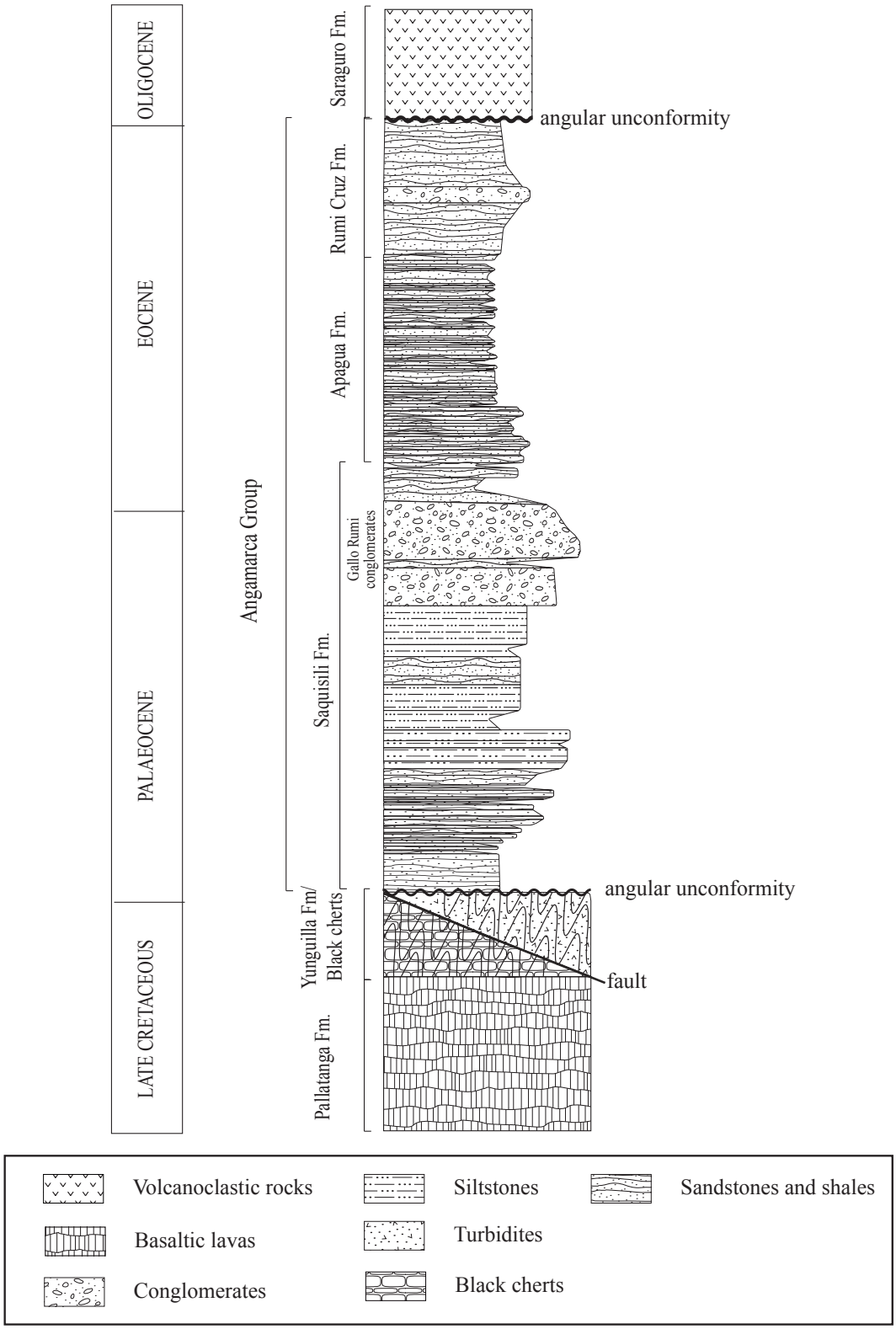

Fig. 2.24. Composite stratigraphic column of the Guaranda - San Juan section.

Occurrence. The Saquisilí Formation is well exposed in the region between La Victoria and Saquisilí (Hughes and Bermúdez, 1997), and the most extensive outcrops are found in the Quebradas El Carnicero, Maca Grande and Pusuchusi. The Saquisilí Formation crops-out extensively east of Guaranda, along the roads between Guaranda and Riobamba, and Chimbo and Riobamba. The Western Cordillera BGS-CODIGEM map (1°S to 2°S) previously included these occurrences as part of the Eocene Apagua Formation. However, Jaillard et al. (2004) obtained biostratigraphic data and showed that a Paleocene turbiditic sequence was present in the area, and hence they correlated the Paleocene sequence with the Saquisilí Formation of the central part of the Western Cordillera.

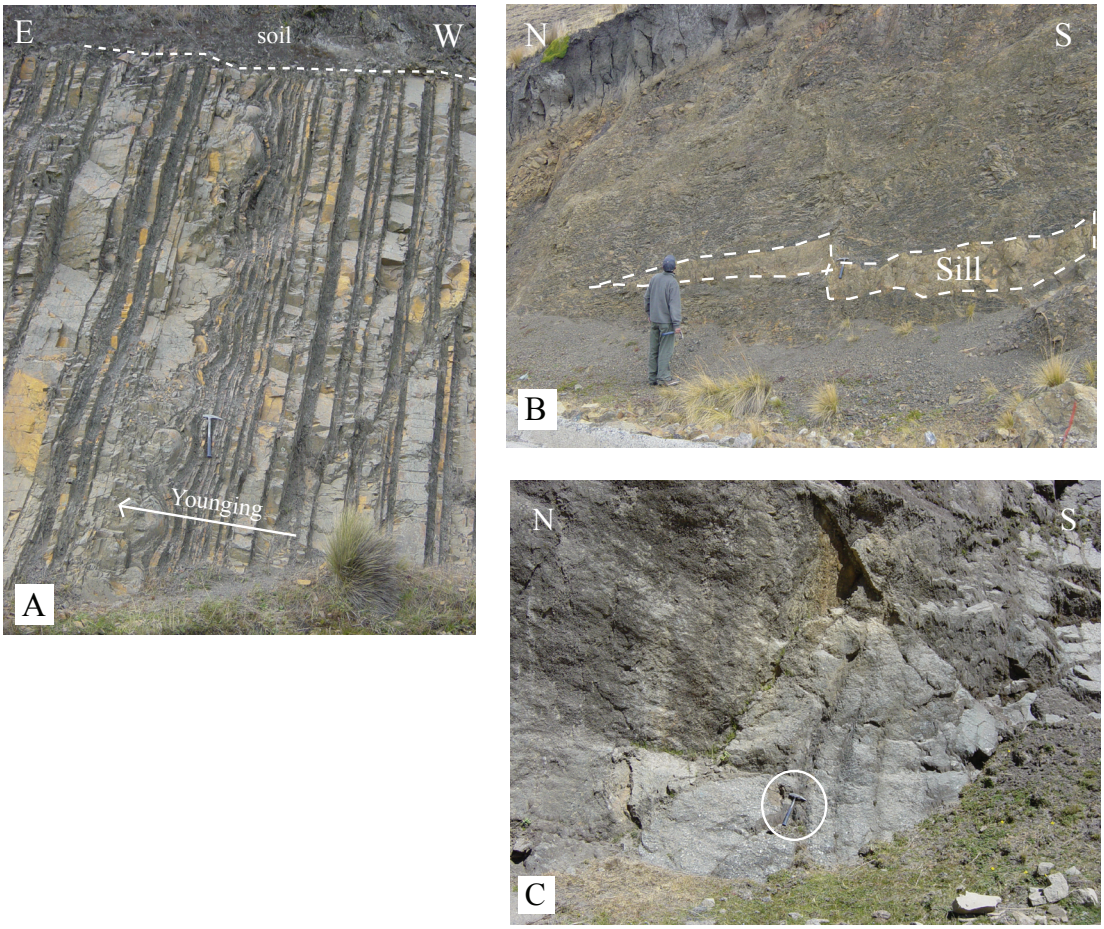

Fig. 2.25. Sedimentary and lithological features of the Angamarca Group in the central part of the Western Cordillera. A) Medium-bedded turbidites of the Saquisilí Fm, including load structures with sharp base and top (UTM: 738259/9821523). B) Thin-bedded turbidites of the Apagua Fm. intruded by an andesitic sill along the Apagua - Angamarca road (UTM: 731437/9882254). C) Thick-bedded conglomerates of the Rumi Cruz Fm. in the Apagua - Angamarca road section. These conglomerates are interpreted as fan delta deposits.

Lithology and thickness. The Saquisilí Formation is a turbiditic sequence composed of grey to dark grey micaceous sandstones, siltstones, and silty mudstones (Fig. 2.24), and some beds are slightly calcareous. The sandstones are fine-grained, quartz and muscovite bearing, feldspathic litharenites, which form 15 – 20 cm thick turbiditic beds. Load structures can be

observed in turbidites of the Saquisilí Formation east of Guaranda (Fig. 2.25).

Along the Riobamba – Guaranda road, the Saquisilí Formation interfingers with thick-bedded conglomerates of the Gallo Rumi Member, which contains abundant quartz and metamorphic clasts. The Gallo Rumi conglomerates may represent the upper part of the Saquisilí Formation submarine fan.

Stratigraphic relationships. In the type locality east of Saquisilí village, the western and eastern boundaries of the Saquisilí Formation are fault bounded, and no primary contact with overlying or underlying formations can be inferred. However, along the Riobamba – Guaranda road, the Saquisilí Formation unconformably overlies Campanian - Maastrichtian pelagic cherts (Jaillard et al., 2004) and turbidites of the Yunguilla Formation, and it is conformably overlain by the Eocene Apagua Formation.

Depositional environment. The Saquisilí Formation was deposited in the distal to medial part of a submarine turbiditic fan. The prograding pattern of the fan is manifested by the occurrence of coarse-grained conglomerates of the Gallo Rumi Member, representing inner fan channel deposits. The entire formation records input from a metamorphic and granitoid source. Field observations along the Riobamba – Guaranda road section indicate that the Saquisilí Formation was deposited unconformably of top of deformed turbidites of the Yunguilla Formation, suggesting that deformation of the Yunguilla Formation occurred prior to deposition of the Saquisilí Formation.

Age. Hughes and Bermúdez, (1997) found foraminifera fauna in the Quebrada Pusuchusi, *Morozovella pseudobulloides*, *Gyroidinoides planatus*, *Trochammina* sp, *Turrillina* sp cf *robertsi*, *Cibicides* sp cf *pseudoperlucidus*, which existed during the Early to Middle Paleocene and the earliest part of the Middle Paleocene.

Unacota Formation

Previous work. Faucher et al. (1971) and Echeverria (1977) described the limestones of the Unacota Formation in outcrops along the Latacunga – La Maná road, near to the village of Unacota. Previously, the limestones were used to produce cement by Cementos Cotopaxi. Egüez (1986) derived an Eocene age for the Unacota Limestone and observed that the Eocene Apagua Formation overlies the Unacota Formation.

Occurrence. The Unacota Formation is exposed west of the village of Apagua, in the La Maná - Latacunga road (UTM: 728252/9891115), and Río Chilcas section (UTM: 728571/9895034). Lithologically similar calcareous rocks are observed in the Quebrada Tenefuerte (UTM: 7152/99020), where the limestones occur as blocks on top of the Macuchi Unit.

Lithology and thickness. The Unacota Formation is a sequence of micritic and sparitic limestones, exposed as discontinuous lenses or blocks overlain by turbidites and pelagic sedimentary rocks of the Apagua Formation. East of Zumbagua (UTM: 728252/9891115), the limestones are mostly bioclastic, including biosparites and biolithites, showing variable bedding with thicknesses of a few centimeters to meters. The fauna reported include the foraminifera

Nummulites, *Amphistegina* sp., *Sphaerogypsina* sp., *Helicolepidina* (Bristow and Hoffstetter, 1977), and bryozoans. Hughes and Bermúdez (1997) reported morphologies typical of algal mounds or reefs, as well as stromatolite-type algal mats. The Unacota Limestone has a variable thickness, with a maximum of 80 m.

Stratigraphic relationships. There is a conformable stratigraphic contact between the Unacota Limestone and the overlying Apagua Formation. Progressive thinning of the limestone beds and the intercalation of thin-bedded turbidites that become coarser upwards, defines the transition. The contact can be observed in the Rio Chilcas (UTM: 728/9895) and west of Zumbagua (UTM: 728252/9891115). West of Pilaló, the Tenefuerte Limestone is considered to be equivalent to the Unacota Limestone, and overlies volcanic rocks of the Macuchi Unit, although the nature of the contact is difficult to establish due to abundant vegetation.

Depositional environment. Echeverria (1977) and Egüez (1986) indicate that the Unacota Limestone was deposited in a reefal environment. We suggest that the Unacota limestones were deposited on a carbonate ramp, corroborating the lack of corals and the high abundance of benthic foraminifera and bryozoans,. The transition to the overlaying deep-water turbidites of the Apagua Formation indicates that the Unacota carbonate system was drowned before the deposition of the turbiditic Apagua Formation. This event may be related to a rise in sea level or tectonic subsidence during the Late Eocene.

Age. Abundant algal and foraminifera fauna have been collected in the Unacota Formation (e.g. Bristow and Hoffstetter, 1977; Egüez, 1986), including: *Discocyclina barkeri*, *Sphaerogypsino*, *Amphistegina* sp., *Nummulites* sp*, Globorotalia*, *Discocyclina marginata*. The foraminifera assemblages indicate a Middle to Late Eocene age.

Apagua Formation

Previous work. The Apagua Formation was established by Egüez and Bourgeois (1986) as a turbidite series exposed close to the village of Apagua. Previous authors erroneously included this sequence within the Yunguilla Formation (e.g. Faucher and Savoyat, 1973; Henderson, 1979), because of the common turbiditic facies.

Occurrence. The real extent of the Apagua Formation is still poorly known because of its lithological similarity with the Yunguilla Formation. The type section lies near to the village of Apagua along the La Maná – Latacunga road (UTM: 729476/9891834). There are further isolated outcrops in Huayrapungu, and beneath the stratovolcano cone of Quilotoa (Hughes and Bermúdez, 1997). The Apagua Formation is also exposed along the Guaranda - Riobamba road and southwest of the Pallatanga Valley, along the Rio Chimbo. Hughes and Bermúdez (1997) also included black shales, medium grained sandstones with intercalated tuffs, which are exposed along the Sigchos to Chugchilán road, into the Apagua Formation. In our view, these rocks do not belong to the Apagua Formation, because they host a significant volcanoclastic content, which contrasts with the Apagua Formation in the type locality, which is rich in quartz and metamorphic minerals. Therefore, we correlate the exposures in the Sigchos area with the

Pilaló Formation.

Lithology and thickness. The Apagua Formation consists of medium-grained sandstones, dark grey siltstones and mudstones, and siliceous silty mudstones deposited within a turbiditic facies. The sandstones are typically feldspathic and contain abundant quartz and micas, and are classified as feldspathic litharenites and sublitharenites. Iron oxides are frequently observed in the matrix. Sills and stocks of andesitic composition are observed across the Apagua Formation (Fig. 2.25), and they are well exposed along the road from Apagua to Angamarca (UTM: 0732482/9880205). South of the Pallatanga Valley, ash flow tuffs are intercalated within the Apagua Formation (UTM: 7172/97627).

Stratigraphic relationships. The Apagua Formation is conformably underlain by the Unacota Limestone, and is transitional with the overlying Rumi Cruz Formation (Fig. 2.22), along the Latacunga - La Maná road. In the Pallatanga Valley, the Apagua Formation conformably overlies volcanic and sedimentary rocks of the Macuchi Unit (Fig. 2.26); however, the Apagua Formation conformably overlies the Saquisilí Formation, without the intervening Unacota Formation, along the Riobamba - Guaranda road.

Depositional environment. The Apagua Formation represents the proximal to medial part of a submarine turbiditic fan, which was sourced from a metamorphic and granitic source. A coeval volcanic source is evident by the abundant volcanic material found within the sequence.

Age. Foraminiferal fauna from the Apagua Formation indicate a Middle Eocene age (Egüez, 1986; Wilkinson, 1997). In the Cumanda area, the Apagua Formation contains ash flows intercalated within the turbiditic beds. Dunkley and Gaibor (1997) dated the tuffs and obtained a zircon fission track age of 37.8±3.5 Ma, which is consistent with the paleontological age. Although the fission track age may also be a reset age.

Rumi Cruz Formation

Previous work. Hughes and Bermúdez (1997) defined this formation as a series of conglomerates and red beds, which crop out along the Apagua - Angamarca road. Previously, Bristow and Hoffstetter (1977) included these strata within the continental deposits of the Cayo Rumi Formation, and correlated them with the red bed sequence of the Silante Formation, exposed in the Alóag – Santo Domingo road.

Occurrence. The Rumi Cruz Formation is extensively exposed along the Apagua - Angamarca road, south of the village of Apagua. Conglomerates that can be correlated with the Rumi Cruz Formation can also be observed northwest of Quito, east of the village of Los Entables de Chespí (UTM: 0776790/10011039).

Lithology and thickness. The Rumi Cruz Formation is a coarsening upward sequence, which overlies the Apagua Formation conformably. Lithologies in the Rumi Cruz Formation include matrix- supported conglomerates, breccias, coarse-grained sandstones, red mudstones and shales. Fossil wood fragments are common along the sequence and suggest a proximal continental source. The conglomerates from the Apagua – Angamarca road section are thick

bedded (Fig. 2.25), and contain clasts of chert and abundant vein quartz, the latter indicating a metamorphic source. The section exposed east of Los Entables de Chespí includes conglomerates with vein quartz together with basaltic to andesitic clasts, suggesting a metamorphic and volcanic source.

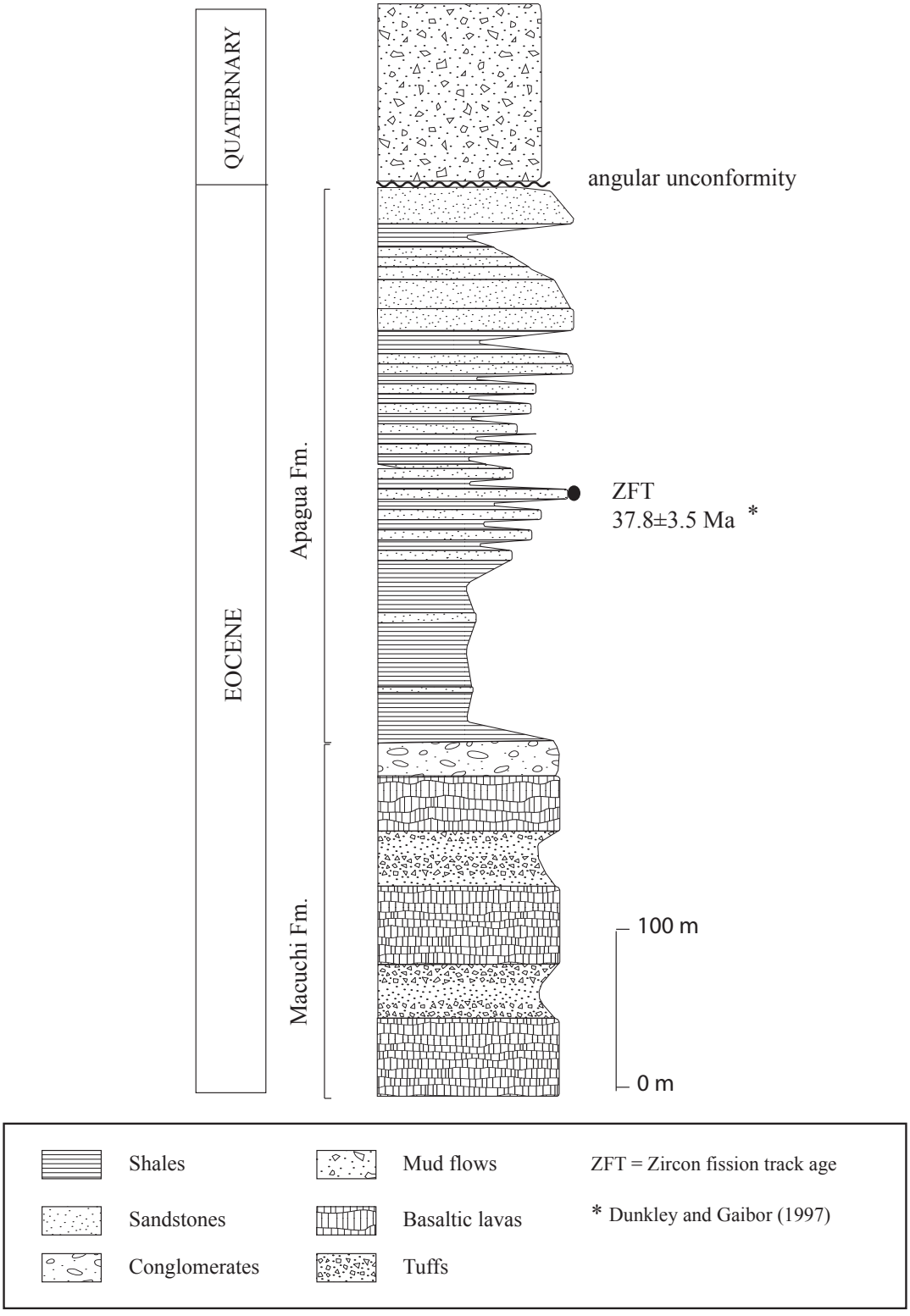

Fig. 2.26. Stratigraphic column of the contact between the Macuchi Unit. and the Apagua Fm. south of the town of Pallatanga, (UTM: 0721613/9769283).

Stratigraphic relationships. Along the Apagua – Angamarca road, the Rumi Cruz Formation conformably overlies the Apagua Formation, and is unconformably overlain by the Miocene Zumbagua Formation.

Depositional environment. Hughes and Bermúdez (1997) suggested a fan-delta environment for the Rumi Cruz Formation, which received material derived from metamorphic and volcanic source rocks. According to our own observations, a fan delta environment is consistent with the overall lithological characteristics of the Rumi Cruz Formation, including red mudstones that are typical of a subaerial environment, abundant continental-derived wood, and the presence of fluvial structures (e.g. imbrication, channelized conglomerates). Therefore, there is a gradual transition within the Angamarca Group, from deep-sea turbidites of the Saquisilí and Apagua Formation, to continental deposits of the Rumi Cruz Formation.

Age. Boland et al. (2000) report the presence of the foraminifera *Epistomina eocenica*, collected east of Los Entables de Chespí. This scarce evidence points to an Eocene age. A Late Eocene to Oligocene age can be assumed after considering the well-established age of the underlying fully marine formations.

El Laurel Formation

Previous work. Van Thournout (1991) introduced the El Laurel Unit, and described it as a series of fine-grained sandstones, which overlie limestones exposed in the northern part of the Western Cordillera. In this study the El Laurel Unit is redefined as a formation, which is included into the Angamarca Group, based on petrographic and provenance analysis similarities.

Occurrence. The El Laurel Formation is restricted to the northern part of the Western Cordillera, close to the Colombian border. The type locality is located in the village of El Laurel (UTM: 827956/10092519) and along the road from Maldonado to Tufiño villages. Good outcrops can also be observed in the Hualchan quarry, northeast of La Carolina (UTM: 772459/10031242).

Lithology and thickness. The El Laurel Formation includes thin-bedded, black and grey mudstones intercalated by fine-grained sandstones. Individual beds are not thicker than 5 cm. In the Hualchan area, limestones rich in bioclastic material including corals, gastropods and bivalves, overlie the fine-grained sandstones.

The total thickness is difficult to estimate because of intense faulting, although Van Thournout suggests that it does not exceed 1800 m.

Stratigraphic relationships. The El Laurel Formation occurs within faulted slices, which are separated from other formations by NNE trending faults. The San Juan de Lachas Formation, unconformably overlies the El Laurel Formation, west of the village of La Carolina (UTM: 804226/10083100).

Depositional environment. Sedimentary rocks of the El Laurel Formation were deposited in the distal part of a submarine fan.

Age. The age of the El Laurel formation is based on foraminifera data from the limestone

member, which occurs at the top of the formation. The fossils include *Asterosomalina*, *Ramena*, *Asilina Subpamiri*, *Lepidociclina Undosa*, *Lithotamnium* s.l. (Van Thournout, 1991). The presence of *Lepidociclina* (*Eulepidina*) *Undosa* suggests that the Upper part of the El Laurel Formation may extend to the Lower Oligocene, and hence it may be coeval with the Rumi Cruz Formation.

2.1.2.11 San Juan de Lachas Formation

Previous work. Van Thournout (1991) defined the San Juan de Lachas Formation as a series of andesites, which crop out along the Salinas – Lita road section, near to the village of San Juan de Lachas. The same author correlated the formation with the Tandapi volcanics of the Silante Formation, because both yield calc-alkaline geochemical compositions; however, radiometric dating in both formations (see chapter four), indicate that both formations are unrelated.

Occurrence. The most complete outcrops of the San Juan de Lachas Formation are found along the Salinas - Lita road, between the villages of La Carolina and Parambas, and in the Río San Francisco (UTM: 806644/100835460). Isolated outcrops occur in the Río Guayllabamba (Boland et al., 2000). Similarly, Spadea and Espinosa (1996) described lithologically similar volcanic rocks from the village of Ricaurte in Colombia, near to the border with Ecuador.

Lithology and thickness. The San Juan de Lachas Formation consists of plagioglase-phyric and hornblende rich andesitic lavas, and breccias. The thickness of the formation is unknown.

Stratigraphic relationships. The San Juan de Lachas Formation unconformably overlies the El Laurel Formation, and volcanoclastic sedimentary rocks of the Pilatón Formation, along the Ibarra – Lita road

Geochemistry. Geochemical analysis of the andesitic lavas, which crop out along the Ibarra – Lita road, shows that they are calc-alkaline, and hence probably erupted in a continental arc setting (Van Thournout, 1991; Boland et al., 2000).

Age. Van Thournout (1991) acquired a K/Ar age of 32.6 Ma (hornblende) from an andesitic dyke, and Boland et al. (2000) obtained K/Ar ages (hornblende) of 36.3±2 Ma and 19.8±3.1 Ma from hornblende-rich andesites. Boland et al. (2000) dated two samples of plagioclase phyric crystal tuffs (Río Guayllabamba) using the zircon fission track method, which yielded coherent ages of 23.5±1.5 Ma and 24.5±3.1 Ma. However, these ages may be partially reset. We obtained a hornblende, plateau $^{40}Ar/^{39}Ar$ age of 32.9±1.2 Ma (2σ) from an andesite east of the village of Jijón y Caamaño (UTM: 806395/83179), which correlates with the K/Ar age reported by Van Thournout (1991). Consequently, we conclude that the San Juan de Lachas Fm. was deposited during the Oligocene possibly extending to the Early Miocene.

2.1.2.12 Macuchi Unit

The north-south elongated Macuchi Unit crops out along the Western border of the Western Cordillera, and its eastern border with the Pallatanga Block coincides with the regional, north-south trending, Chimbo – Toachi Fault. Hughes and Bermúdez (1997) argue that the

Chimbo – Toachi Fault represents a suture, along which the Macuchi Unit accreted against the Pallatanga Block, during the Late Eocene. However, recent studies (including this study) have shown that the Pallatanga and Piñon blocks accreted during the Late Cretaceous (Vallejo et al., 2006; Luzieux et al., 2006). Therefore, given that the Macuchi Unit is sandwiched between the Pallatanga and Piñon blocks (Fig. 1.4), the interpretation of Hughes and Bermúdez (1997) implies that there must have been significant post-accretionary structural re-arrangement of fault blocks. However, we are unable to find convincing arguments to support Late Eocene accretion of the Macuchi Unit, as proposed by previous authors (e.g. Hughes and Pilatasig, 2002).

Previous work. Earlier investigators (e.g. Faucher and Savoyat, 1973; Bristow and Hoffstetter, 1977; Henderson, 1979; Kennerly, 1980) applied the term Macuchi Unit to Late Cretaceous to Tertiary, mafic and ultramafic rocks in the Western Cordillera. However, more recent radiometric and geochemical data (e.g. Egüez, 1986; Hughes and Bermúdez, 1997; Kerr et al., 2002a; this study – see chapter 4) suggests the Macuchi Unit was deposited during the Paleocene to Eocene, as a calc-alkaline and tholeiitic, submarine volcanic sequence.

Occurrence. The Macuchi Unit occupies large areas along the western border of the Western Cordillera. Thick quaternary deposits cover its western contact with the Piñon Block. The most representative outcrops of the Macuchi Unit are located along the road from Alóag to Santo Domingo, especially between La Unión del Toachi (UTM: 728072/9965008) and El Paraiso (UTM: 718651/9965853). Extensive outcrops are exposed along the Pilaló to La Maná road, and in the Chimbo River valley, south of Pallatanga (UTM: 721613/9766370). Good outcrops of pillow lavas of the Macuchi Unit can be observed in the Alóag - Santo Domingo section, east of the town of Alluriquín. In the northern part of the Western Cordillera, the Macuchi Unit can be observed east of the village of Lita (UTM: 784106/10095939).

Lithology and thickness. The Macuchi Unit contains basaltic pillow lavas, lithic tuffs of basaltic and andesitic composition, basaltic breccias, high-level andesitic intrusions, redeposited volcanic material in turbiditic beds (e.g. Arrayanes Unit and Las Juntas turbidites) and cherts (Fig. 2.27). Volcanoclastic beds are the most common lithology in the formation, and comprise approximately 80% of the sequence. The volcanic breccias are polymictic including angular clasts of basalts, andesites, dacites in an epidotized andesitic matrix with abundant glass. The andesites have a porphyritic texture, with phenocrysts of plagioclase and pyroxene, set in a groundmass of altered glass, plagioclase and pyroxene microliths, and frequently pumpellyite. Primary tuffs were not observed in the Macuchi Unit during this study. Sideromelane is present in the volcanoclastic succession of the Macuchi Unit. According to Fisher and Schmincke (1984), sideromelane forms during submarine eruptions of basaltic magma, when it is quenched in seawater, and is normally abundant in volcanoclastic sedimentary rocks that form during the submarine shield-building stage of ocean island volcanoes. Low-grade metamorphism of rocks of the Macuchi Unit is manifested by the presence of epidote, zeolite, and prehnite- pumpellyite mineral assemblages. Kerr et al. (2002a) estimated the thickness of the Macuchi Unit to be 2 to 2.5 km.

Stratigraphic relationships. The stratigraphic relationships of the Macuchi Unit have always been controversial, and hence have led to serious stratigraphic correlation problems within the Western Cordillera. This is because of the poor exposure of the Formation, which mainly occurs in densely vegetated areas.

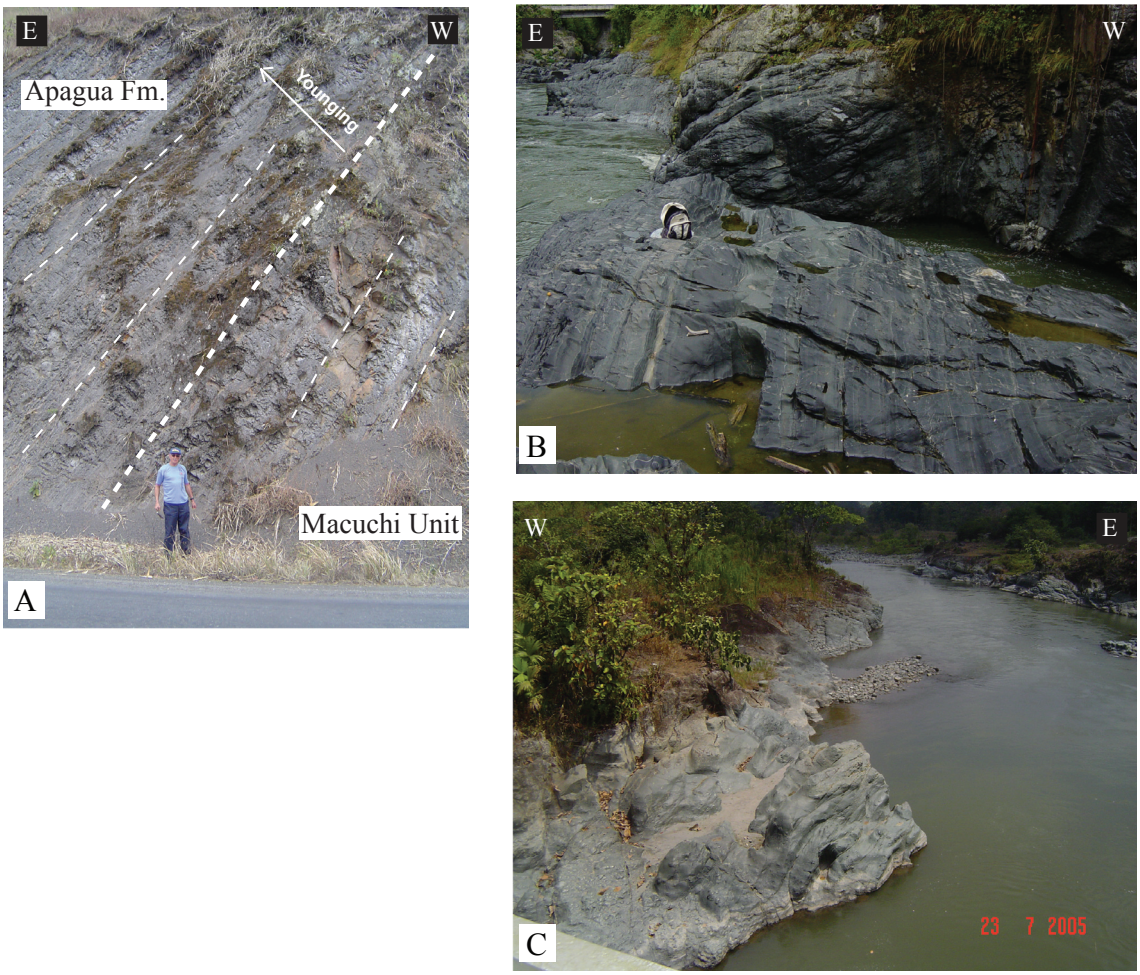

Fig. 2.27. Lithological features of the Macuchi Unit. A) Stratigraphic contact between volcanic rocks of the Macuchi Unit (right) and turbidites of the Apagua Fm (left) at the Pallatanga - Bucay road (UTM:721613/9766370). Note that the dip of beds is similar in both formations. B) Turbidites of the Macuchi Unit. (Las Juntas turbidites) in the Alóag - Santo Domingo road (UTM: 728072/9965008). C) Basaltic lavas of the Macuchi Unit exposed in the Toachi River (UTM: 0717347/9967521).

Aguirre and Atherton (1987) suggested that the Macuchi Unit is stratigraphically overlain by volcanoclastic sedimentary rocks of the Paleocene Pilaló Formation, implying a Paleocene or older age for the Macuchi Unit, along the Latacunga – La Maná road. However, in the same road section, volcanic rocks of the Macuchi Unit are overlain by the Tenefuerte Limestones, which are possibly a lateral equivalent of the Middle Eocene Unacota Limestone. Therefore, two lithologically similar submarine volcanic sequences, one of Paleocene age, and the other of Eocene age, are preserved in the Latacunga – La Maná road section, and both are mapped as the Macuchi Unit.

A stratigraphic contact between volcanic rocks of the Macuchi Unit, and quartz bearing turbidites of the Apagua Formation, can be observed in the Pallatanga Valley, near to the village of Las Rocas (Fig. 2.28) (UTM: 0721613/9769283). At this site, the Macuchi Unit is composed of basaltic andesites with intercalated tuffs, which have the same dip as the overlying Apagua Formation. Furthermore, Dunkley and Gaibor (1997) report a fission track age of 37.8±3.5 Ma for the Apagua Formation, close to its contact with the Macuchi Unit.

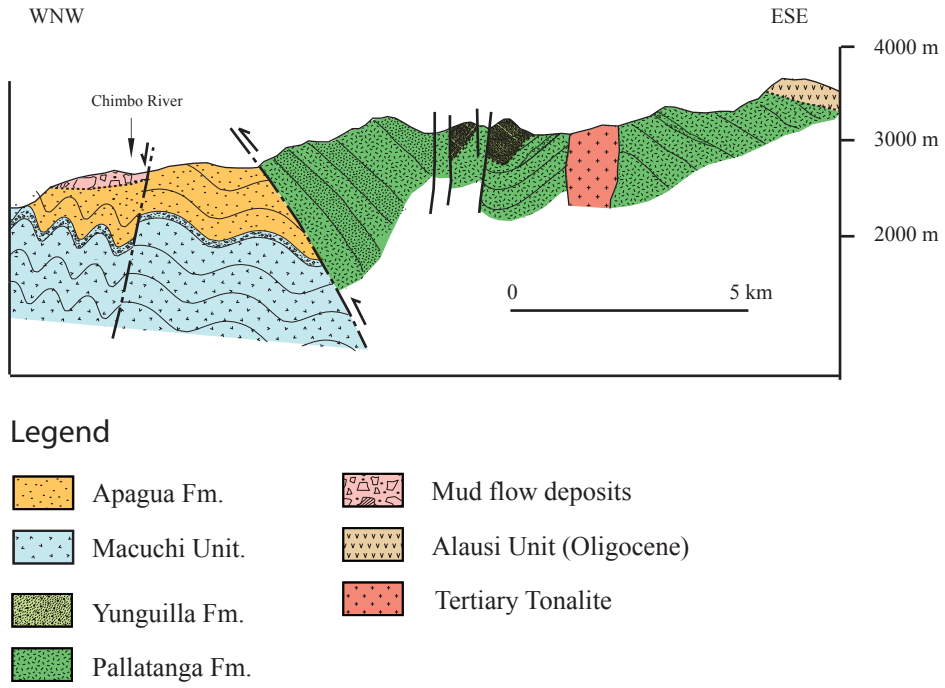

Fig. 2.28. East -west section crossing the Pallatanga Valley north of Bucay, showing the stratigraphic contact between the Macuchi and the Apagua formations. A reverse fault separates this block from basalts of the Pallatanga Fm. Modified from Lebrat et al. (1985).

Consequently, these observations imply that the Macuchi Unit and Apagua Formation were originally part of a single structural block that was subsequently dissected by the Chimbo - Toachi Fault. This interpretation contrasts with previous hypotheses, which proposed that the Macuchi Unit was allochthonous and collided against the Angamarca Group during the Eocene (e.g. Hughes and Bermúdez; 1997; Hughes and Pilatasig, 2002). Furthermore, Spikings et al. (2005) reported an apatite fission track (AFT) age of 2.4±1.4 Ma (1σ) from an andesite in a mylonitic shear band along the Chimbo – Toachi Fault, whereas undeformed basalts adjacent to this structure yielded an AFT age of 8.8±2.9 Ma (1σ). Therefore, there is no conclusive evidence that the Chimbo – Toachi Fault represents a suture between the Macuchi Unit and the Pallatanga Block, and there is no data, which supports Eocene shearing associated with the proposed Late Eocene accretion of the Macuchi Unit.

Geochemistry and depositional environment. Whole rock geochemical data from the Macuchi Unit indicates an arc origin for the volcanic rocks (Hughes and Pilatasig, 2002; Kerr et al., 2002a). Primitive mantle normalized (Sun and McDonough, 1989), multi-element and

REE plots reveal a negative Nb anomaly, and an enrichment in LREE, which are typical for rocks formed in volcanic arc settings (Fig. 2.29). Lebrat et al. (1987) reported the presence of E-MORB type rocks in the Macuchi Unit, but their conclusion was based on erroneous stratigraphic relationships. The geochemistry of volcanic rocks in the Macuchi Unit is consistent with a volcanic arc of tholeiitic and calc-alkaline composition (Fig. 2.29), which formed on oceanic crust.

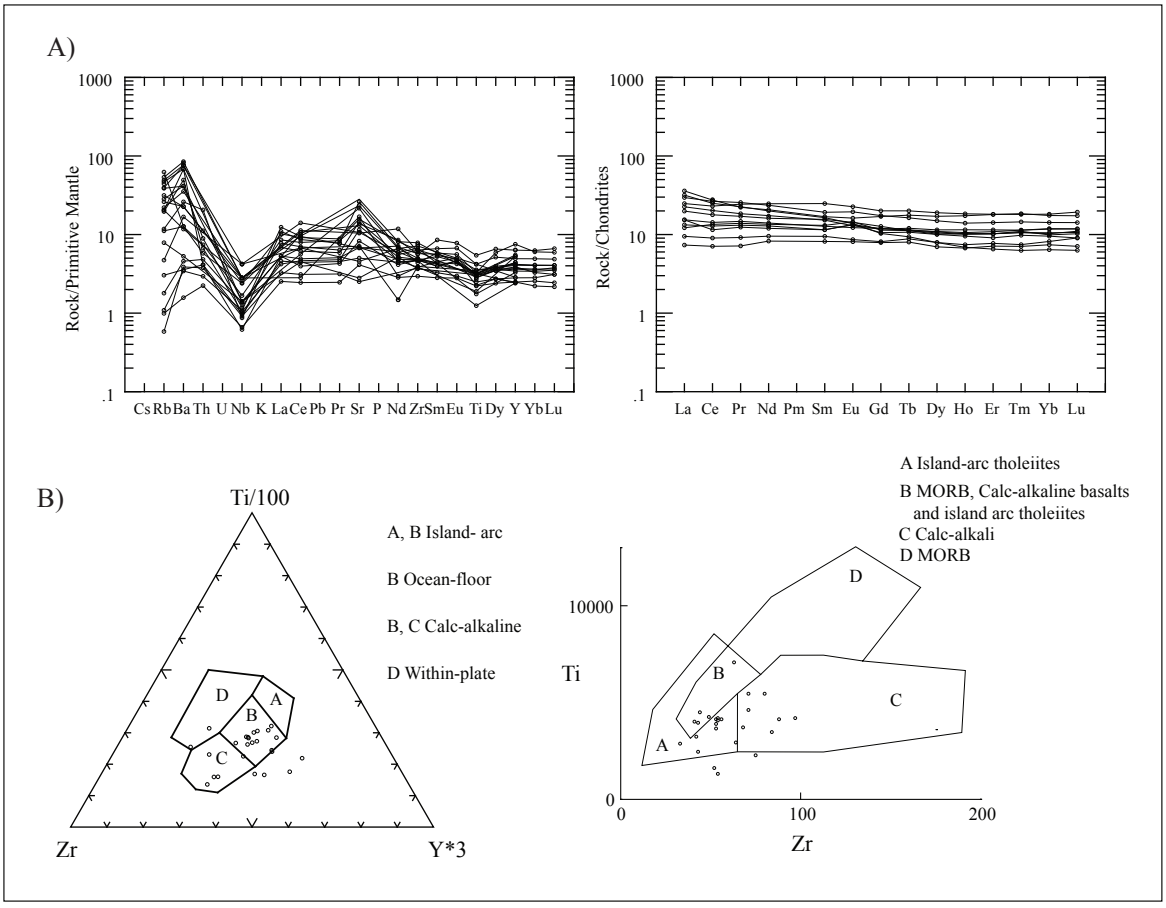

Fig. 2.29. A) Primitive mantle normalized multielemental and REE chondrite normalized (Sun and McDonough, 1989) plots of the Macuchi Unit. Geochemical data compiled from Hughes and Pilatasig (2002) and Chiaradia and Fontboté (2001). B) Discriminatory tectonic plots (Pearce and Cann ,1973) from samples of the Macuchi Unit. Geochemical data compiled from Hughes and Pilatasig (2002) and Chiaradia and Fontboté (2001).

Earlier, Egüez (1986) and Aguirre and Atherton (1987) arrived at a similar conclusion, which served as a model for the investigations of Hughes and Pilatasig (2002) and Kerr et al. (2002a), who concluded that the Macuchi volcanic arc was allochthonous to the South American Plate. However, spatial and chronostratigraphic constraints force the necessity of complicated, post-accretionary structural rearrangements, if their hypotheses are accurate. Chiaradia and Fontboté (2001) showed that the Macuchi Unit is enriched in radiogenic lead (high $^{206}Pb/^{204}Pb$), suggesting assimilation of a ^{206}Pb-enriched source, which, according to the authors, was probably an oceanic plateau.

Furthermore, the presence of detrital zircons with Cambrian ages (see chapter 3) within the Macuchi Unit suggests that the volcanic arc formed adjacent to the South American Plate margin. Therefore, we suggest that volcanic rocks of the Macuchi Unit erupted through mantle-plume derived rocks of the Pallatanga Fm., which had already accreted to the South American Plate. The varied different geochemical affinities (i.e. calc-alkaline and tholeiitic) of volcanic rocks of the Macuchi Unit, suggests that the basement to the Macuchi Arc was heterogeneous.

Age. Egüez (1986) describes the intercalation of sedimentary rocks within andesites and tuffs of the Macuchi Unit at La Union del Toachi (UTM: 727823/9964642). The foraminifera includes: *Eusyringium fistuligerum*, *Giraffospyris didiceros*, *Lychnocanoma* cf. *bandica* and *Dictyopora* cf. *amphora*, which indicate a Late Eocene age. The same author also obtained K/Ar ages ranging from ~42–36 Ma from andesitic, high-level intrusions along the Latacunga – La Maná road section. Spikings et al. (2005) provided a low precision zircon fission track age of ~67.5±10.7 (1σ) Ma from a basaltic andesite, east of the town of Alluriquín (UTM: 724073/9965044).

Formation/intrusion	Locality	Age	Mineral phase/ Fossil	Method	Reference
Basaltic andesite.	Macuchi	41.6±2.1 Ma	whole rock	K/Ar	Egüez, 1986
Basalt	Macuchi	35.8±1.8 Ma	whole rock	K/Ar	Egüez, 1986
Andesite	Alluriquín	68±11 Ma	zircon	ZFT	Spikings et al., 2005
Basaltic andesite	East of Alluriquín	42.62±1.3 Ma	plagioclase	$^{40}Ar/^{39}Ar$	this study
Basaltic andesite	Lita	35.12±1.66 Ma	groundmass	$^{40}Ar/^{39}Ar$	this study
Las Juntas turbidites	Union del Toachi	Late Eocene	foraminifera fauna	Biostratigraphy	Egüez, 1986

Table 2.1 Reported ages from the Macuchi Unit.

In the present study, we obtained a plagioclase $^{40}Ar/^{39}Ar$ age of 42.62±1.3 Ma (2σ) from an andesitic lava flow in the Alóag Santo Domingo road section (UTM: 724880/9964662). The age represents the minimum age of a saddle-shaped age spectrum, implying that it is a maximum, plagioclase $^{40}Ar/^{39}Ar$ age. Similarly, an $^{40}Ar/^{39}Ar$ plateau age (groundmass) of 35.12±1.66 Ma (2σ) Ma was obtained from an andesitic lava flow exposed close to the town of Lita (UTM: 783857/95572). These data, when combined with the stratigraphic relationships with the overlying Unacota and Apagua formations, suggest that the Macuchi Unit erupted during the Early to Late Eocene. With regard to the stratigraphic positions with the Paleocene Pilaló Formation along the Latacunga – La Maná road section (Fig. 2.22), and considering the young age range of the zircon fission track age indicated by Spikings et al. (2005), a Paleocene age for basal terms of the Macuchi Unit can be suggested. Reported ages from the Macuchi Unit are summarized in table 2.1.

2.1.3 Naranjal Block

The Naranjal Block was defined by Kerr et al. (2002a), and is exposed in the north of the studied area; it is separated from the Pallatanga Block by the Mulaute Shear Zone. The western border of the block is poorly defined, and it may coincide with the Canande Fault of the coastal area. The basement of the block is the Naranjal Unit and it is overlain by sedimentary and volcanic formations, which range in age from the Campanian to Oligocene. Most of the area occupied by the Naranjal Block is inaccessible. The next paragraphs describe the Naranjal Unit , which is the basement of the Naranjal Block, discussing the possible relationships with similar formations of the Western Cordillera. Other units into the Naranjal Block were not studied due to availability of time.

2.1.3.1 Naranjal Unit

Previous work. Boland et al. (2000) defined the Naranjal Unit as a volcanic sequence, consisting of andesitic and basaltic rocks of tholeiitic and oceanic plateau affinity, which crop out in the northwestern border of the Western Cordillera, and are separated from the Pallatanga Block by the Mulaute Shear Zone. Kerr et al. (2002a) proposed that the Naranjal Unit is part of an allochthonous block, different than the Pallatanga Block, which accreted during the Eocene. We have been unable to improve on their informal definition of this sequence.

Fig. 2.30. Oxidized pillow basalts of the Naranjal Fm. in the Guayllabamba River, north of Pedro Vicente Maldonado village (UTM:0721344/0026094).

Occurrence. The Naranjal Unit is restricted to the northern part of the Western Cordillera and may extend to the coastal lowlands. The type section of the Naranjal Unit is exposed in the village of Salto de Tigre (UTM: 7213/100260) along the Guayllabamba River. Boland et al. (2000) correlated the exposures in the Guayllabamba River with volcanic rocks exposed along the Salinas – Lita road, west of the village of Cachaco (UTM: 784106/10095939). However

there are significant geochemical and age differences between these two locations (see later). Kerr et al. (2002a) indicate that the Naranjal arc can be temporally and geochemically correlated with the Campanian Ricaurte arc of Colombia, which yields similar biostratigraphic ages and geochemical signatures.

Lithology. The Naranjal Unit, defined by Boland et al. (2000), is composed of a sequence of basaltic pillow lavas (Fig. 2.30) and andesites with intercalated sedimentary rocks. The basalts are aphyric with microliths of plagioclase, pyroxene and olivine, and are mainly exposed in the Guayllabamba River area (southwestern exposures). The andesites have porphyritic textures with phenocrysts of plagioclase and pyroxene in a matrix of plagioclase microliths, glass and opaques. The andesitic rocks are mostly exposed in the Ibarra – Lita road section. The pillow lavas in the Guayllabamba River are strongly oxidized, and intercalated with volcanic breccias and mudstones. Radiolarian fauna is reported in the mudstones (Boland et al., 2000).

Stratigraphic relationships. The Naranjal Unit is in faulted contact with most of the formations in the Western Cordillera. The Eocene Tortugo Formation unconformably overlies pillow basalts of the Naranjal Unit in the Guayllabamba River section. Boland et al. (2000) indicate that the Naranjal Unit is overlain by Campanian turbidites of the Colorado Unit.

Geochemistry and depositional environment. Whole rock geochemical analyses of the Naranjal Unit were presented by Boland et al. (2000) and Kerr et al. (2002a), which showed that the andesites and basalts formed in both, oceanic plateau and volcanic arc settings (Fig 2.31A).

Rocks erupted above an oceanic mantle-plume yield typical flat patterns, characteristic of a plume influenced source (Kerr et al. 2003), whereas rocks with volcanic arc affinities posses a distinctive, negative Nb anomaly, and are enriched in the LREEs with $(La/Yb)_N$ ratios >2 (Kerr et al., 2002a). The arc rocks plot in both the tholeiitic and calc-alkaline fields on the Zr vs. Ti discriminatory diagram of Pearce and Cann (1973) (Fig.2.31B).

One sample from the Guayllabamba River section (sample M5-773, Boland et al., 2000) is enriched in MgO (~8%), and depleted in LREEs, similar to boninitic rocks described in the La Portada Formation. The rocks which yield oceanic plateau affinity are geographically restricted to the southwestern border of the mapped Naranjal Unit (Fig. 2.32).

Age. Boland et al. (2000) reported radiolarian fauna in mudstones intercalated in pillow lavas of island arc affinity (Boland et al., 2000; Kerr et al., 2002a) located in the southwestern part of the sequence, near to the Guayllabamba River. The radiolarian fauna recovered include: *Amhipyndax pseudoconulus*, *Amhipyndax tylotus*, *Archaeodictyomitra lamellicostata*, *Dictyomitra formosa*, *Dictyomitra kozlovae* and *Xitus grandis*, which suggest a Late Campanian age.

The mapped Naranjal Unit probably includes two distinctly different lithotectonic units: a) an oceanic plateau possibly older than the Late Campanian, and b) a Late Cretaceous island arc. These lithotectonic units may be tentatively correlated with the Coniacian Pallatanga Formation, and the Late Cretaceous Rio Cala Group island arc basalts respectively, strongly suggesting that

both the Pallatanga and Naranjal Blocks may have the same oceanic plateau basement sequence, and that their Late Cretaceous island arc sequences formed in the same subduction zone.

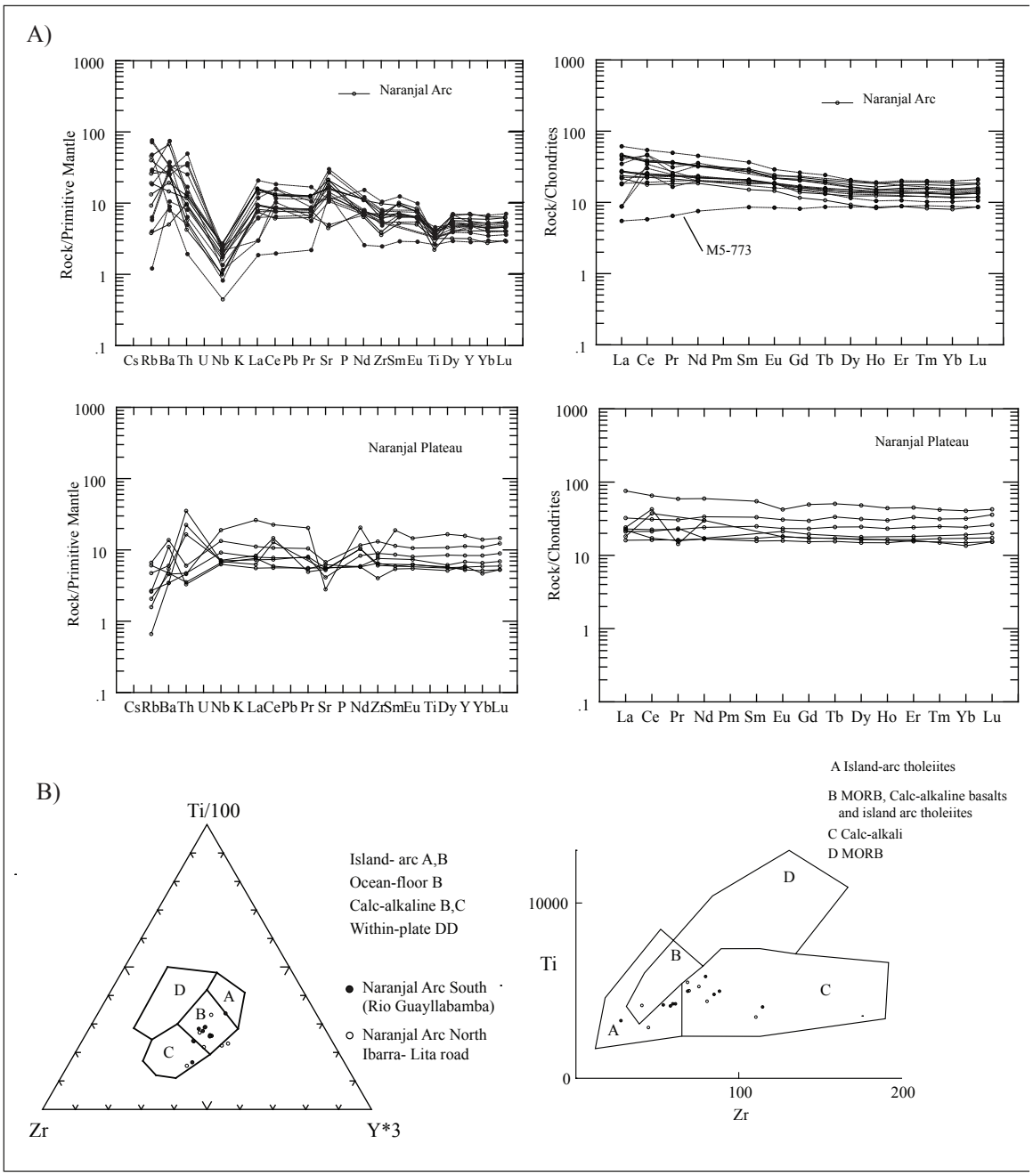

Fig. 2.31. A) Primitive mantle normalized multielemental and REE chondrite normalized (Sun and McDonough, 1989) plots of the Naranjal Unit, showing the volcanic rocks with arc and oceanic plateau affinities. Geochemical data compiled from Hughes and Pilatasig (2002) and Chiaradia and Fontboté (2001). B) Discriminatory tectonic plots of the samples of the Naranjal Unit (Pearce and Cann, 1973). Data compiled from Kerr et al. (2002a) and Boland et al. (2000).

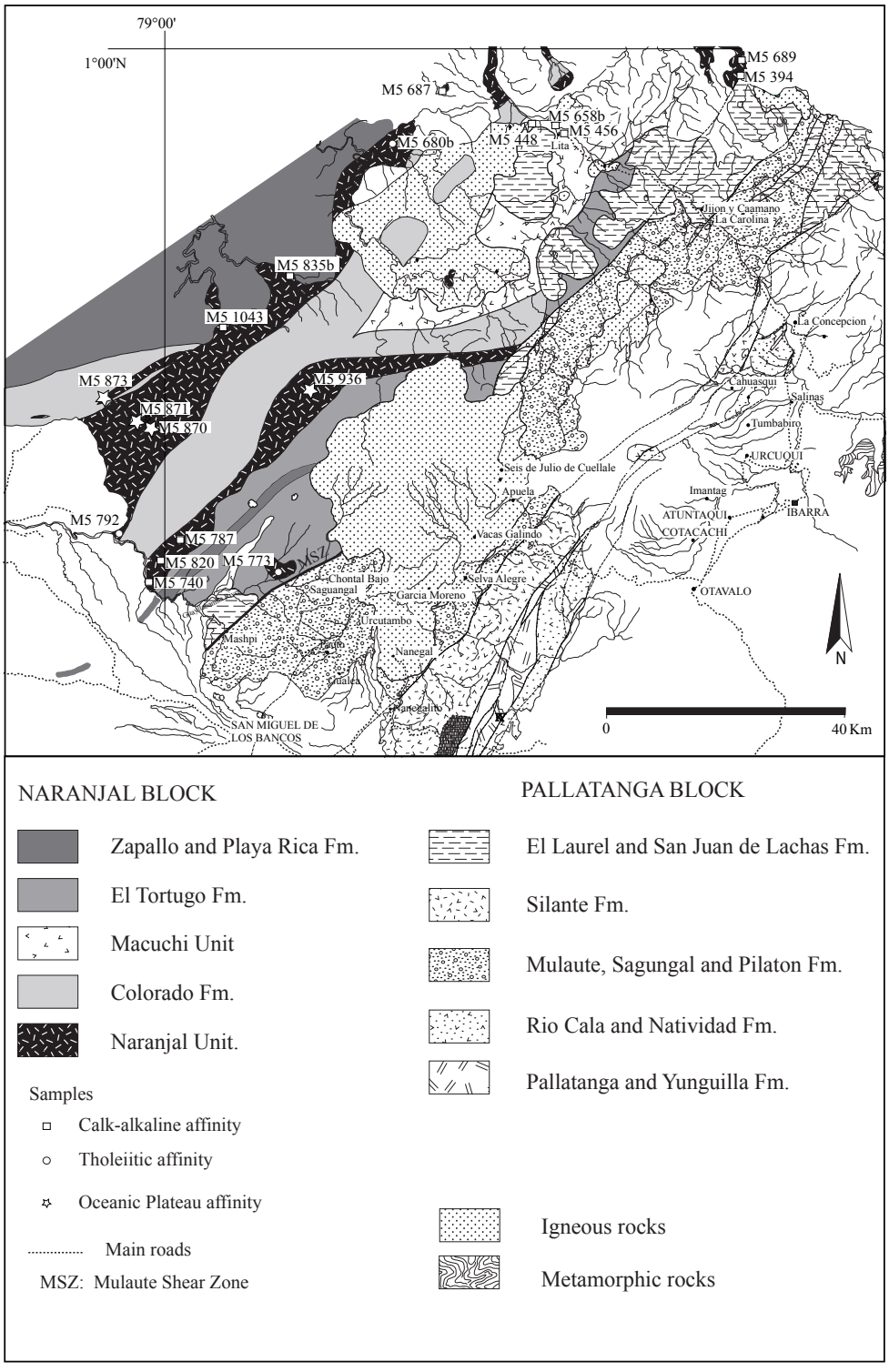

Fig. 2.32. Distribution of known geochemical affinities of volcanic samples of the Naranjal and Macuchi units within the northern part of the Western Cordillera. Geochemical data compiled from Boland et al. (2000).

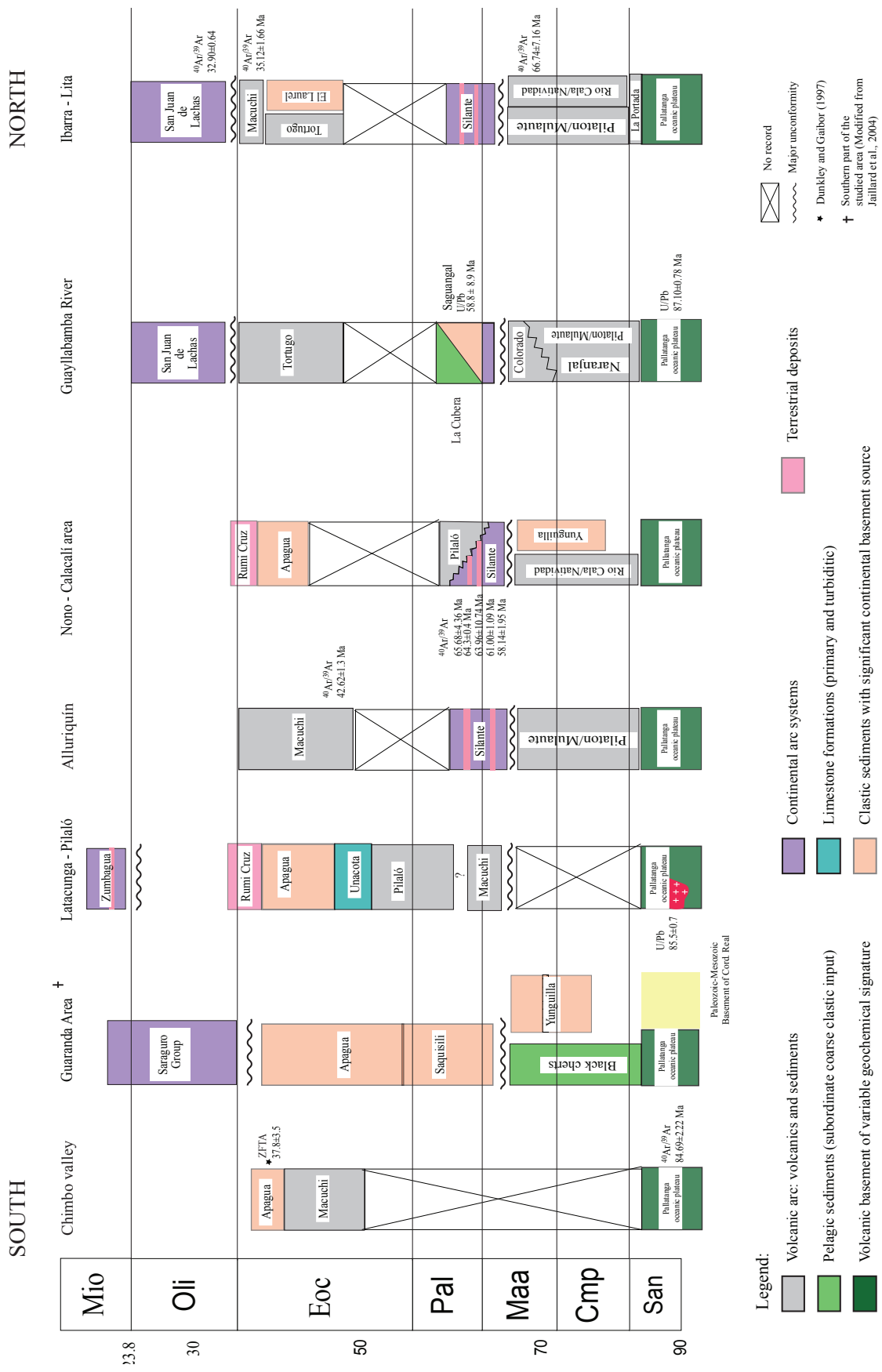

Figure 2.33. Stratigraphic columns from the main sections studied in the present work

CHAPTER 3: PROVENANCE ANALYSIS

3.1 INTRODUCTION AND GOALS

This chapter present the results of a provenance analysis study, which utilizes heavy mineral assemblage (HM) determinations, geochemical analyses of single crystals, and detrital zircon dating using the laser ablation inductively coupled plasma mass spectrometer (LA-ICPMS) method. The aim of this investigation is to determine the nature (i.e. tectonic setting) and age of the source regions of pre- and post-accretionary sedimentary and volcanic formations. Provenance analysis helps to elucidate possible changes in the sedimentary source regions, which may be related to the collision of allochthonous blocks against the South American plate. These methods also permit us to establish stratigraphic correlations between the structurally dissected sedimentary formations of the Western Cordillera.

The provenance analysis results were obtained from turbidites of the Late Cretaceous Mulaute and Pilatón formations, Maastrichtian Yunguilla Formation, Paleocene to Eocene Angamarca Group and the continental arc rocks of the Silante Formation, which collectively overlie the Pallatanga Formation. For comparison with the detrital clinopyroxenes, the single grain clinopyroxene geochemistry of the potential volcanic source rocks was also analyzed.

Sample location, lithology and stratigraphic data is presented in the appendix, and their locations, with respect to local fault blocks, can be seen in Fig. 3.1.

3.2 HEAVY MINERALS ANALYSIS

3.2.1 Rationale of the method

Heavy mineral assemblages are sensitive indicators of sedimentary provenance, that used together with geochemical and detrital mineral radiometric dating, is a powerful provenance indicators of clastic rocks (e.g. Morton, 1985; Nechaev and Ishpording, 1993; Acquafreda et al. 1997), and also as evidence for stratigraphic correlations within monotonous sedimentary strata. Heavy minerals are defined here as sand-sized, mineral grains, with a density equal and higher to 2.9. This group of minerals has many advantages over light minerals, as heavy minerals include a wider spectrum of silicates, sulphates (e.g. barite), sulfides (e.g. pyrite), oxides (e.g. spinel) and phosphates (e.g. apatite) than light minerals in the sand-size fraction, which is normally dominated by quartz, feldspars and calcareous minerals (Dill, 1998).

Heavy mineral determinations on sandstones are useful indicators of source changes, which in the geodynamic context of the Western Cordillera, may help to distinguish between pre-accretionary and post-accretionary rock sequences, and hence constrain the timing of accretion of allochthonous blocks onto the continental margins, if the age of the rock sequences can be determined. This section present an overview of the more commonly occurring heavy mineral assemblages, and the associated rock sources. Zircon, tourmaline, and rutile (ZTR) grains are generally translucent and commonly occur with brookite, anatase and titanite minerals (BRANTI

assemblage) in the erosional detritus of granitic to dioritic terranes.

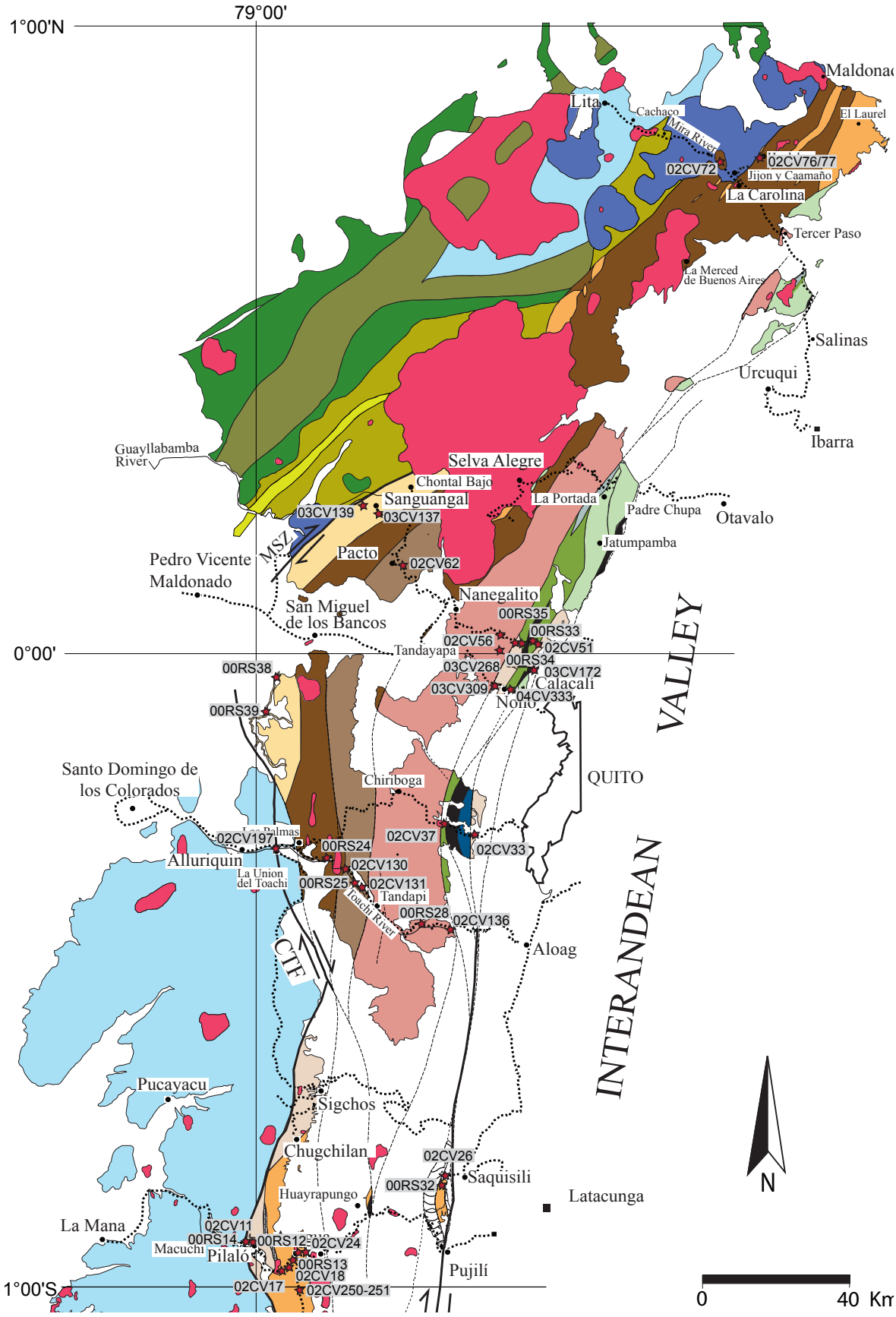

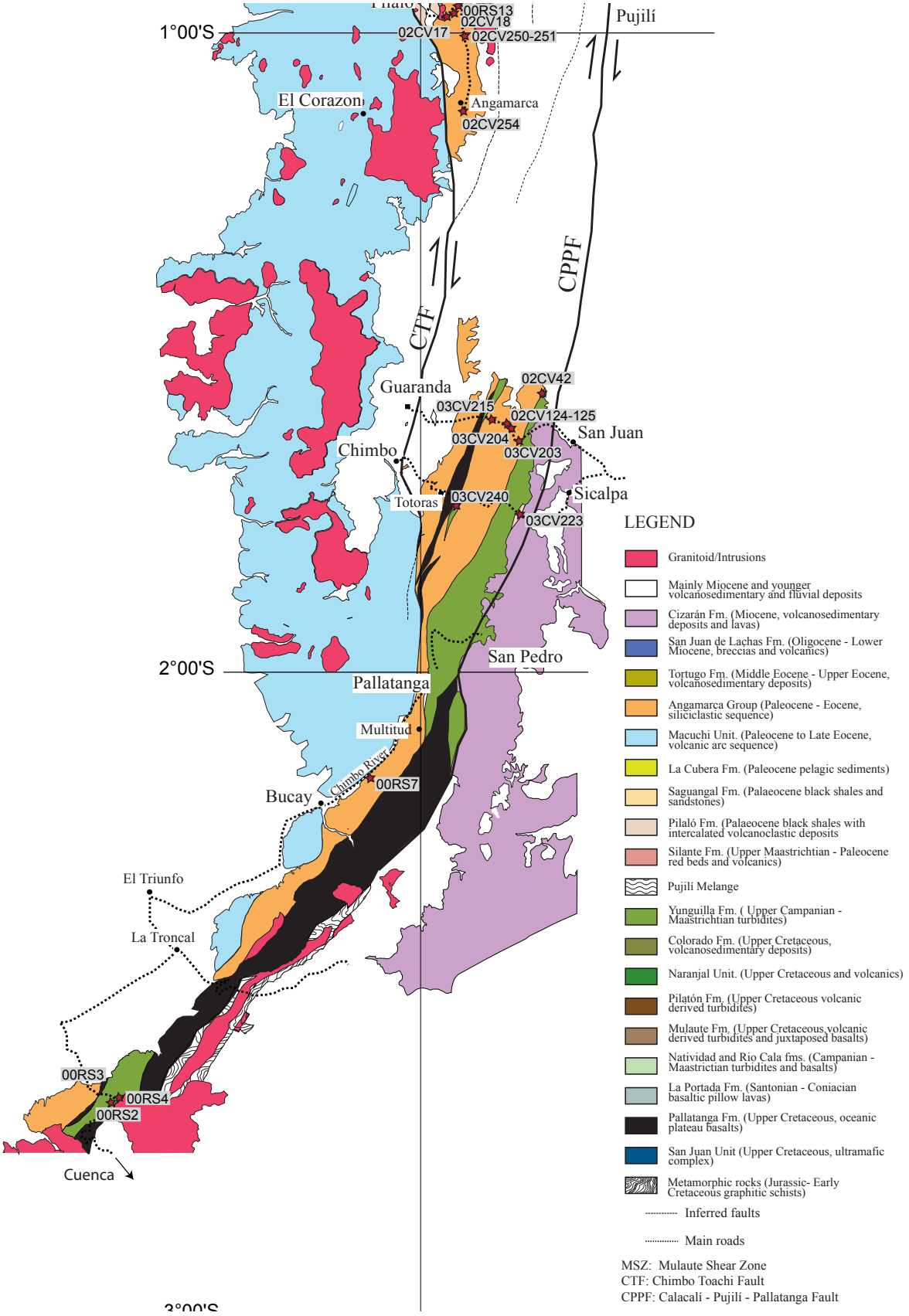

Fig. 3.1. Location of the samples for provenance analysis.

Their presence may be correlated with the shallow continental crust (often with sedimentary

cover) in the source area. Similarly, the mineralogical "maturity" of the heavy mineral assemblages of sandstones is quantitatively defined by a proposed zircon-tourmaline-rutile (ZTR) index (Hubert, 1962). The ZTR index is the percentage of the combined zircon, tourmaline, and rutile grains among the transparent, non micaceous, detrital heavy minerals. Because of their high mechanical and chemical stability, zircon, tourmaline, and rutile are concentrated with quartz plus chert and metaquartzite rock fragments as sandstones become progressively more quartzose.

Commonly occurring metamorphic minerals include, in order of increasing metamorphic grade, pumpellyite (low grade), epidote, clinozoisite, zoisite, chloritoid (medium grade), and amphibole, kyanite, sillimanite and staurolite (high grade). Garnet may be derived from both medium and high grade metamorphic source rocks, depending on the mineralogy of the protolith. A metamorphic assemblage may indicate that the source region was composed of continental crust, if ZTR minerals accompany it. Phyllosilicates including muscovite, biotite and chlorite are also indicative of a granitic and/or metamorphic source; however, their concentration is highly unpredictable, as it depends on the hydrodynamic behavior of the grains. Therefore, micaceous minerals are only estimated qualitatively. Metamorphic minerals such as the epidote group (epidote, clinozoisite, zoisite), may be derived from a source region composed of hydrothermally altered and/or metamorphosed basic igneous rocks, when they are associated with an assemblage of pyroxenes.

Clinopyroxenes (diopside-augite), orthopyroxenes, and green-brown hornblende are abundant in heavy mineral suites derived from a volcanic source (e.g. Nechaev and Ishpording, 1993), and the presence of hypersthene may also point to the presence of granites and syenites. Diopside may be indicative of alkaline basalts, andesites and some sub-alkaline rocks, but its presence in regional and contact metamorphic Ca-rich rocks (skarns) is also documented.

The rocks of the Eastern Cordillera represent the late Cretaceous continental margin of Ecuador (see Chapter 1). The cordillera is composed of metamorphic and granitic rocks of ages older than the Early Cretaceous. Therefore, the earliest time of arrival of metamorphic and/or granitic derived minerals to the allochthonous blocks can be used to estimate their time of accretion against the continental margin. Conversely, the absence of these heavy mineral associations within sedimentary rocks of the allochthonous blocks may indicate that they were still isolated from continental detrital input. However, heavy minerals should not be used as absolute evidence to reconstruct source changes, and it must be combined with other geological data (e.g. single grain geochemistry, sedimentary facies, etc.).

3.2.2 Results

Hundred fine to medium-grained sandstones were analyzed in this study. One third of the samples, which were mainly volcanoclastic turbidites of the Mulaute, Pilatón and Natividad formations, either did not contain a sufficient number of heavy mineral grains, or the heavy mineral grains were produced by secondary alteration. The results of the heavy minerals analysis are presented

in bar diagrams, which show the heavy mineral composition of individual samples. Analytical procedures are indicated in the appendix 3.

3.2.2.1 Pilatón Formation

The samples analyzed in the Pilatón Formation correspond to medium-grained turbiditic sandstones, collected in the Alóag- Santo Domingo road (samples 02CV131, 00RS25) and the Ibarra – Lita road sections (sample 02CV72). Samples collected along the Calacalí – Pacto road did not yield heavy minerals because the sandstones were strongly silicified and weathered. The heavy mineral assemblages from both sections have similar heavy mineral compositions (Fig. 3.2). These assemblages are dominated by clinopyroxenes (98%), with minor amounts of chromium spinel (<1%). This association strongly indicates a basaltic volcanic source for the Pilatón Formation; with no minerals derived from metamorphic rocks or those typical from granitoid rich, continental crust.

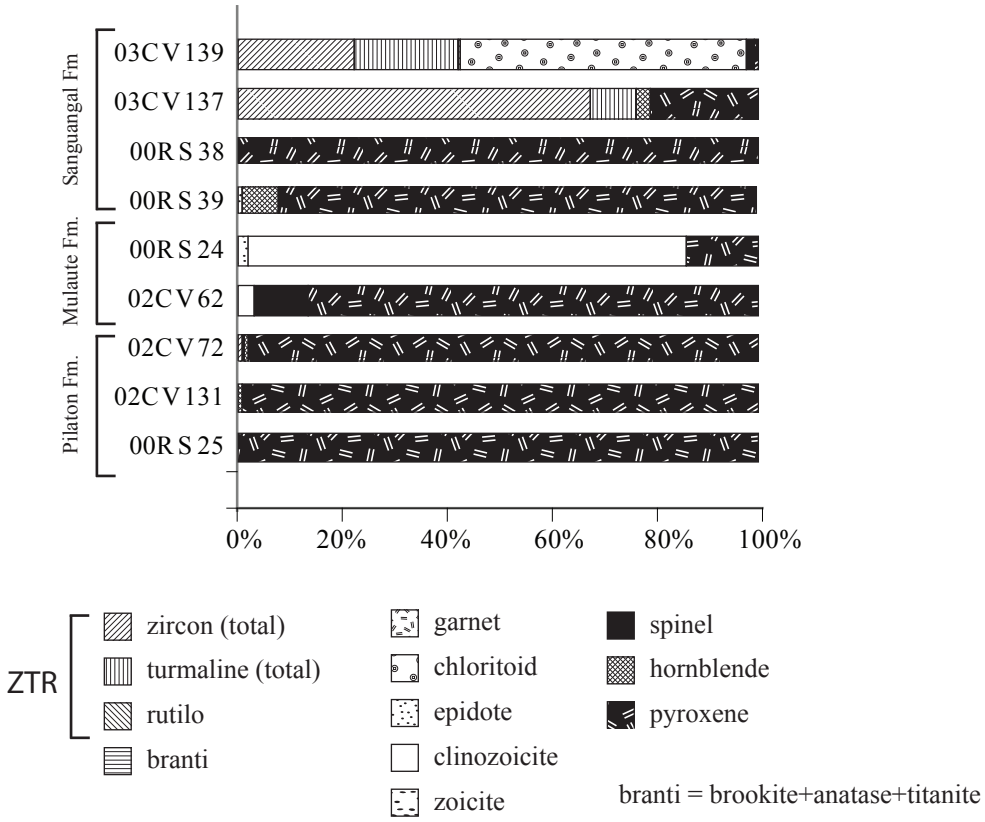

Fig. 3.2: Heavy minerals assemblages from Pilatón, Mulaute and Sanguangal formations.

3.2.1.2 Mulaute Formation

Sample 02CV62 is a medium-grained turbiditic sandstone, collected in the Calacalí – Pacto road Fig. 3.1), near to the contact with the overlying Pilatón Formation. The HM assemblages (Fig. 3.2) include pyroxenes (~86%), chromium spinel (11%) and minor amounts of epidote (4%). Sample 00RS24 was collected in the Alóag – Santo Domingo road, west of la Esperie Batholith

(Fig. 3.1). A majority of HM from this sample (82%) belong to the epidote group (epidote, clinozoicite), which are interpreted as being authigenic, and may be derived from hydrothermal metamorphism of the sedimentary rocks of the Mulaute Formation. Pyroxene occurs as a minor component (< 15%). Similar to the Pilatón Formation, the HM data indicate that turbidites of the Mulaute Formation were derived from of a basaltic volcanic source.

3.2.2.3 Yunguilla Formation

We analyzed samples of the Yunguilla Formation in different regions of the Western Cordillera, which spanned from northwest of Quito, to the latitude of Cuenca. In general, heavy mineral assemblages of the mapped Yunguilla Formation are variable along the Western Cordillera (Fig. 3.3), which may reflect either along-strike variations in the original source regions, or that most of what is mapped as the Yunguilla Formation is actually composed of more than one sedimentary formation.

Samples 00RS33 and 02CV51 are medium grained turbiditic sandstones collected from a slice of the mapped Yunguilla Formation, which is in tectonic contact with the Silante Formation along the Calacalí – Pacto road (Fig. 3.1). Sample 02CV42 was collected from a faulted slice of the Yunguilla Formation in the central part of the Western Cordillera (Guaranda – San Juan road section, Fig. 3.1). The HM association of these samples is dominated by 44 to 57% of ZTR. Among the metamorphic minerals, garnet is the most abundant (23-46%). The metamorphic HM assemblage includes epidote, and minor amounts of chloritoid. Volcanic derived minerals (chromium spinel, hornblende and pyroxene) are also present (~23%).

Sandstone sample 04CV333 was collected at the eastern part of the Alambi River, where it forms part of a deformed, faulted block of thin bedded turbidites of the Yunguilla Formation, close to a tectonic contact with the Pilaló Formation (Figure. 3.1). Only a few rounded crystals of zircon were detected, and therefore the sample is not represented in Figure 3.2. The deficiency of heavy minerals may be due to the very fine grain size of the turbidites, suggesting that the denser grains probably settled earlier in more proximal sites. Therefore, the sample may represent a distal part of the turbiditic fan, from which the Yunguilla Fm. was deposited.

Samples 00RS4 and 00RS2 were collected from turbiditic beds of the Yunguilla Formation, in a tectonic slice juxtaposed with the Pallatanga Formation, exposed in the southern part of the Western Cordillera (Cuenca – La Troncal road section, Fig. 3.1). Sample 00RS4 contains abundant ZTR group minerals (55%), similar to the analyzed samples from northern areas, although the amounts of pyroxene and hornblende is greater (35%). The HM assemblage in sample 00RS2 is different because pyroxenes and brown hornblendes (50%) dominate over smaller amounts of zircon (6%) and garnet (42%), which suggests that both samples were derived from a region with a mixed metamorphic, granitic and volcanic source.

For comparison, we analyzed one sample of the Yunguilla Formation (sample WW3311) in the Cumbe area, south of the studied area. At this locality, the Yunguilla Formation comprises over 1.5 km of strata adjacent to the Eastern Cordillera and is unconformably overlain by the

Paleocene Sacapalca Formation (Pratt et al., 1997). The heavy minerals host a significant ZTR assemblage (82%), with minor amounts of brookite, anatase and titanite (~5%). Garnet and epidote represent ~13% (Fig. 3.2). This assemblage suggests that the detrital material of the Yunguilla basin that is currently exposed in southern Ecuador was predominantly derived from erosion of granitic rocks and/or metamorphic rocks in the Eastern Cordillera.

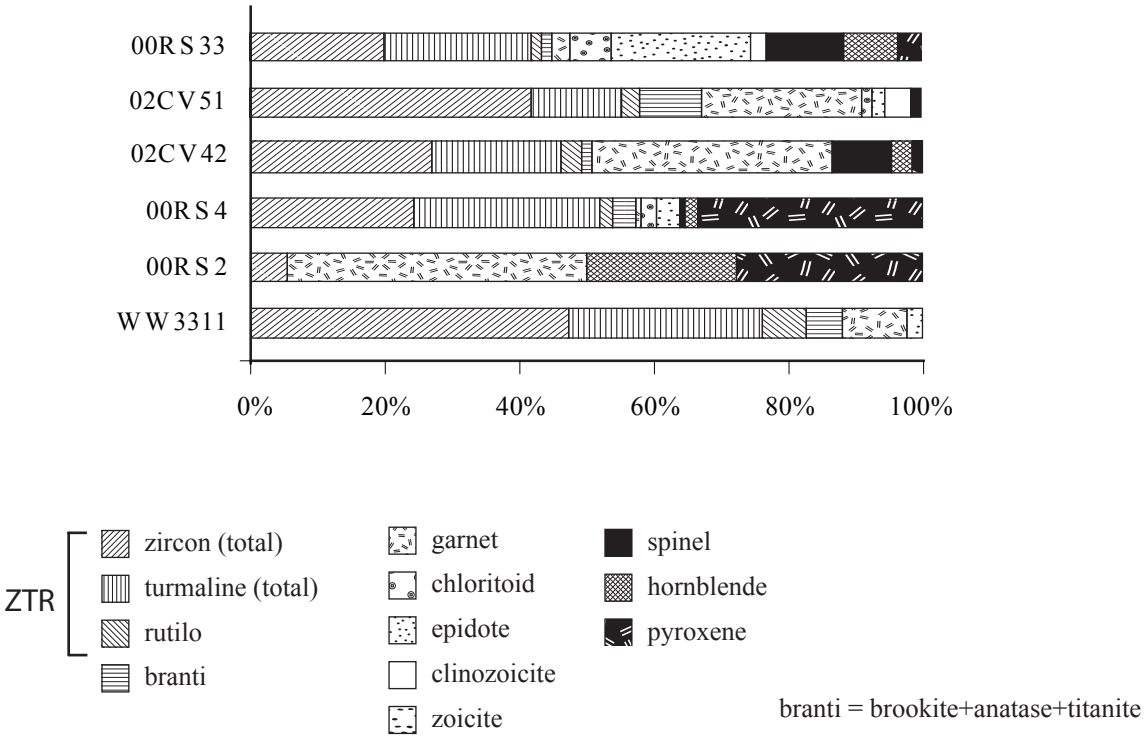

Fig. 3.3: Heavy minerals assemblages from the Yunguilla Formation.

3.2.2.4 Silante Formation

Sample 02CV37 is from a fine-grained quartz arenite, which is intercalated in a sequence of red mudstones that are exposed along the Quito – Chiriboga road (Fig. 3.1). Sample 03CV268 is laminated and coarse-grained fluvial sandstone, located along the Calacalí - Pacto road. Samples 02CV136, 00RS28 and 02CV56 (Fig. 3.1) are medium grained sandstones of the Silante Formation collected along the Alóag – Santo Domingo road. Sample 02CV136 and 00RS28 were collected at the eastern border of the Silante succession, interpreted as the eastern flank of a broad synclinal, near to the contact with the overlying Quaternary volcanic cover. There is not a significant variation within the heavy minerals assemblages (Fig. 3.4). The HM are dominated by variable amounts of brown hornblende (25- 90%) and diopsidic augite (10-95%), and minor amounts of tourmaline and epidote (<4%). Sample 02CV136 includes acicular euhedral crystals of zircon (< 2%) of supposed volcanic origin. In all samples, epidote and garnet only occur in minor amounts (<2%). The presence of brown hornblende of possibly volcanic origin, together with clinopyroxenes and euhedral zircons indicate a coeval andesitic volcanic source.

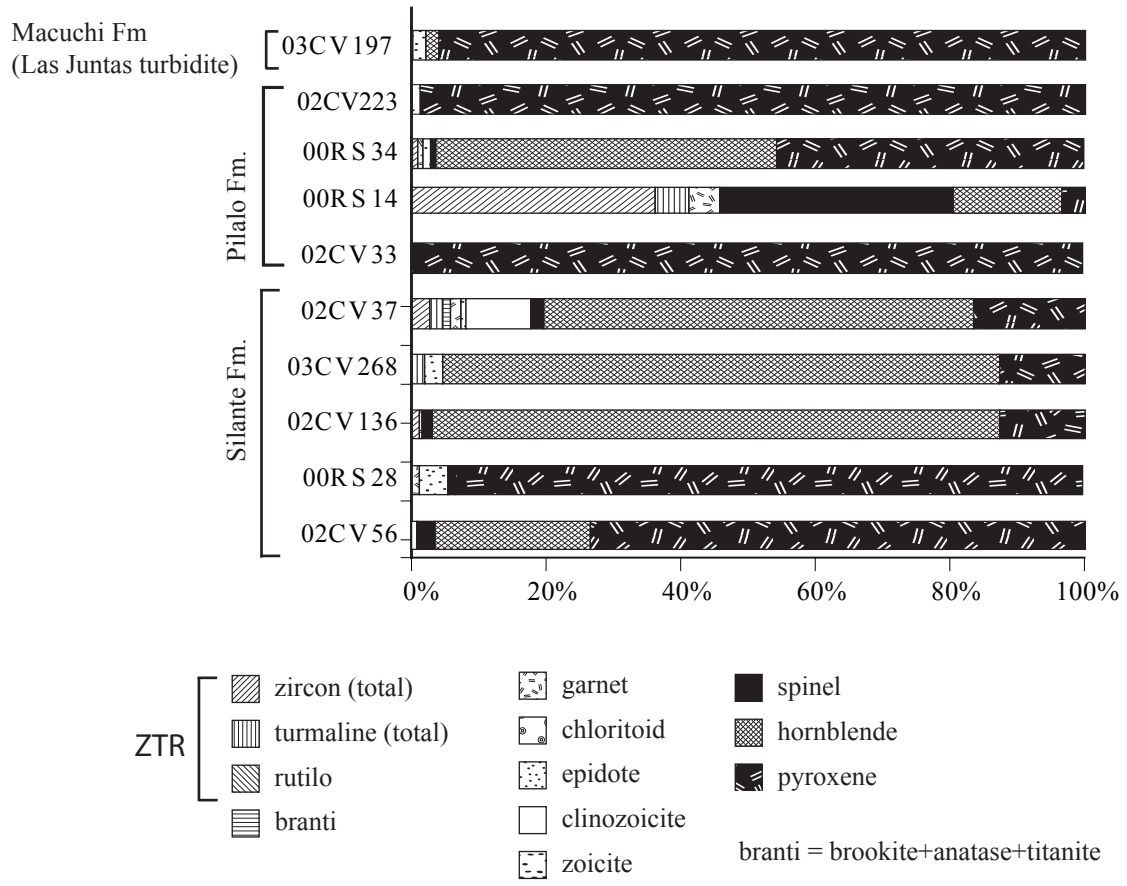

Fig. 3.4: Heavy minerals assemblages from the Silante, Pilaló and Macuchi (Las Juntas turbidite) formations.

3.2.2.5 Pilaló Formation

Sample 00RS14 is a medium-grained sandstone collected along the Latacunga – La Maná road, close to the tectonic contact with volcanic rocks of the Macuchi Unit (Fig. 3.1). The HM assemblage from this sample is poor (Fig. 3.4) because it includes few crystals of euhedral and acicular zircons, with minor amounts of alteration minerals (e.g. pumpellyite, chlorite). The presence of acicular euhedral zircons of possibly volcanic origin may indicate that the sandstone represent reworked tuffaceous material, which is also suggested by glass fragments observed in the thin section of the analyzed sandstone. Sample 02CV11 was collected from an upper level of the Pilaló Formation, and also hosts a small number of heavy minerals, including, brookite, pyroxene, diagenetic apatite and chlorite. The number of heavy minerals recovered from this sample was too small to represent in Figure 3.3. However, the association may indicative a volcanic rock source. The HM assemblage of a sandstone sample in the Alambi River section (sample 03CV309; Fig. 3.1) includes apatite and few euhedral zircon crystals. Similar to sample 00RS14, the HM association of this sample, most likely mirrors reworked tuffaceous material transported to the Pilaló Basin.

Sample 02CV33 is a medium-grained sandstone collected from a tectonic slice in the Quito

– Chiriboga road section, which was previously mapped as Yunguilla Formation (see BGS-CODIGEM Western Cordillera Map, 0°- 1° S). However, heavy minerals assemblages (Fig. 3.4) are composed exclusively of diopsidic augites, indicating that the sediments were possibly derived from a volcanic source. In addition, Hughes and Bermudez (1997) reported sandstones containing red siltstones clasts, a feature that is frequently observed in the Pilaló Formation elsewhere.

Sample 00RS34 is a medium-grained sandstone, located in a fault-bounded block mapped as the Yunguilla Formation on the Calacalí – Pacto road (Fig. 3.1). The heavy minerals associated consist of amphiboles (50%), pyroxenes (46%) and very few euhedral zircons (1%), which indicate a dominantly andesitic volcanic source rock. This result is completely different from the previously described samples of the Yunguilla Formation, which were sampled from the same section (samples 00RS33 and 02CV51) and therefore the sample was assign to the Pilaló Formation, interpretation that is also supported by the single grain geochemical data (see below).

Sample 02CV223 comes from a fault block, which has previously assigned to the Yunguilla Formation (e.g. McCourt et al., 1997) in the Guaranda – Riobamba road (Fig. 3.1). The sample was collected in a tectonized zone close to the Pallatanga Fault, at the contact with the Miocene Cizarán Formation. Jaillard et al. (2004) reported a Paleocene age for rocks occurring in this site, which suggests that they are unrelated to the Late Campanian to Maastrichtian Yunguilla Formation. The HM assemblage of sample 02CV223 (Fig. 3.4) is dominated by diopsidic augites (98%), with minor amounts of apatite and epidote (< 2%). These assemblages indicate that this sample was derived from a volcanic source.

3.2.2.6 Saguangal Formation

Sample 00RS38 is a medium-grained sandstone, collected southwest of the town of San Miguel de Los Bancos (Fig. 3.1). The heavy mineral composition is largely dominated by translucent pyroxene crystals (>98%) and secondary alteration minerals (Fig. 3.2), such as chlorite and pumpellyite, which are present in very small quantities (< 2%). Sample 00RS39 is from a coarse-grained sandstone in the Cocaniguas River, southwest of sample 00RS38. Field relationships indicate that this sample belongs to the lowermost part of the Saguangal Formation succession. The HM assemblages are composed of pyroxene (92%), brown hornblende (~7%) and a few epidote grains (<1%).

Two other samples (03CV137 and 03CV139) were taken near to the village of Saguangal. Zircon is the main constituent (68%) in sample 03CV137, some of which are rounded, indicating that they may have been reworked several times. However, some zircons are also euhedral, suggesting they may be derived from coeval volcanic activity (see LA-ICPMS zircon ages presented later in this chapter). Tourmaline grains represent less than 10%, whereas pyroxene and hornblende occur in approximately 23% of the total assemblage. Sample 03CV139 was taken from a higher level in the stratigraphic succession, very close to the mapped Mulaute

Shear Zone. The sample contains ~55% of chloritoid, at the expense of zircon, pyroxene and hornblende. The presence of chloritoid does not reflect the composition of the source rocks; instead, we suggest that it formed during low to medium-grade metamorphism of the Saguangal Formation, which was possibly related to activity along the Mulaute shear zone.

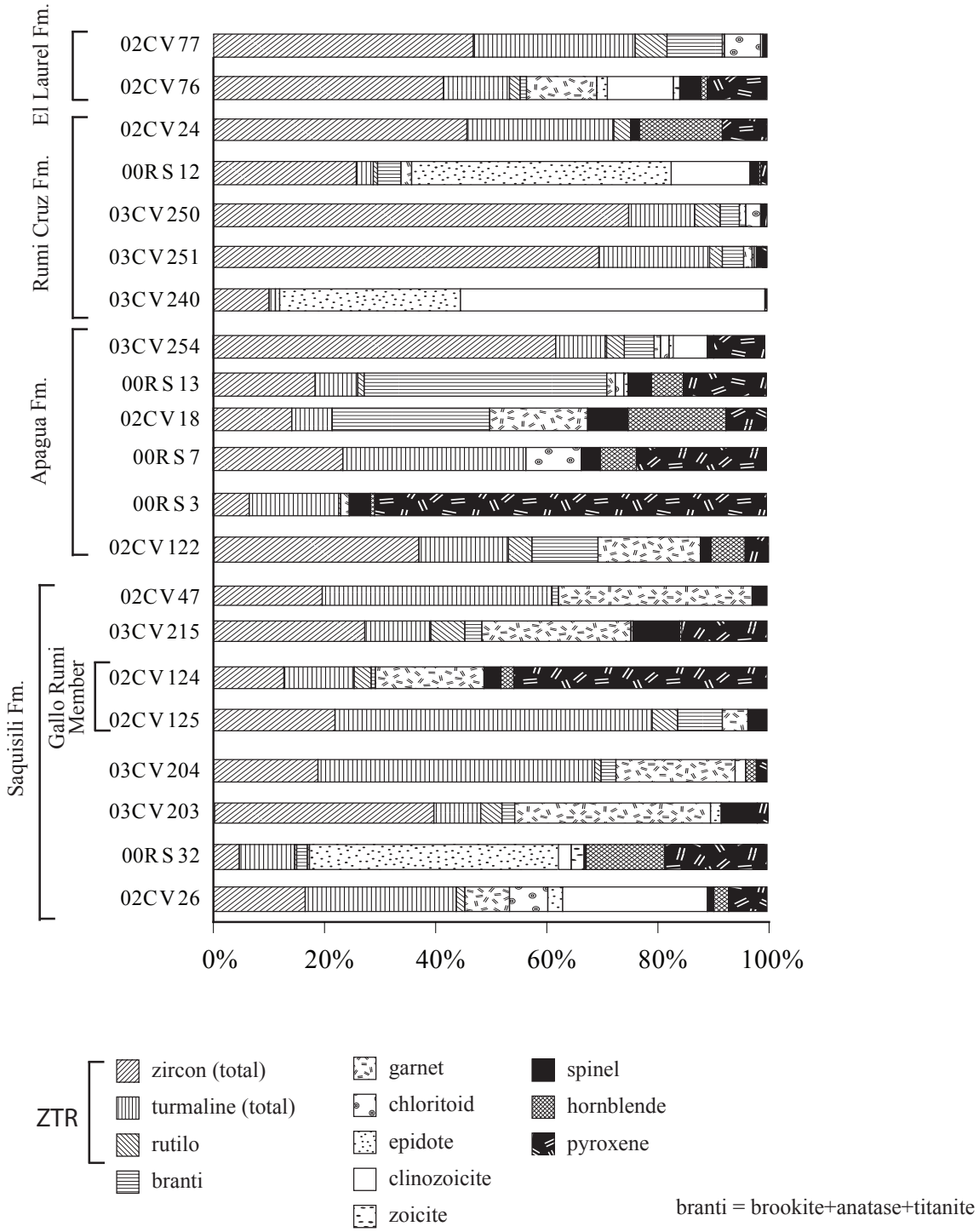

Fig. 3.5: Heavy minerals assemblages of the Angamarca Group.

3.2.2.7 Angamarca Group

Saquisilí Formation

Samples of the Saquisilí Formation were collected in the type locality near the village of Saquisilí, and along the Riobamba to Guaranda road. In the type locality, the formation also occurs as metric blocks within the Pujilí Melange. HM analysis of fine-grained turbidites in the Saquisilí area (samples 00RS32 and 02CV26), contain ZTR minerals ranging between 15 to 45% of the total assemblage. Metamorphic derived minerals, including garnet (colourless), epidote and chloritoid, represent ~45% (Fig. 3.5), whereas pyroxene and hornblende are less abundant (10 - 35%).

Four other samples (03CV203, 03CV204, 03CV215, 02CV47) were collected at different stratigraphic levels within the formation in the Riobamba – Guaranda section. Sample 03CV203 was collected close to the contact with the underlying Yunguilla Formation, whereas sample 02CV47 is from the top of the succession. Additionally, we determined the HM content from the matrix of two conglomerates (02CV124, 02CV125) of the Gallo Rumi Member of the Saquisilí Formation, exposed along the Riobamba – Guaranda road section (Fig. 3.1). The HM assemblages (Fig. 3.5) in all samples are dominated by the ZTR group minerals (52-70%), whereas BRANTI minerals (brookite, anatase and titanite) account for 4%, and metamorphic minerals, including garnet and epidote, comprise ~40% of the total HM assemblages (Fig. 3.5). The geochemical analysis in garnet (see below) indicates that it can be derived from metamorphic rocks. Pyroxene and hornblende are of minor importance (5-18%). The presence of chromium spinel (~8%) suggests that a mafic to ultramafic source may contributed to the detritus of the Saquisilí Formation.

Apagua Formation

The Apagua Fm. was sampled along the Latacunga – La Maná road section. Samples 02CV17, 02CV18, 00RS13 and 03CV254 were collected at different levels within the Apagua Formation, with sample 02CV17 at the base of the succession, near to the stratigraphic contact with the underlying Unacota Formation, whereas sample 03CV254 was collected below the contact with the overlying Rumi Cruz Formation (Fig. 3.1).

The HM assemblages are dominated by minerals of the ZTR and BRANTI (Fig. 3.5), with an upwards increase in these group minerals from 50 to 80%, whereas the amounts of pyroxene, hornblende and chromium spinel decrease from 30 to 10%.

Sample 00RS7 was collected in the Chimbo Valley, south of Pallatanga village (Fig. 3.1) from a coarsening upward sequence of turbidites, which stratigraphically overlie volcanic rocks of the Macuchi Unit. The HM assemblage in sample 00RS7 has a similar composition to the samples collected further north. ZTR minerals are the main constituents (56%), with chloritoid representing 10% of the HM assemblage, whereas pyroxene, hornblende and chromium spinel are 34%.

Sample 00RS3 is a medium-grained turbiditic sandstone, collected in the Cuenca – La Troncal road (Fig, 3.1). The HM assemblages are dominated by volcanic-derived minerals (75%), including translucent pyroxene (diopsidic augite), brown hornblende and chromium spinel. Heavy minerals derived from a granitic source, including rounded and euhedral zircons, account for 22%, whereas minerals derived from a metamorphic source represent less than 3% of the total assemblage.

Rumi Cruz Formation

The Rumi Cruz Formation (samples 03CV250, 03CV251, 02CV24, 00RS12) exposed along the Apagua – Angamarca road yields a HM assemblage that indicates an increase in the input of ZTR minerals (92%), compared to the underlying Apagua Formation (Fig. 3.5). The modal percentages of metamorphic derived material and minerals of the BRANTI group are less important, with a maximum of ~4 % of the total assemblage. Few crystals of pyroxene and hornblende were also observed in the HM assemblages, although their abundance account for less than 2%. Sample 03CV240 was collected from a fault bounded slice of red mudstones with intercalated medium-grained sandstones, juxtaposed against the Saquisilí Formation, exposed in the Riobamba – Chimbo road (Fig. 3.1). The analyzed sample is a medium-grained sandstone, intercalated in a red mudstone-dominated sequence. HM assemblages from this sample include epidote and clinozoicite (87%), zircon (11%), whereas garnet accounts for less than 1% of the total HM assemblage.

El Laurel Formation

Samples from the El Laurel Formation were collected from a quarry in the Hualchán area, north of La Carolina village. Two fine-grained sandstones (02CV76 and 02CV77), which are overlain by massive lumaquela limestones of a possible Late Eocene to Oligocene age (Boland et al. 2000), yield large modal percentages of ZTR minerals (55-82%; Fig 3.5), whereas metamorphic derived minerals correspond to 18 - 28% of the total assemblage and include garnet, epidote and chloritoid. BRANTI minerals account for less than 10% of the total HM assemblage.

3.2.2.8 Macuchi Unit (Las Juntas Turbidites)

We analyzed the heavy mineral assemblages of a Late Eocene turbiditic sequence, located at La Union del Toachi (sample 03CV197) in the Alóag – Santo Domingo road (Fig. 3.1). The turbidites are intercalated by massive andesites of the Macuchi Unit. The heavy mineral assemblages (Fig 3.4) include clinopyroxenes (95%), with minor epidote and hornblende (5%), suggesting that the source region was dominated with volcanic rocks.

3.3 SINGLE GRAIN GEOCHEMISTRY.

3.3.1 Rationale of the method

The compositions of clinopyroxenes vary according to the chemistry of their host lavas (Nisbet and Pearce, 1977; Schweitzer et al., 1979; Leterrier et al., 1982), because the clinopyroxene composition is directly related to the magma type, and hence the tectonic setting (Le Bas, 1962; Nisbet and Pearce, 1977; Leterrier et al., 1982; Beccaluva et al., 1989). According to Beccaluva et al. (1989), clinopyroxene compositional variability is mostly related to differences in the bulk chemistry of the host basic magmas, and it is only partially due to magmatic fractionation and/or the physical conditions of crystallization.

In the next paragraphs is presented the geochemical composition of the possible source areas of the sedimentary rocks that have been studied in this thesis, which has been compared with the geochemical data obtained from clinopyroxenes recovered from the sedimentary formations. All of the samples were subjected to various degrees of ocean-floor hydrothermal alteration under low- to intermediate-green schist facies conditions (e.g. Aguirre and Atherton, 1987); however, the analyzed clinopyroxenes are fresh without signs of alteration.

Leterrier et al. (1982) proposed a set of tectonic discriminatory diagrams that are based on the chemical composition of recent volcanic rocks that erupted in various tectonic settings. Their proposed discrimination has also been successfully applied to highly altered basalts, where the freshest minerals are clinopyroxenes (e.g. Krawinkel et al., 1999). These diagrams compare the atoms per formula unit (apfu) of major elements within individual clinopyroxene grains. The following procedure of Leterrier et al. (1982) was utilized in this study:

(1) Initially, Ca + Na vs. Ti is used to distinguish between alkali basalts and sub-alkaline basalts (tholeiitic and with calc-alkaline affinity). Their hypothesis is based on the observation that clinopyroxenes from alkali basalts are rich in Ca, Al and Ti, but poor in Si, with respect to clinopyroxenes from tholeiites. The alkali basalts from oceanic or continental intraplate volcanism are enriched in Na and Ti and depleted in Si, with respect to basalts, which erupt above a subduction zone.

(2) A second comparison of Ca with Ti+Cr, discriminates between basalts formed in subduction zones, and basalts formed in divergent margins or intraplate settings. Basalts associated with subduction zones (island arc tholeiites, calc-alkaline and shoshonitic basalts) are depleted in Cr and Ti with respect to basalts, which erupt in distensive tectonic settings (ocean ridges, back-arc basins, continental rifts, oceanic islands).

(3) Finally Al vs. Ti distinguishes between tholeiitic and calc-alkaline magmas. Kushiro (1960) and Le Bas (1962) showed that the Al content of calcic pyroxenes (augite and diopside) increases with decreasing SiO_2 concentration in the magma.

In addition, we determined the trace elements compositions, including rare earth element (REE) compositions of the detrital clinopyroxenes. Trace and rare earth element compositions of volcanic rocks are broadly diagnostic of the tectonic setting in which they formed (e.g.

Rollinson, 1993). For example, an enrichment in LREE (relative to HREE) is regularly found in rocks formed in subduction zones, whereas a depletion of LREE, and flat REE patterns are more indicative of MORB type and mantle-plume related, volcanic rocks.

In order to determine the composition of the clinopyroxene parent magmas, REE compositions of melts in equilibrium with these minerals were calculated using experimentally derived partition coefficients for clinopyroxenes crystallizing in basaltic rocks (Hart and Dunn, 1993). The REE composition of the parent magma provides important information about the tectonic setting in which the source rock formed.

Another important discriminatory parameter utilized in this study is the magnesium number (X_{Mg}), [= $Mg/(Mg+Fe_{tot})$], which can be used as an indicator of differentiation of volcanic rocks (e.g. Roddaz et al. 2002, Pinto et al. 2004). Furthermore, we compared X_{Mg} values with the Al concentration of clinopyroxenes, which is a robust indicator of the degree of differentiation of the clinopyroxene-bearing, volcanic rocks.

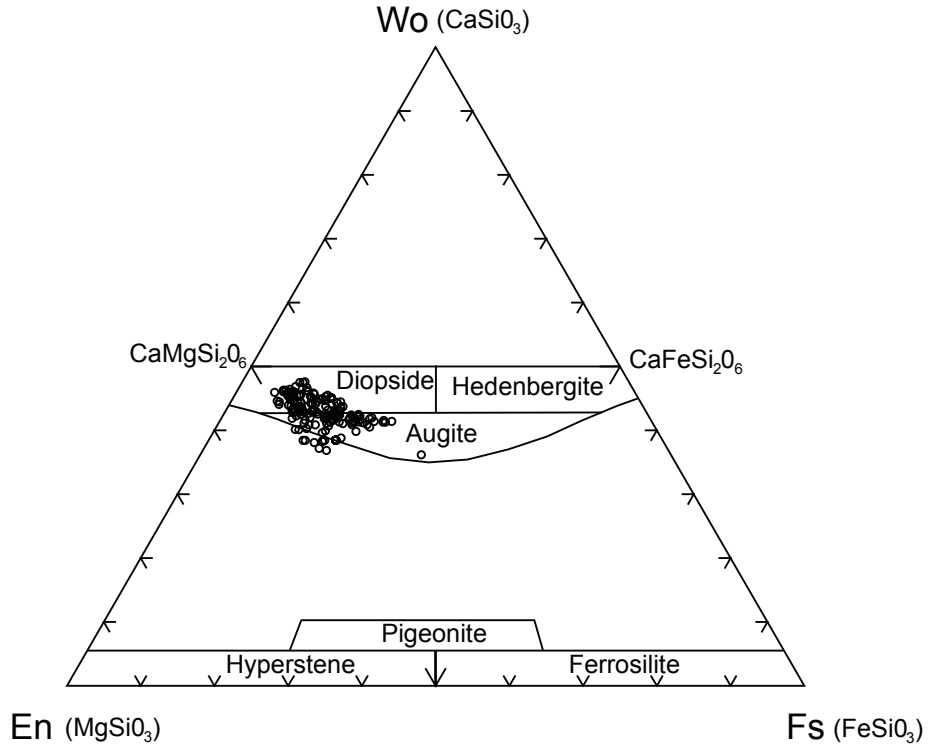

Fig 3.6. Composition of clinopyroxenes (Morimoto, 1988) from the volcanic basement and sedimentary cover of the Pallatanga Block

3.3.2 Results

All analyzed clinopyroxenes were optically homogeneous, and multiple analyses of individual grains indicate that they are chemically homogeneous and lack zoning. Based on this observations, geochemical analyses of detrital clinopyroxenes recovered from sandstones of sedimentary units of the Western Cordillera were used to determine the magmatic affinities of the source

rock regions. Geochemical data of all clinopyroxenes analyzed in this study, indicate that they correspond to calcic clinopyroxenes with diopsidic to augitic compositions, as indicated on the classic wollastonite (Wo) – enstatite (En) – ferrosilite (Fs) diagram (Fig 3.6; Morimoto, 1989).

In order to compare the different sources of the detrital clinopyroxenes, we first describe the single grain geochemistry of clinopyroxenes separated directly from primary volcanic rocks, and then we continue by presenting the single grain geochemistry from the detrital grains. Major and trace elements geochemistry of individual grains are presented in the appendix.

3.3.2.1 Clinopyroxene geochemistry from the volcanic basement

Pallatanga Formation (basalt)

We analyzed clinopyroxenes extracted from a basalt of the Pallatanga Formation (02CV120) in the Guaranda - San Juan road section. The Ca + Na vs. Ti, discriminatory diagram (Fig 3.7), suggests the rock is subalkaline (i.e. tholeiitic or calc-alkaline in composition) field as indicated by relatively low Ti (Cawood, 1983). The clinopyroxenes grains are characterized by distinctly high Cr concentrations (~ 0.028 apfu), and low Ti concentrations. Utilizing the Ca, Ti, Cr and Al concentrations, the discriminatory scheme of Leterrier et al. (1982) suggests the basalts did not erupt above a subduction zone, and are tholeiitic (Fig. 3.7).

Summarizing, basalts of the Pallatanga Formation originated from tholeiitic magmas, which erupted in an intraplate setting, and the primitive nature of the Pallatanga Formation is also evident from the high clinopyroxene X_{Mg} values (0.84-0.89; Fig 3.8). The equilibrium REE composition of the calculated melt from which the clinopyroxenes crystallized shows a slight LREE enrichment, with a $(La/Yb)_N$ value of ~ 2.2 (Fig. 3.9). The calculated melt composition is slightly enriched in REE relative to the whole rock (Fig. 3.9), which may be a result of dilution by olivine in the host rock (Mamberti et al, 2001).

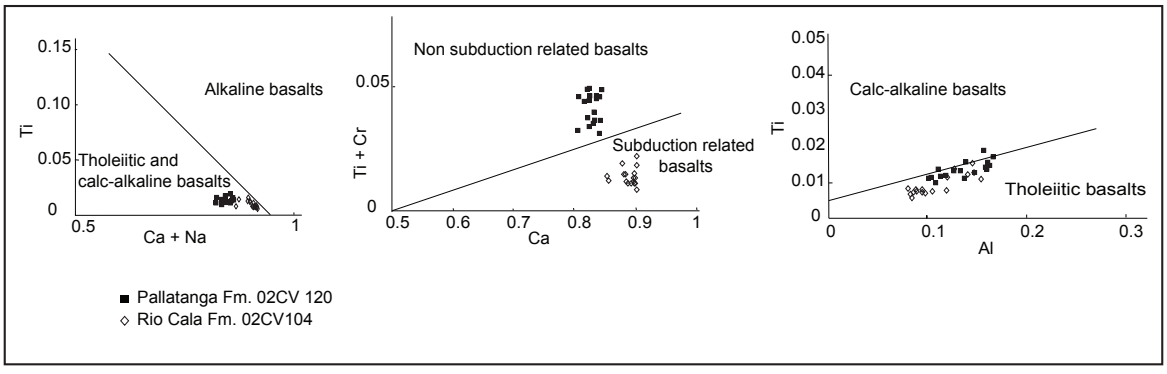

Fig. 3.7 : Discriminatory diagrams (Leterrier et al., 1982) for clinopyroxenes of the Pallatanga and Rio Cala formations.

Rio Cala Formation (basaltic andesite)

Clinopyroxenes from a basaltic andesite of the Rio Cala Formation (sample 02CV104) fall in

the field of tholeiitic or calc-alkaline basalts on the Ca + Na vs. Ti discriminatory diagram (Fig 3.7), as is typical for relatively low Ti values (<0.02 apfu) in sub-alkaline rocks. The calculated melt of the Rio Cala Formation (02CV104) shows a strong enrichment in LREE, with a La/Yb ratio of ~11.6. This sample has anomalously high REE enrichments, which was explained as produced by contamination with a LREE enriched source, possibly an oceanic plateau (Allibon et al., 2005). Similar results were obtained with the whole rock REE geochemistry (see chapter 2). However, the primitive nature of the Rio Cala Formation is evident from the high X_{Mg} values (0.83-0.93), which are the highest X_{Mg} of all of the analyzed samples (Fig 3.8). The clinopyroxene geochemistry of the Rio Cala Formation (Fig. 3.9) is in line with whole-rock geochemistry and isotopic data presented in chapter 2, that also indicate an intraoceanic island arc setting for the Rio Cala Formation.

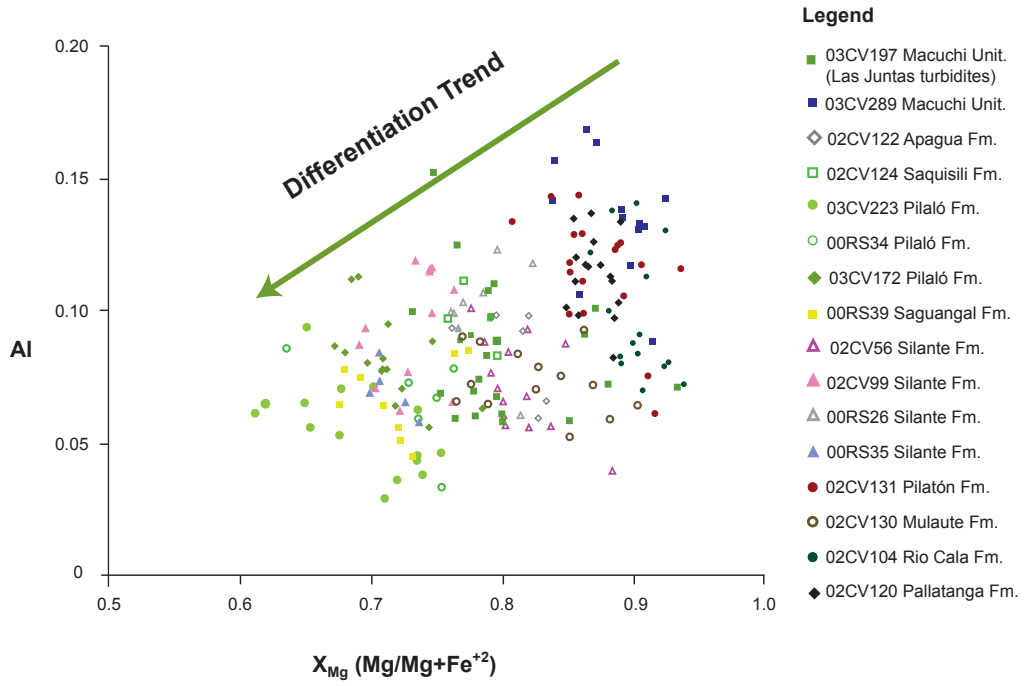

Fig. 3.8. Magnesium Number (X_{Mg}) vs. Al concentrations from clinopyroxenes recovered in sedimentary and volcanic formations of the Western Cordillera. From this graph is possible to observe a general decrease of X_{Mg} from primitive rocks of the Pallatanga and Rio Cala Group towards the more evolved volcanic rocks of the Silante, Pilaló, Angamarca Group, and part of the Macuchi Unit

Mulaute Formation (basalt)

Clinopyroxenes recovered from a basalt juxtaposed against turbidites of the Mulaute Formation in the Alóag – Santo Domingo road (sample O2CV130; UTM: 739121/9962111). The discriminatory scheme of Leterrier et al. (1982) suggests the source rocks of the pyroxenes (Fig 3.10), were tholeiitic, and formed in a subduction zone setting, which can be seen, for example, by the very low Ti content (< 0.008 apfu). The calculated melt in equilibrium with the clinopyroxenes yields a generally flat REE chondrite normalized profile (Fig. 3.9), with

$(La/Yb)_N$ values of ~0.8.

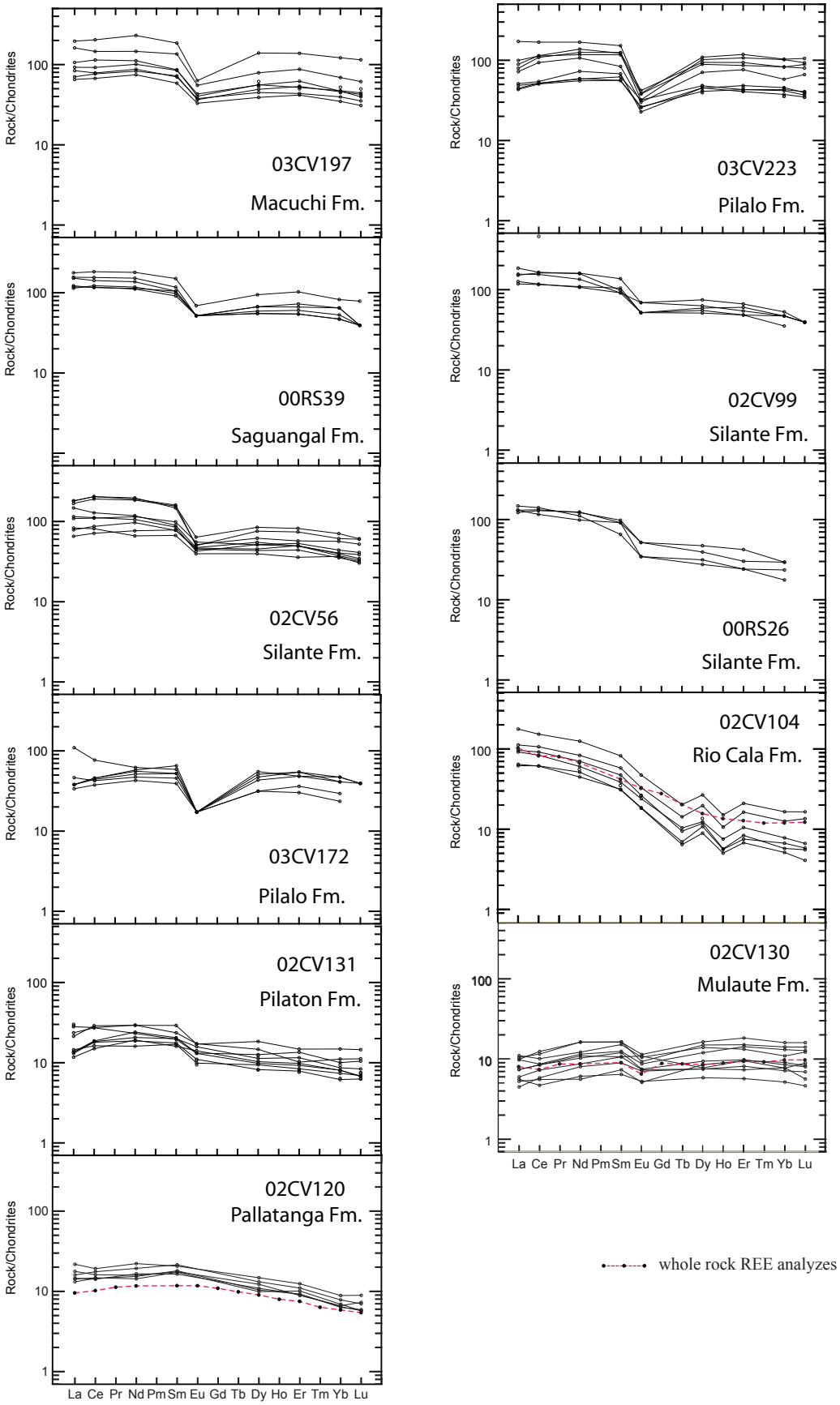

Fig. 3.9 REE plots (normalizing values from Sun and McDonough, 1989) of calculated melts in equilibrium with clinopyroxenes of the Pallatanga, Rio Cala Mulaute, Pilatón, Silante, Pilaló, Saguangal and Macuchi Units. The melt was calculated using partition coefficients obtained experimentally by Hart and Dunn (1993). Clinopyroxenes of the Pallatanga (02CV120), Mulaute (02CV130), Rio Cala (sample 02CV104) and Pilaló (sample 03CV172) formation were extracted directly from the host volcanic rocks, whereas the clinopyroxenes of the Pilatón, Silante, Saguangal, Pilaló and Angamarca formations were obtained from sedimentary rocks. For comparison we included independent whole rock REE analyzes from selected samples.

The primitive nature of the clinopyroxenes, and hence the host basalt, is evident from the high values of X_{Mg} (0.8-0.9) (Fig 3.8).

3.3.2.2 Clinopyroxene geochemistry of the sedimentary rocks

Pilatón Formation

Clinopyroxenes extracted from thick-bedded turbidites of the Pilatón Formation (samples CV131 and CV172) yield low Ti (< 0.02 apfu) and Cr concentrations indicating that the host rock of the clinopyroxenes formed in a subduction zone setting (Fig. 3.10), and a comparison of Al and Ti suggests it had a tholeiitic affinity. The primitive nature of the source is also obvious from the high X_{Mg} values of 0.85- 0.95 (Fig. 3.8), which corroborates the high abundance of Al (~0.15 apfu).

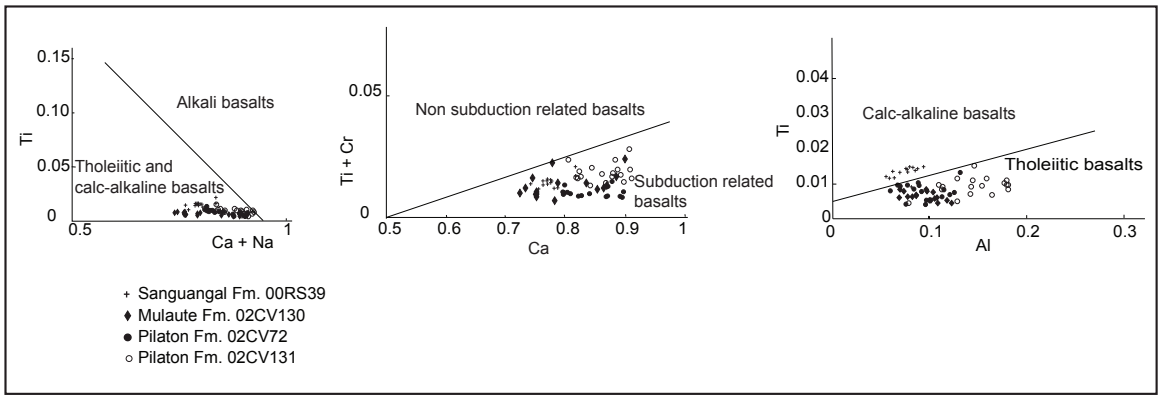

Fig. 3.10. Discriminatory diagrams (Leterrier et al., 1982) for clinopyroxenes of the Pilatón, Mulaute and Saguangal formations

Silante Formation

Clinopyroxenes were extracted from both volcanic and sedimentary rocks of the Silante Formation. A lava flow breccia (00RS35; Fig. 3.1) located near to the contact with the Yunguilla Formation. Sample 02CV56 is a volcanoclastic sandstone derived from a higher stratigraphic level in the succession. Sample 00RS26 is from the matrix of a volcanic breccia exposed in the

Alóag – Santo Domingo road, and sample (02CV99) comes from the matrix of a volcanoclastic conglomerate collected in the Otavalo – Selva Alegre road (Fig. 3.1).

All of the detrital and primary clinopyroxenes plot in the field of subalkaline basalts, (Ti < 0.025 apfu) which formed within a subduction zone setting (Fig 3.11). However, a comparison of Al and Ti does not show a clear distinction between tholeiitic and calc-alkaline affinities, except sample 00RS35, which clearly falls within the tholeiitic field (Fig 3.11). X_{Mg} values lie between 0.7 and 0.85 (Fig 3.8).

Trace element data were obtained for detrital and primary clinopyroxenes from four samples of the Silante Fm. (02CV56, 02CV99, and 00RS26). For all samples, the calculated melt in equilibrium with the clinopyroxenes shows REE enrichments up to 100 times chondritic values (Fig 3.9). Sample 00RS26 shows the strongest LREE enrichments, with the $(La/Yb)_N$ ratios varying between 5.32 (00RS26) and 2.58 (02CV56), which is typical of arc rocks. The geochemistry of clinopyroxenes of the Silante Formation is clearly distinct from rocks of the underlying Rio Cala Group.

The enrichment of LREE (Fig. 3.9) and low Ti values are probably caused by the dehydration of subducted oceanic crust, which release fluids that have high concentrations of REE and low concentrations of Ti. The overall enrichment in the LREE, together with the low to medium values of X_{Mg} and Al, indicates that volcanic rocks of the Silante Formation are more evolved than the Rio Cala Group (e.g. Mulaute, Pilatón, Rio Cala formations).

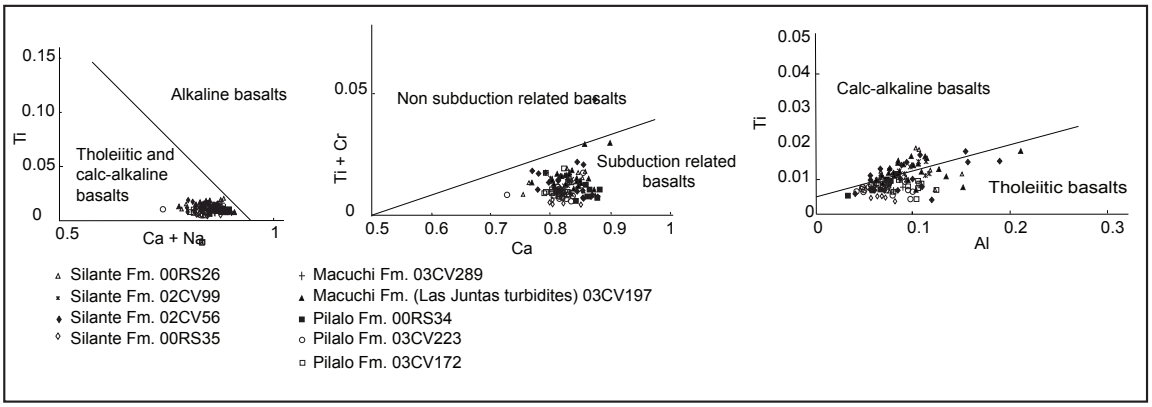

Fig. 3.11. Discriminatory diagrams (Leterrier et al., 1982) for clinopyroxenes of the Silante, Pilaló and Macuchi Units

Pilaló Formation

The analyzed detrital clinopyroxenes were separated from a volcanic sandstone (sample 02CV223), within a tectonized zone of the Pilaló Formation, near to the contact with the Cizarán Formation (Fig. 3.1), and a medium grained sandstone (sample 00RS34) within a fault bounded sliver of the Pilaló Formation on the Calacalí Pacto road. Sample 03CV172 forms part of a faulted block of the Pilaló Formation east of Nono village. Clinopyroxenes were separated from an andesite intercalated with marine sediments. Utilizing the discriminatory criteria of Leterrier

et al. (1982), the clinopyroxenes were derived from a subalkaline volcanic source, although a comparison of Al and Ti does not distinguish between a calc-alkaline or tholeiitic composition for these samples (Fig 3.11). However, the low Al and magnesium numbers (0.62 to 0.65) suggest the source regions were composed of fractionated rocks, which generally supports a calc-alkaline affinity.

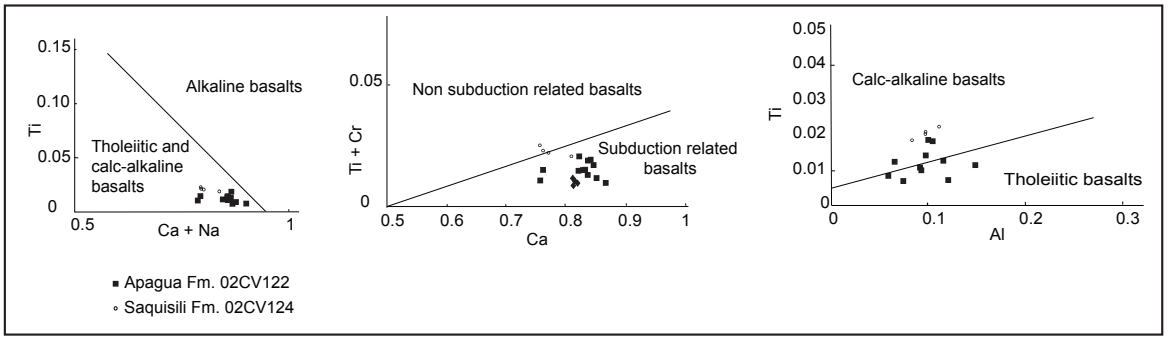

Fig. 3.12. Discriminatory diagrams for detrital clinopyroxenes (Leterrier et al., 1982) of the Angamarca Group

Saguangal Formation

Detrital clinopyroxenes extracted from a coarse-grained sandstone (sample 00RS39), which forms part of the western most Saguangal succession (Fig. 3.1) lie within the calc-alkaline arc field of Leterrier et al. 1982 (Fig 3.10). The evolved nature of the source is also evident from low Al (~0.08 apfu) and X_{Mg} (0.67-0.73) values (Fig. 3.8), as well as the presence of hornblende in the heavy mineral assemblage (Fig 3.2). The calculated equilibrium melt has REE abundance which are approximately one hundred times those of chondrite values, and a $(La/Yb)_N$ ratio of ~2.3 (Fig. 3.9).

Angamarca Group

Saquisilí Formation

Detrital clinopyroxenes recovered from the Gallo Rumi conglomerate member of the Saquisilí Formation (02CV124; Fig. 3.1), yield very low Ti abundance (< 0.02 apfu; Fig 3.12), which according to the discriminatory diagrams of Leterrier et al. (1982) indicate a subduction related environment (Fig 3.12). A comparison of Al and Ti suggests that the source rocks had a calk-alkaline geochemical (Fig 3.12), and X_{Mg} values of the clinopyroxenes range from 0.76 to 0.8 (Fig. 3.9), which overlaps the range obtained from clinopyroxenes of the Silante Formation.

Apagua Formation

The analyzed clinopyroxenes were extracted from turbidites of the Apagua Formation exposed within a narrow faulted block (02CV122), 15 km east of Guaranda. The heavy mineral

assemblage from this sample was composed of a mixed metamorphic and volcanic source (see heavy mineral data). The geochemical composition of the volcanic derived clinopyroxenes from all of the samples of the Apagua Fm. indicate a sub-alkaline affinity (Fig 3.12) and formed in a subduction zone, although we are unable to distinguish between a calc-alkaline and tholeiitic affinity using the criteria of Leterrier et al. (1982). The X_{Mg} values range from 0.76 to 0.84, which are similar to those obtained from clinopyroxenes of the Silante and Macuchi fms. (Las Juntas turbidites, see below), suggesting that the volcanic material found in the Apagua Formation was possibly derived from the partially coeval Macuchi Unit (Las Juntas turbidites). The analyzed sample 03CV197 is part of a turbiditic sequence intercalated in volcanic rocks of the Macuchi Unit. The rock was collected on the Alóag – Santo Domingo road (Fig. 3.1), at the junction of the Pilatón and Toachi rivers (UTM: 727823/9964642). Egüez (1986) proposed that these turbidites are correlatable with the Apagua Formation of central Ecuador. This interpretation was based on lithological similarities and the Late Eocene age of Las Juntas turbidites, similar to the age proposed to the Apagua Formation (Egüez, 1986; Hughes and Bermúdez, 1997).

Detrital clinopyroxenes of Las Juntas turbidites are characterized by low Ti contents. In the Ca + Na vs. Ti they plot in the field defined for a subalkaline source (tholeiitic or calc-alkaline), as it is indicated by the low Ti concentrations (<0.02 apfu). The Ca vs. Ti + Cr discriminatory diagram indicates that the volcanic source of the clinopyroxenes was formed in a subduction-related volcanic arc (Fig 3.11). In the Al vs. Ti diagram the clinopyroxenes cluster in the calc-alkaline field. The evolved nature of the source is evident in the chondrite normalized REE patterns, with the calculated melt in equilibrium with the clinopyroxenes being enriched up to 90 times chondritic values, and clinopyroxene X_{Mg} values between 0.75 to 0.8 (Fig 3.8).

3.3.2.3 Garnet Geochemistry of the Saquisilí Formation

Major elements geochemistry of garnets from the turbiditic sandstones in the Saquisilí Formation (sample 02CV47) are characterized by a high content of almandine (61-77%) and low K content (grossularite <9%), indicating a high-pyrope garnet composition. High-pyrope types indicate derivation from high-grade granulite-facies metamorphic terrains comprising metasediments and/or charnockites (Sabeen et al., 2002). Alternatively, the dominance of the low Ca garnets may also indicate recycling of older sandstones that were subjected to a phase of diagenesis that removed the less stable high-Ca garnets (Morton, 1991).

3.4 U/PB DETRITAL ZIRCON DATING

3.4.1 Results

We have dated with the U/Pb Laser ablation ICPMS method (LA-ICPMS), detrital zircons from the Yunguilla and Saguangal Formation. The results are presented as Concordia diagrams and histograms. Age calculations and plotting were done with ISOPLOT (Ludwig, 2001). The

results are presented on $^{207}Pb/^{235}U$ vs. $^{206}Pb/^{238}U$ Concordia diagrams.

Additionally, zircons extracted from a volcanic sandstone of the Macuchi Unit were analyzed to determine the age of the source rocks. These zircons were analyzed by Mark Fanning, using a SHRIMP ion microprobe available at the Australian National University in Canberra.

The detrital U/Pb zircon ages are grouped within populations, which have similar ages and may share a common source. The analytical procedures and individual U/Pb results are indicated in the appendix.

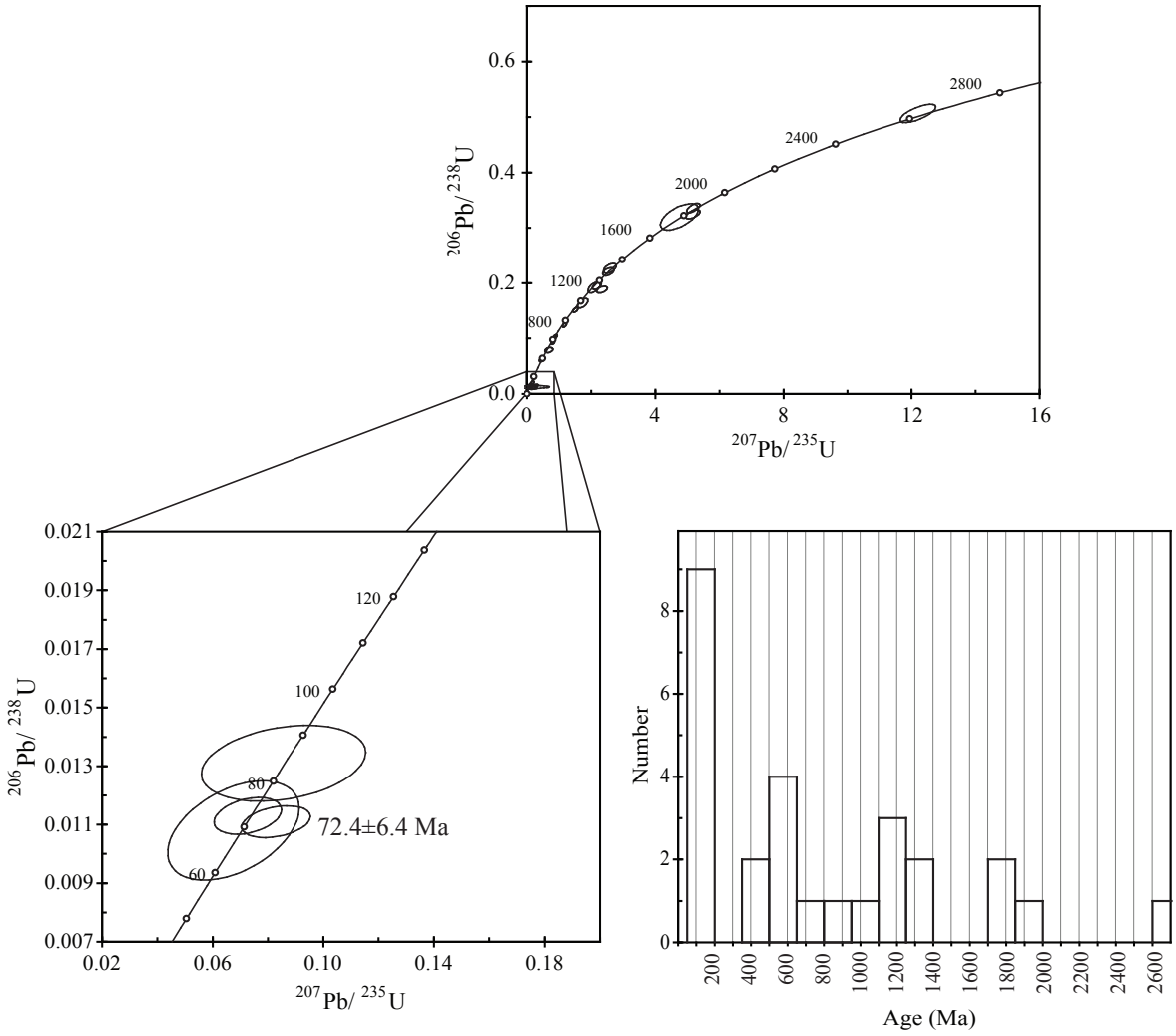

Fig. 3.13. Concordia diagrams and frequency histogram for LA-ICPMS U/Pb detrital zircon dating of the Yunguilla Formation (sample 00RS33).

3.4.1.1 Yunguilla Formation

We analyzed the age of 27 detrital zircons, from one sample of the Yunguilla Formation, which was collected in the Calacalí – Pacto road (sample 00RS33), using the laser ablation ICPMS U/Pb dating method (Fig. 3.13). The results are plotted on Concordia diagrams, together with the age population histogram (Fig. 3.13). Most of the data points are concordant or plot close to the Concordia line.

The ages obtained give important information on the age of the source rocks of the Yunguilla Formation (Fig. 3.13). The zircon ages can be subdivided in 5 populations. Population A1 ranges between 69-100 Ma. Within this population, the three youngest zircons yielded a weighted mean age of 72.4±6.4 Ma (2σ), which is correlatable with the biostratigraphic age reported for the Yunguilla Formation (Jaillard et al., 2004) suggesting the presence of a coeval volcanic source. In addition, population B1 contains zircons of 384-639 Ma, population C1: 755–978 Ma, population D1: 1112–1318 Ma, and population E1: 1789–1867 Ma. A single zircon yielded an age of 2642 Ma, which is the oldest recorded for this sample.

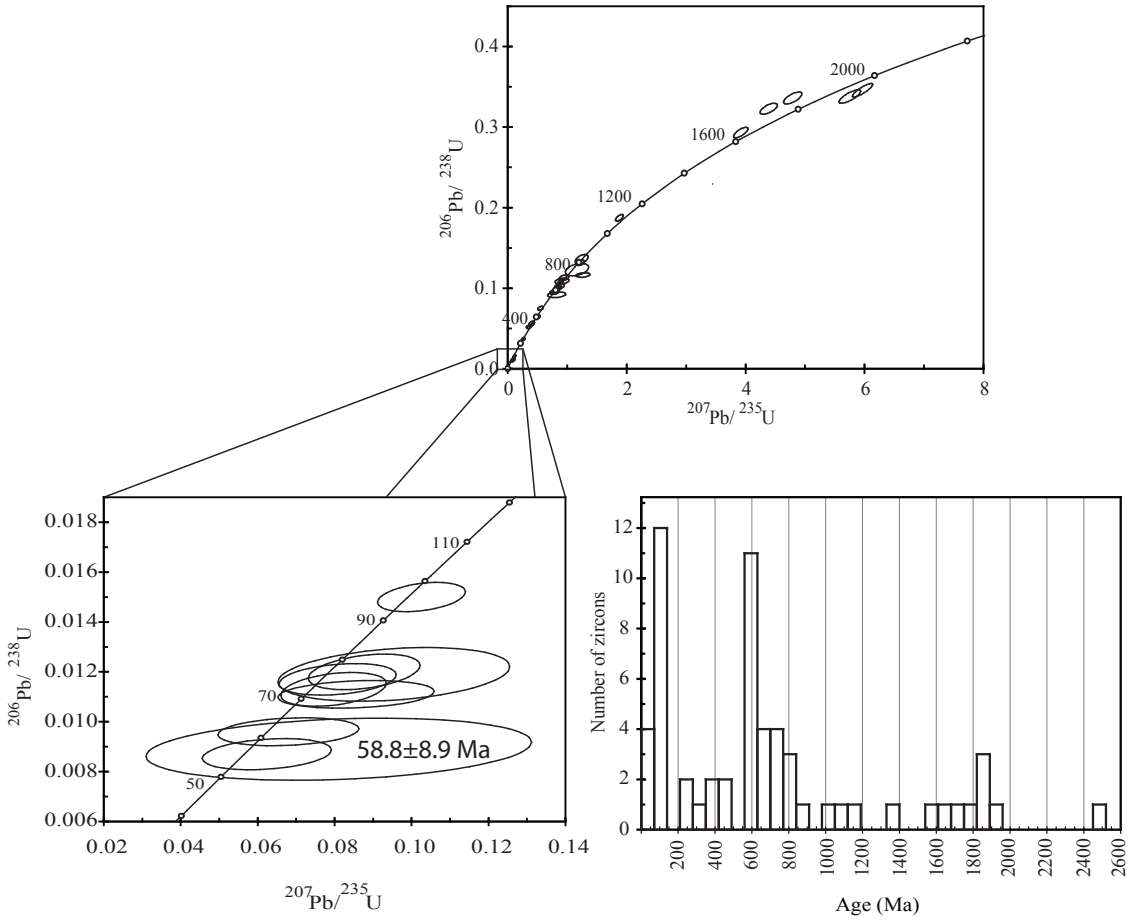

Fig. 3.14. Concordia diagrams and frequency histogram for LA-ICPMS U/Pb detrital zircon dating of the Sanguangal Formation (sample 03CV137).

3.4.1.2 Saguangal Formation

The LA-ICPMS detrital zircon ages from the Saguangal Formation can be divided in five distinctive age populations. Population A2 (56-86 Ma) consists of Campanian to Paleocene grains. Most of these grains are euhedral due to little transport, which may indicate that they were derived from a coeval volcanic source. A weighted age was calculated from the youngest zircons yielded an age of 58.8±8.9 Ma. This age may approximate the stratigraphic age, which is estimated to be Paleocene, as the Sanguangal Fm. is overlying the Campanian – Maastrichtian

Mulaute Formation, and is in turn overlain by the Eocene Tortugo Formation. The zircon ages of population B2 range between 229-478 Ma, population C1 567-881 Ma, population D2 1017-1151 Ma, and the population E2 have the oldest zircons with ages of 1563 to 1914 Ma

3.4.1.3 Macuchi Unit

Five detrital zircon grains recovered from a volcanic sandstone (sample 02CV08) of the Macuchi Unit were dated with the U/Pb SHRIMP method. The analyzed sample was collected in the Latacunga – La Maná road section (UTM: 716283/9902024). The zircon grains are rounded crystals, which possibly indicate multiple recycling. The obtained crystallization ages (Fig. 3.15) range between 538.9±5.8 and 589.9±7.4 (1σ). These ages are very different to the biostratigraphic and radiometric ages obtained for the Macuchi Unit elsewhere, which indicates an Eocene age (e.g. Egüez, 1986; Hughes and Pilatasig, 2002). Therefore the Precambrian – Cambrian zircon ages, represent detrital input of older sources to the Macuchi Unit, most likely located in the South America Craton.

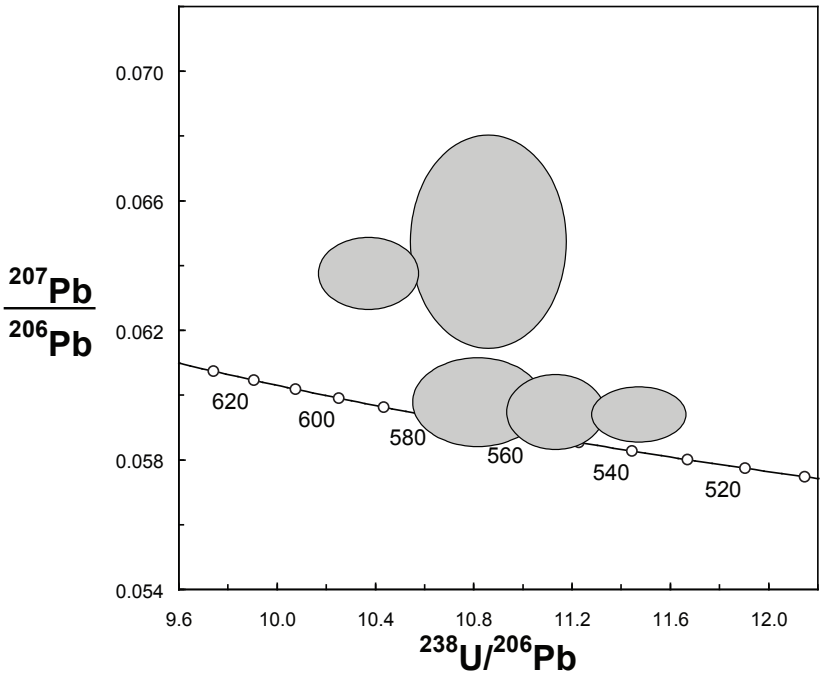

Fig. 3.15. Tera-Wasserburg concordia diagram for U-Pb SHRIMP (zircon) dating of detrital zircons within the Macuchi Unit (sample 02CV08).

3.5 INTERPRETATION

3.5.1 The pre-accretionary Rio Cala arc island arc sequence

Heavy mineral data in the Pilatón, Mulaute, and Natividad Formations of Campanian to Maastrichtian age indicate that these formations were mainly sourced from a volcanic arc

(Table 3.1). These sedimentary formations did not received continental derived material during deposition, which indicates a clear pre-accretionary origin, suggesting that these formations were deposited distant from the continent.

Single grain geochemistry of detrital pyroxenes indicates a primitive volcanic arc source for the Rio Cala Group. This is evidenced by the very low Ti typical of rocks formed in a subduction zone, as well as the low LREE concentrations in the calculated melt from were the clinopyroxenes crystallized. The low REE compositions are typical of primitive island arc rocks, formed in an intraoceanic island arc affinity. The presence of pumpellyite, epidote and chlorite indicates a low-grade submarine metamorphism affecting rocks of the Rio Cala Group. This type of metamorphism occurs by the interaction between volcanic rocks and seawater under a moderate to high thermal gradient (Aguirre and Atherton, 1987), which is also consistent with an intraoceanic island arc setting.

Formation	HM assemblages	Source
El Laurel	ZTR, garnet, with minor hornblende and diopsidic augite	granitic/metamorphic and minor volcanics
Rumi Cruz	ZTR, garnet, with minor hornblende and diopsidic augite	granitic/metamorphic and minor volcanics
Apagua	ZTR, BRANTI, garnet, with minor hornblende and diopsidic augite	granitic/metamorphic and minor volcanics
Saquisilí	ZTR, BRANTI, garnet, with minor hornblende and diopsidic augite	granitic/metamorphic and minor volcanics
Saguangal	ZTR, garnet, with minor hornblende and diopsidic augite	granitic/metamorphic and volcanics
	diopsidic augite, hornblende	andesitic volcanic source
Pilaló	diosidic augite, hornblende, zircon	andesitic volcanic source
Silante	diopsidic augite, hornblende, zircon, minor epidote	andesitic volcanic source
Yunguilla	ZTR, BRANTI, garnet, with minor hornblende and diopsidic augite	granitic/metamorphic and minor volcanics
Mulaute	diopsidic augite, epidote, chormium spinel	basaltic
Pilaton	diopsidic augite, epidote, chormium spinel	basaltic

Table 3.1. Summary of the heavy minerals data. ZTR = zircon, turmaline and rutile. BRANTI=brookite, anatase and titanite.

3.5.2 The syn-collisional Yunguilla Formation

Provenance analysis in the proven occurrences of the Yunguilla Formation indicates that this formation clearly had a continental granitic and metamorphic source, and possibly the Yunguilla Formation received detrital material derived from the reworking of older sedimentary formations, as it is evidenced by the abundant rounded zircons found in the heavy mineral assemblages. This is also confirmed by the single grain laser ablation ICPMS zircon dating, which indicates that

the Yunguilla formation contains detrital material derived from older granitic or metamorphic cratonic provinces.

The Yunguilla Formation has a similar age to the rocks of the Rio Cala Group. However, the provenance and hence the tectonic environment are completely different. The Rio Cala Group was formed in an intraoceanic island arc setting, whereas the Yunguilla Formation was likely deposited proximal to the South American craton as is indicated by the heavy minerals data and the U/Pb LA-ICPMS zircon dating (see discussion below). Other support for this conclusion comes from the tectonic position, the Yunguilla Formation is mostly found in tectonic slices located east of the allochthonous Pallatanga Formation, in southern Ecuador, it unconformably overlies the metamorphic rocks of the Eastern Cordillera.

3.5.3 The post-accretionary formations

3.5.3.1 The Silante volcanic arc

The HM assemblages from sandstones in the Silante Formation are diagnostic for a volcanic source. However, in order to discriminate well this formation from other volcanic edifices, in particular a comparison with the Rio Cala Group is required. The single grain geochemistry in the clinopyroxenes indicates that sediments were sourced mainly from a proximal volcanic unit with a calk-alkaline affinity, which formed in a subduction zone. The geochemistry of the detrital clinopyroxenes of the Silante Formation is more evolved than the underlying sediments and volcanic rocks of the Rio Cala Group; the depositional environment is also very different. The Rio Cala Group was deposited in a deep sea environment, whereas the Silante Formation was formed in a continental system, which points to an important tectonic re-arrangement of the margin occurring before the deposition of the Silante Formation. This event coincided with the accretion of the Pallatanga Block against the continent, which may have produced a westward jump of the subduction zone and the initiation of eastward subduction below the already accreted Pallatanga oceanic plateau units (see chapter five).

The provenance analysis of the Pilaló Formation indicates that this formation was mainly derived from an active volcanic source. This is indicated by the abundance of volcanic derived minerals (e.g. pyroxenes, euhedral zircons, volcanic apatites). Minerals derived from a metamorphic or granitic source were not observed in the HM assemblages. Field relationships indicate that this formation was deposited on top of the Silante Formation. The presence of Silante type clasts in breccias of the Pilaló Formation, as well as the geochemistry of detrital clinopyroxenes, suggests that the volcanic source of the Pilaló Formation was the continental volcanic arc of the Silante Formation. Similarly, geochemical analyses in detrital grains of the Saguangal Formation indicate that this formation was partially derived from an andesitic source of calc-alkaline affinity, which is consistent with an origin from the Silante volcanic arc. However, provenance analysis in the upper part of the Saguangal Formation depicts an

important source change, the heavy mineral assemblages are dominated by detrital grains derived from a granitic and metamorphic source. The U/Pb LA-ICPMS zircon dating yielded different age populations, from Precambrian to Paleocene. The different zircon age populations can be correlated with different sources in the Eastern Cordillera and the South America craton (see below), which contain lithotectonic belts of Paleozoic and Precambrian ages (Litherland et al., 1985).

From detrital zircons a maximum age of 58.8±8.9 (2σ) Ma was calculated for the upper part of the Saguangal Formation. This age is a good approximate to the stratigraphic age, and indicates that the Saguangal Formation was coevally deposited with the latest Maastrichtian to Paleocene Pilaló and Silante Formations.

The data presented imply that during the Paleocene, the Pallatanga Plateau, and the overlying Rio Cala island arc were already accreted to the continental margin. The overlying Saguangal Formation received material derived from the paleo-continental margin, as well as from a coeval volcanic arc (the Silante continental arc). The volcanic arc was established shortly after the accretion of the Pallatanga Block. (~7 Ma).

3.5.3.2 The Angamarca Group

Heavy minerals analysis from the Paleocene Saquisilí Formation indicates that this formation was mainly sourced from a granitic and metamorphic source. Sandstone framework modal analysis (Jaillard et al., 2004) suggests a provenance from a recycled orogen where sedimentary and volcanic rocks were in process of uplift and erosion. The heavy minerals also record a progressive increase of ZTR minerals derived from a granitic source in the Angamarca succession, which may reflect the uplift and erosion of the continental margin, exposing the root of the Eastern Cordillera. The uplift and erosion of the source regions may be explained by the accretion of the Pallatanga Blocks and the successive deformation of the continental margin (Spikings et al., 2001; Jaillard et al., 2004).

With respect to detrital content, there are important differences between the Paleocene sedimentary sequences. For instance, the Saquisilí Formation was likely derived from a metamorphic source, whereas the coeval Pilaló Formation was derived from a volcanic source. These data suggests that the Saquisilí Formation was part of a turbiditic fan formed adjacent to the Eastern Cordillera, whereas the Pilaló Formation was formed adjacent to an active volcanic arc of calc-alkaline composition that may correspond to the Silante or Macuchi volcanic arc.

Provenance analysis in the Eocene sediments of the Apagua Formation that are directly overlying the Unacota Formation in the La Maná – Latacunga road show a gradual upward increase of minerals derived from a granitic and metamorphic sources, which is consistent with a source in the Eastern Cordillera. However, the presence of important amounts of volcanic derived minerals of this formation, particularly such located south of the Pallatanga Valley (sample 00RS7, 00RS3) indicates that a volcanic source coevally was active. The close location of a volcanic arc is also indicated by frequent andesitic sills observed within the Apagua

Formation. The arc was likely the Macuchi volcanic arc, which was active at least until the Late Eocene, as it is evident from the Late Eocene age obtained for the Las Juntas turbidites (Egüez, 1986). This interpretation is also corroborated by similar geochemical signatures in clinopyroxenes of the Las Juntas turbidites, Saquisilí and Apagua formations. The Rumi Cruz Formation is conformably overlying the Apagua Formation and depicts an increase in the ZTR group minerals, which indicates that the granitic root of the Eastern Cordillera was uplifted during the deposition of the Rumi Cruz Formation.

The El Laurel Formation has HM assemblages similar to the other formations within the Angamarca Group, being sourced from a granitic and metamorphic source, which similarly suggest a derivation from the Eastern Cordillera.

3.5.3.3 The Macuchi Unit

Heavy mineral data from Late Eocene turbiditic sandstones within the Macuchi Unit are dominated by material derived from a volcanic source. Single grain geochemistry of detrital clinopyroxene indicates a volcanic source of calc-alkaline composition. However, tholeiitic volcanism is also indicated in clinopyroxenes recovered from primary volcanic rocks (see chapter 2), which indicate that both type of volcanic rocks were comprised in the mapped Macuchi Unit.

3.5.4 Age of the source regions

The Rio Cala Group, as it was presented in the previous section, was formed in an active intraoceanic island arc environment. The Campanian to Maastrichtian age of the island arc as is constrained by biostratigraphic data from sediments of this group (e.g. Natividad Fm), indicates a Campanian to Maastrichtian age. Similarly, island arc volcanics of the San Lorenzo Formation from the coastal region have been dated at 72 Ma (Lebrat et al., 1987). In addition, Luzieux et al. (2006) reported middle-late Campanian ages for the island arc volcanoclastic sediments of the Cayo Formation.

The detrital zircons of the Yunguilla Formation reveal at least five different age populations. The youngest zircons yielded a weighted mean age of 72.4±6.4 Ma (2σ), presumably derived from the coeval Rio Cala island arc. This imprint to the Yunguilla basin was possible, because the Rio Cala arc was approaching from the west to the forearc. The zircons dated at 384– 639 Ma overlap ages reported in Paleozoic rocks of the Eastern Cordillera. Zircon ages of 755 to 978 can be correlated to Pan-African geochronological belts of the interior of the South American Craton (e.g. Litherland et al., 1985). Population D2 (1112–1318 Ma) may correlate with the Sunsas orogeny dated at 1000 Ma (Litherland et al. 1985). A notable equivalent of such source rocks lies in southern Colombia, where the Garzón Granulitic Belt is interpreted to represent an extension of the Sunsas Belt. The age of population E2 (1789–1867 Ma) indicate that the zircons were possibly derived from the Rio Negro – Juruena belt, described by Colombo et al.

(1999).

The Saguangal Formation unconformably overlies the allochthonous island arc sequence of the Rio Cala Group. Therefore, the dated presence of continental derived material within the Saguangal Formation provides important information for the time of collision of the allochthonous blocks. The detrital zircon ages obtained from the Saguangal Formation partially overlap the zircon age populations of the Yunguilla Formation (Fig. 3.13), which may indicate similar sources, or alternatively that the Saguangal Basin partially received recycled material from the Yunguilla Formation. Similar to the Yunguilla Formation, detrital zircons of the Saguangal Formation can be related to potential sources within belts of Paleozoic or Precambrian age in the interior of the South American Continent. The zircon ages of the Saguangal Formation of population B2 (229-478 Ma) partly overlap the ages reported for Paleozoic metamorphic rocks of the Loja Division and Triassic S-type granitoids of the Tres Lagunas Unit of the Eastern Cordillera of Ecuador (Litherland et al., 1994). Population C2 (567-881 Ma) correlates with the core part of the Brazilian orogeny age range, which is correlable to the 800 to 450 Ma Pan African orogeny (Machado and Gauthier, 1996), or the Brazilian mobile belts of Litherland et al. (1985). Population D2 (1017-1151 Ma) overlaps with the Sunsas Province. Population E2 (1563-1914) is the oldest and correlates in age with the Rio Negro - Juruena belt of the Amazonian craton, (e.g. Colombo et al., 1999).

These detrital ages clearly indicate that the Saguangal Formation was sourced from an older terranes forming part of the South American Craton. Two scenarios may explain the presence of the Paleozoic and Precambrian detrital material within the Saguangal Formation: (1) the detrital material was directly supplied from the craton, and (2) the Saguangal formation was derived from the re-erosion of sedimentary and metasedimentary rocks of the Eastern Cordillera. The first hypothesis is highly improbably, because the Eastern Cordillera existed already and presumably formed a barrier between the Amazon Basin and the accreted allochthonous blocks of the forearc (e.g. Ruiz et al., 2004). For the second hypothesis, we must consider the nature of the metasedimentary rocks forming the Eastern Cordillera. Litherland et al. (1994) described the metasedimentary rocks of the Loja Terrane of Paleozoic age, and originally formed in an intracratonic environment, and possibly receiving eroded material from the interior of the craton. Subsequently, these sequences were metamorphosed by a Triassic orogeny (Hall and Calle, 1982; Litherland et al., 1994). Therefore, it appears that the root of the Eastern Cordillera itself formed of material derived from the erosion of older lithotectonic belts that form the South American Craton, and afterwards in a second or third sedimentary cycle they were recycled to the Saguangal Formation.

The presence of detrital zircons of Cambrian age within the Macuchi Unit, strongly suggest that the Macuchi volcanic arc was formed adjacent to an older and most likely granitic source, that may correlate with the Eastern Cordillera similarly as it is proposed for the Yunguilla and Saguangal formations. This is an important argument in favor of the autochthonous origin of the Macuchi arc as it is proposed in chapter 2.

CHAPTER 4: RADIOMETRIC AGES OF THE IGNEOUS ROCKS

Numerous attempts have been made to date the igneous basement of the Western Cordillera, although a majority have failed to acquire accurate ages because of generally low K contents, and a high degree of alteration. The few reported radiometric ages of crystalline rocks of the Western Cordillera (e.g. Egüez, 1986; Wallrabe-Adams, 1990; Van Thournout et al., 1992; Boland et al., 2000) were mainly acquired using the K/Ar method (Table 4.1). Only one study has obtained Sm/Nd ages from the basement sequence. Lapierre et al. (2000) obtained a Sm/Nd internal isochron (amphibole-whole rock-plagioclase) age of 123±13 Ma from a gabbro, which is mapped as part of the San Juan Formation. However, Mamberti et al. (2004) obtained a $^{40}Ar/^{39}Ar$ (amphibole) age of 99.2±1.3 (2σ) Ma for the same rock of the San Juan Formation, although the age spectrum is saddle-shaped, suggesting that excess ^{40}Ar may be present, and the age represents a maximum value.

These contrasting age data suggest that the San Juan Fm. may be inaccurately mapped, and may comprise crystalline rocks with unrelated origins. The Late Cretaceous island arc sequence preserved in the Western Cordillera has not been radiometrically dated, although its potential equivalent in the coastal area (San Lorenzo island arc) yielded a K/Ar age of 72.7±1.4 Ma (Lebrat et al., 1987). Wallrabe-Adams (1990) reported a K/Ar age (whole rock) of 52.7±2.9 for the Silante Formation. Egüez (1986) reports K/Ar ages of 41.6±2.1 (whole rock) for a basaltic andesite and 35.8±1.8 Ma (whole rock) for a basaltic dolerite of the Macuchi Unit along the Latacunga – La Maná road. Similarly, a belt of felsic intrusions of Middle Eocene age (K/Ar method) are reported along the western border of the Western Cordillera (Van Thournout et al., 1992; Hughes and Bermúdez, 1997; Boland et al., 2000), which were coeval with volcanism within the Macuchi Arc, and hence probably represent its intrusive component. An Oligocene K/Ar age of 32.6±1.3 Ma (hornblende) has been obtained from the northern Western Cordillera, in andesites of the San Juan de Lachas Formation (Van Thournout, 1991). The Oligocene volcanism of the northern part of the Western Cordillera has been correlated with the Saraguro volcanic arc of southern Ecuador (e.g. Boland et al., 2000). However, the early Oligocene volcanism on the northern part of the Western Cordillera seems to have occurred still under subaerial conditions, as evidenced by the marine sediments of the El Laurel Formation, whereas the volcanism of the Saraguro Formation occurred in a continental environment. Furthermore, Steinmann (1997) indicated, volcanism of the Saraguro Formation started only during the Late Oligocene (~29.5 Ma)

Despite the paucity in radiometric data, several authors (Hall and Calle, 1982; Egüez, 1986; Van Thournout et al., 1992) proposed that three main phases of volcanism can be identified in the Western Cordillera, which span the Late Cretaceous to Oligocene period: 1) A Late Cretaceous tholeiitic series, 2) Granitoids, shallow level intrusions and basaltic to andesitic lavas of Middle to Late Eocene age, and 3) Andesitic rocks of Oligocene age. Volcanic rocks of Paleocene age are locally found in southern Ecuador (Sacapalca Fm.), and the Paleocene is

normally represented as a hiatus throughout the remaining regions of the Ecuadorian Andes (Hall and Calle, 1982).

Formation/intrusion	Locality	Age	M.P.	Method	Reference
San Juan Fm?.	San Juan	123±13 Ma	amp, w.r., plg.	Sm/Nd*	Lapierre et al., 2000
Saraguro	Santa Isabel	20.3±1.6 Ma	z	ZFT	Hungerbühler, 1997
Tuff intercalated in San Juan de Lachas Fm.	Guayllabamba River	23.5±1.5 Ma	z	ZFT	Boland et al., 2000
Tuff intercalated in San Juan de Lachas Fm.	Guayllabamba River	24.5±3.1 Ma	z	ZFT	Boland et al., 2000
Andesite intruding Pilalo Fm.	Pilalo	24.7±1.2 Ma	w. r.	K/Ar	Egüez, 1986
Condor Samana	East of Pilalo	24.7±1.2 Ma	w. r.	K/Ar	Egüez, 1986
Saraguro	Santa Isabel	26.4±2.6 Ma	z	ZFT	Hungerbühler, 1997
Diorite	San Miguel de los Bancos	28.7±3.2 Ma	hb.	K/Ar	Boland et al., 2000
San Juan de Lachas Fm.	andesite	32.6±1.3 Ma	hb.	K/Ar	Van Thournout, 1991
Granodiorite intruding Tortugo Fm.	Cachaco	34.7±1.7 Ma	hb.	K/Ar	Boland et al., 2000
Saraguro?	South of Saraguro	35.3±0.9 Ma	plg.	K/Ar	Lavenu et al., 1992
Granodiorite intruding Naranjal Fm.	Rio Santiago	35.8±1.8 Ma	hb.	K/Ar	Boland et al., 2000
Macuchi Unit, lava flow	Macuchi	35.8±1.8 Ma	w. r.	K/Ar	Egüez, 1986
San Juan de Lachas Fm.	Guadalupe	36.3±2 Ma	hb.	K/Ar	Boland et al., 2000
Colorado Fm.	Rio Santiago	38.2±1.9 Ma	hb.	K/Ar	Boland et al., 2000
Diorite intruding Mulaute Fm.	Southwest of la Palma	38.6±1.9 Ma	w. r.	K/Ar	Egüez, 1986
Macuchi Unit.	Macuchi	41.6±2.1 Ma	w. r.	K/Ar	Egüez, 1986
Granodiorite intruding Naranjal Fm.	Rio Santiago	41.9±2.1 Ma	bio.	K/Ar	Boland et al., 2000
Granodiorite intruding Naranjal Fm.	Lita	42.2±2.1 Ma	bio.	K/Ar	Boland et al., 2000
Tonalite intruding Naranjal Fm.	Lita	42.4±2.1 Ma	hb.	K/Ar	Boland et al., 2000
Granodiorite intruding Naranjal Fm.	Rio Santiago	44.6±2.2 Ma	hb.	K/Ar	Boland et al., 2000
Lita Gabbro	Lita	45±0.9 Ma	px, hb.	K/Ar	Van Thournout et al., 1992
Granitoid intruding Naranjal Fm.	Rio Guayabamba	47.2±2.4 Ma	hb.	K/Ar	Boland et al., 2000

Diorite intruding the Mulaute Fm.	North of La Palma	48.28±0.55 Ma	hb.	K/Ar	Hughes and Bermudez, 1997
Silante Fm.	West of Nono	52.7±2.9 Ma	w.r.	K/Ar	Wallrabe Adams, 1990
Sacapalca Fm.	Catacocha	66.9±5.8 Ma	z	ZFT	Hungerbühler et al., 2002
Macuchi Unit.	Alluriquin	68±11 Ma	z	ZFT	Spikings et al., 2005
Dacitic block (Pujili Melange)	West of Saquisili	83±2 Ma	hb.	$^{40}Ar/^{39}Ar$	Spikings et al., 2005
Pujili Granite	West of Saquisili	86±1 Ma	w.m.	$^{40}Ar/^{39}Ar$	Spikings et al., 2005
San Juan Fm?.	San Juan	99.2±1.3 Ma	amp.	$^{40}Ar/^{39}Ar$	Mamberti et al., 2004

Tabla 4.1 Radiometric age reported from the Cretaceous to Oligocene in the Western Cordillera. Sm/Nd is a intern isochron. M.P = mineral phase, amp. = amphibole, w.r. = whole rock, z. = zircon, hb. = hornblende, plg. = plagioclase, bio. = biotite, w.m. = white mica, px. = pyroxene.*

4.1 U/Pb SHRIMP ANALYSES

4.1.1 Rationale of the method

The uranium-lead radiometric dating method is one of the most precise radiometric methods, especially when it is applied to zircon ($ZrSiO_4$), although it can also be utilized with other uranium bearing minerals such as titanite, monazite, and baddeleyite. Zircon incorporates uranium and thorium atoms into its crystalline structure, but strongly rejects incompatible lead at the time of formation (Faure, 1986). However, zircon retains radiogenic lead, formed by the decay of uranium and thorium, at temperatures lower than approximately 900°C. Accumulated radiation damage disrupts the ordered, crystalline lattice, rendering partially metamict zones more diffuse, which can potentially result in the loss of radiogenic lead at temperatures significantly lower than 900°C.

A significant advantage of uranium-lead dating is that any sample provides two independent radiogenic paths, one based on the decay of ^{235}U to ^{207}Pb with a half-life of approximately 700 million years, and a second based on the decay of ^{238}U to ^{206}Pb, with a half-life of approximately 4.5 billion years. Collectively, these decay chains provide a means to determine the accuracy of an age. When the mineral being dated has remained closed to U and all of its daughter isotopes, both decay chains will yield identical, and hence concordant ages. However, if significant lead occurs, there will be a discordance between both U/Pb ages. Growth zonation within single crystals can also generate inaccuracies in single crystal dating methods, such as thermal ionization mass spectroscopy, and in-situ methods (e.g. SHRIMP, SIMS, LA-ICPMS) are required if growth zonation is identified.

The SHRIMP (Sensitive High-mass Resolution Ion Microprobe) is an ion microprobe that performs in-situ isotopic analysis of minerals with a resolution of ~30 μm, and is particularly

useful for U/Pb dating of specific growth zones of single crystals.

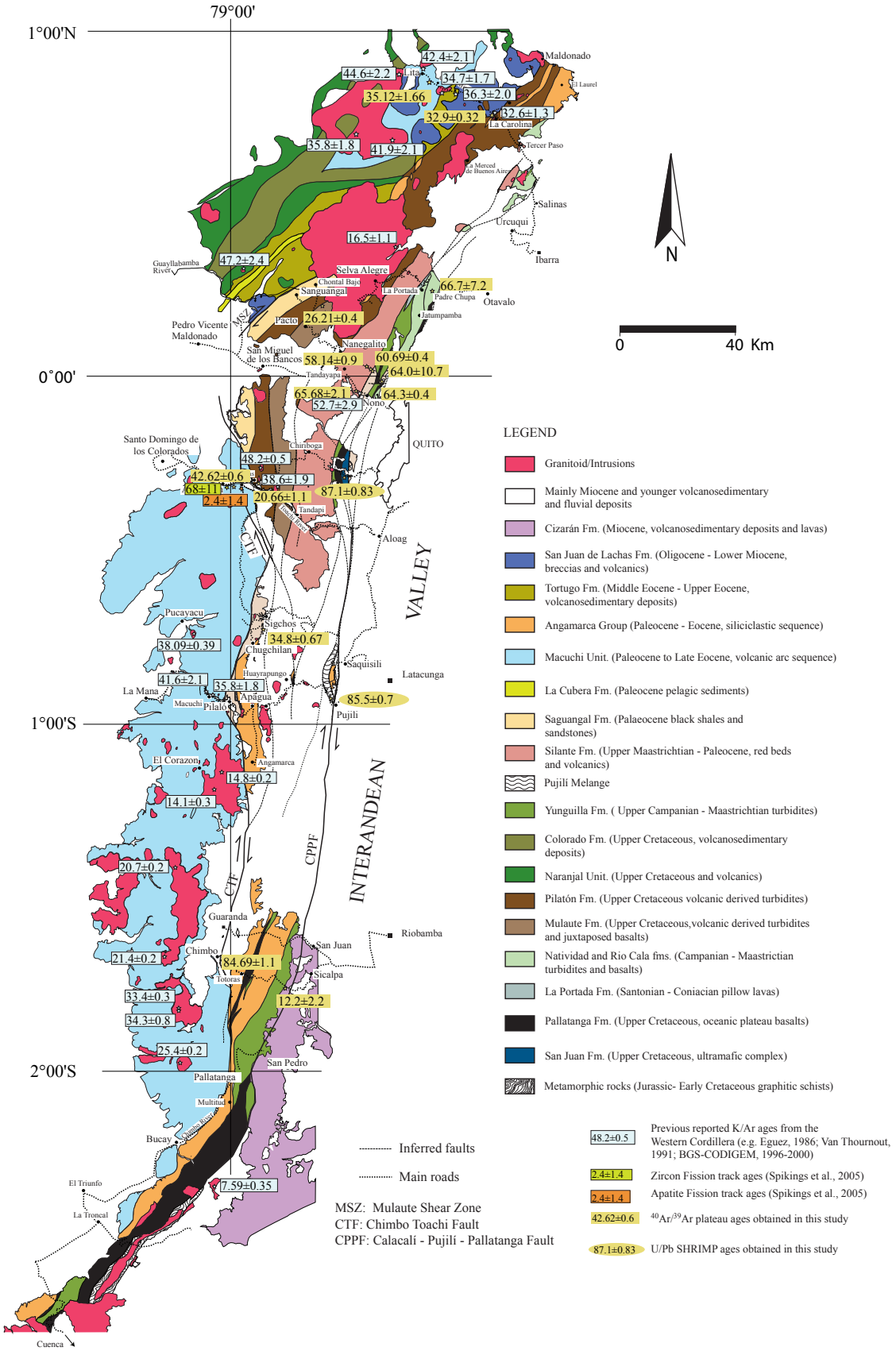

Fig. 4.1. Radiometric dating from igneous rocks of the Western Cordillera. Geological map from the BGS-CODIGEM mapping program (1996-1997) and own observations.

The apparatus is most commonly used for zircon and monazite U-Th-Pb geochronology, although it can also be used to analyze additional isotope systems. Further details on the SHRIMP technique are to be found in Compston et al. (1992) or Williams (1998).

In this study, the SHRIMP technique was used to date the igneous basement of the Western Cordillera, because most of these rocks are basaltic or andesitic in composition, with zircon crystals occurred as very small crystals in minute amounts, therefore, the analytical precision in minute zircon grain, make the U/Pb SHRIMP method very useful for the analyzed rocks. Similarly, the stability of zircon for long periods of time may remain as a closed system; even at high temperature (~900 °C) make the method suitable for this study, considering the long deformation history of the Western Cordillera

4.1.2 SHRIMP-Results

Zircon crystals were successfully recovered from a gabbro of the San Juan Formation and a granite in the mélange zone (Pujilí Granite). For the other volcanic formation, which are mostly basaltic and andesitic, either the zircon grains were too small, or the number of grains was not sufficient for U/Pb analysis using the SHRIMP method.

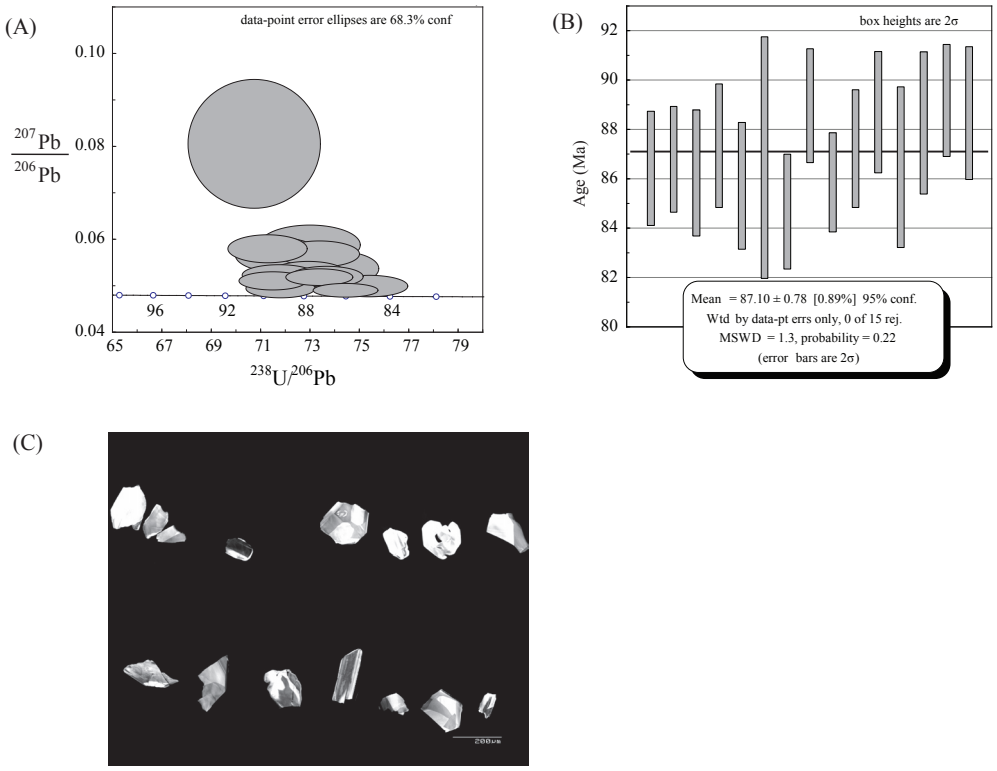

Fig. 4.2. A) Tera-Wasserburg diagram for sample 02CV34, B) Weighted average age from all analyses and C) Cathodoluminiscense (CL) image of the analyzed zircons.

Sample 02CV34 San Juan Formation, gabbro

Zircons were obtained from a coarse-grained layered gabbro, located west of the San Juan

village, along the Quito – Chiriboga road (Fig. 4.1), which was previously mapped as part of the San Juan Fm. Petrographic thin section analysis shows that the gabbro is holocrystalline with an ophitic texture, containing crystals of plagioclase, clinopyroxene, orthopyroxenes and amphibole, the latter produced by alteration of the ortho and clinopyroxenes (uralitization). The plagioclase has an interlocking texture. Cathodoluminiscense images (Fig. 4.2C) show that the zircons have undisturbed oscillatory zoning, which is indicative of a magmatic origin, and no relict cores were identified. U/Pb (SHRIMP) analyses on both core and rims of 15 crystals yielded analytically concordant ages, except one with minor reverse discordance, which are interpreted to have experienced Pb-loss. The ages range between 84.6±2.4 and 89.1±2.2 Ma (2σ), defining a weighted mean age of 87.10±1.66 Ma (2σ). The sample do not show evidence of high grade metamorphism and deformation. The age of 87.10±1.66 Ma represent the time of crystallization of the San Juan ultramafic-mafic assemblage, which may represent a fragment of the Coniacian oceanic plateau sequence.

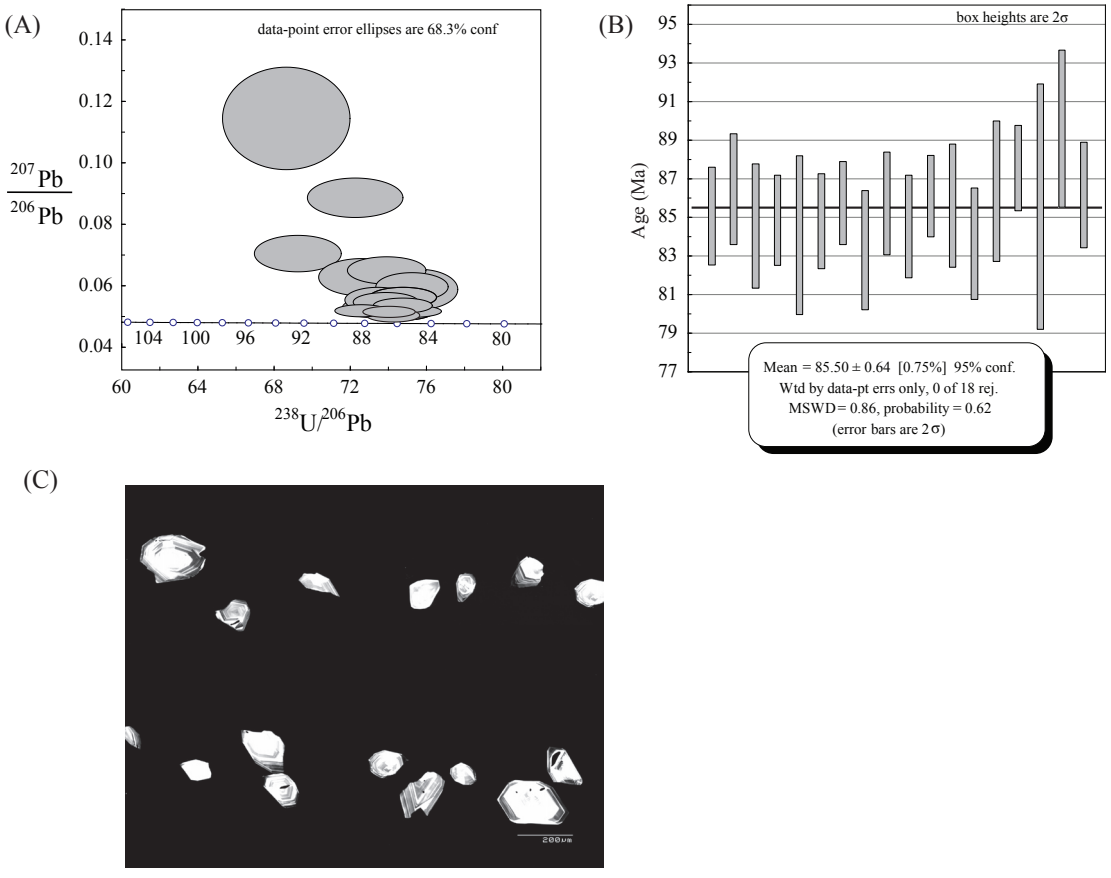

Fig. 4.3. A) Tera-Wasserburg diagram for sample 02CV258, B) Weighted average age from all analyses and C) Cathodoluminiscense (CL) image of the analyzed zircons.

Sample 02CV258 Pujilí Granite

The analyzed sample is a coarse-grained granite (pegmatite) clast, which crops out within a tectonic mélange, located along the eastern flank of the Western Cordillera, west of the town of Saquisilí, within the Quebrada Picisí. The granitic block hosts S-C structures and is surrounded

by serpentinized basalt, which. The block is entrained in a tectonized zone of the Pallatanga Formation (Pujilí Melange). The granite consists of feldspar, quartz, and muscovite, with feldspar partially replaced by fine-grained sericite. Accessory minerals include zircon and rutile. Cathodoluminiscense images of the zircon crystals reveal undisturbed growth textures (Fig. 4.3C), suggesting they are magmatic, and no relict cores were found. Core and rims of 17 zircon crystals were analyzed in this study, which yielded ages between 83.3±3 and 89.6±4.0 Ma (2σ), defining a weighted mean age of 85.5±1.4 (2σ) Ma. The sample does not show sign of high-grade metamorphism. This U/Pb (SHRIMP) age is interpreted as the crystallization age of the granite.

4.2 $^{40}Ar/^{39}Ar$ ANALYSES

4.2.1 Rationale of the method

$^{40}Ar/^{39}Ar$ dating is based on the natural radiogenic decay of ^{40}K to ^{40}Ar, and the natural transformations that are utilized are identical to those for the K/Ar method. Briefly, crystalline species which contain K will accumulate radiogenic $^{40}Ar^*$ at an empirically determined rate, and hence the K/Ar age can be determined after quantifying the $^{40}K/^{40}Ar$ value. Inaccuracies are introduced by argon loss (caused by recrystallization, alteration or thermally activated diffusion), and excess ^{40}Ar in the non-radiogenic component (Lanphere and Dalrymple, 1976). Argon loss occurs when radiogenic $^{40}Ar^*$ produced within a rock/mineral escapes after its formation.

Clearly, Ar loss results in a reduction of the total fusion age, relative to the crystallization age of a mineral, whereas excess argon ($^{40}Ar_E$) can cause the calculated K/Ar age to be older than the crystallization age of the dated material (MacDougall et al., 1969). Similarly, Ar recoil within a sample can cause low temperature step ages greater than crystallization ages. Ar recoil is caused during irradiation of a sample in a nuclear reactor, a fast neutron enters the ^{39}K atom, converting it to ^{39}Ar as a proton is released (Baksi, 1994).

The $^{40}Ar/^{39}Ar$ dating permits inaccuracies caused by Ar loss, excess ^{40}Ar, and ^{39}Ar to be identified, hence theoretically increasing the overall accuracy, and precision, of the method. Individual mineral phases are irradiated with high-energy neutrons in a nuclear reactor, which are captured by ^{39}K nuclei driving its transformation to $^{39}Ar_K$. $^{39}Ar_K$ is taken as a proxy for the parent ^{40}K isotope because the natural $^{40}K/^{39}K$ ratio is known, and is constant. Consequently, both the daughter isotope, and the proxy for the parent isotope, are isotopes of Ar, which can routinely be analyzed simultaneously on a multi-collector mass spectrometer (e.g. Alexandre et al., 2006), significantly increasing the precision over the more cumbersome K/Ar analytical method.

The $^{40}Ar/^{39}Ar$ age relates to the measurement of the $^{40}Ar^*/^{39}Ar_K$ ratio. All analyses performed in this study were performed using the $^{40}Ar/^{39}Ar$ step-heating technique, where Ar is released in successive steps, at progressively higher temperatures. Assuming that the sample did not homogenize by dehydration reactions during *in-vacuo* heating, this approach allows the user

to identify Ar loss, excess ^{40}Ar, and ^{39}Ar recoil (in most cases), and hence inaccuracies can be omitted during the final data reduction procedure. If a rock or mineral sample has been a closed system to potassium and argon since its formation, then the ratio of radiogenic ^{40}Ar to neutron-produced ^{39}Ar, and thus the apparent age, should be constant in each incremental step (Lanphere and Dalrymple, 1971), and the $^{40}Ar/^{39}Ar$ method can be used as a geochronological tool. Partially disturbed systems can be used to extract thermochronological information, assuming that the daughter isotopes were lost by thermally activated diffusion (Harrison and MacDougall, 1981). However, this study did not attempt to perform any thermochronological analyses.

4.2.2 Results

Twenty-six samples were separated for dating with the $^{40}Ar/^{39}Ar$ method. The analyzed samples are mainly andesites and basalts from the oceanic basement and volcanic cover of the Western Cordillera. Basalts in general have low potassium contents, and a majority of the outcrops in the study area are partially altered, which does not render them particularly suitable for the $^{40}Ar/^{39}Ar$ method. However, several successful studies have been published, which analyzed glass and phenocrysts free basaltic groundmass with the $^{40}Ar/^{39}Ar$ method (e.g. Sinton et al., 1998; Kooppers et al., 2000). To minimize the influence of alteration of the samples, only those samples that appeared to be unaltered after thin-section analysis were selected for dating.

$^{40}Ar/^{39}Ar$ step-heating analyses were performed on amphibole, plagioclase, groundmass and even pyroxene separates. The analytical details for the mineral separation are indicated in the appendix 9.

Plateaus are herein defined as the release of ≥50% of the total ^{39}Ar gas released in three or more successive steps concordant within 2σ error. Individual ages for each $^{40}Ar/^{39}Ar$ step were calculated after corrections for blanks, mass fractionation, and atmospheric argon content. For the data reduction, ArArcalc v22 by Koppers (2002) was used. The raw data is presented in the appendix, and age spectra and inverse isochrons are shown in figures 4.4 to 4.10.

In addition, isochron ages were calculated using the inverse-isotope correlation diagrams that plot $^{39}Ar/^{40}Ar$ against $^{36}Ar/^{40}Ar$. These plots are included on figures adjacent to the respective age spectrum diagram, as well as the MSWD of the data (a goodness of fit indicator), the number of points used in the age regression, and the percentage of gas included in the correlation. In the $^{36}Ar/^{40}Ar$–$^{39}Ar/^{40}Ar$ correlation diagrams, the cubic least squares fitting scheme outlined by York (1969) was employed to regress the data.

The regression line yields two intercepts; the inverse of $^{39}Ar/^{40}Ar$ intercepts produces an intercepted age (calculated from the inverse of the x-axis intercept), whereas the inverse of the $^{36}Ar/^{40}Ar$ intercept (y-axis) indicates the composition of a non-radiogenic argon component (initial $^{40}Ar/^{36}Ar$ ratio). 2σ standard deviation in each apparent age is reported. Analytical details are indicated in the appendix 12, and results are summarized in table 4.2.

Formation	Lithology	Sample	Locality	UTM		Age	Mineral phase	Method
San Juan Fm.	cpx+opx+plag coarse grained gabbro	02CV34	Southwest of Quito	759907	9967451	87.10±1.66 Ma	zircon	U/Pb SHRIMP
Pujili Granite	Kfeldspr+quartz+muscovite granite	03CV258	West of Saquisilí	755300	9898600	85.5±1.4 Ma	zircon	U/Pb SHRIMP
Totoras amphibolite	amphibole+quartz+plag amphibolite	03CV234	East of Totoras	730472	9809654	84.69±2.22 Ma	hornblende	$^{40}Ar/^{39}Ar$
Río Cala Fm.	basaltic andesite	02CV104	North of Padre Chupa	787170	10027797	66.7±7.16 Ma	pyroxene	$^{40}Ar/^{39}Ar$
Silante Fm.	basalt	03CV174	West of Nono	763379	9995871	65.68±2.18 Ma	groundmass	$^{40}Ar/^{39}Ar$
	andesite	03CV162	West of Calacalí	768285	10001600	61±1.09 Ma	groundmass	$^{40}Ar/^{39}Ar$
	andesite	02CV55	West of Calacalí	766935	10002688	58.14±1.95 Ma	groundmass	$^{40}Ar/^{39}Ar$
	diorite	03CV263	West of Calacalí	769015	10001259	63.96±10.74 Ma	plagioclase	$^{40}Ar/^{39}Ar$
Pilalo Fm.	andesite	03CV172	Northeast of Nono	771610	9996629	64.3±0.4 Ma	pyroxene	$^{40}Ar/^{39}Ar$
Macuchi Unit.	basaltic andesite	02CV120	East of Alluriquin	725129	9965028	42.62±1.3 Ma	plagioclase	$^{40}Ar/^{39}Ar$
Macuchi Unit.	andesite	02CV67	Lita	784106	10095939	35.12±1.66 Ma	groundmass	$^{40}Ar/^{39}Ar$
Andesite intruding Pilalo	andesite	03CV185	Sigchos	733838	9919774	34.81±1.35 Ma	hornblende	$^{40}Ar/^{39}Ar$
San Juan de Lachas Fm.	andesite	02CV75	La Carolina	806395	10083179	32.90±0.64 Ma	hornblende	$^{40}Ar/^{39}Ar$
Andesite intruding Saguangal Fm	hornfelsed andesite, with amphibole overgrowths	02CV144	Chontal Bajo	752716	10023463	25.6±0.81 Ma	hornblende	$^{40}Ar/^{39}Ar$
Mulaute Fm.	hornfelsed andesite, with amphibole overgrowths	03CV165	East of La Palma	736880	9966987	20.66±2.2 Ma	groundmass	$^{40}Ar/^{39}Ar$
Cizaran Fm.	andesite	03CV232	West of Sicalpa	740461	9806100	12.16±2.24 Ma	groundmass	$^{40}Ar/^{39}Ar$

Table. 4.2 Summary of U/Pb zircon ages and $^{40}Ar/^{39}Ar$ plateau ages of igneous rock from the Western Cordillera obtained in this study.

4.2.2.1 Basement rocks

Totoras amphibolite (Sample 03CV234)

Sample 03CV234 is an amphibolite collected east of the village of Totoras (Fig. 4.1). The amphibolites are in tectonic contact with basalts of the Pallatanga Formation. The analyzed sample is a medium to coarse-grained amphibolite with quartz, plagioclase and K-feldspar. Geochemical data from the amphibolite indicate that the protolith of the rock has an oceanic plateau affinity (Beaudon et al., 2005). $^{40}Ar/^{39}Ar$ step heating of a pure hornblende separate yields an almost undisturbed age spectrum (Fig. 4.4), with a plateau age of 84.69±2.22 Ma (2σ) obtained from 3 consecutive steps that account for 96.15% of the total ^{39}Ar released, and with an acceptable MSWD of 0.5 (below the 2.5 critical value).

The same sample yields an indistinguishable inverse isochron age of 88.68±8.82 Ma (2σ) (MSWD 0.25) corroborating the plateau age, and an initial $^{40}Ar/^{36}Ar$ intercept of 274.24±22.97, which is indistinguishable from the atmospheric value (~295). The plateau age indicates the time of cooling below ~550-500°C, during retrogression after amphibolite facies metamorphism.

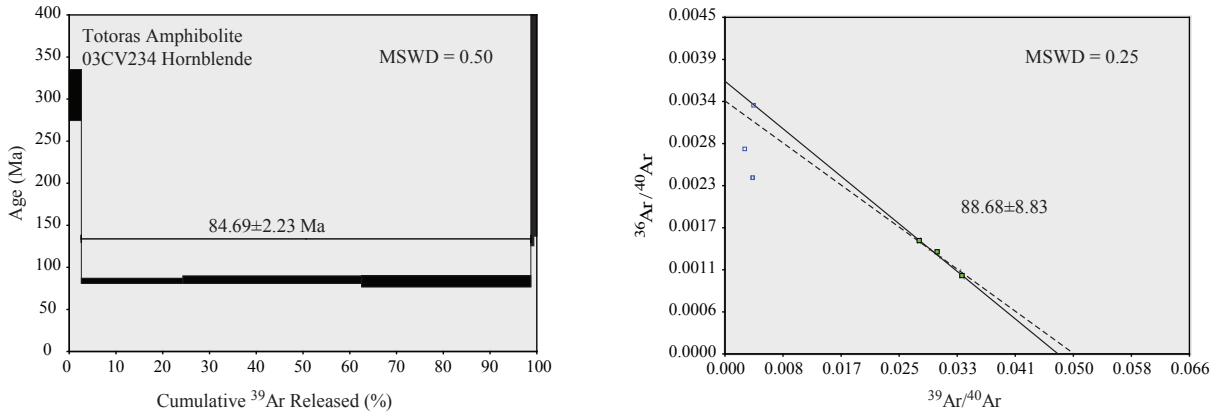

Fig. 4.4. Apparent age spectra and inverse-isotope correlation diagrams for samples of the Totoras amphibolite. A plateau age (indicated) has been determined from the weighted mean of contiguous, concordant step-ages. Boxes for each step extend vertically to ± 2σ, and horizontally in proportion to the fraction of ^{39}Ar released in the step.

4.2.2.2 Volcanic cover sequence

Rio Cala Formation (Sample 02CV104)

Sample 02CV104 is a basalt of the Rio Cala Formation collected along the Otavalo – Selva Alegre road, north of the village of Padre Chupa (Fig. 4.1). The basalt hosts fresh pyroxene phenocrysts up to 1 cm in size. Plagioclase phenocrysts are a minor component, and they are partially replaced by sericite and calcite. The matrix is slightly chloritized, and has an intersertal texture, which includes microliths of plagioclase and pyroxenes. Major and trace element geochemical analyses (see chapter 2) indicate that this rock was formed in an intraoceanic island arc setting, which built on top of an oceanic plateau.

$^{40}Ar/^{39}Ar$ analysis of pyroxenes yielded and age spectrum with a plateau age of 66.7±7.16 Ma (2σ) that has an acceptable MSWD of 1.17 (Fig. 4.5). The plateau age was calculated from six consecutive steps, accounting for 81% of the total ^{39}Ar released.

The Maastrichtian plateau age may approximate to the crystallization age of the volcanic rock, and within the error partially overlap Campanian to Maastrichtian ages reported for the Natividad Formation, which is interpreted to be derived from the Rio Cala Formation (Boland et al., 2000).

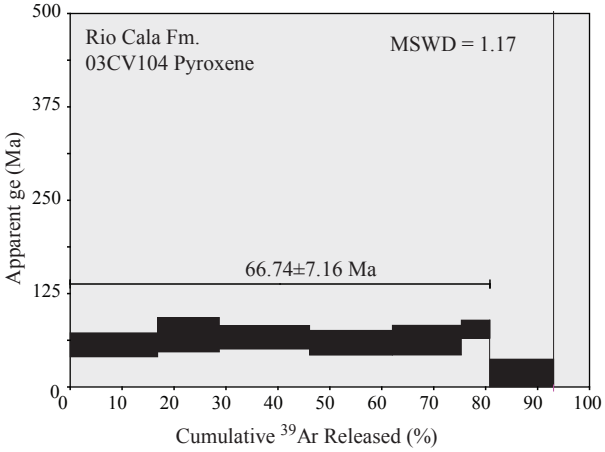

Fig. 4.5. Apparent age spectra for sample of the Rio Cala Fm. A plateau age (indicated) has been determined from the weighted mean of contiguous, concordant step-ages. Boxes for each step extend vertically to ± 2σ, and horizontally in proportion to the fraction of 39Ar released in the step.

Silante Formation (Tandapi volcanic facies)

Sample 02CV174

Sample 02CV174 is a fine to medium grained basalt, having an ophitic to granular texture, similar to dolerites. The sample was collected from a volcanic sequence exposed in the Nono–Tandayapa road section (Fig. 4.1), which overlies continental deposits of the Silante Formation, also evidenced by the presence of xenoliths of the underlying red bed sequence in the lavas. $^{40}Ar/^{39}Ar$ step-heating of a groundmass concentrate yielded a plateau age of 65.68±4.36 Ma (2σ), which accounts for three consecutive steps (Fig. 4.6A) spanning 86% of ^{39}Ar released, with a MSWD of 1.02. The plateau age is concordant within error with the imprecise inverse isochron age of 67.32±32.14 Ma (2σ), which yields a MSWD of 1.04. The initial $^{40}Ar/^{36}Ar$ content of 283.47±116.83 suggests that the groundmass may not be contaminated with excess ^{40}Ar (although clearly the result is imprecise). The plateau age is interpreted as an approximate of the crystallization age of the volcanic rock, and it is consistent with similar ~65 Ma ages obtained in the same area, as well as with Maastrichtian – Paleocene biostratigraphic ages of overlying sediments of the Pilaló Formation.

(A)

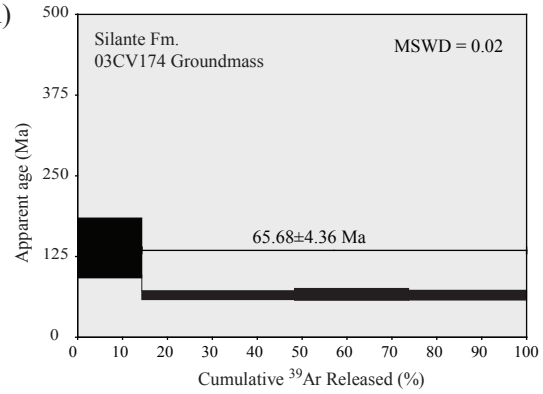
Silante Fm.
03CV174 Groundmass
MSWD = 0.02
65.68±4.36 Ma
Apparent age (Ma)
Cumulative ^{39}Ar Released (%)

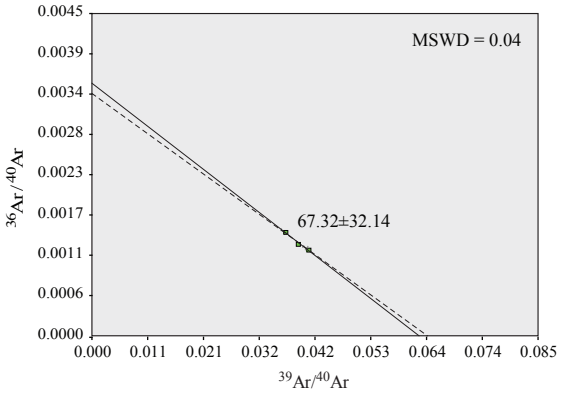
MSWD = 0.04
67.32±32.14
^{36}Ar/^{40}Ar
^{39}Ar/^{40}Ar

(B)

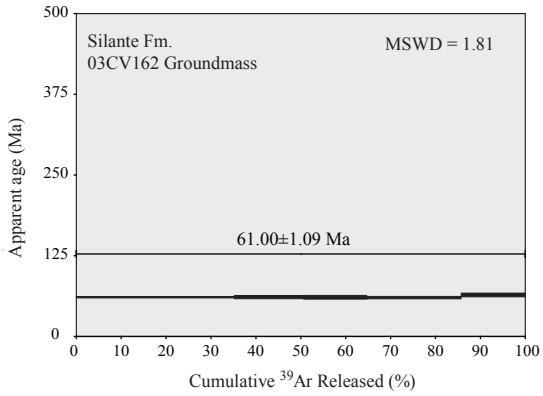
Silante Fm.
03CV162 Groundmass
MSWD = 1.81
61.00±1.09 Ma
Apparent age (Ma)
Cumulative ^{39}Ar Released (%)

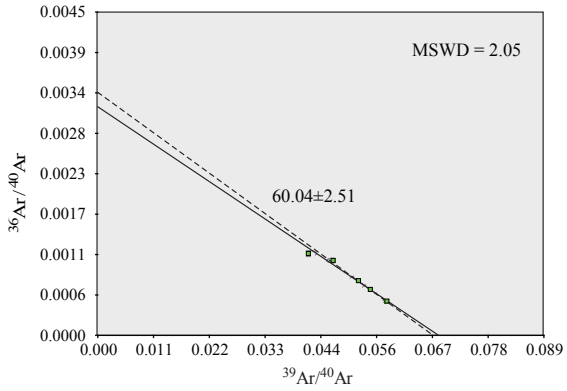
MSWD = 2.05
60.04±2.51
^{36}Ar/^{40}Ar
^{39}Ar/^{40}Ar

(C)

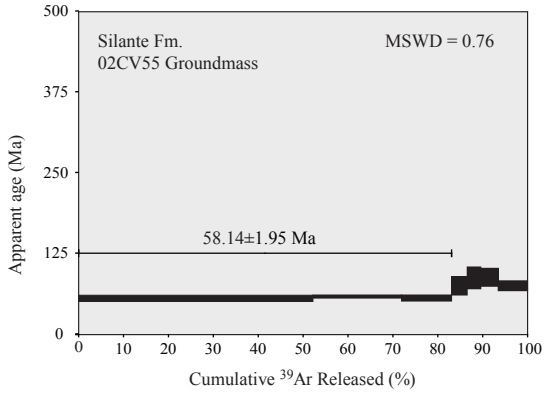
Silante Fm.
02CV55 Groundmass
MSWD = 0.76
58.14±1.95 Ma
Apparent age (Ma)
Cumulative ^{39}Ar Released (%)

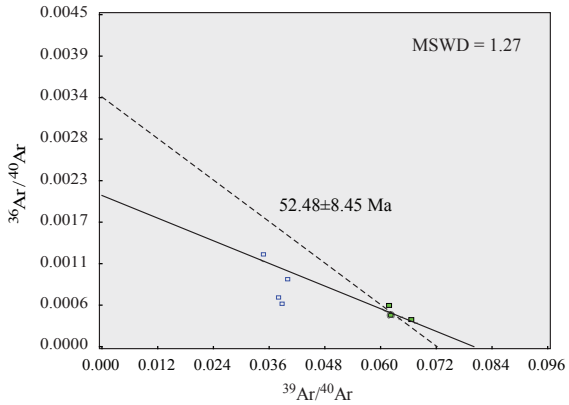
MSWD = 1.27
52.48±8.45 Ma
^{36}Ar/^{40}Ar
^{39}Ar/^{40}Ar

(D)

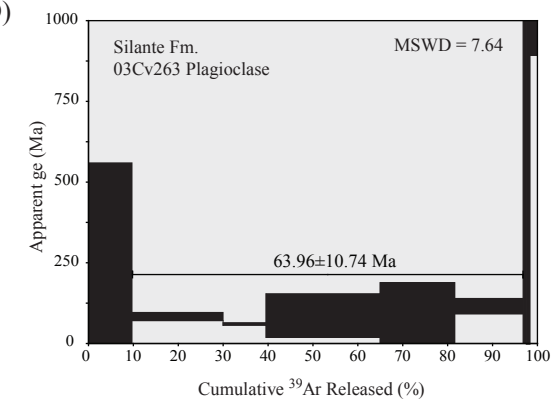
Silante Fm.
03Cv263 Plagioclase
MSWD = 7.64
63.96±10.74 Ma
Apparent ge (Ma)
Cumulative ^{39}Ar Released (%)

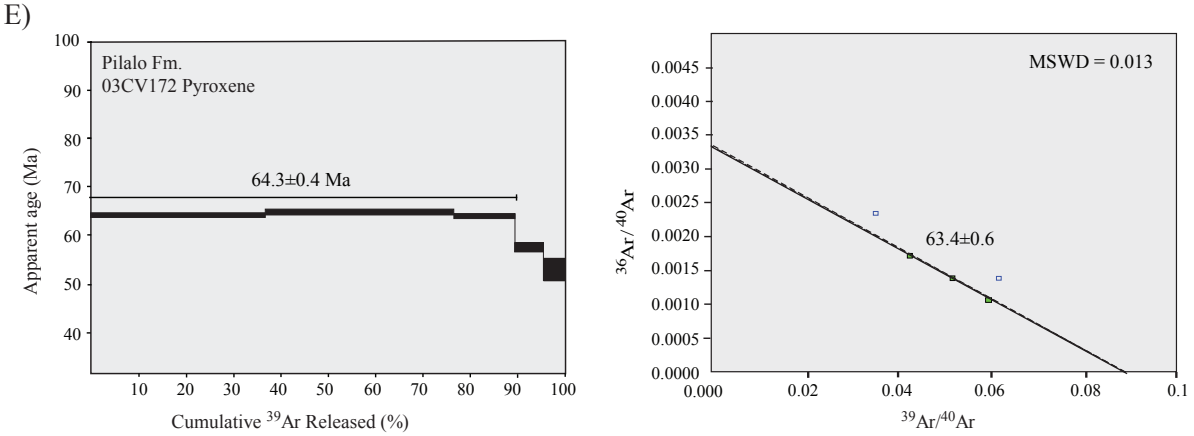

Fig. 4.6. Apparent age spectra and inverse-isotope correlation diagrams for samples of the Silante and Pilaló fms. A plateau age (indicated) has been determined from the weighted mean of contiguous, concordant step-ages. Boxes for each step extend vertically to ± 2σ, and horizontally in proportion to the fraction of ^{39}Ar released in the step

Sample 03CV162

Sample 03CV162 was taken from a quarry, west of Calacalí (Fig. 4.1). The sample was collected near to the tectonic contact with the Yunguilla Formation. The sample is an andesite, which has a porphyritic texture with phenocrysts of plagioclase and clinopyroxene. The matrix is composed of acicular microliths of plagioclase with minor amounts of pyroxene and glass. The plagioclase phenocrysts have a dusty aspect and are partially altered and replaced by sericite and chlorite, whereas the microliths in the matrix remain fresh. Clinopyroxene geochemistry of an andesitic lava breccia (sample 00RS35; Chapter 3) indicates a volcanic arc affinity for the succession at this locality. Groundmass separates from this sample yielded a plateau ^{40}Ar/^{39}Ar age of 61±1.09 Ma (2σ), with an acceptable MSWD of 1.81. The plateau age was calculated from four consecutive steps (Fig. 4.6B), which released 99% of the total ^{39}Ar. The plateau age is concordant with an inverse isochron age of 60.04±2.51 Ma (MSWD=2.05), and the ^{40}Ar/^{36}Ar non-radiogenic intercept of 284.379±18.74 is indistinguishable from an atmospheric composition.

Sample 02CV55

Sample 02CV55 was collected along the Calacalí – Pacto road (Fig. 4.1), 2 km west of sample 02CV162, and similarly it is interpreted to rest on top of continental sediments of the Silante Formation. The sample is a porphyritic andesite, with plagioclase and clinopyroxene phenocrysts and a matrix composed of glass and microliths of plagioclase and minor pyroxenes. The phenocrysts are partially replaced by chlorite and sericite. A groundmass separate yielded a ^{40}Ar/^{39}Ar age of 58.14±1.95 Ma (2σ), with an MSWD of 0.76 (Fig. 4.6C). This age was calculated from three consecutive steps, which yield 83.07% of the total ^{39}Ar released. The plateau age is concordant with an inverse isochron age of 52.48±8.45 Ma (2σ), which also

yields an extremely imprecise initial $^{40}Ar/^{36}Ar$ ratio of 487.89±366.6.

Sample 03CV263

Sample 03CV263 forms part of the Silante Fm. and was collected in the Calacalí – Pacto road (Fig. 4.1), where it is in tectonic contact with turbidites of the Yunguilla Formation. The rock is a diorite with crystals of plagioclase, clinopyroxene and quartz. A plagioclase separate yielded an imprecise weighted mean age of 63.96±10.74 (2σ) and an MSWD of 7.64 (Fig. 4.6D), indicating that the data does not strictly define a plateau. Furthermore, the sample does not yield an inverse isochron (MSWD = 0.00), although the weighted mean age is consistent with similar ages obtained for the Silante Formation in the same area.

Pilaló Formation (Sample 03CV172)

Sample 03CV172 is an andesite tentatively assigned to the Pilalo Fm. The sample was collected north of the village of Nono (Fig. 4.1) in a 100 meters wide tectonic slice previously mapped as the Natividad Formation (e.g. Boland et al., 2000). The andesite is intercalated with black shales, lithologically similar to the Pilaló Formation exposed to the west in the Nono-Tandayapa road section, and is fault bounded against the Yunguilla Formation. Geochemical data from clinopyroxenes of this sample shows that the volcanic rock is highly fractionated, and formed in a volcanic arc setting (see chapter 3), which contrast with the more primitive nature of rocks of the Rio Cala Group (including the Natividad Formation). The sample was collected in the same area where Early Paleocene ages were obtained for the top of the Silante Formation. The analyzed sample has a porphyritic texture, with phenocrysts of clinopyroxene and plagioclase in a matrix of glass and chlorite. The plagioclase phenocrysts are partially replaced by sericite, whereas the clinopyroxenes are generally unaltered. $^{40}Ar/^{39}Ar$ analyses of clinopyroxenes separates yielded a plateau age of 64.3±0.4 Ma (2σ), which is interpreted as an approximate to the time of crystallization of the volcanic rock which hosts the pyroxenes. The plateau age was obtained from three consecutive steps that cover 90% of the total ^{39}Ar released (Fig. 4.6E). This age is concordant with an inverse isochron age of 63.4±0.6 Ma (2σ), and the non-radiogenic $^{40}Ar/^{36}Ar$ intercept of 301±3, is extremely close to an atmospheric composition, suggesting the age is not affected by excess ^{40}Ar.

Macuchi Unit

Sample 02CV126

Sample 02CV126 forms part of the Macuchi Unit., and was collected in the Alóag - Santo Domingo road, 1 km east of the village of Alluriquín (Fig. 4.1). The sample is a fine-grained, moderately clinopyroxene-plagioclase-phyric dolerite with a subophitic to slightly intersertal texture. Geochemical data from a sample (RH278b) collected in the same locality by Hughes and Pilatasig (2002) indicates that this rock is a primitive arc basalt. $^{40}Ar/^{39}Ar$ step-heating yielded a saddle-shaped age spectrum, suggesting that excess ^{40}Ar is present within the sample, although

this could not be categorically identified due to the low precision of the inverse isochron (initial $^{40}Ar/^{36}Ar$ ratio of 317.18±23.93; Fig. 4.7A). The weighted mean age for the six steps, which define the flattest part of the age spectrum, and span approximately 54% of the ^{39}Ar released, yield a weighted mean age of 42.62±1.3 Ma (2σ) and an MSWD of 7.43.

The weighted mean age is concordant with the inverse isochron age of 39.75±6.19 (2σ; MSWD = 7.53), and is considered to represent a maximum $^{40}Ar/^{39}Ar$ plagioclase age for the sample. However, the Late Eocene age is consistent with biostratigraphic ages (Egüez, 1986) obtained from sedimentary rocks intercalated within volcanic rocks of the Macuchi Unit. in the same area.

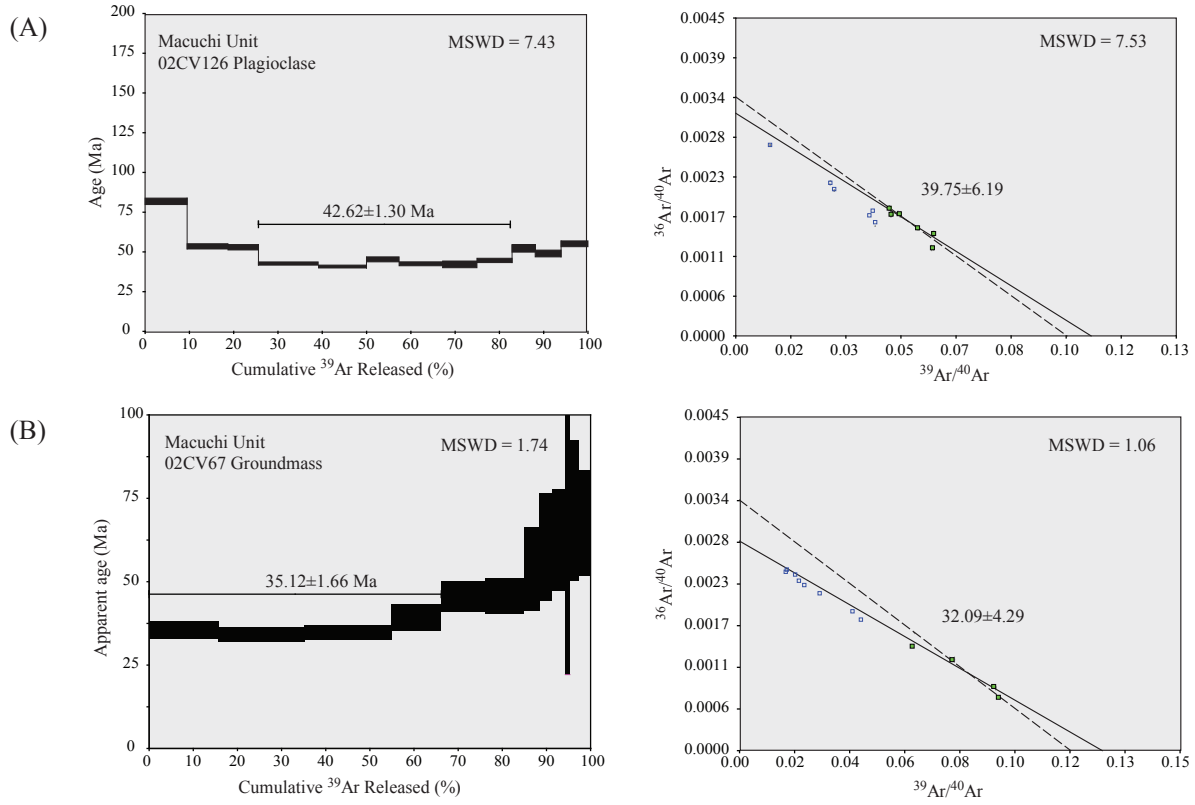

Fig. 4.7. Apparent age spectra and inverse-isotope correlation diagrams for samples of the Macuchi Unit. A plateau age (indicated) has been determined from the weighted mean of contiguous, concordant step-ages. Boxes for each step extend vertically to ± 2σ, and horizontally in proportion to the fraction of ^{39}Ar released in the step.

Sample 02CV67

Sample 02CV67 is represents part of an andesite lava flow, collected in the Lita area (Fig. 4.1), along the Ibarra – Lita road. This volcanic sequence was previously mapped as part of the Naranjal Unit (Boland et al., 2000). However based on field relationships and radiometric data, these exposures are assign to the Macuchi Unit.

The andesite has a porphyritic texture, with phenocrysts of plagioclase and clinopyroxene, and a matrix with a trachytic texture, composed of sub-parallel oriented acicular microliths of plagioclase. Sericite and chlorite partially replace the plagioclase phenocrysts, whereas the

plagioclase microliths in the matrix remain fresh. Boland et al. (2000) reported geochemical data from samples in this locality, which indicate that the rocks have a calk-alkaline affinity. $^{40}Ar/^{39}Ar$ step heating analysis of a groundmass separate yields an overall discordant age spectra, with the oldest ages occurring late within the step-wise, gas release experiment (Fig. 4.7B). However, heating steps at lower and intermediate temperatures yielded a concordant, plateau age of 35.12±1.66 Ma (2σ), with an acceptable MSWD of 1.74, which is concordant within the inverse isochron age of 32.09±4.29. The imprecise, initial $^{40}Ar/^{36}Ar$ ratio of 354.05±79 suggests that excess ^{40}Ar may not be present, and therefore the plateau age approximates the crystallization age of the volcanic rock. The age is consistent with the Late Eocene K/Ar ages reported for volcanic and intrusive rocks in the area (Fig. 4.1), which range between 32 and 44 Ma (e.g. Van Thournout, 1991; Boland et al., 2000).

Pilaló stock (Sample 03CV185)

Sample 03CV185 was taken from the central part of the cordillera, in the Sigchos to Chugchilán road, north of the Taxojaló village (Fig. 4.1), and forms part of an andesitic stock, which cuts the volcano-sedimentary sequence of the Pilaló Formation. The andesite is porphyritic, with phenocrysts of hornblende, plagioclase and clinopyroxene, and a matrix composed of glass and microliths of plagioclase and pyroxene. The minerals do not show signs of alteration. Step-wise $^{40}Ar/^{39}Ar$ analysis of hornblende (Fig. 4.8A) yielded a plateau age of 34.81±1.35 Ma (2σ, MSWD 0.58), from the last five (high temperature) steps, which account for 49% of the total ^{39}Ar released.

The plateau age is concordant with an inverse isochron age of 34.91±7.75 Ma (2σ), which yields a MSWD of 0.77. The initial $^{40}Ar/^{36}Ar$ is 295±32.28 is indistinguishable from an atmospheric composition, suggesting that excess ^{40}Ar is not present with the gas reservoirs represented by the last five steps. The plateau age is interpreted as the crystallization age of the andesitic intrusion and possibly correlates with the Late Eocene granitoids exposed at the western border of the Western Cordillera (Fig. 4.1).

San Juan de Lachas Formation (Sample 02CV75)

Sample 02CV75 was collected from an andesitic flow of the San Juan de Lachas Formation, located south of the Jijón y Caamaño village along the Ibarra – Lita road (Fig. 4.1). At this locality, the volcanic rocks of the San Juan de Lachas are unconformably overlying Late Cretaceous sediments of the Pilatón Formation and Eocene sediments of the El Laurel Formation. The andesite has a porphyritic texture, with phenocrysts of hornblende and plagioclase. Glass and microscopic crystals of quartz, plagioclase and opaque minerals form the matrix. Sericite has partially replaced the plagioclase crystals, whereas the hornblende crystals are fresh. $^{40}Ar/^{39}Ar$ step heating analysis yielded a plateau age of 32.90±0.64 Ma (2σ), with a MSWD of 1.02 (Fig. 4.8B). The plateau age was calculated from five consecutive steps, which span the entire age spectrum (98% of ^{39}Ar released).

The plateau age is concordant with an inverse isochron age of 29.06±7.52 Ma (2σ), which has an imprecise $^{40}Ar/^{36}Ar$ intercept of 408.6±109.22, which overlaps with an atmospheric composition. The concordance of plateau and isochron ages, and the low MSWD values for the isochrons, imply that the age is valid, and given the high closure temperature of hornblende (550-500°C), probably represents the time of crystallization of the rock.

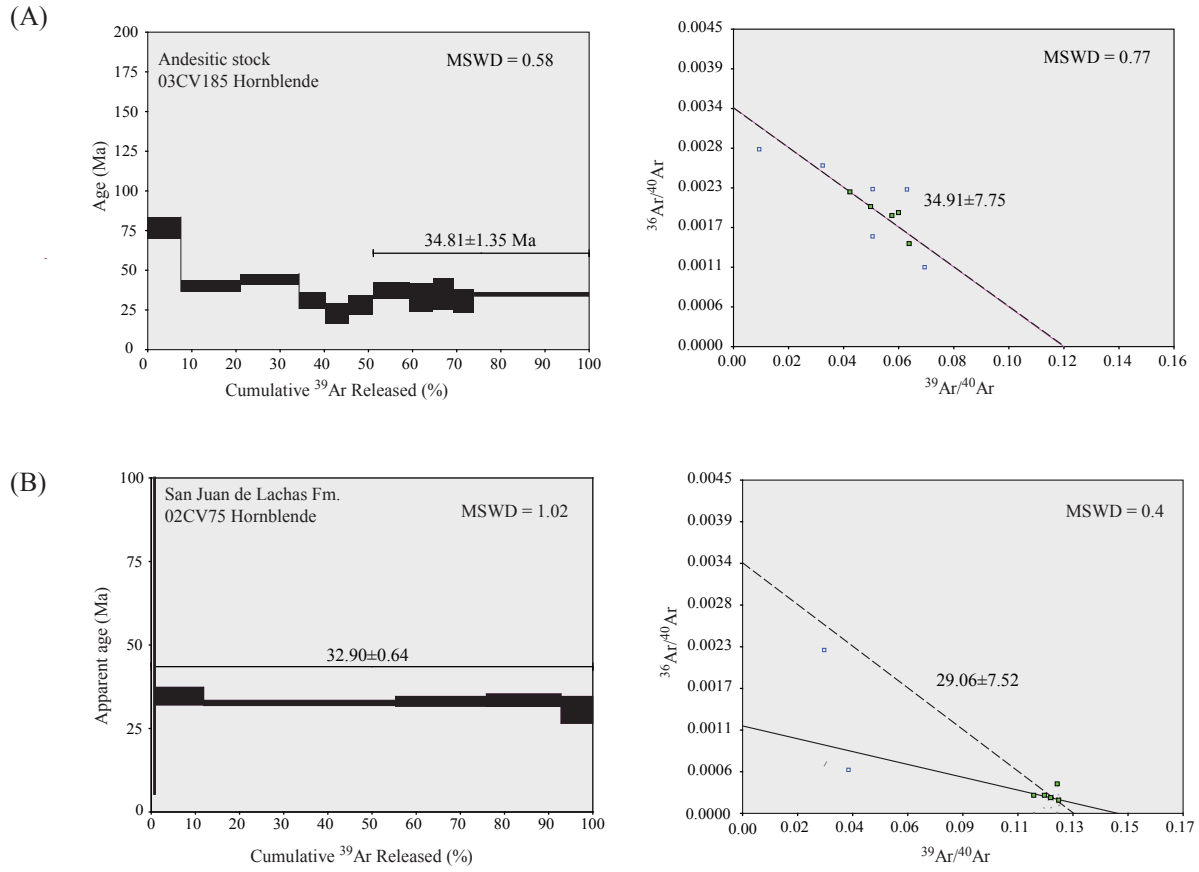

Fig. 4.8. Apparent age spectra and inverse-isotope correlation diagrams for an andesitic stock intruding the Pilaló Formation (A) and San Juan de Lachas (B) formation (see Fig. 4.1 for locations). Plateau ages (indicated) have been determined from the weighted mean of contiguous, concordant step-ages. Boxes for each step extend vertically to ± 2σ, and horizontally in proportion to the fraction of ^{39}Ar released in the step.

Saguangal Formation (Sample 02CV144)

Sample 03CV144 was collected from a quarry (Fig. 4.1) in the road from Pacto to El Chontal village, southwest of the Apuela Batholith, and is intruding metamorphosed sediments of the Saguangal Formation. Evidence of contact metamorphism is provided by parallel aligned amphibole overgrowths, superposing the original porphyritic texture of the andesite. Similarly, the matrix of the andesite is strongly recrystallized. The sample was collected to determine a maximum age for the sediments of the Saguangal Formation. The rock was originally an andesite having a porphyritic texture with phenocrysts of plagioclase slightly seritized. Amphibole separates yielded a plateau age of 25.6±0.81 Ma (2σ), with a MSWD of 0.59 (Fig. 4.9A). The plateau age includes six consecutive steps, which account for 92% of the ^{39}Ar

released. The corresponding inverse isochron age of 25.75±1.85 is concordant (MSWD 0.73) with the plateau age, and yields an imprecise initial $^{40}Ar/^{36}Ar$ intercept of 292.71±31.59, which is indistinguishable from an atmospheric composition. The plateau age is interpreted as a reset age, probably associated to contact metamorphism by the Apuela Batholith.

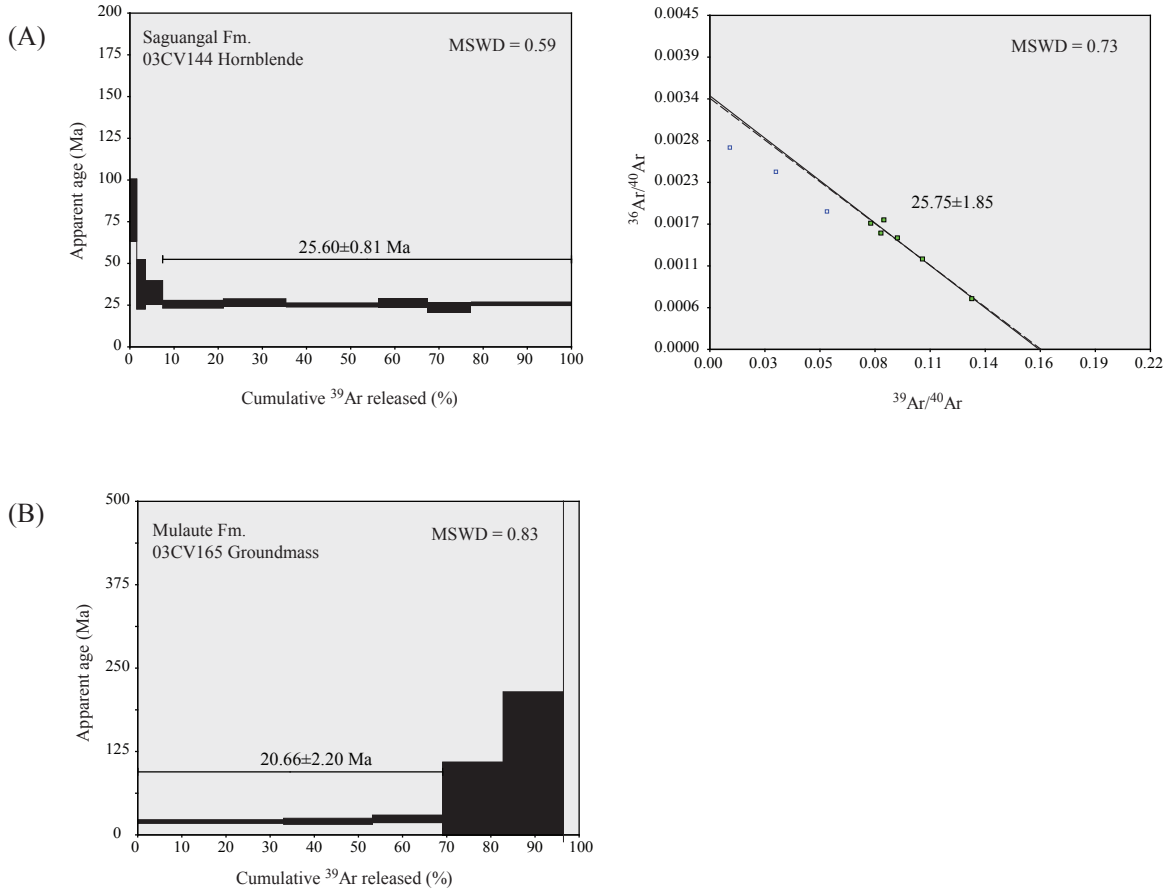

Fig. 4.9. Apparent age spectra and inverse-isotope correlation diagrams for samples of the Saguangal and Mulaute formations. A plateau age (indicated) has been determined from the weighted mean of contiguous, concordant step-ages. Boxes for each step extend vertically to ± 2σ, and horizontally in proportion to the fraction of ^{39}Ar released in the step.

Mulaute Formation (Sample 03CV165)

Sample 03CV165 was taken from an andesitic stock, part of the volcanic succession of the Mulaute Formation along the La Palma – Chiriboga road (Fig. 4.1). $^{40}Ar/^{39}Ar$ step-heating of a groundmass separate yielded a plateau age of 20.66±2.2 Ma (2σ, MSWD 0.83), calculated from three consecutive steps, which account for 69% of the total ^{39}Ar released (Fig. 4.9B). Unfortunately, the sample was irradiated more than one year prior to its analysis, resulting in large errors on the inverse isochron plot due to enhanced correction from the decay of ^{37}Ar. The plateau age is clearly a reset age, due to the Late Cretaceous age of volcanic and sedimentary rocks of the Mulaute Formation. The reset was most likely produced by a thermal disturbance produced by the intrusions, which occurred in the area, but most of them have not

been radiometrically dated.

Cizarán Formation (Sample 03CV232)

Sample 03CV232 is an andesite of the Cizarán Formation, collected close to the tectonic contact with the Yunguilla Formation, in the road from Sicalpa to Chimbo (Fig. 4.1). The nature of the contact was not observed, although Dunkley and Gaibor (1997) interpreted the field relationships to suggest that the Cizarán Formation lies unconformably above the Yunguilla Formation. The analyzed sample is an andesite containing large phenocrysts of plagioclase and pyroxene, with a matrix composed of small acicular microliths of plagioclase. The phenocrysts are partially replaced by calcite and chlorite, whereas the matrix remains quite fresh. A groundmass separate yielded a $^{40}Ar/^{39}Ar$ plateau age of 12.16±2.24 Ma (2σ, MSWD=2.27), which was calculated from the last six consecutive steps, spanning 49% of the total ^{39}Ar released (Fig. 4.10).

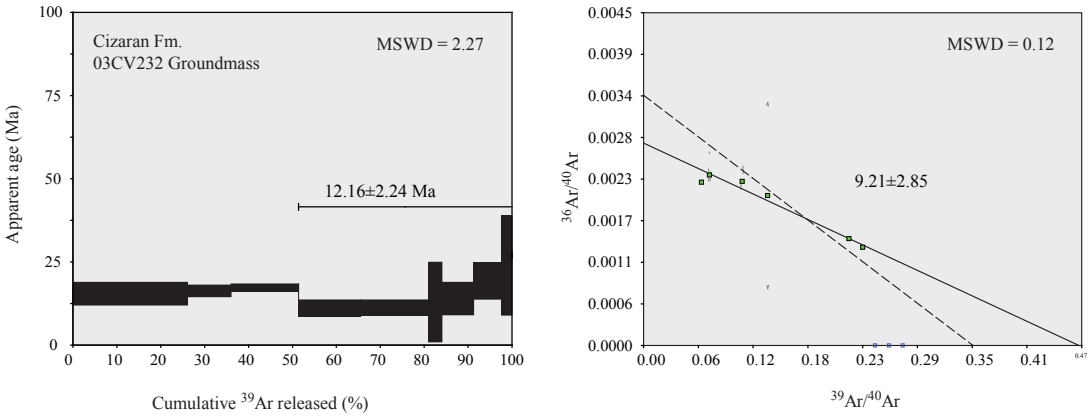

Fig. 4.10. Apparent age spectra and inverse-isotope correlation diagrams for sample of the Cizarán Fm. A plateau age (indicated) has been determined from the weighted mean of contiguous, concordant step-ages. Boxes for each step extend vertically to ± 2σ, and horizontally in proportion to the fraction of ^{39}Ar released in the step.

The plateau age is concordant with an inverse isochron age of 9.21±2.85 Ma (2σ; MSWD 0.12), and the imprecise initial $^{40}Ar/^{36}Ar$ intercept of 365.23±52.2 is indistinguishable from the atmospheric composition. This age is considered as an approximate to the crystallization age. Previous radiometric dating of this Formation yielded K/Ar (hornblende) age of 7.15±0.38 Ma (Dunkley and Gaibor, 1997) and zircon fission track age of 6.8±0.8 Ma (Steinmann, 1997). Therefore our new $^{40}Ar/^{39}Ar$ indicates that volcanism within the Cizarán Formation can be older than previously suggested.

4.3 INTERPRETATION

4.3.1 The age of the basement of the Western Cordillera

Zircons extracted from a layered gabbro, which is mapped as the San Juan Formation, yield a weighted mean U/Pb (SHRIMP) age of 87.10 ± 1.66 Ma (2σ; Fig. 2). However, Lapierre et al.

(2000) obtained an Early Cretaceous Sm/Nd age from an isotropic gabbro, which is also mapped as the San Juan Fm. Lapierre et al. (2000) also performed geochemical analyses on the sample that they dated (sample SJ13), and concluded that the Early Cretaceous rocks erupted above a mantle plume in an oceanic setting. However, the Late Cretaceous U/Pb age obtained in this study represents the time of crystallization of mafic components of the Pallatanga Formation, which also erupted above a mantle plume, in an oceanic environment. Consequently, the age reported by Lapierre et al. (2005) is possibly inaccurate or it may represent an older Early Cretaceous ultramafic basement sequence in the easternmost Western Cordillera (e.g. Litherland et al., 1994; Jaillard et al., 2004).

The U/Pb (zircon) age obtained in this study overlaps with the peak of ages (92–88 Ma) obtained from basalts of the present day Caribbean Plateau using the $^{40}Ar/^{39}Ar$ method (Sinton *et al*., 1998; Kerr et al., 2003). The U/Pb age is also indistinguishable from a plateau hornblende $^{40}Ar/^{39}Ar$ age of 88±1.6 Ma (2σ), obtained from mantle-plume derived basalts of the Piñón Fm. in the coastal forearc of Ecuador (Luzieux et al., 2006). The Early Cretaceous rock sequences reported by Lapierre et al. (2000) may represent detached fragments of the Early Cretaceous ultramafic – mafic Peltetec Unit, exposed at the western border of the Eastern Cordillera, which yields both enriched MORB and subduction related signatures (R. Spikings, pers. com.), and may have accreted to the South American continent during the Aptian (Litherland et al., 1994).

The Totoras Amphibolite yields a hornblende plateau $^{40}Ar/^{39}Ar$ age of 84.69±2.23 Ma, which represents the time of cooling through 550-500°C during retrogression from peak metamorphism. The amphibolites probably formed by metamorphic reactions at the base of the thick oceanic plateau sequence (Pallatanga Fm.; see chapter 2) that forms the basement of the Western Cordillera. Retrogression of the amphibolites through ~550-500°C at 84.69±2.23 Ma was probably simply the result of thermal relaxation of the oceanic plateau, as it drifted from regions of high heat flow.

4.3.2 The age of the Rio Cala Island arc.

The Pujilí Granite yields a U/Pb age of 85.5±1.4 Ma, which is indistinguishable from plateau $^{40}Ar/^{39}Ar$ ages of 86±1 (muscovite) and 82±1 (biotite) Ma reported by Spikings et al. (2005). Earlier interpretations, which proposed that the Pujilí Granite represents fragments of Triassic crustal anatectites that are currently exposed in the Eastern Cordillera (Tres Lagunas Granite, Litherland et al., 1994), and became incorporated into the melange zone during ocean-continent collision (Hughes and Pilatasig, 2002; Spikings et al., 2005) are no longer plausible. In our interpretation (see chapter 2), the Pujilí Granite may have formed as a fractionated intrusive fragment produced during the initiation of west-dipping subduction beneath the leading edge of mantle-plume derived rocks, resulting in the formation of a Late Cretaceous island arc sequence. The radiometric ages of the plateau and arc sequences suggest that the initiation of subduction below the oceanic plateau may have occurred shortly after (~3 my).

The age of the Pujilí Granite (85.5±1.4 Ma) is also consistent with Santonian to Early Campanian (Boland et al., 2000) ages reported for boninites (Van Thournout, 1991) of the La Portada Formation (see chapter 2), which may have also been produced during the initiation of subduction below the oceanic plateau (Vallejo et al., 2006). The association of a Santonian to Maastrichtian intraoceanic island arc overlying mantle-plume derived rocks is documented by abundant island arc related, sedimentary and volcanic rocks reported in the Caribbean region (e.g. Donnelly et al., 1990), as well as the coastal area (San Lorenzo Arc) and Western Cordillera of Ecuador (Lebrat et al., 1987; Jaillard et al., 1995; Cosma et al., 1998; Vallejo et al., 2006; Luzieux et al., 2006). Additional evidence for a Late Cretaceous island arc sequence is found in southern Colombia, where Spadea and Espinosa (1996) reported Campanian radiolarian ages from rocks that intercalate island arc lavas (Ricaurte Arc).

An imprecise plateau $^{40}Ar/^{39}Ar$ age of 66.74±7.16 Ma (2σ) was obtained from a volcanic rock of the Rio Cala Formation, part of the Late Cretaceous island arc sequence in the Western Cordillera. Despite the large error, this age is consistent with Campanian – Maastrichtian biostratigraphic ages obtained from sedimentary rocks of the Natividad Formation, which is interpreted as derived from the Rio Cala Formation (e.g. Boland et al., 2000). Similarly, in the coastal area of Ecuador, Reynaud et al. (1999) reported island arc rocks of the Las Orquideas Formation, northwest of Guayaquil. According to Luzieux (2007), magnetostratigraphic results document Campanian activity in the Las Orquideas island arc sequence. Lebrat et al. (1987) reported a $^{40}Ar/^{39}Ar$ age of 72.7±1.4 Ma for an island affinity basalt in the San Lorenzo Formation of the coastal region of Ecuador, indicating that the island arc sequence preserved in the coastal area and the Western Cordillera may have been coeval, and possibly part of the same system, active between the Santonian until the early Maastrichtian, with possible equivalents in Colombia and the Caribbean region (see chapter 5).

4.3.3 The latest Maastrichtian to Paleocene Silante continental arc

Maastrichtian and Paleocene, calc-alkaline andesites and basaltic andesites exposed northwest of Quito are included in the Silante Formation (Tandapi volcanic facies), and provide important constraints on the Cenozoic evolution of the region now defined by the Western Cordillera. These rocks, which were previously unknown in Ecuador, are considered to be equivalent to the andesitic volcanic rocks of calc-alkaline affinity exposed in the Alóag – Santo Domingo road (Tandapi Unit of Egüez, 1986). In both areas, the andesitic rocks are associated with continental sedimentary rocks of the Silante Formation. The latest Maastrichtian to Paleocene eruption ages of the Silante Formation also corroborate Maastrichtian to Danian biostratigraphic ages (e.g. Savoyat et al., 1970) reported for sedimentary rocks of the Pilaló Formation east of the village of Nono (Fig. 4.1), which was partially derived from the Silante Formation.

The calc-alkaline composition of the Tandapi volcanic facies of the Silante Formation contrasts with the mostly tholeiitic signatures of the underlying Rio Cala island arc sequence, and the mantle-plume derived Pallatanga Formation, suggesting that an important geological event may

have separated these igneous sequences. Radiometric ages from the Silante Formation indicate that the sudden change from marine to terrestrial environment, and initiation of continental arc volcanism occurred before 65 Ma, which most likely was driven by the collision of the Pallatanga Block and the subsequent westward jump of the subduction zone and flip of the subduction direction. Furthermore, any invoked "event" would have to account for a transition from submarine island arc volcanism of the Rio Cala Group, to a continental volcanic arc of the Silante Formation. The termination of the Late Cretaceous tholeiitic volcanism indicates the cessation of west-dipping subduction beneath the mantle-plume derived rocks, and the onset of subduction along the accreted margin gave rise to continental arc volcanism of the Silante Formation.

The ages obtained in this study suggest that the Silante Formation may correlate with the Sacapalca Formation of southern Ecuador, which yielded a zircon fission track age of 66.9±5.8 Ma (Hungerbühler, 1997), and is intruded by the El Tingo Pluton, which is dated radiometrically (K/Ar, biotite) at 50±3 Ma (Kennerly, 1980). Bearing in mind that the zircon fission-track age may be partially or completely reset by heating to temperatures >200°C, it is reasonable to suggest that Paleocene volcanism was widespread, although it is poorly preserved.

4.3.4 The Middle to Late Eocene volcanic arc

Only a few radiometric ages have been obtained from basalts and basaltic andesites of the Macuchi Unit, and hence its age is not precisely constrained. However, an age of 42.62±1.30 Ma was obtained in this study from basaltic andesites of the Macuchi Unit along the Alóag – Santo Domingo road, which is interpreted to be a crystallization age. Similarly, Egüez (1986) reported an indistinguishable K/Ar age (whole rock) of 41.6±2.1 Ma from a basaltic andesite of the Macuchi Unit east of Pilaló village, and a K/Ar (whole rock) age of 35.8±1.8 Ma from a basaltic lava collected along the Alóag – Santo Domingo road. Middle Eocene ages are also reported in a belt of granitoids located at the western border of the Western Cordillera (Fig. 4.1), which coincides with the actual position of the Macuchi Unit, and may represent the intrusive igneous rocks associated to the Macuchi volcanic arc.

Boland et al. (2000) reported K/Ar ages (hornblende) of 42.4±2.1 and 44.6±2.2 Ma for the Santiago Batholith in the northern part of the Western Cordillera, and 47.2±2.4 Ma for a diorite intruding island arc basalts of the Naranjal Formation in the Guayllabamba River, west of the Apuela Batholith (Fig. 4.1). Therefore, assuming that the radiometric ages are accurate, and have not experienced post-crystallization isotopic disturbance, these rocks may all relate to the Middle Eocene Macuchi volcanic arc, which developed at the western border of the actual Western Cordillera.

An andesitic stock, which intrudes sedimentary rocks of the Pilaló Formation, south of Sigchos village (Fig. 4.1), yields an $^{40}Ar/^{39}Ar$ age of 34.81±1.34 Ma. Hughes and Bermúdez (1997) reported a K/Ar (hornblende) age of 38.09±0.39 Ma for a granodioritic intrusion in the same region, located southeast of Pucayacu village, and Egüez (1986) report a K/Ar (whole

rock) age of 38.6±1.9 Ma for the La Esperie Batholith in the Alóag – Santo Domingo road. Similarly, volcanic rocks previously mapped as the Naranjal Unit (e.g. Boland et al., 2000), in the northern part of the Western Cordillera, yield a $^{40}Ar/^{39}Ar$ age of 35.12±1.66 Ma, indicating that Late Eocene volcanism was widespread, and may in fact represent a northern continuation of the Eocene Macuchi arc. This also corroborated by Late Eocene biostratigraphic ages reported for turbidites intercalated with volcanic rocks of the Macuchi Unit (Egüez, 1986).

4.3.5 The latest Eocene - Oligocene volcanic arc

The Oligocene $^{40}Ar/^{39}Ar$ age from the San Juan de Lachas Formation are consistent with a K/Ar age (hornblende) of 32.6 Ma, reported by Van Thournout et al. (1992). Previous authors correlated the San Juan de Lachas Formation with the Silante Formation (e.g. Van Thournout, 1991); however, the new data presented here demonstrated that both formations are different in age, and most likely, the San Juan de Lachas Formation may represent the Oligocene continuation of the volcanism of the Macuchi Unit. However, an important deformation event had to occur at the beginning of the Oligocene, before deposition of the San Juan de Lachas Formation, because this formation is unconformably overlying sedimentary rocks of the Eocene El Laurel Formation.

CHAPTER 5: GEOLOGICAL EVOLUTION OF THE WESTERN CORDILLERA

Several authors have proposed that basement rocks of the flat coastal region and the Western Cordillera of Ecuador consist of volcanic rocks that have geochemical affinities with oceanic plateaus (e.g. Lapierre et al. 2000; Boland et al., 2000; Kerr et al., 2002b; Mamberti et al., 2003). Furthermore, it has also been emphasized that the basement of western Ecuador can be specifically correlated with oceanic plateau rocks that are currently exposed in the Caribbean Plate, and in western Colombia (e.g. Lapierre et al., 2000; Spikings et al., 2001; Kerr et al., 2002b). Therefore, this chapter initially presents the main geological features of the fragmented Caribbean Plateau and associated volcanic rocks, which provides useful information for understanding the tectonic provenance of the Late Cretaceous allochthonous oceanic blocks accreted to the Ecuadorian continental margin.

5.1 THE CARIBBEAN PLATEAU

Seismic data (Mauffret and Leroy, 1997) reveal the presence of anomalously thick oceanic crust in the Caribbean Plate. Extensive geochemical analyses of rocks drilled in the Caribbean Basin, as well as onshore, yield E-MORB geochemical characteristics, which have been interpreted to represent an oceanic plateau, which comprises a majority of the Caribbean Plate basement (e.g. Lapierre et al., 2000; Kerr et al., 2003; Mamberti et al., 2003).

Fragments of the Caribbean Plateau are exposed in Panama, Costa Rica, northern Venezuela, Aruba, Curacao, and the Dominican Republic (Fig. 5.1; Revillon et al., 2000; Lapierre et al., 2000; Kerr et al., 2003). However, it has recently been suggested that the oceanic plateau sequences in Colombia and Ecuador may represent accreted fragments of the Caribbean Plateau (e.g. Spikings et al., 2001; Kerr et al., 2003). The crustal thickness of the Caribbean Plateau is ~20 km (Sinton et al., 1998; Revillon et al., 2000), and a majority of authors agree that the rocks erupted in the Pacific Ocean (e.g. Duncan and Hargraves 1984; Pindell et al. 1988; Burke, 1988; Pindell and Barret 1990; Kerr et al., 2003). A key piece of evidence for a Pacific origin is the presence of Cretaceous microfossil fauna across the Caribbean Plateau, which is similar to contemporary fauna in the Pacific Ocean (Montgomery et al., 1994).

The South and North American continental plates rifted apart during the Triassic to Late Cretaceous, resulting in the formation of a continental gap, which permitted the Caribbean Plateau to migrate towards the east-northeast, from the Pacific Ocean, into its present position. ENE drift of the Caribbean Plateau resulted in the subduction of proto-Caribbean oceanic crust below the leading edge of the oceanic plateau. The Caribbean Plateau was probably wider than the inter-continental gap between the North and South American Plates, resulting in collisions between those plates and the Caribbean Plateau during the Late Cretaceous (e.g. Burke, 1988; Pindell et al., 2005). The subsequent eastward migration of the Caribbean Plateau between the American continental plates resulted in complex transcurrent boundaries, and deformation

of the plate boundaries in, for example, Yucatan, Colombia and Venezuela, and subduction beneath the northern margin of the South American Plate (Pindell et al., 2005). Faulted units of T-MORB and E-MORB picrites, basalts, dolerites and ankaramites in the forearc and arc regions of Ecuador and Colombia are testament to fragmentation of the plateau, which may have occurred during its collision with the continental plate.

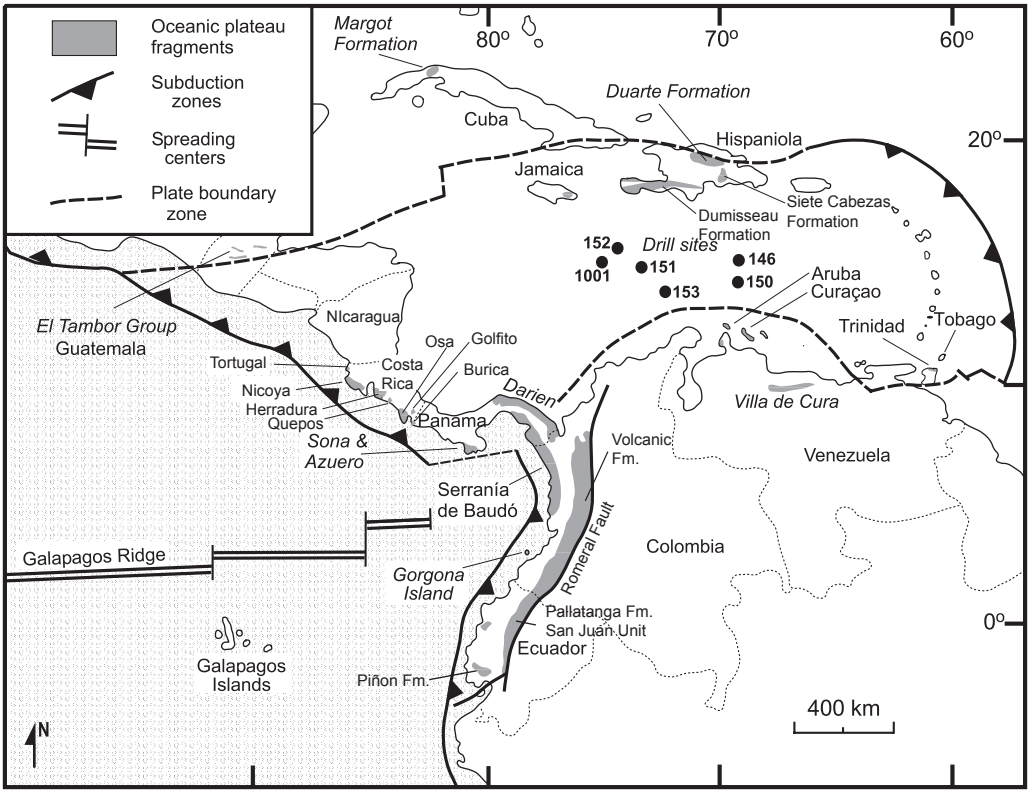

Fig. 5.1. Exposures of oceanic plateau fragments in northern South America and Caribbean region. After Kerr et al. (2003).

5.2 AGE AND ORIGIN OF THE CARIBBEAN PLATEAU

Table 5.1 presents a summary of radiometric ages obtained from basalts, basaltic andesites and gabbros in plateau sequences, as well as biostratigraphic ages from intercalated sediments within the plateau rocks in the Caribbean region and northwestern South America. Clearly, a majority of ages cluster between 92-88 Ma, although a younger, minor phase of volcanism occurred during 76-72 Ma (e.g. Kerr et al; 2003).

Hoernle et al. (2004) obtained $^{40}Ar/^{39}Ar$ ages from glasses and whole rock samples of oceanic plateau basalts in the Nicoya Peninsula (Costa Rica), of 118±5 Ma and 137±2 Ma. These authors suggest the ages reveal the presence of an earlier volcanic pulse of plateau volcanism, fragments of which may also include Albian –Aptian lavas in Cuba (Kerr et al., 1999), and ultramafic and mafic cumulate rocks that yield a Sm/Nd age of 123±13 Ma age (Lapierre et al., 2000), in the Western Cordillera of Ecuador. However, is not possible to confirm that these geographically scattered Early Cretaceous ages are genetically related, or even if they are accurate.

Possibly the 123±13 Ma age reported in Ecuador may represent a fragment of Jurassic to Early Cretaceous oceanic crust, which accreted against South America during the Early Cretaceous (e.g. Litherland et al., 1994). Consequently, a majority of oceanic plateau volcanism that is now located in the Caribbean region, erupted during 92-88 Ma, which coincides with the radiometric crystallization ages obtained from the Piñon and Pallatanga blocks in Ecuador (Luzieux et al., 2006; Vallejo et al., 2006).

Location	Method	Age range (Ma)	References
Northern Caribbean Plate Boundary			
DSDP Leg 15 Site 146	$^{40}Ar/^{39}Ar$	90.6-92.1	Sinton et al. (1998)
DSDP Leg 15 Site 150	$^{40}Ar/^{39}Ar$	94.3	Sinton et al. (1998)
ODP Leg 165 Site 1001	$^{40}Ar/^{39}Ar$	80.8-81.3	Sinton et al. (2000)
Dumisseau Formation, Haiti	$^{40}Ar/^{39}Ar$	88.7–92.0	Sinton et al. (1998)
Duarte Complex, Dominican Republic	$^{40}Ar/^{39}Ar$	86.1 and 86.7	Lapierre et al. (1999a)
Siete Cabezas Formation, Dominican Republic	$^{40}Ar/^{39}Ar$	68.5 and 69.0	Sinton et al. (1998)
El Tambor Group, Guatemala	biostratigraphy	Older than Cenomanian	Donnelly et al. (1990)
Margot and Encrucijada Formations, Cuba	biostratigraphy	Aptian-Cenomanian (124–90)	Kerr et al . (1999)
Bath-Dunrobin Formation, Jamaica	biostratigraphy	Campanian (83–74)	Wadge et al. (1982)
Southern Caribbean Plate Boundary			
Golfito and Burica Complexes, Costa Rica	biostratigraphy	Maastrichtian (74–68)	Di Marco (1994)
Nicoya Complex, Costa Rica	$^{40}Ar/^{39}Ar$	94.7–87.5* and 83.0#	Sinton et al.(1997); Hauff et al. (2000b)
	$^{40}Ar/^{39}Ar$	118 ± 5 Ma and 137±2 M	Hoernle et al. (2004).
Tortugal Complex, Costa Rica	$^{40}Ar/^{39}Ar$	89.7	Alvarado et al. (1997)
Herradura Complex, Costa Rica	$^{40}Ar/^{39}Ar$	86.0–83.4	Sinton et al.(1997); Hauff et al. (2000b)
Quepos Complex, Costa Rica	$^{40}Ar/^{39}Ar$	59 and 63.9	Hauff et al. (2000) ; Sinton et al. (1997)
Osa Complex, Costa Rica	$^{40}Ar/^{39}Ar$	62.1	Hauff et al. (2000)
Curacao Lava Formation	$^{40}Ar/^{39}Ar$ (Re-Os)	88.0–89.5 and 75.8 85.6 ± 8.1 (Re-Os)	Sinton et al. (1998) Walker et al. (1999)
Aruba Lava Formation	biostratigraphy	Turonian (90.5–88.5)	Beets et al. (1984); White et al. (1999)
Tiara Formation, Villa de Cura, Venezuela	biostratigraphy	Albian (97–112)	Beck et al. (1984)
Northern Andes			
Central Cordillera, Colombia	$^{40}Ar/^{39}Ar$	82.6 and 84.7	Kerr et al. (2002b)
Western Cordillera, Colombia	$^{40}Ar/^{39}Ar$	91.7 and 76.3	Kerr et al. (1997); Sinton et al. (1998)
Serranía de Baudó, Colombia	$^{40}Ar/^{39}Ar$	77.9–72.5	Kerr et al. (1997)
Gorgona Island, Colombia	$^{40}Ar/^{39}Ar$ (Re-Os)	88.3–86.7 88.1 ± 3.8 / 89.2 ± 5.2	Sinton et al. (1998) Walker et al. (1991; 1999)
Piñón Fm. Ecuador	biostratigraphy	At least Turonian (90.5–88.5)	see Jaillard et al. (1995)
Piñón Fm. Ecuador	$^{40}Ar/^{39}Ar$	88.8 ± 1.6	Luzieux et al. (2006)
San Juan Unit?, Ecuador	Sm-Nd	123 ± 13	Lapierre et al. (2000)
San Juan Unit, Ecuador	(U/Pb SHRIMP)	87.1 ± 1.66	Vallejo et al. (2006)
Totoras Amphibolite, Ecuador	$^{40}Ar/^{39}Ar$	84.69±2.22	Vallejo et al. (2006)

The $^{40}Ar/^{39}Ar$ ages from Sinton etal (1997; 1998 ;2000); Kerr et al.(1997a; 2002b) Alvarado et al. (1997) and Luzieux et al. (2006) are all step-heating plateau ages, whereas the $^{40}Ar/^{39}Ar$ ages reported by Hauff et al. (2000) are isochron ages.
*Ages for Nicoya basalts and dolerites.
#Ages for Nicoya intrusives.

Table 5.1. Summary of radiometric (mostly $^{40}Ar/^{39}Ar$) and biostratigraphic ages on oceanic plateau rocks from the Caribbean and Northern South America not all papers report their ages fully, and hence is not possible to evaluate their precision and accuracy. (Modified from Kerr et al., 2003).

Reconstruction of the Late Cretaceous history of the Caribbean Plateau is hampered by the lack of spreading ridges and a paucity of datable magnetic anomalies in the Caribbean region. Apart from incomplete geological mapping, there has been no formal identification of the original oceanic crust through which the Caribbean plateau intruded and erupted. Most models of the geological evolution of the Caribbean Plateau propose that it originated from the Galápagos mantle plume, located beneath oceanic crust of the Farallon Plate (e.g. Duncan and Hargraves, 1984; Spikings et al., 2001, Hoernle et al., 2002; Thompson et al., 2003).

The wide range of radiometric and paleontological ages, combined with variations in geochemical composition, are considered to reflect the presence of multiple plume heads, which were active during the Cretaceous, some of which may be represented by the Sala and Gómez hotspot in the southern Pacific (e.g. Reynaud et al., 1999; Lapierre et al., 2000, Kerr et al., 2002b; Kerr and Tarney, 2005). However, paleomagnetic data acquired from E-MORB type rocks of the Ecuadorian forearc (Roperch et al., 1987, Luzieux et al., 2006) and the Caribbean Basin (Acton et al., 2000) suggest that oceanic plateau rocks, which crystallized at ~90 Ma, erupted at equatorial paleolatitudes. Consequently, a multiple plume model is not required to account for the ~90 Ma E-MORB ultramafic and mafic rocks found in the flat forearc and Western Cordillera of Ecuador. However, as suggested by Revillon et al. (2000), older episodes of plateau volcanism (assuming that their Early Cretaceous ages are accurate) may be related to a mantle plume that was located in the southern Pacific Ocean.

5.3 THE GREAT ARC OF THE CARIBBEAN

Intrusive and extrusive Cretaceous rocks with island arc geochemical affinities are associated with the oceanic plateau rocks, in the Caribbean region and northwestern South America, (Fig. 5.2). The Late Cretaceous island arc sequences in the Caribbean region included both IAT (island arc tholeiites) and CA (calc-alkaline series) types. Burke (1988) indicated that this island arc system originated in the eastern Pacific Ocean, and subsequently migrated towards the central Atlantic Ocean. The oldest arc rocks yield Late Jurassic ages (e.g. on the island of La Desirade; Fig. 5.2), and formed above an east-dipping subduction zone, which consumed the Farallon Plate beneath the North American Plate (Fig. 5.3). This early arc sequences in commonly referred to as the Great Arc of the Caribbean. Fragments of subducted crust are still preserved in the Caribbean Plate (e.g. Tobago), where they are usually associated with high-pressure metamorphic rocks, and are overlain by Albian sedimentary rocks (Mattson and Pessagno, 1979; Pindell et al., 2005).

According to several authors (Burke, 1998; Kerr et al., 1998; White et al., 1999), the Caribbean Plateau may have collided with the proto-Great Arc of the Caribbean during the Late Cretaceous. Burke (1988) suggested that this event resulted in a subduction polarity change, from east-dipping to west-dipping subduction. However, more recently Pindell et al. (2005) proposed that the polarity reversal event occurred in the Aptian, prior to the eruption of a plateau

(Fig.5.3). The subduction polarity event, which resulted in a west-dipping subduction zone, was subsequently responsible for northeasterly drift of the Caribbean Plateau from the Pacific, to the oceanic gap that formed between the North and South American plates. This subduction zone is active today at the eastern boundary of the Caribbean Plate, where it is responsible for volcanic activity in the Lesser Antilles Arc. Regardless of when the subduction polarity flip occurred, westward subduction consumed the proto-Caribbean ocean floor below the oceanic plateau during the Santonian, giving rise to a Late Cretaceous arc, which is commonly referred to as the Great Arc of the Caribbean (Fig. 5.3).

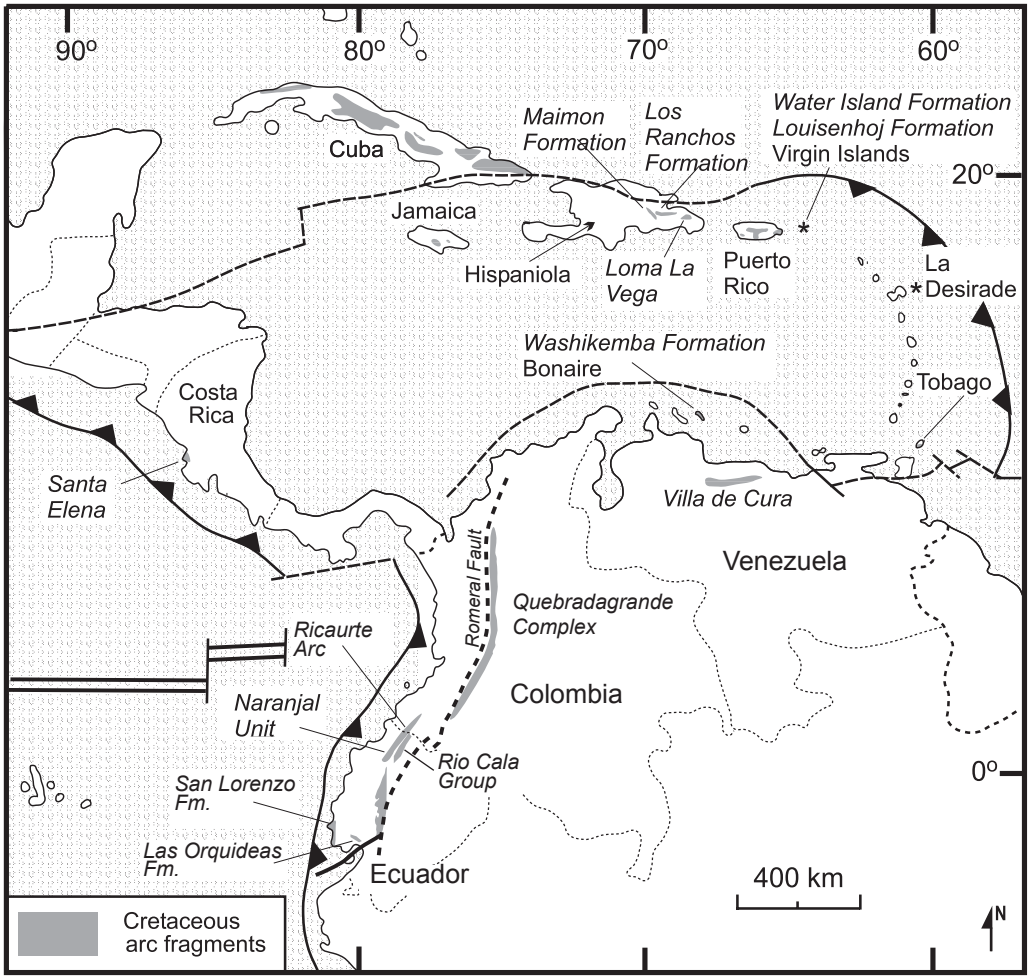

Fig. 5.2: Map showing the location of known Cretaceous island-arc rocks in the Caribbean and Central and South America. (Kerr et al., 2003).

5.4 LATE CRETACEOUS OCEANIC PLATEAU AND ISLAND ARC SEQUENCES IN THE NORTHERN ANDES (ECUADOR AND COLOMBIA)

Volcanic rocks with E-MORB, mantle plume affinity have been recognized in Colombia by several authors (e.g. McCourt et al., 1984; Millward et al., 1984; Nivia et al., 1996; Kerr et al., 1998). These rocks are exposed west of the Romeral Fault (Restrepo and Toussaint, 1974; Aspden

and McCourt, 1986; Aspden et al., 1987; Megard, 1987; Spadea et al., 1989; Nivia, 1996; Kerr et al., 1997), which is considered to be the northern extension of the Peltetec Fault of Ecuador (Fig. 5.4). Lithologies include tholeiitic basalts, dolerites and gabbros, with intercalations of cherts and shales, which collectively crop-out in the Western Cordillera of Colombia that is the northward continuation of the Western Cordillera of Ecuador.

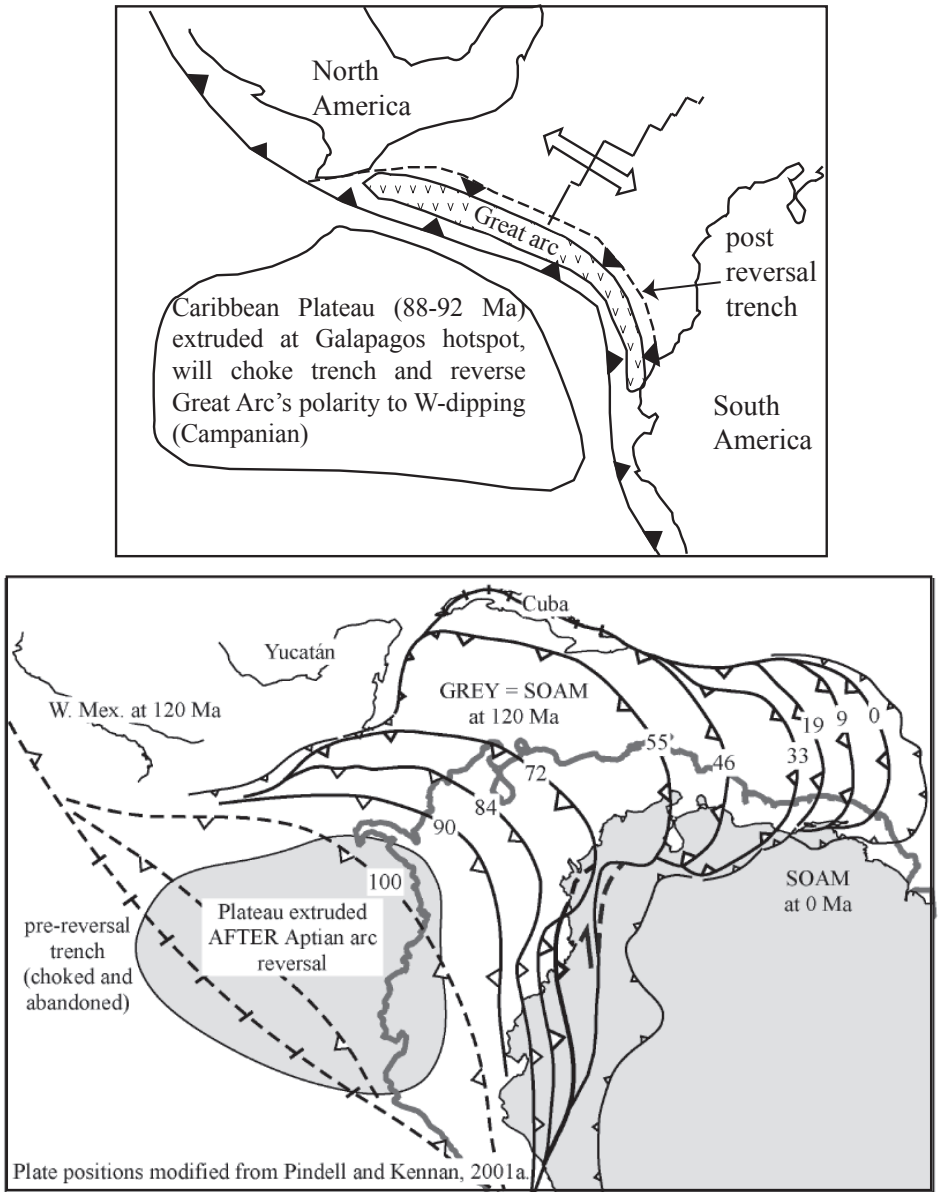

Fig. 5.3. A) Tectonic reconstruction of the Caribbean region during the Coniacian, based on Burke (1998). The Caribbean Plateau originated in the Pacific Ocean and then moved between North and South America, colliding with the Great Arc of the Caribbean and reverse the polarity of subduction in the Campanian. B) According to Pindell (1993) the Caribbean Plateau extruded onto Farallon Crust after the subduction polarity reversal, which may have occurred in the Early Cretaceous (from Pindell et al., 2006).

The oceanic plateau basement of the Colombian Western Cordillera is known as the Diabase Group (Millward et al., 1984), or the Volcanic Formation (Nivia, 1996; Kerr et al., 1997).

The western most sequences in Colombia are Cretaceous, plume-derived (Kerr et al., 1997) volcanic rocks (basalts, gabbros and dolerites), exposed in the Serranía de Baudó region along the Pacific coast (Figure 5.4). Fragments of volcanic rocks with oceanic plateau affinities are also exposed on the western border of the Central Cordillera. (Fig. 5.4), and Gorgona Island includes high magnesium komatites and picrites, which have oceanic plateau affinities (e.g. Kerr and Tarney, 2005).

Geochemical and petrographic similarities between oceanic plateau sequences in Colombia and the Caribbean region lead several authors (e.g. Millward et al., 1984; Nivia, 1996; Kerr et al., 2003) to group them together as part of the genetically related "Caribbean-Colombian Oceanic Plateau" (CCOP).

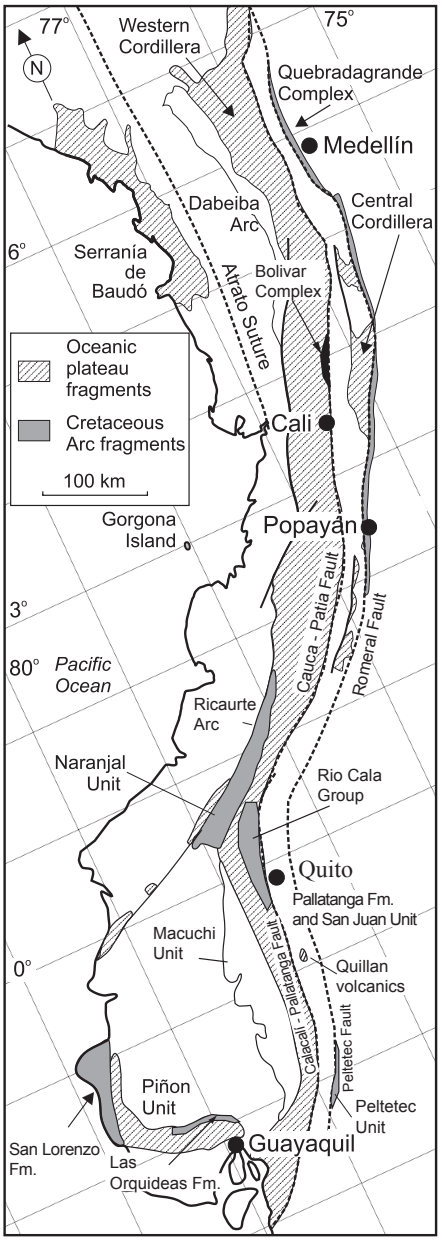

Fig. 5.4. Map showing the exposures of Cretaceous oceanic plateau and island arc sequences in the western regions of Colombia and Ecuador (modified from Kerr et al., 2003).

Oceanic plateau rocks in the Western Cordillera of Colombia yield $^{40}Ar/^{39}Ar$ ages (whole rock) of 91.7±2.7 and 76.3±1.6 Ma (Sinton et al., 1998), and similar rocks in Gorgona Island yield Re-Os isochrons with ages of 89.2±5.2 (Walker et al., 1999). These ages are similar to those found in the Caribbean Plate. However, mantle-plume derived rocks of the Serranía de Baudo yield whole rock and plagioclase $^{40}Ar/^{39}Ar$ plateau ages ranging between 78 – 73 Ma (Kerr et al., 1997), and an age of 70±3.5 Ma (although the geochronological method is unspecified; Bourgois et al., 1982), which are younger than a majority of ages obtained from the Caribbean Plate.

In Ecuador, oceanic plateau sequences are exposed in the Western Cordillera and coastal region. In the Western Cordillera they are referred to as the Pallatanga Unit, which crystallized during 87.1±1.66 Ma (see chapter 4). The oceanic plateau basalts and gabbros of the Piñón Formation in coastal Ecuador, yield an indistinguishable $^{40}Ar/^{39}Ar$ plateau age (hornblende) of 88±1.6 Ma (Luzieux et al., 2006; Luzieux, 2007). A small inlier of basalts and dolerites, which yield oceanic plateau geochemical affinities (Mamberti et al., 2003), is exposed in the central Interandean Valley, east of Ambato (Quillán; Fig. 5.4). Unfortunately, they have not been dated using an accurate radiometric method, but their presence may suggest that the basement to the Interandean Valley is partly formed by fragments of oceanic plateau rocks.

Coteccia and Zezza (1969) report a K/Ar age (mineral phase not reported) of 51.5 ± 2.5 Ma, although this age may be partially reset. Cretaceous island arc sequences are preserved in Colombia in the Quebrada Grande Complex (Nivia et al., 1996; Kerr et al., 1997) and the Ricaurte Arc of southern Colombia (Spadea and Espinosa, 1996). Both sequences yield arc geochemical signatures, including negative Nb anomalies, high LREE and LILE (Kerr et al., 2003). Fossils from sedimentary rocks of the Quebrada Grande Complex yield Hauterivian to Albian ages, whereas biostratigraphic ages from sedimentary rocks intercalated in the Ricaurte Arc yield Campanian ages (Spadea and Espinosa, 1996).

Late Cretaceous island arc sequences in Ecuador are found in two areas; the costal region and the Western Cordillera. In the coastal region, basalts and gabbros with island arc geochemical affinities are known as the San Lorenzo and Las Orquideas Formations (Reynaud et al., 1999; Luzieux et al., 2006).

Both sequences overlie oceanic plateau volcanic rocks of the Piñón Formation. Basalts of the San Lorenzo Formation yield a $^{40}Ar/^{39}Ar$ age (plagioclase) of 72.7±1.4 Ma (Lebrat et al., 1987), whereas the Las Orquideas Formation may have a Campanian age (Luzieux, 2007), although its exposure is poor and it is undated.

In the Western Cordillera the Rio Cala Group has geochemical signatures similar to rocks formed in an intraoceanic island arc sequence on top of an oceanic plateau. Biostratigraphic (Boland et al., 2000) and radiometric dating (this study), strongly indicates that the island arc sequence preserved in the Western Cordillera was active from the Santonian until the Early Maastrichtian, which overlaps with the biostratigraphic and radiometric ages reported for

island arc sequences in the coastal region (Lebrat et al., 1987; Luzieux, 2007). Similarly, trace element concentrations of island arc basalts in the coastal region partially overlap with their concentrations within the island arc basalts and andesites of the Western Cordillera (Fig. 5.5), which implies that both volcanic series may correspond to the same island arc system.

Late Cretaceous island arc rock types of Colombia have similar island arc geochemical signatures to those yielded by the island arc rock types preserved in the coastal region and Western Cordillera of Ecuador (Fig. 5.5). Kerr et al. (2002) already noticed similarities between the island arc rocks of the Ricaurte Arc of southern Colombia with the island arc volcanic rocks of the Naranjal Unit, both of which yield Campanian biostratigraphic ages. Similarly, there is an overlap of the REE concentrations of volcanic rocks of the Ricaurte Arc of Colombia and San Lorenzo arc of the coastal region (Fig. 5.5), which suggests that the Ricaurte Arc is the northern continuation of the Late Cretaceous island arc sequences of the Western Cordillera and coastal region of Ecuador.

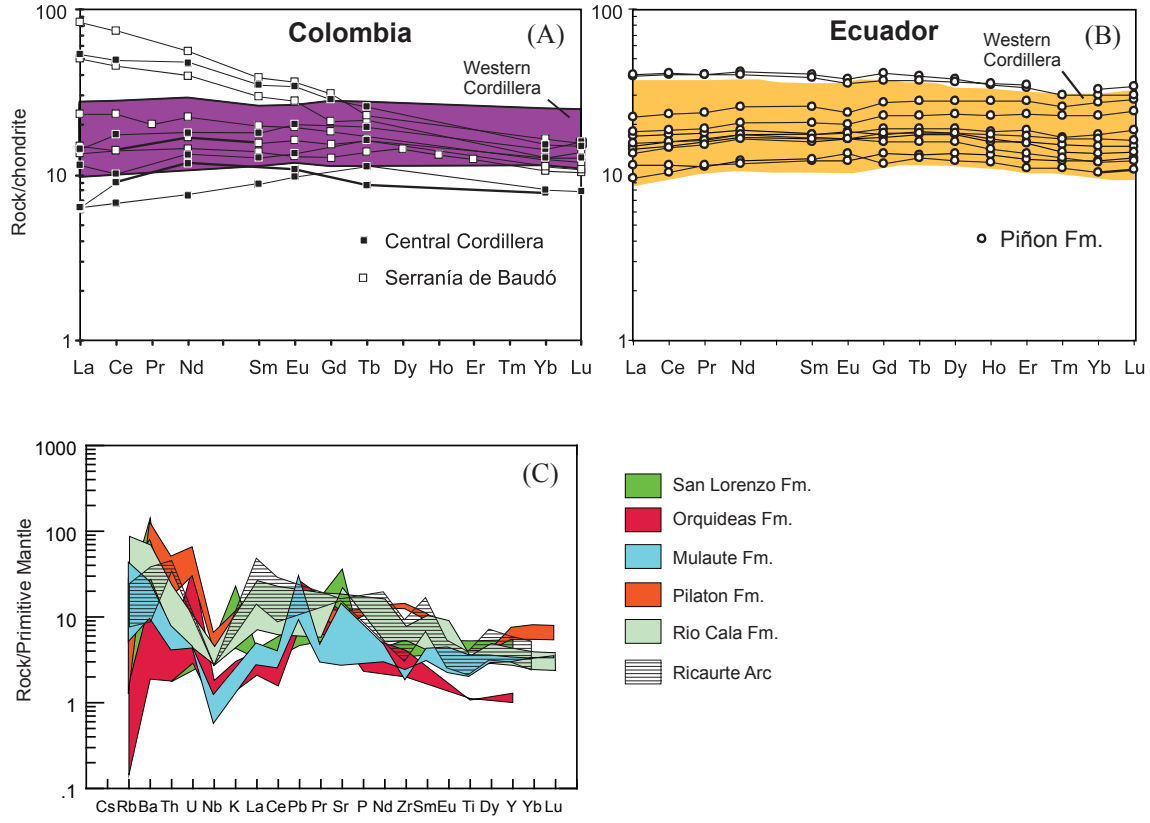

Fig. 5.5. Chondrite normalized (Sun and MacDonough 1989) REE concentrations of volcanic rocks with oceanic plateau affinity in Colombia (A) and Ecuador (B). Primitive mantle normalized (Sun and McDonough 1989) multi-element plot of Late Cretaceous island arc rocks of the Western Cordillera and coastal region of Ecuador, and the Ricaurte Arc of the Western Cordillera of Colombia (C). (Redraw from Kerr et al., 2002; Kerr et al., 2003, Spadea and Espinosa, 1996 and own data).

Therefore, given the chronological and geochemical similarities of island basalts and

gabbros, and oceanic plateau lithologies in the northern Andes and the Caribbean Plate (Table 5.1), as well as the late Cretaceous oceanic plateau and island arc rocks in the coastal region and Western Cordillera of Ecuador represent accreted fragments of the same large igneous province that collided against the South American Plate during the Late Cretaceous.

5.5 INACCURANCE IN PREVIOUS GEODYNAMIC MODELS OF THE WESTERN CORDILLERA

Several models have been proposed for the tectonic evolution of the Western Cordillera of Ecuador (e.g. Feininger and Bristow, 1980; Eguez, 1986; Lebrat et al., 1987; Van Thournout, 1991; Kerr et al., 2002; Spikings et al., 2005). Most of these models suggest that allochthonous oceanic blocks (i.e. Pallatanga and/or Macuchi) drifted towards the South American Plate by double eastward subduction of oceanic crust with an intervening island arc (e.g. Egüez, 1986; Lebrat et al., 1987; Kerr et al., 2002).

The proposed time of collision of the allochthonous basement of the Western Cordillera, varies from the Late Cretaceous to Late Eocene (Aspden et al., 1992b; Lebrat et al., 1987, Kerr et al., 2002, Spikings et al., 2005). Aspden et al. (1992b) proposed that reset K/Ar isotopic ages in the Eastern Cordillera at 85-65 Ma, and the deposition of Maastrichtian terrestrial, red bed sediments in the Oriente Basin (Tena Fm.) were driven by regional uplift related to accretionary processes in the Western Cordillera and fore arc regions. Hughes and Pilatasig (2002) and Kerr et al. (2002) utilized stratigraphic relationships to propose that the Pallatanga Block accreted against the continent during the Campanian (83-74 Ma). Several models assumed a Late Cretaceous age for the undated Macuchi Unit (e.g. Henderson, 1979; Kennerly, 1980). Similarly, different ages reported for the mantle-plume derived basement rocks of the Piñon and Pallatanga blocks, which are based in erroneous stratigraphic relationships, lead to suggestions that these blocks collided with the South American Plate at different times, during the Late Cretaceous to the Late Eocene (e.g. Jaillard et al., 1995; Hughes and Pilatasig, 2002; Kerr et al., 2002; Spikings et al., 2005).

The results obtained in the current study do not support previous models that invoke multiple accretion events since the Late Cretaceous because:

- There is no evidence for east-dipping subduction beneath the Ecuadorian sector of the South American Plate during the Late Cretaceous. Late Cretaceous volcanism is restricted to intraplate alkaline basalts, which are intercepted in boreholes in the Oriente Basin, which formed via intracratonic, asthenospheric upwelling (Barragán et al., 2005); subduction related volcanism was restricted to northern Peru. Paleotectonic reconstructions (e.g. Ross and Scotese, 1988) place a transform fault proximal and parallel to the border of the Ecuadorian margin. Consequently, the consumption of oceanic crust between the South American Plate and the Caribbean Plateau, was achieved by west-dipping subduction beneath the Caribbean Plateau.
- Previous evolutionary models of the Western Cordillera, assigned an Early Cretaceous age to the Piñón Formation (e.g. Goosens and Rose, 1973; Jaillard et al., 1995), based on

erroneous biostratigraphic dating of the overlying marine sedimentary rocks, and the Pallatanga Fm. was undated. However, the Pallatanga and Piñon formations have the same age (~ 88 Ma; Luzieux et al., 2006; Vallejo et al., 2006).

- Late Eocene accretion of the Macuchi Block is unlikely, because the Macuchi Unit yields Late Eocene ages (Las Juntas Turbidites), which is confirmed with our $^{40}Ar/^{39}Ar$ radiometric analyses of a basalt of the Macuchi Unit (see chapter four). Furthermore, and possibly more importantly, Luzieux et al., (2006) utilized paleomagnetic data to show that the Piñón Block accreted during the Late Cretaceous, at the same time that the Pallatanga Block accreted (Vallejo et al., 2006), implying that they formed a single block. Consequently, it is geometrically challenging to suggest that the Macuchi Block accreted in the Late Eocene, and inserted itself between the Piñon and Pallatanga Blocks. Such a scenario implies the existence of complicated transcurrent faulting of large magnitude (e.g. 100's kms).

5.6 GEODYNAMIC EVOLUTION OF THE WESTERN CORDILLERA

This study propose a new, testable model for the geological evolution of the rocks of the Western Cordillera of Ecuador, which is based on the data presented in this, and earlier studies (e.g. Egüez, 1986; BGS-CODIGEM mapping program 1996-2002).

The model presented here, is supported by a consistent stratigraphic framework for the igneous volcanic basement and the sedimentary and volcanic cover, considering that the mantle-plume derived mafic and ultramafic rocks of the basement of the Western Cordillera and the coastal region were originally part of the same oceanic plateau (Vallejo et al., 2006; Luzieux et al., 2006; Luzieux, 2007) that is equivalent to the ~88 Ma CCOP. According to the results presented in this study, the geology can be accounted for by only one accretion event, and that subsequent volcanic activity was almost continuous since the latest Maastrichtian.

5.6.1 Coniacian (88 Ma): The origin of the crystalline basement.

The zircon U/Pb (SHRIMP) age of 87.1±1.66 Ma (2σ) from an E-MORB type gabbro of the San Juan Unit, is the first U/Pb radiometric age to be obtained from mafic basement rocks of the oceanic plateau rocks of the Western Cordillera. The U/Pb age is consistent with volcanism associated with the Caribbean Plateau during 91–88 Ma (Sinton et al., 1998) and an $^{40}Ar/^{39}Ar$ age of 88±1.6 Ma (2σ) from oceanic plateau rocks of the coastal Piñón Formation (Luzieux et al., 2006). The Totoras amphibolites may have formed shortly after the plateau extruded at the base of the plateau, and the $^{40}Ar/^{39}Ar$ age (hornblende) of 84.69±2.22 Ma (2σ) indicates the time of cooling below ~550-500°C, during retrogression after amphibolite facies metamorphism.

Paleomagnetic analyses of the Piñón Formation (Luzieux et al., 2006) show that these rocks crystallized at equatorial or low southern latitudes. However, is not possible to reconstruct their original longitudinal separation from the margin of the South American Plate.

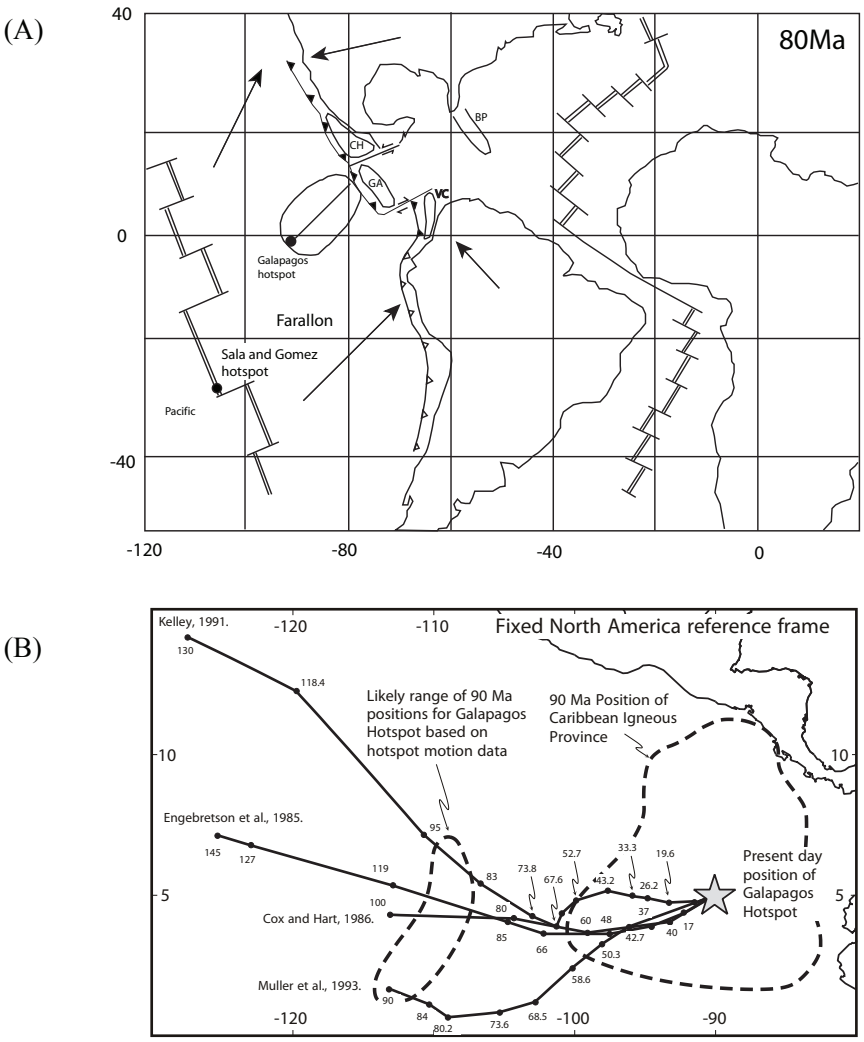

Fig. 5.6 Two contrasting interpretations for the positions of the Galapagos hotspot during the late Cretaceous and its relationship with the origin of the Caribbean Plateau. (A) Paleotectonic reconstruction of the Caribbean region at 80 Ma. Plate positions and motions in the hotspot reference frame (Duncan and Hargraves, 1984). In this model the Caribbean Plateau was originated from the Galapagos hotspot, however, according to the direction of movement of the Farallon Plate (NE), the plateau would have not collide against South America. (B) Position of the Caribbean Plate at ~90 Ma after Pindell et al., 2006. These authors indicate that the Caribbean Plateau was located at least 1000 km east of the Galapagos Hotspot at that time, which suggest that the plateau was not extruded from the Galapagos Hotspot.

The Late Cretaceous paleotectonic reconstruction and plate movements of the Caribbean Plateau and Farallon Plate relative to South America are still not well constrained, and plate reconstructions of the Caribbean Plate tend to be inaccurate for the Ecuadorian region because of the lack of quantitative data. Duncan and Hargraves (1984) proposed a model in which the ~90 Ma Caribbean Plateau formed above the Galapagos hotspot (Fig. 5.6A) and its eastern edge was located ~2200 km east of the South American Plate. Consequently, the plateau would have

to drift eastwards to collide with the north-western South American Plate. However, this is not fully consistent with NE directed drift of the Farallon Plate, as proposed by Pilger (1983) and Engebretson (1985). Furthermore, Pindell et al. (2006) suggested that the Galápagos hotspot was located ~1000 km west of the site were the Caribbean Plateau extruded (Fig. 5.6B).

Such contrasting reconstructions reflect the paucity of quantitative data, and as already suggested by Pindell et al. (2006), the Caribbean Plateau may have originated closer to the South American margin. By considering the northeast ward movement of the Farallon Plate during the Late Cretaceous, it is likely that the leading edge of the Caribbean Plateau obliquely collided with the north-western South American Plate (Fig. 5.7).

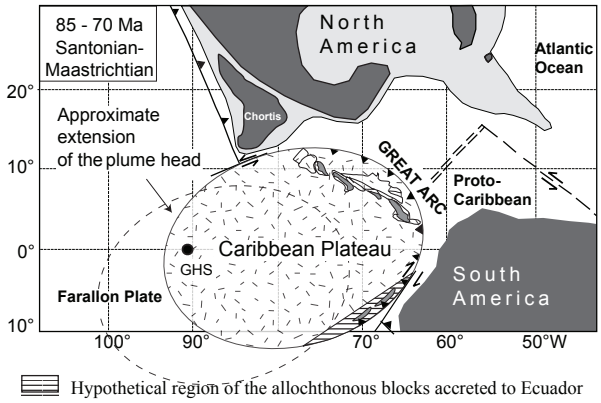

Fig. 5.7. Reconstruction of the Caribbean Plateau during the Santonian-Maastrichtian. (modified from Ross and Scotese, 1988). Schematic postulated extensions to the Great Arc of the Caribbean have been made to include the Rio Cala Arc sequence. The Pallatanga Block is shown as a fragment of the Caribbean Plateau. GHS: Galapagos hotspot.

5.6.2 Santonian to Early Campanian (85-83 Ma): Initiation of subduction below the oceanic plateau

The initiation of west-dipping subduction at the leading edge of the plateau was probably responsible for the generation of the Santonian ocean island-arc related, Pujilí Granite, and boninites of the La Portada Formation. The time-span between the eruption of oceanic plateau basalts and the island-arc sequence suggests that migration of the Caribbean Plateau and subsequent initiation of westward subduction below the plateau occurred within ~3 my of the eruption of the plateau.

Given the short time span between the initiation of subduction, and arc volcanism, it is worth considering the mechanism that initiated subduction at the leading edge of the plateau. Burke (1988) argued that collision of the oceanic plateau with the pre-90 Ma Proto-Great Arc of the Caribbean (Fig. 5.3) occurred shortly after the plateau was erupted (~3 Ma), resulting in subduction polarity reversal and the initiation of westward subduction below the oceanic plateau. White et al. (1999) proposed a similar scenario for the origin of the ~86 Ma Aruba

Batholith in the Leeward Antilles. According to their model, the time span between eruption of the oceanic plateau, estimated at around 89-87 Ma and the eruption of the Aruba Batholith is only ~2 Ma, suggesting that the process of collision, subduction polarity reversal and arc magmatism occurred within this interval, which is unrealistic. An analogue is provided by the Ontong Java Plateau, which collided against the Solomon island arc in the southwestern Pacific Ocean.

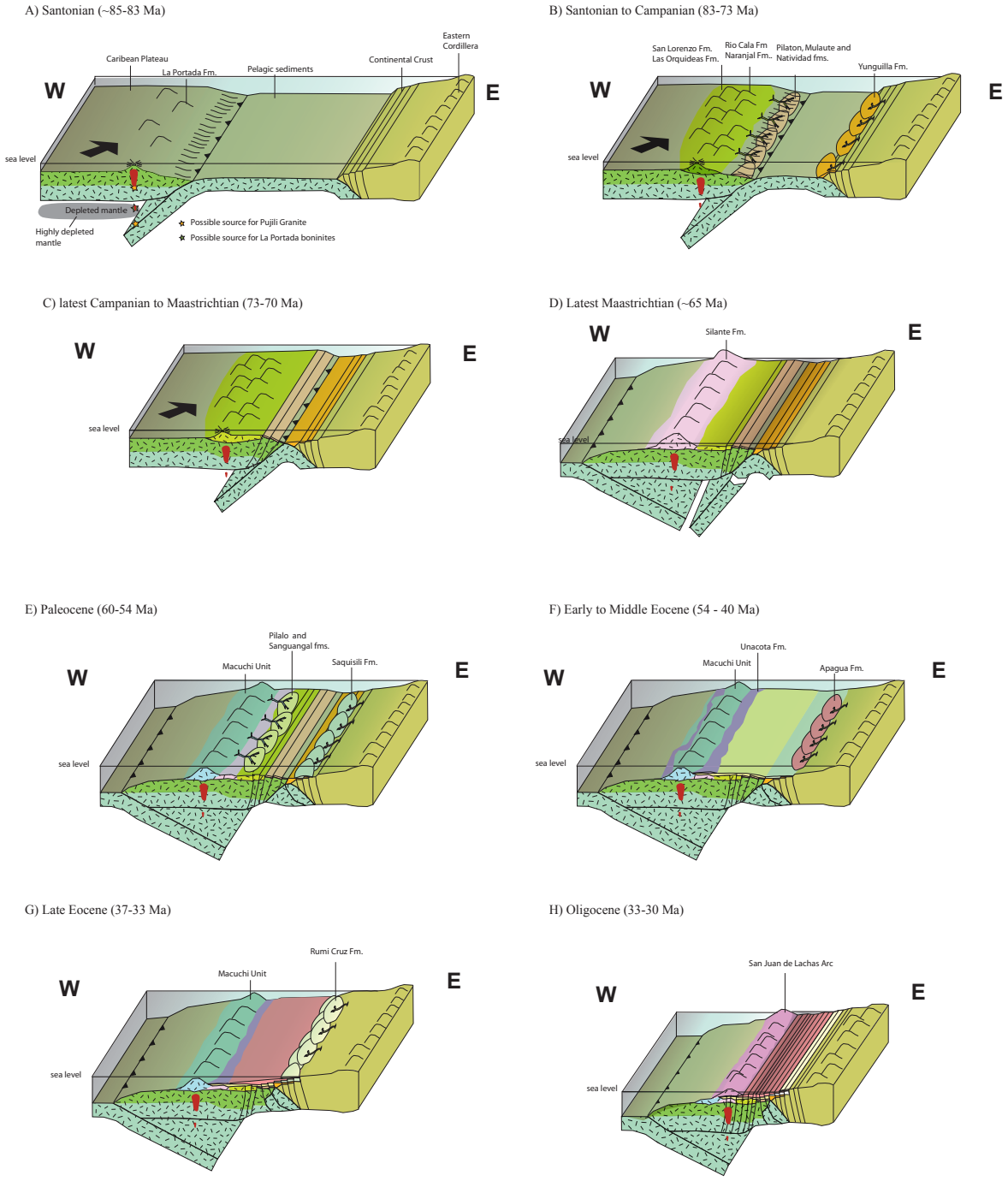

Fig. 5.8 Paleotectonic reconstruction of the Western Cordillera and neighboring areas from the Late Cretaceous to Oligocene. See text for details.

Petterson et al. (1999) indicated that the collision occurred in the Early Miocene, and that subduction flip may have occurred at the Middle Miocene, which suggest that collision and subduction polarity flip processes occur during protracted periods of time (~6 Ma), which is inconsistent with the models of Burke (1988) and White et al. (1999). Therefore, a different mechanism should be invoked to explain the short time between the production of oceanic plateau basalts and island arc rocks.

Niu et al. (2003) proposed that initiation of subduction below an oceanic plateau may be produced by a difference in density between the young and buoyant oceanic plateau and the surrounding MORB of oceanic crust. According to these authors, the edges of buoyant oceanic plateaus that are under deviatoric compression (e.g. ridge push) can fail via reverse faults, allowing the denser MORB to subduct beneath the buoyant overriding oceanic plateau, if frictional forces are overcome. Their model may also account for the formation of Santonian–Campanian boninites of the La Portada Formation, via the initiation of subduction of normal oceanic crust below a hot and highly depleted mantle wedge, beneath the Caribbean Plateau, during the early stages of arc magmatism (Fig. 5.8A), which coincides with a tectonic setting shortly after eruption of the Caribbean Plateau.

The Pujilí Granite, which yields geochemical affinities typical of TTGs and adakitic siliceous melts (see chapter 2), and εNd isotopic values similar to the oceanic plateau (+6), may have also formed during this period via ponding and fractional crystallization of melts at the base of the thick oceanic plateau, and a component derived from the subducting slab during the initiation of subduction. Furthermore rocks with TTG affinities and boninites are broadly considered to be indicative of subduction initiation below thickened oceanic crust (e.g. Niu et al., 2003; Escuder Viruete et al., 2006).

5.6.3 Campanian to Maastrichtian (83-75 Ma): The Rio Cala island arc

The Rio Cala Arc sequence, which is exposed in the northern Western Cordillera, is defined as a series of volcanoclastic turbidites (Natividad, Pilatón and Mulaute formations), with intercalated sequences of basaltic lavas (e.g. the volcanic facies of the Mulaute Formation, the Rio Cala and La Portada formations). This arc sequence may also include the Naranjal Unit of the western border of the Western Cordillera. Trace and major element geochemical signatures of the sedimentary and volcanic facies are typical of rocks formed in an island arc setting. High εNd_i values (+6 to +9) have been obtained from the Rio Cala arc sequence (see chapter 2), which overlap with those acquired from basalts of the Late Cretaceous Caribbean Plateau and Great Arc in the present-day Caribbean region (e.g. Thompson et al., 2003). Turbiditic sedimentary rocks were deposited in submarine fans derived from island arc volcanoes (Fig. 5.8B). As previously demonstrated, the island arc rocks of the Western Cordillera can be temporally and geochemically correlated with island arc rocks of the coastal area, that include the Las Orquideas, San Lorenzo and Cayo formations (Fig. 5.9). Therefore, it is likely that they formed parts of the same island arc system. Trace elements and isotopic data (Pb) indicates that island

arc rocks of the Rio Cala Formation may have erupted throughout an oceanic plateau (Allibon et al., 2005), strongly suggesting a west dipping subduction below the oceanic plateau.

The Yunguilla Formation was deposited in a north-south oriented passive margin basin along the South American continental margin, and is coeval with island arc volcanism. The detritus was eroded from rocks of the present day Eastern Cordillera (Fig. 5.8B), as indicated by our provenance analyses (chapter 3), which defined the contemporaneous continental plate margin.

5.6.4 Latest Campanian to Maastrichtian (~73-70 Ma): Collision of the Pallatanga Block

Subduction related magmatism below the leading edge of the oceanic plateau terminated during the Maastrichtian, indicating that west-dipping subduction ceased, which was probably caused by clogging of the subduction zone during oceanic plateau-continental crust collision (Fig. 5.8C). The cessation of arc magmatism was synchronous with rapid changes in paleomagnetic declination (20-50° vertical axis clockwise rotation; Luzieux et al., 2006) between 73 and 70 Ma in both the Piñon and the San Lorenzo blocks. Furthermore, sedimentary rocks of the Yunguilla Formation, were highly deformed, prior to the deposition of the Paleocene Saquisilí Formation

Collectively, these dramatic and significant events, which occurred simultaneously over large distances (e.g. 1000 km), are interpreted to be a consequence of collision between the South American Plate and the Caribbean Plateau. The same time period is also characterized by rapid cooling and exhumation (>1km/my) in the Eastern Cordillera and the Amotape Complex (Spikings et al., 2000, 2001, 2005), which was probably associated with rock uplift because it was synchronous with the deposition of high-energy sedimentary rocks in the foreland and retro-foreland regions. Aspden et al. (1992b) report widespread resetting of K/Ar ages acquired from Jurassic-Lower Cretaceous rocks in the Cordillera Real during 85–65 Ma. However, it is difficult to assess whether any individual K/Ar age is discordant (excess ^{40}Ar; partially or complete resetting), which may account for the extended age range (20 my), rendering it unsatisfactory for distinguishing between Santonian–early Campanian and late Campanian–Maastrichtian cooling, for example.

The earliest significant cooling and exhumation event detected along the continental margin by ^{40}Ar/^{39}Ar (white mica, biotite) and fission track (zircon, apatite) thermochronology occurred during 75-65 Ma in the Amotape Complex (Spikings et al., 2001; 2005). This has been confirmed by new indistinguishable plateau ^{40}Ar/^{39}Ar ages from Triassic migmatites (U/Pb zircon age of 227 ± 2 Ma; Litherland et al., 1994) of 68.5 ± 0.4 (white mica) and 68.6 ± 0.5 (biotite) Ma from the southern Eastern Cordillera (Vallejo et al., 2006), which are interpreted to indicate rapid cooling through 380°-330°C during the Maastrichtian. Rock uplift and exhumation of the Eastern Cordillera gave rise to the major detrital source for the Maastrichtian Yunguilla Formation.

In the Oriente Basin, located to the east of the Eastern Cordillera, the Tena Formation was

deposited in an overfilled, retro-foreland basin, which received increasing modal proportions of metamorphic minerals, as a result of the progressive exposure of deep levels of the exhuming Eastern Cordillera (e.g. Baldock, 1982; Aspden and Litherland., 1992).

Collectively, this evidence, collected from both the study region (which is located proximal to the collision zone), and elsewhere in the northern Andes, strongly favours the hypothesis that the leading edge of the Caribbean Plateau and its associated arc collided with the Ecuadorian sector of the South American Plate, in the Late Campanian–Maastrichtian (~75–65 Ma).

The presence of mafic cumulate rocks within faulted blocks of the Pallatanga Block (San Juan Unit), and as blocks within shear zones in the Guaranda region, indicates that the collision may have been responsible for the exhumation of deep levels of the plateau. Shear sense indicators in the Calacalí – Pujilí - Pallatanga Fault suggest a dextral sense of movement, associated with east-northeast ward oriented collision of the Caribbean Plateau.

5.6.5 Latest Maastrichtian: The Silante Arc

During the latest Maastrichtian, the Pallatanga and Piñon blocks (and their associated San Lorenzo and Rio Cala island arc sequences) had already accreted to the continental margin, and formed the north-western margin of the South American Plate. Our identification of a series of volcanic rocks that yield calc-alkaline geochemical signatures (Tandapi volcanic facies) during ~65–60 Ma, which are associated with continental sedimentary rocks of the Silante Formation, strongly indicates that a new phase of volcanism along the NW South American margin commenced at the end of the Maastrichtian.

The abrupt and regional change from island-arc tholeiites to a high-K, calc-alkaline volcanic series is coincident with east-dipping subduction during the Maastrichtian (Fig. 5.8D). The Silante Arc erupted on top of the accreted allochthonous block in the northern part of the Cordillera, and on top of continental crust in southern latitudes (Sacapalca Fm.). The land mass became emergent during the latest Maastrichtian to the Early Paleocene, because the overlying Silante Formation was deposited in a terrestrial environment.

Elevated exhumation rates continued after the initial collision possibly caused by isostatic rebound combined with prolonged compressive stresses. Thermochronological data from the Eastern Cordillera indicate accelerated cooling from 65 to 55 Ma, driven by increased exhumation rates (Spikings et al., 2000, 2001), which was synchronous with the deposition of red beds of the Tena Formation in the Oriente Basin of Ecuador, indicating that a terrestrial environment was widespread at the end of the Maastrichtian..

5.6.6 Paleocene: The Macuchi Arc

Marine conditions recommenced during the Early Paleocene (Fig. 5.8E) in the forearc, because the volcanic rocks of the Macuchi Unit erupted below sea level, and may represent a continuation of the latest Maastrichtian Silante Arc. The sedimentary Pilaló and Saguangal

formations were deposited at northern latitudes, and were probably sourced from the Macuchi Arc, and the Silante Formation, as suggested by the geochemical signatures of their volcanic detritus (see chapter 3). However, the Saguangal Basin also received detrital material from metamorphic and granitic source rocks, corroborating the complete welding of the present-day Ecuadorian forearc.

The hemipelagic sedimentary rocks of the La Cubera Formation in the Naranjal Block, and the Guayaquil Formation of the coastal area (Fig. 5.9) presumably represent distal equivalents of the Pilaló and the Saguangal formation. During the same period, the Saquisilí Basin formed between the Macuchi Arc and the Eastern Cordillera. The basin was dominantly supplied from the emerging Eastern Cordillera.

5.6.7 Early to Middle Eocene

The deposition of the Pilaló Formation, probably continued until the Early Eocene, as indicated in the Latacunga – La Maná road section, where the Pilaló Formation is conformably overlain by Middle Eocene limestones of the Unacota Formation, which may have formed along the flanks of the Macuchi Arc (Fig. 5.8F), as previously suggested by Egüez (1986). During the Middle Eocene, the emplacement of I-type granites along what is now the western border of the Western Cordillera was coeval with the eruption of volcanic rocks of the Macuchi Unit (see the $^{40}Ar/^{39}Ar$ data in chapter 4).

The transitional geochemical data (tholeiitic and calc-alkaline series) acquired from basalts and basaltic andesites suggests that this arc system may have erupted through basement rocks that comprise both oceanic crust, and geochemically evolved continental crust, although this study is unable to account for such a potential juxtaposition of basement sequences.

5.6.8 Late Eocene

During the Late Eocene, turbiditic rocks of the Apagua Formation were deposited over the limestones of the Unacota Formation (Fig. 5.8G). A similar lithostratigraphic succession is recorded (1) in the basement sequence of the Manabí Basin of coastal Ecuador, where turbidites of the San Mateo Formation cover the limestones of the San Eduardo Formation (e.g. Kennerly, 1980), and (2) on the Piñón Block the deep sea fan deposits of Las Masas and Ancon Formation overlies the San Eduardo Limestones (Luzieux, 2007).

Such a widespread change of depositional environment reflects general deepening of the basins. In contrast, rapid cooling of the Eastern Cordillera, driven by exhumation between 40 and 30 Ma (Spikings et al., 2001), was occurring. This Late Eocene changes correlate with a period of rapid oblique convergence of the Nazca (Pardo Casas and Molinar, 1987) and South American plates. The deposition of coarse conglomerates rich in metamorphic clasts in the Oriente Basin, attests to rapid surface uplift of the Eastern Cordillera (Spikings et al., 2000; Ruiz, 2002; Ruiz et al., 2004).

The Macuchi Arc was active during the Late Eocene, as shown by extrusive and intrusive igneous rocks in the Western Cordillera, which yield ages of ~35 Ma. Furthermore, volcanic material from this volcanic arc can be locally found in turbidites of the Apagua Formation. The volcanic detritus was regionally distributed, because Late Eocene sedimentary rocks of the coastal region (Punta Blanca, San Mateo and Zapallo formations) received large quantities of volcanic derived minerals (Bristow and Hoffstetter, 1977; Luzieux, 2007).

The Late Eocene turbiditic sedimentary rocks of the Apagua and El Laurel formations, were deposited in the central and northern part of the Cordillera, respectively. Provenance analysis indicates that these formations record an upward increase of metamorphic and ZTR minerals, which suggest that the deeper Paleozoic and older core of the Eastern Cordillera was progressively being uplifted and eroded. Toro et al. (2005) reached similar conclusions from modal analyses of sandstones from the Apagua and Rumi Cruz formations. The fan delta facies of the Rumi Cruz Fm. documents the final stage of basin closure. Finally, this study conclude that there is no evidence for Late Eocene accretion of an allochthonous Macuchi Arc, as suggested by previous authors (Jaillard et al., 1995; Hughes and Pilatasig, 2002) to account for structural inversion of the Angamarca Basin. On the contrary, as shown in previous chapters, volcanic rocks of the Macuchi Unit are conformably overlain by turbidites of the Apagua Formation. Furthermore, continuous volcanism throughout the Eocene, and part of the Oligocene, precludes a collision event during this period.

There is no evidence, which supports Eocene structural displacement along the Chimbo – Toachi Fault, which is currently located along the eastern margin of the Macuchi Unit (Fig. 1.4). The Chimbo - Toachi Fault, is a NNE-SSW oriented structure that developed west of the larger Calacalí - Pujilí - Pallatanga Fault. Late Miocene fission-track ages from the Chimbo - Toachi fault zone suggest it may be a Neogene structure, which formed as part of an extensive transcurrent system, that was responsible for opening the Interandean Depression (Winkler et al., 2005; Spikings and Crowhurst, 2004; Spikings e al., 2005), and may be one of several structures, which accommodate the large-scale displacement of the Northern Andean Block towards the northeast (e.g. Winkler et al., 2005)

5.6.9 Latest Eocene - Oligocene

A major tectonic event affected broad areas of Ecuador during the latest Eocene to Oligocene. During this period, surface uplift within the central Western Cordillera generated an emergent land mass (Fig. 5.8H), as documented by an angular unconformity between the Rumi Cruz formation and the overlying, Miocene Zumbagua Formation. In the northern part of the Western Cordillera, the Oligocene San Juan de Lachas Formation is deposited unconformably on top of the Eocene Laurel Formation and the Late Cretaceous Pilatón Formation. These relationships presumably match with a major Oligocene event of the Western Cordillera, which produced N-S fold axes in the pre-Oligocene sequences of the Western Cordillera. Similarly. the Oligocene period is represented by a widespread hiatus in the coastal region (Luzieux, 2007), whereas in

the Oriente Basin, Oligocene sediments of the Orteguaza Formation lie above truncated beds of the Tiyuyacu Formation (e.g. Balkwill, 1995). This unconformity may be related with regional tectonic event in the adjacent western and eastern cordilleras, and forearc regions.

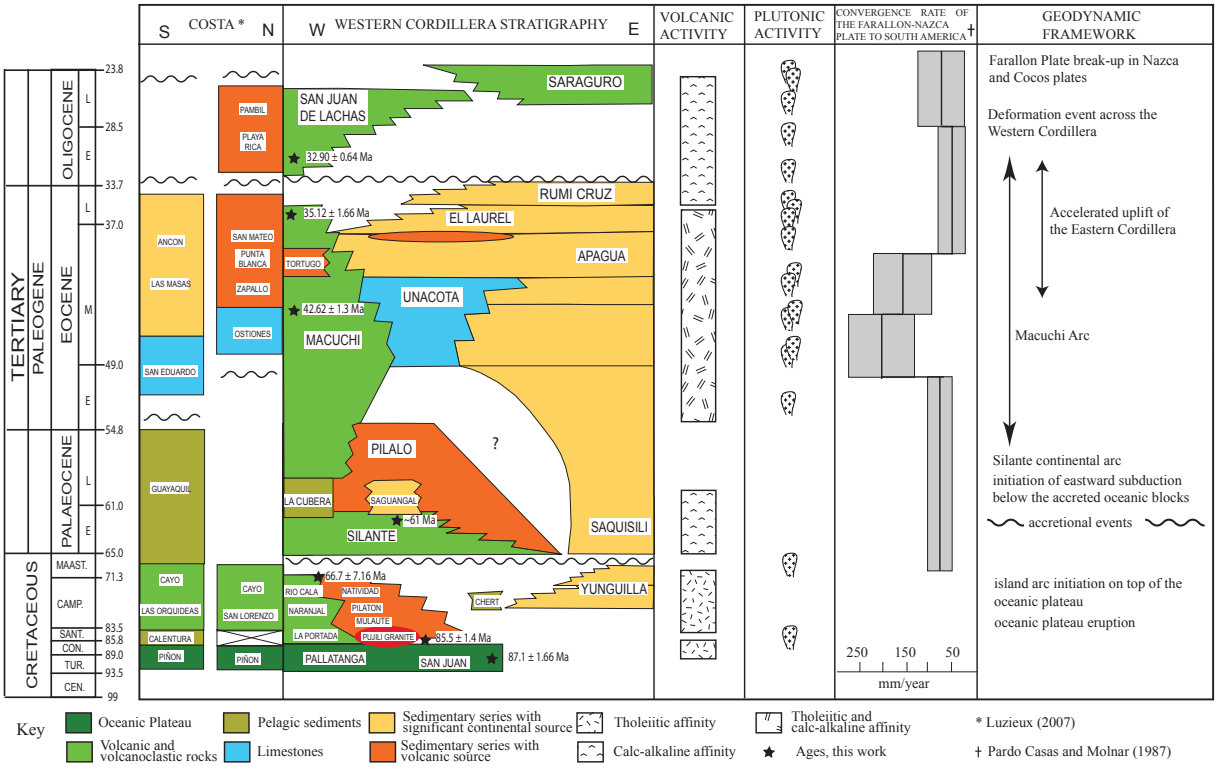

Fig. 5.9 Geological evolution of the Western Cordillera of Ecuador, including correlation with stratigraphic series from the coastal region, the igneous activity and the geodynamic framework during Late Cretaceous to Oligocene

CHAPTER 6: CONCLUSIONS

1. Our new U/Pb SHRIMP (zircon) age of 87.1±1.66 Ma (2σ) and $^{40}Ar/^{39}Ar$ (hornblende) age of 84.69±2.22 Ma (2σ), are the first radiometric ages acquired from the mafic basement rocks of the Pallatanga Fm. in the Western Cordillera of Ecuador, which represent an accreted fragment of an oceanic plateau. Collectively, these ages, when combined with the geochemical affinities of the rocks, strongly supports a derivation from the coeval Caribbean Plateau. The radiometric ages are consistent with volcanism associated with the Caribbean Plateau during 92–88 Ma (Sinton et al., 1998; Kerr et al., 2003) and an $^{40}Ar/^{39}Ar$ age of 88 ± 1.6 Ma from oceanic plateau rocks of the Piñón Fm. (Luzieux et al., 2006), located along coastal Ecuador.

2. The initiation of subduction at the leading edge of the plateau was probably responsible for the generation of the ocean island-arc related Pujilí Granite, at ~85 Ma. Furthermore, Santonian–early Campanian (~85-75 Ma) boninites of the La Portada Unit (Rio Cala Group) were also produced during the early stages of arc magmatism, via west-dipping subduction beneath the Caribbean Plateau. The radiometric ages and chemical compositions of the Late Cretaceous island arc rocks of the Western Cordillera correlate with the island arc rocks of coastal Ecuador, Colombia and the Caribbean region. Therefore, it is reasonable to suggest that the island arc rocks of the Western Cordillera and coastal region of Ecuador may represent the southward extension of the Great Arc of the Caribbean.

3. The absence of regional-scale, subduction related igneous activity along the Ecuadorian continental margin during 85–65 Ma is indicative of a cessation of subduction beneath the continental margin, as a consequence of ocean basin closure being solely accommodated by westward subduction beneath the Caribbean Plateau.

4. The oceanic plateau and overlying island arc drifted to the east and collided with the South American continental margin during the Campanian (~73 Ma). The termination of arc magmatism in the early Maastrichtian (~70 Ma) period corresponds to clogging of the subduction zone by collision between the buoyant Caribbean Plateau and the South American Plate. Paleomagnetic declination data from basement and sedimentary cover rocks in the coastal region (Luzieux et al., 2006) indicate they experienced 20–50^{o} of clockwise rotation during the late Campanian (73-70 Ma), which was synchronous with the collision of the oceanic plateau and arc sequence with the South American Plate, indicating that the collision may have been oblique.

5. The collision between the South American Plate and the Caribbean Plateau resulted in rapid exhumation (>1km/my) and surface uplift in the Eastern Cordillera, with erosion and deposition in the fore- and retroarc. Furthermore, the onset of rapid exhumation

throughout the continental margin during ~75–65 Ma temporally corroborates the onset of clastic sedimentation derived from the continental margin during the late Campanian–Maastrichtian.

6. Collision of the Caribbean Plateau and the South American Plate initiated eastward dipping subduction beneath the accreted oceanic plateau. The new active margin gave rise to the latest Maastrichtian (ca 65 Ma) Silante volcanic arc, which was deposited in a terrestrial environment.

7. During the Paleocene to Eocene, volcanic rocks of the Macuchi Unit were deposited, which may represent a temporal continuation of the Silante volcanic arc. This submarine volcanism was coeval with the deposition of siliciclastic sedimentary rocks of the Angamarca Group, and Saguangal Formation, which were mainly derived from the emerging Eastern Cordillera.

8. There is no evidence for accretion of the Macuchi Arc during the Late Eocene as suggested by previous authors, who claim that accretion was responsible for structural inversion of the Angamarca Basin. On the contrary, volcanic rocks of the Macuchi Unit are conformably overlain by turbidites of the Angamarca Group. Furthermore, it is geometrically difficult to reconcile Late Eocene accretion of the Macuchi Unit, given that it is currently located between the Piñon and Pallatanga Blocks, which accreted in the Late Cretaceous.

REFERENCES

Acquafredda, P., Fornelli, A., Piccarreta, G., and Summa, V. 1997. Provenance and tectonic implications of heavy minerals in Pliocene-Pleistocene siliciclastic sediments of the southern Apennines, Italy: Sedimentary Geology, v. 113, p. 149-159.

Acton, G.D., Galbrun, B, and King, J.W. 2000. Paleolatitude of the Caribbean Plate since the Late Cretaceous. In Leckie, R.M., Sigurdsson, H.R., Acton, G.D., and Draper, G. (Eds.), Proc. ODP, Sci. Results, 165, College Station, TX (Ocean Drilling Program), 149-173.

Aguirre, L., Atherton, M.P. 1987. Low-grade metamorphism and geotectonic setting of the Macuchi Formation, Western Cordillera of Ecuador: Journal of metamorphic Geology, v. 5, p. 473-494.

Alexandre, P., Hamilton, D. and Barfod, D., 2006. The ARGUS multicollection noble gas mass spectrometer: Geochimica et Cosmochimica Acta Supplement, v. 70, p. 8

Allibon, J., Monjoie, P., Lapierre, H., Jaillard, E., Bussy, F., Bosch, D., 2005. High Mg-basalts in the Western Cordillera of Ecuador: evidence of plateau root melting during Late Cretaceous arcmagmatism. In: Proceedings of the Sixth International Symposium on Andean Geodynamics, Program and Abstracts, Barcelona, Spain, pp. 3335.

Alvarado, G.E., Deyner, P., Sinton, C.W. 1997. Implications for the Caribbean region of the high-MgO volcanic rocks of the Costa Rican ophiolitic complexes: The case of the Tortugal komatiitic-like suite: Zentralblatt fur Geolologie und Palaontologie, v. 36, p. 409-429.

Aspden, J.A. and Litherland, M. 1992. The Geology and Mesozoic Collisional History of the Cordillera Real, Ecuador. Andean Geodynamics. Oliver, R.A. et al. (Editors): Tectonophysics, v. 205, p. 187-204.

Aspden, J.A., McCourt, W.J., 1986. Mesozoic oceanic terranes in the central Andes of Colombia: Geology, v. 14, p. 415-418.

Aspden, J. A., McCourt, W. J. & Brook, M. 1987. Geometrical Control of Subduction – Related Magmatism: The Mesozoic and Cenozoic Plutonic History of Western Colombia: Journal of the Geological Society, v. 144, p. 893-905.

Aspden, J.A., Harrison, S.H., Rundle, C.C. 1992b. New Geochronological Control For The Tectono-Magmatic Evolution Of The Metamorphic Basament, Cordillera Real and El Oro Province Of Ecuador: Journal Of South American Earth Sciences, v. 6, p. 77-96.

Baldock, J.W. 1982. Geology of Ecuador: Explanatory Bulletin of the National Geological map of the Republic of Ecuador. Quito, DGGM.

Balkwill, H. R., Rodriguez, G., Paredes, F. I. & Almeida, J. P. 1995. Northern part of Oriente Basin, Ecuador: reflexion seismic expression of structures. In Petroleum basins of South America (eds Tankard, A. J., Suarez, S. & Welsink, H. J.), American Association of Petroleum Geologists, Memoir 62, 559-571.

Baksi, A.K., 1994 Geochronological studies on whole-rock basalts, Deccan Traps, India: Evaluation of the timing of volcanism relative to the K-T boundary: Earth and Planetary Science Letters, v. 121, p. 43-56.

Barragán, R., Baby, P., Duncan, R., 2005. Cretaceous alkaline intra-plate magmatism in the Ecuadorian Oriente Basin: Geochemical, geochronological and tectonic evidence: Earth and Planetary Science Letters, v. 236, p. 670-690.

Beaudon, E., Martelat, J.E., Amortegui, A., Lapierre, H., Jaillard, E. 2005. Metabasites de la cordillere occidentale dEquateur, temoins du soubassement oceanique des Andes dEquateur: C. R. Geoscience, v. 337, p. 625-634.

Beccaluva, L., Macciotta, G., Piccardo, G.B., Zeda, O. 1989. Clinopyroxene composition of ophiolite basalts as petrogenetic indicator: Chemical Geology, v. 77, p. 165-182.

Beck, C. M., D. Girard, and P. DeWeber, 1984, Volcano-sedimentaire du Rio Guare: Un element de la nappe ophiolitique de Lomo de Hierro, chaone Caraobe Venezuelienne: Comptes Rendus de Seances (D), v. 299, p. 337-342.

Beets, D.J., Maresch, W.V. Klaver, G.T. Mottana, R. Bocchio, R. Beunk F.F., Monen, H.P. 1984. Magmatic rock series and high-pressure metamorphism as constraints on the tectonic history of the southern Caribbean: Geological Society of America Memoir, v. 162, p. 95-130.

Boland, M.P., Pilatasig, L.F., Ibandango, C.E. McCourt, W.J., Aspden, J.A., Hughes, R.A., Beate, B. 2000. Geology of the Western Cordillera between 0°-1°N, Proyecto de Desarrollo Minero y Control Ambiental, Programa de Informacion cartografica y Geológica, Informe No. 10. CODIGEM-BGS, Quito, Ecuador, 72 pp.

Bourgois, J., Calle, B., Tournon, J. and Toussaint, J.F., 1982. The Andean Ophiolitic Megastructures on the Buga-Buenaventura transverse (Western Cordillera-Valle Colombia): Tectonophysics, v. 82, p. 201-229.

British Geological Survey and Corporación de Desarrollo e Investigación Geologico, Minero y metalúrgico. 1997. Geological map of the Western Cordillera, Ecuador between 0° and 1° N. (1:200,000). BGS, Keyworth, UK.

British Geological Survey and Corporación de Desarrollo e Investigación Geologico, Minero y metalúrgico. 1997. Geological map of the Western Cordillera, Ecuador between 0° and 1° S. (1:200,000). BGS, Keyworth, UK.

British Geological Survey and Corporación de Desarrollo e Investigación Geologico, Minero y Metalúrgico. 1997. Geological map of the Western Cordillera, Ecuador between 1° and 2° S. (1:200,000). BGS, Keyworth, UK.

British Geological Survey and Corporación de Desarrollo e Investigación Geologico, Minero y Metalúrgico, 1997. Geological map of the Western Cordillera, Ecuador between 2° and 3° S. (1:200,000). BGS, Keyworth, UK.

British Geological Survey and Corporación de Desarrollo e Investigación Geologico, Minero y metalúrgico. 1997. Geological map of the Western Cordillera, Ecuador between 3° and 4° S. (1:200,000). BGS, Keyworth, UK.

Bristow, C.R., Hoffstetter, R. 1977. Lexique Stratigraphique International; Ecuador. Second edition. Paris: Centre National de la Recherche Scientifique, 412 p.

Burke, K., 1988. Tectonic evolution of the Caribbean: Ann. Rev. Earth and Planetary Sciences. v. 16, p. 201-230.

Case, J.E., Duran, A.R., Moore, W.R. 1971. Tectonic investigations in western Colombia and eastern Panama: Geological Society of America Bulletin, v. 82, p. 2685-712.

Cawood, P.A. 1983. Modal composition and detrital clinopyroxene geochemistry of lithic sandstones from the New England Fold belt (east Australia): a Palaeozoic forearc terrane: Geological Society of America Bulletin, v. 94, p. 1199–1214.

Chiaradia, M., Fontboté, L. 2001. Radiogenic Lead Signatures in Au-Rich Volcanic-Hosted Massive Sulfide Ores and Associated Volcanic Rocks of the Early Tertiary Macuchi Island Arc (Western Cordillera of Ecuador): Economic Geology, v. 96, p. 1361-1378.

Colombo, C., Tassinari, G., Moacir, J.B., Macambira, J.B. 1999. Geochronological provinces of the Amazonian Craton: Episodes, v. 22, p. 174-182.

Condie, K.C., Abbot, D.H. 1999. Oceanic plateaus and hotspot islands: Identification and role in continental growth: Lithos, v. 46, p. 1-4.

Condie, K.C. 2005. TTGs and adakites: are they both slab melts?: Lithos, v. 80, p. 33–44

Compston, W., Williams, I.S., Kirschvink, J.L., Zichao, Z., Guogan, M., 1992. Zircon U–Pb ages for the Early Cambrian time-scale: J. Geol. Soc. London, v. 149, p. 171–184.

Cotteccia, V., Zezza, F. 1969. The Eocene basement of the inter-Andean corridor in the Latacunga Ambato trough (Ecuador). Geol. Appl. Idrogeol., v. 4, p. 43-46.

Cosma, L., Lapierre, H., Jaillard, E., Laubacher, G., Bosch, D., Desmet, A., Mamberti, M., Gabriele, P., 1998. Petrographie et geochimie des unites magmatiques de la Cordillere Occidentale d'Equateur (0°30'S): implications tectoniques: Bulletin Societe Geologique de France, v. 169, p. 739-751.

Crawford, A.J., Beccaluva, L., Serri, G. 1981. Tectono-magmatic evolution of the West Philippine-Mariana region and the origin of boninites. Earth and Planetary Science Letters, v. 54, p. 346- 356.

Crawford, A.J., Fallon, T.J. Green, D.H. 1989. Clasification, petrogenesis and tectonic setting of boninites, in Crawford, A.J., ed., Boninites and related rocks: Boston, Massachusetts, Unwin Hyman, p. 1-49.

Di Marco, G., 1994, Les terrains accretes du sud du Costa Rica. Evolution tectonostratigraphic de la marge occidentale de la plaque Caraibe: Ph.D. dissertation, Universite de Lausanne, Lausanne, Switzerland.

Dill, H.G. (1998) A review of heavy minerals in clastic sediments with case studies from the alluvial-fan through the nearshore-marine environments. Earth-Science Reviews, 45(1-2), 103-132.

Donnelly, T., Beets, D., Carr, M., Jackson, T., Klaver, G., Lewis, J., Maury, R., Schellekens, H., Smith, A., Wadge, G. and Westercamp, D., 1990. History and tectonic setting of the Caribbean magmatism. In: G. Dengo and J. Case (Editors), The Caribbean Region, The Geology of North America. Geol. Sot. Am., Boulder, Colo., v. H, p. 339-374.

Duncan, R.A., Hargraves, R.B. 1984. Plate tectonic evolution of the Caribbean region in the mantle reference frame. In: Bonini, W.E., Hargraves, R.B., Shagam, R. (Eds.), The Caribbean– South America Plate Boundary and Regional Tectonics. Geol. Soc. Am. Mem. 162, 81–93.

Dunkley, P. and Gaibor, A., 1997. Geology of the Cordillera Occidental of Ecuador between 2° - 3°S. Proyecto de Desarollo Minero y Control Ambiental, Programa de Informacion Cartografica y Geologica, Informe 2CODIGEM–BGS, Quito, Ecuador, 139pp.

Drummond, M.S., Defant, M.J. 1990. A model for trondhjemite-tonalite-dacite genesis and crustal growth via slab melting: Archean to modern comparisons. J. Geophys. Res., v. 95, p. 503-521.

Echeverria, J., 1977. Geologia del cuerpo calcareo de Unacota, Pilaló, Cotopaxi. Tesis de grado, Escuela Politecnica Nacional, Quito, 123 pp.

Egüez, A., 1986. Evolution Cenozoique de la Cordillere Occidentale septentrionale d'Equateur (0°15' S - 01°10' S), les mineralisations associetees. Doc. Thesis, UPMC, Paris, 116 pp. (unpublished).

Egüez, A., Bourgois, J., 1986. La Formacion Apagua, edad y posiciòn estructural en la Cordillera Occidental del Ecuador. Cuarto Congreso Ecuatoriano de geologia Minas y petroleos, 161-178.

Egüez, A., Cajas, M., Davila, F. 1988. Distribuciòn de Terrenos oceánicos alóctonos y de terrenos continentales en la Cordillera Occidental del Ecuador: Evidencias en las geotravesias Otavalo – Selva Alegre y Cañar – La Troncal: Politécnica, Monografía de Geología, v. 13, p. 101–136.

Engebretson, D.C., Cox, A., Gordon, R.G., 1985. Relative Motions Between Oceanic and Continental Plates in the Pacific Basin. Boulder, Geological Society of America Special Paper, v. 206, 59 pp.

Escuder Viruete, J., Díaz de Neira, A., Hernáiz Huerta, P.P., Monthel, J. García Senz, J. Joubert, M., Lopera, E., Ullrich, T., Friedman, R., Mortensen, J., Pérez-Estaún, A. 2006. Magmatic relationships and ages of Caribbean Island arc tholeiites, boninites and related felsic rocks: Lithos, v. 90, p. 161-186.

Faucher, B., Vernet,. R., Bizón, G., Visón, J.J., Greekoff, N., Lys, M., Sigal, J. 1971. Sedimentary formations in Ecuador. A stratigraphic and micropaleontological survey. Bureau d'etudes industrielles et de cooperation del Institut Francais du Petrole (IFP) y Servicio Nacional de Geologia y Mineria. Quito.

Faucher, B., Savoyat, E. 1973. Esquisse Geologique des Andes de L´ Equator. Revue de géographie physique et de gélogie dynamique (2), vol. XV, Fasc. 1-2, pp 115-142.

Faure, G. 1986. Principles of Isotope Geology, second edition, John Wiley and Sons, New York, pp. 66-92.

Feininger, T. and Bristow, C.R. 1980 Cretaceous and Palaeogene geologic history of Coastal Ecuador: Geologische Rundschau, v. 69, p. 40-44.

Feininger, T., Seguin, M.K. 1983. Simple Bouguer gravity anomaly field and the inferred crustal structure of continental Ecuador: Geology, v. 11, p. 40-44.

Guillier, B. Chatelain J.L. Jaillard, E., Yepes, H., Poupinet, G., Fels, J.F. 2001. Seismological evidence on the geometry of the orogenic system in central-northern Ecuador (South America): Geophysical Research Letters, v. 28, p. 3749-3752.

Goosens, P.J. and Rose, W.I., 1973. Chemical composition and age determination of tholeiitic rocks in the Basic Igneous Complex, Ecuador: Geological Society of America Bulletin, v. 84, p. 1043-1052.

Hall, M. and Calle, J., 1982. Geochronological control for the main Tectono-Magmatic events of Ecuador: Earth Science Review, v. 10, p. 215-239.

Harrison, T.M., MacDougall, I. 1981, Excess ^{40}Ar in metamorphic rocks from Broken Hill, New South Wales: implications for 40Ar/39Ar age spectra and the thermal history of the region. Earth and Planetary Science Letters, v. 55, p. 123-149.

Hart, S.R., Dunn, T. 1993. Experimental cpx/melt partitioning of 24 elements. Contrib Mineral Petrol, v. 113, p. 1-18.

Hauff, F., Hoernle, K., Bogaard, P.V.D., Alvarado, G.E., Garbe-Schonberg, D., 2000. Age and geochemistry of basaltic complexes in western Costa Rica: Contributions to the geotectonic evolution of Central America: Geochemistry, Geophysics, Geosystems, v. 1, no. 5, doi: 10.1029/1999GC000020.

Henderson, W.G. 1979. Cretaceous to Eocene volcanic arc activity in the Andes of northern Ecuador: Journal of the Geological Society of London, v. 136, p. 73-78.

Hoernle, K., Hauff, F., Van den Bogaard, P., 2004. 70 m.y. history (139–69 Ma) for the Caribbean large igneous province: Geology, v. 32, p. 697–700.

Hoernle, K., Van den Bogaard, P., Werner, R., Lissina, B., Hauff, F., Alvarado, G., and Garbe-Schonberg, D., 2002, Missing history (16-71Ma) of the Galapagos hotspot: Implications for the tectonic and biological evolution of the Americas: Geology, v. 30, p. 795-798.

Hubert, J.F. 1962. A Zircon-tourmaline-rutile maturity index and the interdependence of the composition of heavy mineral assemblages with the gross composition and texture of sandstones: Jour. Sedimentary Petrology, v. 32, p. 440–449.

Hughes R., Bermudez R. 1997. Geology of the Cordillera Occidental of Ecuador between 0°00´and 1° 00´S. Proyecto de desarollo minero y control ambiental, programa de información cartográfica y geológica. Report Number 4. CODIGEM – British Geological Survey, Quito, Ecuador, 75 pp.

Hughes, R.A., Pilatasig, L.F. 2002. Cretaceous and Tertiary Block accretion in the Cordillera Occidental of the Andes of Ecuador: Tectonophysics, v. 345, p. 29-48.

Hungerbühler, D. 1997. Tertiary basins in the Andes of southern Ecuador (3º00´-4º20´): Sedimentary evolution, deformation and regional tectonic implications. PhD Thesis, Institute of Geology ETH Zurich, Switzerland, p. 182.

Hungerbühler, D., Steinmann, M., Winkler, W., Seward, D., Egüez, A., Peterson, D.E., Helg, U., Hammer, C. 2002. Neogene stratigraphy and Andean geodynamics of southern Ecuador: Earth-Science Reviews, v. 57, p. 75-124.

Jaillard, E., Bengtson, P., Dhondt, A. 2005. Late Cretaceous marine transgressions in Ecuador and northern Peru: A refined stratigraphic framework: Journal of South American Earth Sciences, v. 19, p. 307–323.

Jaillard, E., Ordoñez. M., Benitez, S, Berrones, G., Jimenez, N., Montenegro, G., And Zambrano, I. 1995. Basin Develoment in an Accretionary, Oceanic-floored Fore-Arc Setting: Southern Coastal Ecuador During Late Cretaceous-Late Eocene time: AAPG Memoir, v. 62, p. 615-631.

Jaillard, E., Ordoñez, M., Suarez, J., Toro, J., Iza, D., Lugo, W. 2004. Stratigraphy of the late CretaceousPaleogene deposits of the cordillera occidental of central Ecuador: geodynamic implications: Journal of South American Earth Sciences, v. 17, p. 49-58.

Juteau, T., Megard, F., Raharison, L., Whitechurch, H. 1977. Les assemblages ophiolitiques de l' occident equatorien: nature petrographique et position structurale. Bulletin Societe Geologique de France, v. 19, p. 1127-1132.

Kay, R. W. (1978). Aleutian magnesian andesites; melts from subducted Pacific Ocean crust: Journal of Volcanology and Geothermal Research, v. 4, p. 117–132

Kehrer, W., Van Der Kaaden, G. 1979. Notes on the geology of Ecuador, with special reference to the Western Cordillera: Geologische Jahrbuch, v. 35, p. 5-57.

Kennerly, J.B., 1980. Outline of the Geology of Ecuador. Overseas Geologic and Mineral Resources, 55 pp.

Kerr, A.C., Aspden, J.A., Tarney, J. Pilatasig, L.F. 2002a. The nature and provenance of accreted oceanic Blocks in western Ecuador: geochemical and tectonic constraints: Journal of the Geological Society, v. 159, p. 577-594.

Kerr, A. C., Iturralde-Vinent, M. A. Saunders, A. D. Babbs, T. L., Tarney, J. 1999. A new plate tectonic model of the Caribbean: Implications from a geochemical reconnaissance of Cuban Mesozoic volcanic rocks: Geological Society of America Bulletin, v. 111, p. 1581-1599.

Kerr, A.C., Marriner, G.F., Tarney, J., Nivia, A., Saunders, A.D., Thirlwall, M.F., Sinton, C.W. 1997. Cretaceous basaltic terranes in Western Colombia: elemental, chronological and Sr-Nd isotopic constraints on petrogenesis: Journal of Petrology, v. 38, p. 677–702.

Kerr, A.C., Tarney, J., 2005. Tectonic evolution of the Caribbean and northwestern South America: The case for accretion of two Late Cretaceous oceanic plateaus: Geology, v. 33, p. 269–272.

Kerr, A.C., Tarney, J. Kempton, P.D. Spadea, P. Nivia, A. Marriner, G.F., Duncan, R.A. 2002b, Pervasive mantle plume head heterogeneity: Evidence from the late Cretaceous Caribbean-Colombian Oceanic Plateau: Journal of Geophysical Research, v. 107, no. 7, doi:10.1029/2001JB000790.

Kerr, A.C. Tarney, J. Nivia, A., Marriner, G.F. and Saunders, A.D., 1998. The internal structure of oceanic plateaus: inferences from obducted Cretaceous Blocks in western Colombia and the Caribbean: Tectonophysics, v. 292, p. 173-188.

Kerr, A.C., White, R.V., Thompson, P.M., Tarnez, J. and Saunders, A.D., 2003. No Oceanic Plateau- No Caribbean Plate? The Seminal Role of an Oceanic Plateau in Caribbean Plate Evolution. In: C. Bartolini, R.T. Buffler, and J. Blickwede, eds. The Circum-Gulf of Mexico and the Caribbean: Hydrocarbon habitats, basin formation, and plate tectonics: AAPG Memoir, v. 79, p. 126-168.

Koppers, A.A.P. 2002. ArArCALC -- software for 40Ar/39Ar age calculations. Computers and Geosciences, v. 28, p. 605-619.

Koppers, A.A.P., Staudigel, H., Wijbrans, J.R. 2000. Dating Crystalline Groundmass separates of Altered Cretaceous Seamount Basalts by the $^{40}Ar/^{39}Ar$ Incremental Heating Technique. Chemical Geology, v. 166, p. 139-158.

Krawinkel, H., Wozazek, S., Krawinkel, J., Hellmann, W. 1999. Heavy-mineral analysis and clinopyroxene geochemistry applied to provenance analysis of lithic sandstones from the Azuero-Soná Complex (NW Panama): Sedimentary Geology, v. 124, p. 149-168.

Kushiro, I. 1960. Si-Al relation in clinopyroxenes from igneous rocks: Amer J Sci., v. 258, p. 548–554

Lanphere, M.A., Dalrymple, G.B., 1976, Identification of excess 40Ar by the 40Ar/39Ar age spectrum technique, Earth Planetary Science Letters, v. 32, p. 141-148.

Lapierre, H., Bosch, D., Dupuis, V., Polve, M., Maury, R., Hernandez, J., Monie, P., Yeghicheyan, D., Jaillard, E., Tardy, M., Mercier de Lepinay, B., Mamberti, M., Desmet, A., Keller, F. and Senebier, F., 2000. Multiple plume events in the genesis of the peri-Caribbean Cretaceous oceanic plateau province: Journal of Geophysical Research, v. 105, p. 8403-8421.

Lapierre, H., Dupuis, V., de Lepinay, B.M., Bosch, D., Monie, P., Tardy, M., Maury, R.C., Hernandez, J., Polve, M., Yeghicheyan, D., Cotten, J. 1999. Late Jurassic oceanic crust and Upper Cretaceous Caribbean plateau picritic basalts exposed in the Duarte igneous complex, Hispaniola: Journal of Geology, v. 107, p. 193-207.

Lavenu, A,, Noblet, C., Bonhomme, M.G., Egüez, A,, Dugas, F., Vivier, G. 1992. New K-Ar age dates of Neogene and Quaternary volcanic rocks from the Ecuadorian Andes: implications for the relationship between sedimentation, volcanism, and tectonics: J South Amer Earth Sci., v. 5, p. 309–320.

Le Bas, M.J. 1962. The role of aluminium in igneous clinopyroxenes with relation to their parentage. Am. J. Sci., v. 260, p. 267–288.

Lebrat, M., Mégard, F., Juteau, T.. Calle, J. 1985. Pre-orogenic volcanic assemblage and structure in the Western Cordillera of Ecuador. between 1° 40'S and 2° 20'S Geol. Rundschau, v. 74, p. 343–351.

Lebrat, M., Megard, F., Dupuy, C., Dostal, J. 1987. Geochemistry and tectonic setting of pre-collision Cretaceous and Paleogene volcanic rocks of Ecuador: Geological Society of America Bulletin, v. 99, p. 569-578.

Leterrier, J., Maury, R., Thonon, P., Girard, Marchal, M. 1982. Clinopyroxene composition as a method of identification of the magmatic affinities of paleo-volcanic series: Earth and Planetary Science Letters, v. 59, p. 139-154.

Litherland, M., Aspden, J.A. 1992. Terrane-boundary reactivation: a control on the evolution of the Northern Andes: Journal of S. Am. Earth Sci., v. 5, p. 71–76.

Litherland, M., Aspden, J., Jemielita, R.A. 1994. The metamorphic belts of Ecuador. British Geological Survey, Overseas Memoir, 11, 147 pp.

Litherland, M., Klinck, B.A., O'Connor, E.A., Pitfield, P.E. 1985. Andean-trending mobile belts in the Brazilian Shield: Nature, v. 314, p. 345-348.

Lonsdale P. 1978. Ecuadorian Subduction System: AAPG Bulletin, v. 62, p. 2454-2477.

Lonsdale, P. Klitgord, K.D. 1978. Structure and tectonic history of the eastern Panama Basin, Geological Society of America Bulletin, v. 89, p. 981–999.

Lonsdale, P. 2005. Creation of the Cocos and Nazca plates by fission of the Farallon Plate: Tectonophysics, v. 404, p. 237-264.

Ludwig KR (2001) Isoplot /Ex version 2.49. A geochronological toolkit for Microsoft Excel. Berkeley Geochronological Center Spec Publ la.

Luzieux, L.D.A., Heller, F., Spikings, F., Vallejo, C.F., Winkler, W. 2006. Origin and Cretaceous tectonic history of the coastal Ecuadorian forearc between 1°N and 3°S: Paleomagnetic, radiometric and fossil evidence. Earth and Planetary Science Letters, v. 249, p. 400-414

Luzieux, L.D.A. 2007. Origin and Late Cretaceous-Tertiary evolution of the Ecuadorian forearc. PhD Thesis, Institute of Geology ETH Zürich, Switzerland, p. 197.

MacDougall, I., Polach, H.A., Stipp, J., 1969. Excess radiogenic argon in young subaerial basalts from the Auckland volcanic field, New Zealand: Geochim. Cosmochim. Acta, v. 33, p. 1485-1520.

Machado, N., Gauthier, G. 1996. Determination of $^{207}Pb/^{206}Pb$ ages on zircon and monazite by laser-ablation ICP-MS and application to a study of sedimentary provenance and metamorphism in southeastern Brazil: Geochim Cosmochim Acta, v. 60, p. 5063-5073.

Mamberti, M., 2001. Origin and evolution of two distinct Cretaceous oceanic plateaus accreted in Western Ecuador (South America): petrological, geochemical and isotopic evidence. Unpublished Phd Thesis, Universite de Lausanne, 241 pp.

Mamberti, M., Lapierre, H., Bosch, D., Ethien, R., Jaillard, E., Hernandez, J., Polve, M. 2003. Accreted fragments of the Late Cretaceous Caribbean-Colombian plateau in Ecuador: Lithos, v. 66, p. 173–199.

Mamberti, M., Lapierre, H., Bosch, D., Jaillard, E., Hernandez, J., Polve, M. 2004. The Early Cretaceous San Juan Plutonic Suite, Ecuador: a magma chamber in an oceanic plateau?: Canadian Journal of Earth Sciences, v. 41, p. 1237–1258.

Mann, P., Taira, A. 2004. Global tectonic significance of the Solomon Islands and Ontong Java Plateau convergent

zone: Tectonophysics, v. 389, p. 137-190.

Mapa Geológico de la República del Ecuador, 1: 1000000. 1969. Servicio Nacional de Geologia y Minas, Quito.

Mattson, P.H., Pessagno, E.A., 1979. Jurassic and Early Cretaceous radiolarians in Puerto Rican ophiolite – Tectonic implications: Geology, v. 7, p. 440-444.

Mauffret, A., Leroy, S. 1997. Seismic stratigraphy and structure of the Caribbean igneous province: Tectonophysics, v. 293, p. 61-104.

McCourt, W.J., Aspden, J.A., Brooks, M. 1984. New geological and geochronological data from the Colombian Andes: Continental growth by multiple accretion: Journal of the geological Society of London, v. 141, p. 831-845.

McCourt, W.J., Duque, P. and Pilatasig, L.F., 1997. Geology of the Western Cordillera between 1°-2ºS, Proyecto de Desarrollo Minero y Control Ambiental, Programa de Información cartografica y Geológico, Informe No. 3, CODIGEM-BGS, Quito, Ecuador, 69 pp.

Megard, F. 1987. Cordilleran Andes and Marginal Andes: a review of Andean geology north of the Arica elbow (18%). In: Circum Pacific erogenic belts and evolution of the Pacific Ocean basin (edited by J.W.H. Manger and J. Francheteau), American Geophysical Union, Geodynamic Series, v. 18, p. 71-95.

Millward, D., Marriner, G.F., Saunders, A.D. 1984. Cretaceous tholeiitic volcanic rocks from the Western Cordillera of Colombia: Journal of the Geological Society (London), v. 141, p. 847-860.

Molinares, C., Jaramillo, C., 2005. Biostratigraphic value of Rzehakina epigona in the Paleocene – Early Eocene of Northern South America. 7th IWAF, International Workshop about Agglutinated Foraminifera. Urbino, Italy.

Montgomery, H., Pessagno, E., Lewis, J., Schellekens, J., 1994. Paleogeography of Jurassic fragments in the Caribbean: Tectonics, v. 13, p. 725-732.

Morimoto, N. 1989. Nomenclature of pyroxenes. Can Mineral, v. 27, p.143-156

Morton, A.C. 1985. Heavy minerals in provenance studies. In: Zuffa, G.G. (Eds), Provenance of arenites. Reidel, Dordrecht, pp. 249-277.

Morton, A.C., 1991. Geochemical studies of detrital heavy minerals and their application to provenance studies. In: Morton A.C., Todd, S.P., Haughton, P.D.W. (Eds.), Developments in Sedimentary Provenance Studies. Geol. Soc. London, Spec, v. 57, p. 31–45.

Nechaev, V.P., Ishpording, W.C., 1993. Heavy-mineral assemblages of continental margin as indicators of plate-tectonic environments: J. Sediment. Petrol, v. 63, p. 1110-1117.

Niu, Y., O`Hara, M.J. and Pearce, J., 2003. Initiation of subduction zones as a consequence of lateral compositional buoyancy contrast within the lithosphere: a petrological perspective. Journal of Petrology, v. 44, p. 851-866.

Nivia, A., 1996. The Bolivar mafic-ultramafic complex, SW Colombia: the base of an obducted oceanic plateau: Journal of South American earth Sciences, v. 9, p. 59-68.)Nivia, A., Marriner, G., Kerr, A. 1996. El Complejo Quebradagrande, una posible Cuenca marginal intracratonica del Cretaceo Inferior en la Cordillera Central delos Andes colombianos: VII Cong. Col. Geol. Mem. 3, 108-123.

Nisbet, E., Pearce, J. 1977. Clinopyroxene Composition in Mafic Lavas from Different Tectonic Settings: Contributions to Mineralogy and Petrology, v. 63, p. 149-160.

Pardo-Casas, Molnar, 1987. Relative Motion of The Nazca (Farallón) and South American Plates Since Late Cretaceous Time: Tectonics, v. 6, p. 233-248.

Pearce, J.A., Cann, J.R. (1973): Tectonic setting of Basic Volcanic Rocks Determined using Trace Element analysis: Earth Planetary Science Letters, v. 19, p. 290-300.

Pearce, J.A., Van der Laan, S.R., Arculus, R.J., Murton, B. J., Ishii, T., Peate, D.W., Parkinson, I.J. 1992. Boninite and harzburgite from Leg 125 (Bonin-Mariana forearc): a case study of magma genesis during the initial stage of subduction. Proc. ODP, Sci. Results (Fryer, P.; Coleman, P.; Pearce, J. A.; and Stokking, L. B., eds.) 125, College Station, Tex. (Ocean Drilling Program), p. 623-659)Petterson M. G., Babbs T., Neal C. R., Mahoney J. J., Saunders A. D., Duncan R. A., Tolia D., Magu R., Qopoto C., Mahoa H. and Natogga D., 1999. Geological–tectonic framework of Solomon Islands, SW Pacific: crustal accretion and growth within an intra-oceanic setting. Tectonophysics, v. 301, p. 35–60.

Pilger, R. 1983. Plate reconstructions, aseismic ridges and low-angle subduction beneath the Andes: Geological Society of America Bulletin, v. 92, p. 448–456.

Pindell, J. L. 1993. Determination of Euler pole for relative motion of Caribbean and North American plates using slip vectors of interplate earthquakes. EOS: Trans. Am. Geophys. Union 74:586.

Pindell J. L., Barrett S. F. 1990. Geological evolution of the Caribbean region: a plate tectonic perspective. In Dengo G., Case J. E. (eds.) The Caribbean Region. Geological Society of America Special Paper. H, 405–32.

Pindell J. L., Cande S.C., Pitam W.C. 1988. A plate-kinematic framework for models of Caribbean evolution: Tectonophysics, v. 155, p. 121–38.

Pindell, J., Kennan, L., Maresch, W., Stanek, K., Draper, G., Higgs, R., 2005. Plate kinematics and crustal dynamics of circum-Caribbean arc-continent interactions; tectonic controls on basin development in proto-Caribbean margins. In: Caribbean-South American plate interactions, Venezuela. Ave-Lallemant-Hans-G (editor); Sisson-Virginia-B (editor). Special Paper Geological Society of America, v. 394, p. 7-52.

Pindell, J., Kennan, L., Stanek, K., Maresch, W., Draper, G., 2006. Foundations of Gulf of Mexico and Caribbean evolution: eight controversies resolved: Geologica Acta, v. 4, p. 303-341.

Pratt, W.T., Figueroa, J., Flores, B. 1997. Geology of the Cordillera Occidental of Ecuador between 348S. Proyecto de Desarollo Minero y Control Ambiental, Programa de Informacion Cartografica y Geologica, CODIGEM-BGS, Quito, Informe 1.

Restrepo, J.A., Toussaint, J.F. 1974. Obducción cretácea en el Occidente Colombiano: Anales Fac. Minas, Medellín. v. 58, p. 73-105.

Revillon, S., Hallot, E., Arndt, N.T., Chauvel, C., Duncan, R.A. 2000. A Complex History for the Caribbean Plateau: Petrology, Geochemistry, and Geochronology of the Beata Ridge, South Hispaniola: The Journal of Geology, v. 108, p. 641-661.

Reynaud, C., Jaillard, E., Lapierre, H., Mamberti, M., Mascle, G. 1999. Oceanic Plateau Island arcs of Southwestern Ecuador: Their place In the Geodynamic Evolution of Northwestern South America: Tectonophysics, v. 307, p. 235-254.

Roddaz, M., Brusset, S., Soula, J.C., Beziat, D., Ben Abbou, M., Debat, P., Driouch, Y., Christophoul, F., Ntarmouchant, A., Deramond, J. 2002. Foreland basin magmatism in the Western Moroccan meseta and

geodynamic inferences: Tectonics, v. 21, p. 1-23.

Rollinson, H. 1993. Using geochemical data: evaluation, presentation, interpretation. pp. 352, Longman, Singapore.

Roperch, P., Megard, F., Laj, C., Mourier, T., Clube, T. and Noblet, C., 1987. Rotated oceanic blocks in Western Ecuador: Geophys. Research Letters, v. 14, p. 558-561.

Ross, M.I., Scotese, C.R. A hierachial tectonic model of the Gulf of Mexico and Caribbean region: Tectonophysics, v. 155, p. 139-168.

Ruiz, G.M.H., 2002. Exhumation of the northern sub-Andean zone of Ecuador and its source region: A combined thermochronological and heavy mineral approach. PhD Thesis, Institute of Geology ETH Zürich, Switzerland, p. 132.

Ruiz, G.M.H, Seward, D., Winkler, W. 2004. Detrital thermochronology - a new perspective on hinterland tectonics, an example from the Andean Amazon Basin, Ecuador: Basin Research, v. 16, p. 413–430.

Sajona, F. G., Maury, R. C., Bellon, H., Cotten, J., Defant, M. J., Pubellier, M., Rangin, C. (1993). Initiation of subduction and the generation of slab melts in western and eastern Mindanao, Philippines: Geology, v. 21, p. 1007–1010.

Sauer, W. 1965. Geología del Ecuador. Ministerio de Educación, Quito. pp. 583.

Saunders, A.D., Tarney, J., Kerr, A.C., Kent, R.W. 1996. The formation and fate of large igneous provinces: Lithos, v. 37, p. 81-95.

Savoyat, F., Vernet, R., Sigal, J., Mosquera, C., Granja, B., Guevara, R. 1970. Estudio General de la Cuenca de Esmeraldas. Estudio micropantologico de las formaciones de la Sierra. SNGM - Inst. Franc. Petrole, Unpubl. Report.

Schweitzer , E., Papike, J., Bence, E. 1979. Statistical analysis of clinopyroxenes from deep-sea basalts: American Mineralogist, v. 64, p. 501-513.

Sinton, C.W., Sigurdsson, H., Duncan, R.A. 2000. Geochronology and petrology of the igneous basement at the lower Nicaraguan Rise, Site 1001 roceedings of the Ocean Drilling Program, Scientific Results, Leg 165: College Station, Texas, Ocean Drilling Program, Texas A&M, University, p. 233–236.

Sinton, C.W., Duncan, R.A., Denyer, P. 1997. Nicoya Peninsula, Costa Rica: A single suite of Caribbean oceanic plateau magmas: Journal of Geophysical Research, v. 102, p. 15507-15520.

Sinton, C.W., Duncan, R.A., Storey, M., Lewis, J., Estrada, J.J. 1998. An oceanic flood basalts province within the Caribbean plate: Earth and Planetary Science Letters, v. 155, p. 221-235.

Sigal, J. 1968. Estratigrafìa micropaleontològica del Ecuador, datos anteriores y nuevos. Informe Instituto Francés de petròleo y Servicio Nacional de Geologìa y Minerìa. Quito.

Sobolev, A.V., Danyushevsky, L.V. 1994. Petrology and geochemistry of boninites from the north termination of the Tonga Trench: constraints on the generation conditions of primary high-Ca boninite magmas: Journal of Petrology, v. 35, p. 1183–1213.

Souris M., 2001, Repùblica del Ecuador : modelo numérico del relieve, escala 1:1000000, Modèle numérique calculé à partir des cartes topographiques del I'IGM (1:50000, 1:1000000), édité et distribuée par I'IGM, Quito.

Spadea, P. and Espinosa, A., 1996. Petrology and chemistry of late Cretaceous volcanic rocks from the southernmost

segment of the Western Cordillera of Colombia (South America): Journal of South American Earth Sciences, v. 9, p. 79-90.

Spadea, P., Espinosa, E., Orrego, A., 1989. High-Mg extrusive rocks from the Romeral zone ophiolites in the south western Colombian Andes: Chemical Geology, v. 77, p. 303–321.

Spikings, R.A., Crowhurst, P.V., 2004. (U–Th)/He thermochronometric constraints on the late Miocene–Pliocene tectonic development of the northern Cordillera Real and the Interandean Depression, Ecuador: Journal of South American Earth Sciences, v. 17, p. 239-251.

Spikings, R.A., Seward, D., Winkler, W. and Ruiz, G.M., 2000. Low temperature thermochronology of the northern Cordillera Real, Ecuador tectonic insights from zircon and apatite fission-track analysis: Tectonics, v. 19, p. 649-668.

Spikings, R.A., Winkler, W., Hughes, R.A., Handler, R., 2005. Thermochronology of Allochthonous Blocks in Ecuador: unraveling the accretionary and post-accretionary history of the Northern Andes: Tectonophysics, v. 399, p. 195–220.

Spikings, R.A. Winkler, W., Seward, D., Handler, R. 2001. Along-strike variations in the thermal and tectonic response of the continental Ecuadorian Andes to the collision with heterogeneous oceanic crust: Earth and Planetary Science Letters, v. 186, p. 57-73.

Steinmann, M. 1997. The Cuenca basin of southern Ecuador: tectono-sedimentary history and the Tertiary Andean evolution. Ph.D. dissertation, Institute of Geology, ETH Zurich, Switzerland.

Stern R. J., Bloomer S. H. 1992. Subduction zone infancy; examples from the Eocene Izu-Bonin-Mariana and Jurassic California arcs: Geological Society of America Bulletin, v. 104, p. 1621-1636.

Stern, R.J., Morris, J., Bloomer, S.H., Hawkins, J.W.Jr. 1991. The source of the subduction component in convergent margin magmas: trace element and radiogenic isotope evidence from Eocene boninites, Mariana forearc: Geochim. Cosmochim. Acta, v. 55, p. 1467-1481

Sun, S.S., McDonough, W.F. 1989. Chemical and isotopic systematics of oceanic basalts: implications for mantle compositionand processes. Magmatism in the ocean basins. Geological Society Special Publication, v. 42, p. 313-345.

Tagami, T., Galbraith, R.F., Yamada, R., Laslett, G.M. 1998. Revised annealing kinetics of fission tracks in zircon and geological implications. In: Van den Haute, P., de Corte, F. (Eds.), Advances in Fission-Track Geochronology. Kluwer Academic Publishers, Dordrecht, pp. 99– 112.

Thalmann, H.E. 1946. Micropaleontology of upper Cretaceous and Paleocene in western Ecuador: AAPG Bulletin, v. 30, p. 337-347.

Thompson, P.M., Kempton, P.D., White, R.V., Kerr, A.C., Tarney, J., Saunders, A.D., Fitton, J.G., McBirney, A. 2003. Hf-Nd isotope constraints on the origin of the Cretaceous Caribbean Plateau and its relationship to the Galapagos plume: Earth and Planetary Science Letters, v. 217, p. 59-75.

Toro, J.A., Jaillard, E. 2005. Provenance of the Upper Cretaceous to upper Eocene clastic sediments of the Western Cordillera of Ecuador: Geodynamic implications: Tectonophysics, v. 399, p. 279-292.

Trenkamp, R., Kellog, J.N. Freymueller, J.T. Mora, H.P. 2002. Wide plate margin deformation, southern Central America and northwestern South America, CASA GPS observations: Journal of South American Earth Sciences, v. 15, p. 157-171.

Tschopp, H.J. 1948. Geological sketch of Ecuador. Bulletin de l'Association Suisse de Geologie Ingenieur et Petrologie, v. 15, p. 14–45.

Vallejo, C., Spikings, R.A., Winkler, W., Luzieux, L., Chew, D., Page, L. 2006. The early interaction between the Caribbean Plateau and the NW South American Plate: Terra Nova, v. 18, p. 264-269

Van Thournout, F. 1991. Stratigraphy, magmatism and tectonism in the Ecuadorian northwestern cordillera: Metallogenic and Geodynamic implications. PhD thesis, Katholieke Universiteit Leuven, 150 pp.

Van Thournot, F., Hertogen, J., Quevedo, L. 1992. Allochtonous Blocks in northern Ecuador: Tectonophysics, v. 205, p. 205-222.

Wadge, G., Jackson, T.A., Issacs, M.C., Smith, T.E. 1982. The ophiolitic Bath-Dunrobin Formation, Jamaica: Significance for Cretaceous plate margin evolution in the NW Caribbean: Journal of the Geological Society, v. 139, p. 321-333.

Walker, R.J., Echeverria, I.M., Shirey, S.B., Horan, M.F. 1991. Re-Os isotopic constraints on the origin of volcanic rocks, Gorgona Island, Colombia: Os isotopic evidence for ancient heterogeneities in the mantle: Contributions to Mineralogy and Petrology, v. 107, p. 150-162.

Walker, R.J., Storey, M.J. Kerr, A.C. Tarney, J., Arndt, N.T. 1999. Implications of 187Os isotopic heterogeneities in a mantle plume: Evidence from Gorgona Island and Curacao: Geochemica et Cosmochemica Acta, v. 63, p. 713-728.

Wallrabbe-Adams, H.J., 1990. Petrology and geotectonic development of the Western Ecuadorian Andes: the Basic Igneous Complex: Tectonophysics, v. 185, p. 163-182.

White, R., Tarney, J., Kerr, A., Saunders, A., Kempton, P., Pringle, M., Klaver, G. 1999. Modification of an oceanic plateau, Aruba, Dutch Caribbean: Implications for the generation of continental crust: Lithos, v. 46, p. 43–68.

Wilkinson, I.A. 1996. Foraminifera from a suite of slides from the Western Cordillera of the Ecuadorian Andes. Technical Report WH/96/99R, Biostratigraphy and Sedimentology Research Group BGS, Nottingham UK.

Wilkinson, I.P. 1997. Foraminifera from a suite of samples from Ecuador. Technical report WH/96/85R Biostratigraphy and sedimentology Research Group BGS, Nottingham UK.

Wilkinson, I.P. 1998. Foraminifera from a suite of Late Cretaceous to Palaeogene samples of the Cordillera occidental, Ecuador. Technical Report WH/98/163R Biostratigraphy and Sedimentology Group BGS. Nottingham UK.

Williams, I.S., 1998. U–Th –Pb Geochronology by Ion Microprobe. In: McKibben, M.A., Shanks III, W.C., Ridley, W.I. (Eds.), Applications of Microanalytical Techniques to Understanding Mineralizing Processes: Rev. Econ. Geol., v. 7, p. 1–35.

Winkler, W., Villagómez, D., Spikings, R., Abegglen, P., Tobler, S. and Egüez, A., 2005. The Chota basin and its significance for the inception and tectonic setting of the inter-Andean depression in Ecuador: Journal of South American Earth Sciences, v. 19, p. 5-19.

Wolf, T. 1892. Geografía y geología del Ecuador. Brockhaus, Leipzig. 671 pp. / (1933). Geography and geology of Ecuador (Flanagan, J.W., transl.). Grand & Toy, Toronto. 684 pp.

York, D., 1969. Least-squares fitting of a straight line with correlated errors: Earth and Planetary Science Letters,

v. 5, p. 320–324.

APPENDIX 1: Analytical procedures of whole-rock geochemistry and isotopic data.

Whole-rock samples were analyzed for major oxides and trace elements by X-ray fluorescence spectroscopy using a Phillips PW 1400 at the Centre d'Analyses Minérale, University of Lausanne, Switzerland. Rare-earth element and trace element concentrations were also determined by inductively coupled plasma mass spectrometry (ICP-MS) using a Hewlett Packard 45000 at the Institute F.-A. Forel, Versoix, Switzerland. Strontium, and neodymium isotope analyses were carried out at the Department of Mineralogy, University of Geneva, Switzerland. Rb, Sr, Sm, Nd, U, Th and Pb concentrations for age-correcting the isotopic data used the values determined by ICP-MS.

Samples for isotopic analysis were digested in a 5 ml of *ca* 40% HF and 1 ml of *ca* 15M HNO_3. For the digestion, samples were stored in closed PTFE beakers for one week at a temperature of 165°C. When dry, the sample were treated with 2 x 2 ml additions of *ca* 15M HNO_3 followed by 1 ml of *ca* 6M HCl. 5 ml of ca 6M HCl was then added and left to stand overnight at 165°C. Following digestion, the sample was converted to nitrate by 3 x 1 ml additions of 4M HNO_3, dissolved in 2 ml of 1M HNO_3, centrifuged and then loaded onto the ion exchange columns. Teflon-distilled HCl and HF and Ultrex-II HNO_3 were used throughout the dissolution and chemical separation procedures, and reagent and total procedure blanks are neglible. Sr and Pb separation used Eichrom Sr-Spec cation exchange resin (50- 100 μm) in disposable PP columns, and is similar to the procedure described by Deniel & Pin (2001). Sr was further purified by a second column separation on the same columns. Nd separation employed Eichrom TRU-Spec Resin (50 - 100 μm) in disposable PP columns in series with Ln-Spec Resin (50 - 100 μm), using the methods described in Pin & Zaldegui (1997).

Fractions of the purified lead were loaded onto zone-refined rhenium filaments using the silica gel technique, and lead isotope ratios were measured on a MAT Finnigan 262 mass spectrometer in static mode. Lead isotope ratios were corrected for fractionation by a + 0.10% amu correction factor, based on more than 100 analyses of the SRM-981 international standard. Strontium and neodymium isotope ratios were measured on a seven-collector Finnigan MAT 262 thermal ionization mass spectrometer with extended geometry and stigmatic focusing using double Re filaments. Strontium isotopic analysis was conducted in a semidynamic mode (triple collectors, measurement jumping mode). The Sr isotope ratios are mass fractionation corrected to $^{88}Sr/^{86}Sr = 8.375209$ and normalized to the E&A standard, with $^{87}Sr/^{86}Sr = 0.708000$ using an average of $0.708028 \pm 5 \times 10^{-6}$ (2σ; n = 52) measured during the period of analysis. $^{143}Nd/^{144}Nd$ was measured in a semidynamic mode (quadruple collectors, measurement jumping mode), mass fractionation corrected to $^{146}Nd/^{144}Nd = 0.721903$, and normalized to the La Jolla standard = 0.511835. An average of $0.511838 \pm 6 \times 10^{-6}$ ($2\ \sigma$; n = 28) was measured during the analysis.

References

Deniel, C. & Pin, C., 2001, Single-stage method for the simultaneous isolation of lead and strontium from silicate samples for isotopic measurements, Analytica Chimica Acta, v. 426, p. 95-103.

Pin, C. & Zalduegui, J.F.S., 1997, Sequential separation of light rare-earth elements, thorium and uranium by miniaturized extraction chromatography: Application to isotopic analyses of silicate rocks: Analytica Chimica Acta, v. 339, p. 79-89.

APPENDIX 2: Major, trace elements and isotopic composition (ICPMS) from selected Western Cordillera samples

Formation	Pujilí Granite	Mulaute			Rio Cala	Silante	Pallatanga	
Sample	**03CV258**	**02CV130**	**02CV165**	**00RS40**	**02CV104**	**02CV98**	**02CV120**	**03CV316**
SiO_2	56.92	49.72	54.21	50.60	50.25	53.35	44.58	49.23
TiO_2	0.07	0.47	0.51	0.84	0.77	0.84	0.89	1.3
Al_2O_3	10.04	16.04	16.45	19.02	14.18	18.11	8.73	12.99
Fe_2O_3	0.39	9.90	7.91	10.67	10.16	10.25	12.73	12.92
MnO	0.02	0.18	0.13	0.17	0.19	0.21	0.18	0.2
MgO	0.21	6.78	6.86	4.64	7.01	3.8	16.47	6.61
CaO	21.75	9.26	10.01	8.24	9.60	8.28	11.48	9.76
Na_2O	8.29	2.84	2.49	3.07	2.82	2.7	0.3	2.61
K_2O	0.20	0.25	0.41	1.07	1.75	0.52	0.01	0.15
P2O5	0.13	0.11	0.21	0.22	0.43	0.35	0.19	0.16
Cr_2O_3	0.00	0.03	0.06	0.01	0.02	0.01	0.27	0.01
NiO	0.00	0.01	0.01	0.00	0.01	0.00	0.1	0.01
Total	100.53	99.39	99.60	99.97	99.38	99.7	99.45	98.29
LOI	2.51	3.80	0.34	1.43	2.18	1.3	3.52	2.36
Ga	10.000	14.000	16.000	20.000	16.000	19	15	18
Sc	5.610	38.796	34.893	39.616	41.779	30.24	36.727	48.409
Ti	352.283	2613.795	2873.219	4696.168	4362.280	5209.64	4837.95	5707.23
V	2.758	254.746	239.690	398.558	314.557	251.61	255	317
Cr	11.695	147.627	303.497	23.431	74.328	9.916	1588	59
Co	1.377	29.076	25.415	26.667	34.289	23.346	72.58	41.05
Ni	10.135	48.580	71.409	15.341	42.010	7.964	734	79
Zn	4.627	58.491	51.329	72.275	65.950	83	84	83
Rb	1.342	3.275	8.723	28.020	37.154	6.7	0.486	1.88
Sr	303.984	57.339	345.055	305.686	916.418	421	22	104.17
Y	2.673	13.643	19.369	15.463	17.198	18.8	12.2	20.976
Zr	11.247	27.130	17.251	20.569	88.816	63	14	48.038
Nb	1.034	0.403	0.556	0.878	3.343	3.1	3.4	4.147
Ba	162.012	67.805	226.174	183.000	416.716	288	8.37	12.02
La	10.211	1.891	4.326	3.408	19.059	2.28	2.28	3.012
Ce	20.916	4.497	9.185	7.114	40.995	5	6.28	8.637
Pr	2.643	0.819	1.642	1.324	6.155	1.85	1.078	1.395
Nd	8.725	4.042	7.644	6.508	25.871	8.52	5.496	6.853
Sm	1.233	1.373	2.064	1.906	5.349	2.24	1.813	2.239
Eu	0.206	0.375	0.713	0.749	1.510	0.798	0.686	0.867
Gd	0.923	1.801	2.416	2.384	5.083	2.611	2.258	3.157
Tb	0.103	0.323	0.419	0.412	0.625	0.460	0.371	0.561
Dy	0.505	2.149	2.673	2.643	3.467	2.928	2.308	3.682
Ho	0.091	0.499	0.616	0.564	0.638	0.646	0.454	0.803
Er	0.231	1.536	1.804	1.637	1.767	1.859	1.250	2.359
Tm	0.038	0.233	0.265	0.248	0.244	0.298	0.162	0.347
Yb	0.217	1.644	1.781	1.625	1.668	2.019	1.0039	2.352

Lu	0.034	0.246	0.270	0.260	0.253	0.318	0.138	0.370
Hf	0.374	0.892	0.700	0.822	2.436	2.380	1.340	1,451
Ta	0.418	0.381	0.572	0.376	0.519	1.627	0.490	0.520
Pb	1.876	0.661	1.344	2.176	2.470	2.714	0.55	0.061
Th	2.248	0.349	0.765	0.674	3.328	2.329	0.275	0.281
U	0.105	0.091	0.202	0.096	0.680	0.450	0.043	0.040
$^{87}Sr/^{86}Sr$	0.705	0.704	0.704	0.703	0.704	0.7036	0.70309	0.7039
$^{143}Nd/^{144}Nd$	0.513	0.513	-	0.513	0.513	0.5128	0.5132	0.5128
εNd	6.876	8.933	-	7.501	5.986	6.887	14.346	7.013
εSr	8.414	-11.821	-9.53	-21.538	-14.894	-14.7	-22.64	-10.42

APPENDIX 3: Analytical procedures for heavy minerals determinations, clinopyroxene chemistry and U/Pb laser ablation ICPMS zircon dating.

Heavy minerals determinations

The separation method is described in Winkler (1988), and includes, rock crushing, followed by acid dissolution in warm 10% acetic solution (70°C) to eliminate carbonates and organic matter. Small quantities of H_2O_2 were added to the acid solution to avoid the formation of acetates, which would prevent further reaction. When acid dissolution was not effective (mainly in highly silicified sandstones) we use an iron mortar to accelerate the mineral desegregation. The acid dissolution was followed by sieving, using a 63 to 400μ mesh sieve. The heavy fraction was then separated from the light fraction using bromoform of density 2.82. The heavy minerals were mounted in slides, using piperine. Between 200 and 250 grains were point counted per slide. Midpoint counting was used to avoid bias by grain size effects.

Clinopyroxene geochemistry

Clinopyroxene grains were separated from the heavy fraction using the Frantz magnetic separator and individual grains were hand picked and mounted in epofix resine, which was then polished and coated with a film of carbon. For the single grain geochemistry, at least 12 clinopyroxene grains were analyzed per sample. All analyzed pyroxenes were optically homogeneous and multiple analyses of individual grains indicate that they are chemically homogeneous and lack zoning. The absence of quenching texture suggests that the clinopyroxenes were in equilibrium with the melt from which they crystallized. (Cawood, 1983). Clinopyroxene grains extracted from the volcanic rocks of the basement were also analyzed to correlate the different possible sources with the detrital grains. Major elements geochemistry in pyroxenes was determined using a JEOL JXA-8200 microprobe analyzer at ETH Zurich. The accelerating voltage was 15 kV for a beam current of 10 and 20 ηA. The structural formulae of clinopyroxenes were calculated based on four cations and six oxygens.

Trace elements analyses in clinopyroxenes were performed using the LA-ICPMS available at the Mineralogy Institute at ETH. The clinopyroxenes were analyzed from the same mounted grains used for the major elements analysis; previously the carbon coating was eliminated from the mounts. Clinopyroxenes were ablated using an optically homogenized UV beam from a 193 nm ArF Eximer laser. The size of the laser spot was adjusted at 30

μm using pinhole apertures. The ablated material was transported by He carrier gas to an Elan 6100 quadrupole mass-spectrometer, which sequentially recorded signals for all the elements of interest. Ablation was monitored through an optical microscope and the recorded signal was displayed in real time on a computer. The obtained data was processed using the program LAMTRACE (Jackson, 1997).

U/Pb laser ablation ICPMS zircon dating.

For U/Pb laser ablation ICPMS dating, zircons were extracted from the heavy minerals fraction, following standard procedures: Frantz magnetic separator, di-iodomethane (δ= 3,3 g/cm^3) heavy liquids separation and hand picking. The grains were mounted in epofix resine known to be devoid of Pb and U. The mount was then polished and washed in an ultrasonic bath with distilled water. The U-Pb analyses were undertaken using a Perkin-Elmer 6100 DRC Laser Ablation - Inductively Coupled Plasma Mass Spectrometer in the laboratory Managed by François Bussy, at the Institute of Mineralogy and Geochemistry (University of Lausanne). NIST 610 zircon was used as an external standard. Zircon was analyzed using 5Hz laser frequency and beam diameters between 30 and 60 μm.
The raw data was processed using LAMTRACE (Jackson, 1997) and age results were plotted with Isoplot-Ex Version 2.49 (Ludwig, 2001).

References

Cawood, P.A., 1983. Modal composition and detrital clinopyroxene geochemistry of lithic sandstones from the New England Fold Belt (east Australia): A Paleozoic forearc Block: Geological Society of America Bulletin, v. 94, p. 1199-1214.

Jackson, S.E., 1997. LAMTRACE v 1.73, LAM-ICP-MS data reduction spreadsheet. Department of Earth Sciences, Memorial University of Newfoundland, St John's, Canada.

Ludwig KR (2001) Isoplot /Ex version 2.49. A geochronological toolkit for Microsoft Excel. Berkeley Geochronological Center Spec Publ la.

Winkler, W. 1988. Mid- to Early Cretaceous flysch and melange formations in the western part of the Eastern Alps, Palaeotectonic implications: Geologische Bundesanstalt Wien, Jahrbuch, v. 131, p. 341–389.

APPENDIX 4: Samples for Heavy Mineral analysis from the Western Cordillera.

Sample	Location	Formation	UTM		Lithology
			X	Y	
00RS13	Saquisilli -La Mana	Apagua	729476.34	9891834.38	medium-grained turbiditic sandstone
00RS3	Cuenca - La Troncal	Apagua	671485.22	9710248.840	medium-grained turbiditic sandstone
00RS7	La Troncal - Cumanda	Apagua	708519.45	9756821.3	medium-grained turbiditic sandstone
02CV17	La Mana- Latacunga	Apagua	728319.34	9891250.370	medium-grained turbiditic sandstone
02CV18	La Mana- Latacunga	Apagua	728434.34	9891262.370	medium-grained turbiditic sandstone

03CV254	Apagua - Angamarca	Apagua	731489.39	9875271.270	sandstone
02CV76	Ibarra-Alto Tambo	El Laurel	809134.36	10085536.77	fine-grained sandstone
02CV77	Ibarra-Alto Tambo	El Laurel	809134.36	10085536.77	fine-grained sandstone
00RS24	Santo Domingo - Aloag	Mulaute	737222.24	9963618.88	coarse-grained turbiditic sandstone
02CV62	Calacali-Pacto	Mulaute	747824.19	10017889.24	sandstone
00RS14	Saquisilli -La Mana	Pilaló	722368.29	9895648.39	medium-grained turbiditic sandstone
00RS34	M.D. Mundo - L. Bancos	Pilaló	769606.36	10001069.190	medium-grained turbiditic sandstone
02CV11	La Mana- Latacunga	Pilaló	722672.29	9895844.39	coarse sandstone
02CV33	Quito-Chiriboga	Pilaló	761925.39	9967437.96	sandstone
03CV223	Riobamba - Pallatanga	Pilaló	740966.61	9806358.770	medium-grained sandstone
03CV309	Nono - Tandayapa	Pilaló	765615.35	9994229.14	sandstone
00RS25	Santo Domingo - Aloag	Pilatón	741300.28	9959616.860	coarse-grained turbiditic sandstone
02CV131	Sto. Domingo-Aloag	Pilatón	741694.28	9958725.860	coarse-grained turbiditic sandstone
02CV72	Ibarra-Alto Tambo	Pilatón	804325.33	10086291.76	sandstone
00RS12	Saquisilli -La Mana	Rumi Cruz	731404.35	9893974.4	medium-grained turbiditic sandstone
02CV24	La Mana- Latacunga	Rumi Cruz	732488.36	9894977.41	conglomerates with milky qtz+chert
03CV240	Riobamba - Chimbo	Rumi Cruz	730487.53	9808200.760	fluvial sandstones
03CV250	Apagua - Angamarca	Rumi Cruz	730667.36	9888775.360	sandstone
03CV251	Apagua - Angamarca	Rumi Cruz	730667.36	9888775.360	conglomerate
00RS38	M.D. Mundo - L. Bancos	Sanguangal	727817.12	9995739.06	fine-grained sandstone
00RS39	M.D. Mundo - L. Bancos	Sanguangal	726111.12	9989071.020	fine-grained sandstone, sheared
03CV137	Calacali-Saguangal	Sanguangal	747194.17	10023517.27	fine-grained sandstone
03CV139	Calacali-Saguangal	Sanguangal	744478.15	10025652.280	black shale
00RS32	Saquisilli (Q. Pusu-chusi)	Saquisilli	755739.5	9906190.540	medium-grained turbiditic sandstone
02CV124	Guaranda- San Juan	Saquisilli	737786.55	9821586.88	conglomerates with milky qtz+chert
02CV125	Guaranda- San Juan	Saquisilli	737786.55	9821586.88	quartz-rich turbiditic sand-stone
02CV26	La Mana- Latacunga	Saquisilli	756986.5	9908179.55	medium-grained turbiditic sandstone
02CV47	Guaranda- San Juan	Saquisilli	735497.58	9822700.860	medium-grained turbiditic sandstone
03CV203	Guaranda- San Juan	Saquisilli	740475.58	9818662.860	conglomerates
03CV204	Guaranda- San Juan	Saquisilli	738539.56	9821496.88	coarse sandstone with micas
03CV215	Guaranda- San Juan	Saquisilli	735833.54	9822532.88	sandstone
00RS28	Santo Domingo - Aloag	Silante	751991.37	9951726.840	Breccia
02CV136	Sto. Domingo-Aloag	Silante	757809.41	9950588.840	conglomeratic sandstone

02CV37	Quito-Chiriboga	Silante	756246.35	9969348.96	crevasse splay sandstone with ripples
02CV56	Calacali-Pacto	Silante	766015.33	10002663.190	volcanoclastics
03CV268	Calacali - Pacto	Silante	765557.33	10001411.18	laminated sandstone
00RS2	Cuenca - La Troncal	Yunguilla	672716.23	9707354.81	medium-grained turbiditic sandstone
00RS33	M.D. Mundo - L. Bancos	Yunguilla	771490.37	10001497.200	medium-grained turbiditic sandstone
00RS4	Cuenca - La Troncal	Yunguilla	672954.24	9706390.8	medium-grained turbiditic sandstone
02CV42	Guaranda- San Juan	Yunguilla	744324.59	9827522.940	medium-grained turbiditic sandstone
02CV51	Calacali-Pacto	Yunguilla	772829.38	10001271.200	coarse sandstone
04CV333	Nono - Tandayapa	Yunguilla	768556.37	9992839.14	turbidites
WW3311	Cumbe	Yunguilla	721350	9658750	fine-grained sandstone

APPENDIX 5: Heavy Minerals of samples from the Western Cordillera.

Sample	Formation	zircon	turmaline	rutile	branti	garnet	chloritoid	epidot	clinozoicite	zoicite	spinel	hornblend	pyroxene	TOTAL
00RS13	Apagua	47	20	3	111	4	4	2			11	15	38	255
00RS3	Apagua	13	31	1		3					7	2	137	194
00RS7	Apagua	27	30			0	23				21	22	27	150
02CV18	Apagua	24	22		28	25					22	25	22	168
03CV254	Apagua	108	16	6	9	2	3	1	11		2		16	174
02CV76	El Laurel	42	12	2	1	13		2	12	1	4	1	11	101
02CV77	El Laurel	81	50	10	17	1	11		1		1			172
00RS24	Mulaute				0	0		3	123				20	146
02CV62	Mulaute	0			0				12		17	0	68	97
00RS14	Pilaló	32	13		0	13					31	20	12	121
00RS34	Pilaló	2				3		3			3	157	141	309
02CV33	Pilaló						1						305	306
00RS25	Pilatón				0	0					0	0	150	150
02CV131	Pilatón											3	337	340
02CV72	Pilatón	2			0						1	1	224	228
00RS12	Rumi Cruz	72	9	2	11	6		131	39		5	1	3	279
02CV24	Rumi Cruz	33	21	7	0						6	14	10	91
03CV240	Rumi Cruz	18	2			2		59	100	4			1	186
03CV250	Rumi Cruz	195	31	12	9	3	7				2		1	260
03CV251	Rumi Cruz	160	46	5	9	4	1		1		2		2	230
00RS38	Sanguangal				0								132	132
00RS39	Sanguangal				0	1		3			0	22	295	321
03CV137	Sanguangal	35	15							13		13	19	95

Sample	Formation	zircon	turmaline	rutile	branti	garnet	chloritoid	epidot	clinozoicite	zoicite	spinel	Hb.	monazite	pyroxene	TOTAL
03CV139	Sanguangal	31	28	1			77				2			1	140
00RS32	Saquisilli	8	17	1	3	1		77	4	4	1	24		32	172
02CV124	Saquisilli	16	16	4	1	25					4	3		58	127
02CV125	Saquisilli	24	55	9	12	9					8				117
02CV26	Saquisilli	17	25	6	0	11	10	7	24		6	7		10	123
02CV47	Saquisilli	20	37		6	32					7				102
03CV203	Saquisilli	29	14	12	11	27		11			13			11	128
03CV204	Saquisilli	59	26	13	7	58	1				18	1		33	216
03CV215	Saquisilli	20	53	1	3	23	2					2		2	106
00RS28	Silante				1	2		9			2			193	207
02CV136	Silante	4			0	1					4	254		38	301
02CV37	Silante	5	4		2	3		1	18		4	120		31	188
02CV56	Silante				0				2		8	64		205	279
03CV268	Silante		5					7				219		34	265
00RS2	Yunguilla	21			0	28						24		25	98
00RS33	Yunguilla	33	36	3	2	5	10	34	4		19	13		6	165
00RS4	Yunguilla	29	33	2	4	1	3	4			1	2		40	119
02CV42	Yunguilla	28	23	11	11	34					16	12		11	146
02CV51	Yunguilla	53	17	3	12	30	2	2	5		2				126
WW3311	Yunguilla	44	27	6	5	9		2					8		101
02CV51	Yunguilla	53	17	3	12	30	2	2	5		2				126
WW3311	Yunguilla	44	27	6	5	9		2					8		101

APPENDIX 6: Composition of the clinopyroxenes of samples from the Western Cordillera. Wo = wollastonite, En = enstatite, Fs = Ferrosilite Ac = Acmite

Sample RS44 - San Juan de Lachas Fm

Grain	Wo	En	Fs	Ac
1.10	44.626	41.256	13.136	0.982
1.20	44.626	41.256	13.136	0.982
1.30	44.626	41.256	13.136	0.982
1.40	44.626	41.256	13.136	0.982
1.50	44.626	41.256	13.136	0.982
1.60	44.626	41.256	13.136	0.982
1.70	44.626	41.256	13.136	0.982
1.80	44.626	41.256	13.136	0.982
1.90	44.626	41.256	13.136	0.982
1.10	44.626	41.256	13.136	0.982
1.11	44.626	41.256	13.136	0.982
1.12	44.626	41.256	13.136	0.982
1.13	44.626	41.256	13.136	0.982
1.14	44.626	41.256	13.136	0.982

Sample 03CV289 – Macuchi Unit

Grain	Wo	En	Fs	Ac
1.10	44.349	48.935	6.165	0.551
1.20	44.180	48.646	6.545	0.629
1.30	45.261	46.557	7.401	0.781
1.40	45.792	43.953	9.643	0.612
1.50	45.081	47.089	7.323	0.506
1.60	44.875	41.905	12.302	0.918
1.70	43.943	40.841	14.203	1.013
1.80	46.398	43.860	9.143	0.600
1.90	46.119	46.211	6.974	0.696
1.10	44.251	42.288	12.559	0.902
1.11	44.415	43.682	10.926	0.977
1.12	45.261	43.258	10.621	0.860
1.13	42.474	44.320	12.339	0.867
1.14	43.758	48.884	6.683	0.675
1.15	46.615	45.340	7.546	0.500

Sample 03CV223 – Pilaló Fm.

Grain	Wo	En	Fs	Ac
1.10	41.352	39.035	18.737	0.876
1.20	40.905	40.454	17.884	0.757
1.30	43.764	47.792	8.025	0.419
1.40	44.031	44.613	10.877	0.479
1.50	41.555	39.798	17.800	0.848
1.60	41.153	37.383	20.843	0.621

Sample 02CV124 - Gallo Rumi Fm.

Grain	Wo	En	Fs	Ac
1.1	44.626	41.256	13.136	0.982
1.2	44.626	41.256	13.136	0.982
1.3	44.626	41.256	13.136	0.982
1.4	44.626	41.256	13.136	0.982

Sample 03CV197–Macuchi Fm. (Las Juntas turbidites)

Grain	Wo	En	Fs	Ac
1.10	44.567	46.984	7.848	0.602
1.20	43.347	40.351	15.454	0.848
1.30	42.483	41.968	14.606	0.942
1.40	43.990	40.234	14.731	1.045
1.50	38.562	43.166	17.662	0.610
1.60	42.652	41.846	14.713	0.789
1.70	45.832	47.421	6.266	0.482
1.80	40.602	40.627	18.088	0.683
1.90	41.858	42.150	15.193	0.799
1.10	42.488	42.113	14.725	0.675
1.11	42.873	46.109	10.325	0.693
1.12	41.960	41.446	15.650	0.944
1.13	42.870	44.641	11.909	0.580
1.14	43.906	44.299	11.129	0.666
1.15	41.761	43.430	14.102	0.707
1.16	41.899	41.671	15.423	1.008
1.17	41.636	41.979	15.511	0.873
1.18	42.619	41.022	15.333	1.026
1.19	42.105	43.057	14.131	0.708
1.20	40.924	42.031	16.123	0.922
1.21	42.016	42.205	14.780	0.998
1.22	42.731	41.308	14.929	1.032
1.23	40.662	41.675	16.733	0.929

Sample 02CV99 - Silante Fm.

Grain	Wo	En	Fs	Ac
1.10	44.626	41.256	13.136	0.982
1.20	44.626	41.256	13.136	0.982
1.30	44.626	41.256	13.136	0.982
1.40	44.626	41.256	13.136	0.982
1.50	44.626	41.256	13.136	0.982
1.60	44.626	41.256	13.136	0.982
1.70	44.626	41.256	13.136	0.982
1.80	44.626	41.256	13.136	0.982

1.70	41.971	39.820	17.167	1.042
1.80	40.978	40.215	18.127	0.680
1.90	41.086	34.990	23.168	0.757
1.10	35.925	33.604	29.751	0.721
1.11	41.916	38.828	18.434	0.823
1.12	41.186	35.977	21.997	0.840
1.13	42.165	38.898	18.163	0.774
1.14	43.033	40.651	15.167	1.150
1.15	41.624	37.324	20.198	0.854
1.16	40.965	35.899	22.390	0.747
1.17	40.975	36.222	22.033	0.770
1.18	41.672	40.380	17.301	0.647
1.19	40.925	43.282	14.958	0.835
1.20	41.635	39.836	17.874	0.654

Sample 02CV56 - Silante Fm.

Grain	Wo	En	Fs	Ac
1.10	41.398	43.748	13.821	1.033
1.20	40.294	43.788	14.984	0.935
1.30	41.144	42.471	15.235	1.150
1.40	40.449	45.447	13.132	0.972
1.50	40.842	46.962	11.519	0.677
1.60	42.253	42.009	14.676	1.062
1.70	43.570	40.449	14.227	1.754
1.80	40.689	43.776	14.493	1.042
1.90	43.597	43.726	11.524	1.152
1.10	39.774	48.540	10.791	0.895
1.11	39.302	45.198	14.675	0.825
1.12	41.229	42.874	14.753	1.143
1.13	42.689	42.574	13.649	1.088
1.14	43.629	41.509	13.626	1.235
1.15	43.024	40.471	15.107	1.397
1.16	39.307	44.322	14.857	1.514
1.17	44.052	46.277	9.132	0.540
1.18	44.626	41.256	13.136	0.982

Sample 02CV131 - Pilatón Fm.

Grain	Wo	En	Fs	Ac
1.10	42.121	43.296	13.538	1.045
1.20	46.175	47.383	6.175	0.267
1.30	45.999	44.125	9.318	0.558
1.40	41.721	45.745	11.899	0.635
1.50	41.298	46.622	11.432	0.648
1.60	45.449	46.073	7.870	0.608
1.70	45.575	43.388	10.453	0.584
1.80	44.664	42.551	12.152	0.634
1.90	44.626	41.256	13.136	0.982
1.10	44.626	41.256	13.136	0.982
1.11	44.626	41.256	13.136	0.982

Sample RS26 - Silante Fm.

Grain	Wo	En	Fs	Ac
1.10	44.626	41.256	13.136	0.982
1.20	44.626	41.256	13.136	0.982
1.30	44.626	41.256	13.136	0.982
1.40	44.626	41.256	13.136	0.982
1.50	44.626	41.256	13.136	0.982
1.60	44.626	41.256	13.136	0.982
1.70	44.626	41.256	13.136	0.982
1.80	44.626	41.256	13.136	0.982
1.90	44.626	41.256	13.136	0.982
1.10	44.626	41.256	13.136	0.982
1.11	44.626	41.256	13.136	0.982
1.12	44.626	41.256	13.136	0.982

Sample 00RS35 - Silante Fm.

Grain	Wo	En	Fs	Ac
1.10	44.626	41.256	13.136	0.982
1.20	44.626	41.256	13.136	0.982
1.30	44.626	41.256	13.136	0.982
1.40	44.626	41.256	13.136	0.982
1.50	44.626	41.256	13.136	0.982

Sample RS39 - Mulaute Fm.

Grain	Wo	En	Fs	Ac
1.10	44.626	41.256	13.136	0.982
1.20	44.626	41.256	13.136	0.982
1.30	44.626	41.256	13.136	0.982
1.40	44.626	41.256	13.136	0.982
1.50	44.626	41.256	13.136	0.982
1.60	44.626	41.256	13.136	0.982
1.70	44.626	41.256	13.136	0.982
1.80	44.626	41.256	13.136	0.982
1.90	44.626	41.256	13.136	0.982
1.10	44.626	41.256	13.136	0.982
1.11	44.626	41.256	13.136	0.982
1.12	44.626	41.256	13.136	0.982
1.13	44.626	41.256	13.136	0.982
1.14	44.626	41.256	13.136	0.982
1.15	44.626	41.256	13.136	0.982

Sample 02CV130 - Mulaute Fm.

1.90	44.195	43.458	11.581	0.766
1.10	42.333	45.537	11.380	0.751
1.11	42.604	44.928	11.842	0.627
1.12	45.066	45.396	8.761	0.777
1.13	47.347	43.707	8.426	0.520
1.14	47.255	44.013	8.218	0.514
1.15	42.149	44.315	12.604	0.932
1.16	41.892	43.087	14.226	0.795
1.17	43.512	46.697	9.352	0.438
1.18	45.741	48.627	5.173	0.460
1.19	47.259	44.463	7.805	0.472

Sample 02CV72 – Pilatón Fm.

Grain	Wo	En	Fs	Ac
1.00	38.193	43.991	17.100	0.716
1.10	38.193	43.991	17.100	0.716
1.20	38.193	43.991	17.100	0.716
1.30	38.193	43.991	17.100	0.716
1.40	38.193	43.991	17.100	0.716
1.50	38.193	43.991	17.100	0.716
1.60	38.193	43.991	17.100	0.716
1.70	38.193	43.991	17.100	0.716
1.80	38.193	43.991	17.100	0.716
1.90	38.193	43.991	17.100	0.716
1.10	38.193	43.991	17.100	0.716
1.11	38.193	43.991	17.100	0.716
1.12	38.193	43.991	17.100	0.716
1.13	38.193	43.991	17.100	0.716
1.14	38.193	43.991	17.100	0.716
1.15	38.193	43.991	17.100	0.716
1.16	38.193	43.991	17.100	0.716
1.17	38.193	43.991	17.100	0.716

Sample 02CV104 - Rio Cala Fm.

Grain	Wo	En	Fs	Ac
1.10	45.947	47.149	6.311	0.593
1.20	45.033	44.037	10.266	0.663
1.30	45.426	45.351	8.737	0.486
1.40	45.109	41.570	12.480	0.841
1.50	45.363	47.057	7.220	0.360
1.60	45.462	47.052	6.849	0.636
1.70	43.261	47.223	9.060	0.456
1.80	44.576	42.947	11.764	0.713
1.90	45.666	46.370	7.361	0.603
1.10	45.237	45.275	8.858	0.630
1.11	46.041	46.917	6.533	0.509

Grain	Wo	En	Fs	Ac
1.1	37.897	47.209	14.436	0.458
1.2	38.171	48.441	12.730	0.658
1.3	45.361	45.973	8.438	0.229
1.4	44.134	45.838	9.496	0.533
1.5	45.908	46.048	7.680	0.365
1.6	39.664	40.712	19.198	0.426
1.7	38.021	45.963	15.420	0.596
1.8	43.448	46.120	9.922	0.510
1.9	42.685	46.175	10.550	0.590
1.10	44.407	46.838	8.461	0.293
1.11	40.054	47.114	12.290	0.541
1.12	38.115	45.840	15.372	0.674
1.13	39.863	48.185	11.329	0.623
1.14	38.151	48.123	13.021	0.705
1.15	38.164	45.597	15.658	0.580
1.16	36.584	46.011	16.634	0.771
1.17	36.945	46.955	15.523	0.577

Sample 03CV172- Pilaló Unit.

Grain	Wo	En	Fs	Ac
1.10	41.415	40.606	17.263	0.716
1.20	41.135	39.954	18.113	0.797
1.30	40.899	39.459	18.643	0.998
1.40	41.481	43.629	14.009	0.881
1.50	42.740	45.123	11.676	0.461
1.60	40.595	38.572	20.117	0.716
1.70	40.109	38.297	20.604	0.989
1.80	40.839	38.972	19.318	0.872
1.90	41.473	42.689	15.304	0.534
1.10	42.273	46.795	10.390	0.541
1.11	40.645	46.507	12.330	0.518
1.12	41.453	37.712	19.995	0.840
1.13	41.890	39.264	18.289	0.557

Sample 02CV122 - Yunguilla Fm.

Grain	Wo	En	Fs	Ac
1.10	44.626	41.256	13.136	0.982
1.20	44.626	41.256	13.136	0.982
1.30	44.626	41.256	13.136	0.982
1.40	44.626	41.256	13.136	0.982
1.50	44.626	41.256	13.136	0.982
1.60	44.626	41.256	13.136	0.982
1.70	44.626	41.256	13.136	0.982
1.80	44.626	41.256	13.136	0.982
1.90	44.626	41.256	13.136	0.982

1.12	45.564	46.788	7.226	0.423
1.13	43.366	42.636	13.071	0.927
1.14	45.612	46.028	7.800	0.560
1.15	44.797	44.055	10.589	0.559
1.16	45.838	46.180	7.488	0.494
1.17	45.693	46.742	7.076	0.488

Sample 02CV120 - Pallatanga Fm.

Grain	Wo	En	Fs	Ac
1.10	42.524	47.746	9.184	0.545
1.20	42.759	47.399	8.999	0.842
1.30	43.360	46.166	9.621	0.854
1.40	43.957	46.702	8.659	0.683
1.50	43.269	46.310	9.556	0.865
1.60	43.135	47.239	8.955	0.671
1.70	41.618	48.207	9.519	0.656
1.80	43.140	46.175	9.884	0.801
1.90	42.758	46.654	9.792	0.796
1.10	43.960	45.754	9.535	0.751
1.11	43.214	46.280	9.670	0.836
1.12	43.308	45.377	10.511	0.803
1.13	42.652	46.639	10.020	0.689
1.14	43.443	47.278	8.414	0.865
1.15	42.467	47.455	9.254	0.824
1.16	42.891	47.557	8.840	0.712
1.17	43.155	47.148	8.948	0.749
1.18	41.960	47.434	9.912	0.695

1.10	44.626	41.256	13.136	0.982
1.11	44.626	41.256	13.136	0.982
1.12	44.626	41.256	13.136	0.982

Sample 00RS34 - Yunguilla Fm.

Grain	Wo	En	Fs	Ac
1.10	44.626	41.256	13.136	0.982
1.20	44.626	41.256	13.136	0.982
1.30	44.626	41.256	13.136	0.982
1.40	44.626	41.256	13.136	0.982
1.50	44.626	41.256	13.136	0.982
1.60	44.626	41.256	13.136	0.982
1.70	44.626	41.256	13.136	0.982

APPENDIX 7: Chemical composition and structural formula of clinopyroxene phenocrysts used for this study

Formation	**San Juan de Lachas Fm.**
Sample	**00RS44**
Lithology	**Porphyritic Andesite**
UTM	**0806372 / 0082720**

Grain	1.10	1.20	1.30	1.40	1.50	1.60	1.70	1.80
$Si0_2$	48.260	50.730	50.760	50.290	50.820	51.490	51.900	51.840
Al_2O_3	2.550	1.770	2.100	2.850	2.870	2.420	2.070	2.780
CaO	19.290	19.620	19.610	19.120	21.130	20.480	20.070	21.780
K	0.000	0.010	0.000	0.000	0.010	0.000	0.000	0.010
FeO	10.420	9.670	9.860	10.590	8.030	9.290	9.720	7.410
Fe_2O_3	0.000	0.000	0.000	0.000	0.000	0.000	0.000	0.000
MgO	15.030	15.860	15.810	15.050	16.010	15.630	15.650	15.940
Na_2O	0.270	0.240	0.270	0.300	0.300	0.240	0.250	0.160
Cr_2O	0.000	0.010	0.130	0.110	0.120	0.010	0.010	0.290

TiO_2	0.440	0.350	0.350	0.370	0.410	0.430	0.400	0.300
MnO	0.300	0.320	0.400	0.320	0.280	0.310	0.360	0.210
Total	96.570	98.560	99.290	98.990	99.970	100.300	100.420	100.710
Si(T)	1.880	1.922	1.912	1.902	1.891	1.914	1.927	1.908
Al(T)	0.117	0.079	0.093	0.127	0.126	0.106	0.091	0.121
Cr(M)	0.000	0.000	0.004	0.003	0.004	0.000	0.000	0.008
Fe^{3+}	0.000	0.000	0.000	0.000	0.000	0.000	0.000	0.000
Fe^{2+}	0.340	0.306	0.310	0.335	0.250	0.289	0.302	0.228
Ti	0.013	0.010	0.010	0.011	0.012	0.012	0.011	0.008
Mn	0.010	0.010	0.013	0.010	0.009	0.010	0.011	0.007
Mg	0.873	0.896	0.887	0.849	0.888	0.866	0.866	0.875
Ca	0.805	0.797	0.791	0.775	0.843	0.816	0.798	0.859
Na	0.021	0.017	0.020	0.022	0.021	0.018	0.018	0.011
K	0.000	0.000	0.000	0.000	0.000	0.000	0.000	0.001

Formation	**San Juan de Lachas**						**Saquisili (Gallo Rumi)**	
Sample	**00RS44**						**02CV124**	
Lithology	**Porphyritic Andesite**						**Conglomerate**	
UTM	**0806372 / 0082720**						**737786 / 9821586**	
Grain	1.90	1.10	1.11	1.12	1.13	1.14	1.1	1.2
$Si0_2$	51.750	50.600	51.840	50.220	50.460	50.610		
Al_2O_3	2.510	4.140	1.870	3.180	3.450	2.660		
CaO	20.200	20.630	20.330	18.670	20.450	19.320		
K	0.010	0.010	0.000	0.000	0.010	0.010		
FeO	9.130	8.060	9.040	11.960	8.430	10.840		
Fe_2O_3	0.000	0.000	0.000	0.000	0.000	0.000		
MgO	15.640	16.030	16.100	14.440	15.500	15.090		
Na_2O	0.260	0.270	0.250	0.360	0.290	0.300		
Cr_2O	0.020	0.340	0.000	0.100	0.130	0.050		
TiO_2	0.410	0.520	0.360	0.590	0.400	0.480		
MnO	0.310	0.150	0.360	0.370	0.330	0.300		
Total	100.240	100.740	100.140	99.900	99.440	99.660		
Si(T)	1.920	1.864	1.927	1.892	1.888	1.904	1.907	1.900
Al(T)	0.110	0.180	0.082	0.141	0.152	0.118	0.098	0.112
Cr(M)	0.001	0.010	0.000	0.003	0.004	0.001	0.002	0.003
Fe^{3+}	0.000	0.000	0.000	0.000	0.000	0.000	0.078	0.078
Fe^{2+}	0.284	0.248	0.281	0.377	0.264	0.341	0.261	0.247
Ti	0.012	0.015	0.010	0.017	0.011	0.014	0.021	0.022
Mn	0.010	0.005	0.011	0.012	0.010	0.010	0.008	0.010
Mg	0.865	0.881	0.892	0.811	0.864	0.846	0.829	0.835
Ca	0.803	0.815	0.810	0.754	0.820	0.779	0.763	0.758
Na	0.019	0.019	0.018	0.026	0.021	0.022	0.033	0.037
K	0.001	0.000	0.000	0.000	0.001	0.001	0.000	0.000

Formation	**Saquisili (Gallo Rumi)**		**Macuchi**					
Sample	**02CV124**		**03CV289**					
Lithology	**Conglomerate**		**Basalt**					
UTM	**737786 / 9821586**		**713108 / 9869440**					
Grain	1.3	1.4	1.10	1.20	1.30	1.40	1.50	1.60
$Si0_2$			48.017	47.888	46.452	46.087	47.336	45.792
Al_2O_3			3.112	2.944	4.668	4.806	3.596	5.303
CaO			21.269	21.406	21.722	22.231	21.938	21.580
K			0.017	0.000	0.000	0.000	0.000	0.001
FeO			2.918	3.119	3.499	4.601	3.503	5.825
MgO			23.468	23.570	22.344	21.338	22.915	20.151
Na_2O			0.264	0.305	0.375	0.297	0.246	0.442
Cr_2O			0.732	0.475	0.648	0.138	0.194	0.000
TiO_2			0.165	0.241	0.240	0.421	0.210	0.815
MnO			0.039	0.052	0.053	0.080	0.061	0.091
Total			100.000	99.999	100.000	100.000	99.999	100.000
Si(T)	1.898	1.883	1.921	1.916	1.858	1.844	1.893	1.832
Al(T)	0.084	0.097	0.079	0.085	0.142	0.157	0.107	0.168
Al(M)			0.045	0.033	0.045	0.036	0.037	0.044
Cr(M)	0.002	0.002	0.029	0.019	0.026	0.006	0.008	0.000
Fe^{3+}	0.109	0.126	0.003	0.025	0.067	0.094	0.055	0.077
Fe^{2+}	0.211	0.221	0.114	0.100	0.073	0.091	0.086	0.156
Ti	0.018	0.020	0.007	0.010	0.010	0.017	0.008	0.033
Mn	0.008	0.008	0.002	0.002	0.002	0.003	0.002	0.004
Mg	0.832	0.841	0.939	0.943	0.894	0.854	0.917	0.806
Ca	0.811	0.772	0.851	0.856	0.869	0.889	0.878	0.863
Na	0.028	0.030	0.011	0.012	0.015	0.012	0.010	0.018
K	0.000	0.001	0.001	0.000	0.000	0.000	0.000	0.000

Formation	Macuchi							
Sample	03CV289							
Lithology	Basalt							
UTM	713108 / 9869440							
Grain	1.70	1.80	1.90	1.10	1.11	1.12	1.13	1.14
$Si0_2$	45.914	46.542	46.622	47.064	46.725	46.668	46.695	47.782
Al_2O_3	5.530	5.266	4.863	4.025	4.387	4.480	4.350	3.067
CaO	21.034	22.191	21.827	21.448	21.470	21.908	20.579	21.176
K	0.000	0.000	0.000	0.001	0.008	0.017	0.003	0.006
FeO	6.649	4.301	3.248	5.984	5.189	5.070	5.872	3.173
MgO	19.549	20.977	21.871	20.497	21.116	20.939	21.474	23.657
Na_2O	0.485	0.287	0.329	0.437	0.472	0.416	0.420	0.327
Cr_2O	0.011	0.009	0.903	0.011	0.150	0.024	0.073	0.568
TiO_2	0.680	0.355	0.285	0.429	0.389	0.408	0.426	0.182
MnO	0.150	0.072	0.052	0.103	0.093	0.071	0.107	0.061
Total	100.000	100.000	100.000	100.000	100.000	100.000	99.999	100.000
Si(T)	1.837	1.862	1.865	1.883	1.869	1.867	1.868	1.911

Al(T)	0.164	0.138	0.135	0.117	0.131	0.133	0.132	0.089
Al(M)	0.058	0.072	0.059	0.044	0.045	0.046	0.042	0.034
Cr(M)	0.000	0.000	0.036	0.000	0.006	0.001	0.003	0.023
Fe^{3+}	0.070	0.049	0.030	0.057	0.069	0.071	0.070	0.031
Fe^{2+}	0.196	0.123	0.100	0.183	0.139	0.132	0.165	0.096
Ti	0.027	0.014	0.011	0.017	0.016	0.016	0.017	0.007
Mn	0.006	0.003	0.002	0.004	0.004	0.003	0.004	0.002
Mg	0.782	0.839	0.875	0.820	0.845	0.838	0.859	0.946
Ca	0.841	0.888	0.873	0.858	0.859	0.876	0.823	0.847
Na	0.019	0.012	0.013	0.018	0.019	0.017	0.017	0.013
K	0.000	0.000	0.000	0.000	0.000	0.001	0.000	0.000

Formation	Macuchi	Macuchi (Las Juntas)					
Sample	03CV289	03CV197					
Lithology	Basalt	Volcanic sandstone					
UTM		727823 / 9964642					
Grain	1.15	1.10	1.20	1.30	1.40	1.50	1.60	1.70
$Si0_2$	46.442	47.505	46.184	48.274	48.513	46.874	47.775	47.728
Al_2O_3	5.434	3.786	5.279	1.898	1.712	3.177	2.505	2.576
CaO	22.096	21.392	20.850	21.033	21.786	19.140	21.057	22.442
K	0.000	0.006	0.000	0.000	0.022	0.014	0.009	0.016
FeO	3.546	3.692	7.298	7.017	7.061	8.533	7.060	3.024
MgO	21.492	22.552	19.409	20.778	19.926	21.425	20.659	23.220
Na_2O	0.237	0.289	0.408	0.467	0.518	0.303	0.390	0.236
Cr_2O	0.435	0.530	0.001	0.012	0.027	0.000	0.015	0.565
TiO_2	0.289	0.173	0.435	0.307	0.200	0.302	0.328	0.149
MnO	0.031	0.075	0.135	0.214	0.235	0.233	0.203	0.044
Total	100.000	100.000	100.000	99.999	99.999	99.999	100.000	100.000
Si(T)	1.858	1.900	1.847	1.931	1.941	1.875	1.911	1.909
Al(T)	0.142	0.100	0.153	0.069	0.060	0.125	0.089	0.091
Al(M)	0.075	0.052	0.059	0.007	0.009	0.002	0.011	0.012
Cr(M)	0.017	0.021	0.000	0.000	0.001	0.000	0.001	0.023
Fe^{3+}	0.036	0.025	0.076	0.056	0.055	0.112	0.067	0.054
Fe^{2+}	0.106	0.123	0.216	0.225	0.227	0.230	0.215	0.067
Ti	0.012	0.007	0.017	0.012	0.008	0.012	0.013	0.006
Mn	0.001	0.003	0.005	0.009	0.009	0.009	0.008	0.002
Mg	0.860	0.902	0.776	0.831	0.797	0.857	0.826	0.929
Ca	0.884	0.856	0.834	0.841	0.872	0.766	0.842	0.898
Na	0.010	0.012	0.016	0.019	0.021	0.012	0.016	0.009
K	0.000	0.000	0.000	0.000	0.001	0.001	0.000	0.001

Formation	**Macuchi (Las Juntas)**							
Sample	**03CV197**							
Lithology	**Volcanic sandstone**							
UTM	**727823 / 9964642**							
Grain	1.80	1.90	1.10	1.11	1.12	1.13	1.14	1.15

$Si0_2$	48.255	48.491	48.137	47.922	47.311	47.551	47.239	47.783
Al_2O_3	1.989	2.013	1.878	2.381	2.810	2.708	3.372	2.637
CaO	20.082	20.588	21.106	21.169	20.755	21.202	21.533	20.545
K	0.011	0.034	0.005	0.008	0.007	0.000	0.000	0.004
FeO	8.700	7.259	7.149	4.980	7.531	5.776	5.354	6.792
MgO	20.095	20.731	20.919	22.767	20.501	22.077	21.725	21.366
Na_2O	0.338	0.393	0.335	0.342	0.467	0.287	0.327	0.348
Cr_2O	0.009	0.021	0.032	0.090	0.017	0.001	0.097	0.041
TiO_2	0.274	0.257	0.274	0.223	0.390	0.284	0.248	0.338
MnO	0.246	0.213	0.165	0.118	0.211	0.114	0.104	0.146
Total	99.999	100.000	99.999	100.000	100.000	99.999	99.999	100.000
Si(T)	1.930	1.940	1.926	1.917	1.892	1.902	1.890	1.911
Al(T)	0.070	0.060	0.075	0.083	0.108	0.098	0.110	0.089
Al(M)	0.010	0.020	0.001	0.012	0.005	0.010	0.025	0.017
Cr(M)	0.000	0.001	0.001	0.004	0.001	0.000	0.004	0.002
Fe^{3+}	0.052	0.036	0.065	0.064	0.090	0.076	0.075	0.057
Fe^{2+}	0.296	0.255	0.222	0.136	0.211	0.155	0.139	0.215
Ti	0.011	0.010	0.011	0.009	0.016	0.011	0.010	0.014
Mn	0.010	0.009	0.007	0.005	0.008	0.005	0.004	0.006
Mg	0.804	0.829	0.837	0.911	0.820	0.883	0.869	0.855
Ca	0.803	0.824	0.844	0.847	0.830	0.848	0.861	0.822
Na	0.014	0.016	0.013	0.014	0.019	0.012	0.013	0.014
K	0.000	0.001	0.000	0.000	0.000	0.000	0.000	0.000

Formation	**Macuchi (Las Juntas)**							**Pilaló**
Sample	**03CV197**							**00RS34**
Lithology	**Volcanic sandstone**							**Sandstone**
UTM	**727823 / 9964642**							
Grain	1.16	1.17	1.18	1.19	1.20	1.21	1.22	1.10
$Si0_2$	48.303	48.476	48.547	48.533	47.723	47.469	48.191	47.710
Al_2O_3	2.111	2.108	1.692	1.563	2.454	2.857	2.159	1.840
CaO	20.614	20.424	21.096	20.915	20.224	20.704	21.094	20.270
K	0.011	0.000	0.006	0.009	0.012	0.006	0.000	0.000
FeO	7.417	7.421	7.370	6.802	7.798	7.135	7.185	9.040
MgO	20.502	20.593	20.305	21.388	20.771	20.797	20.391	15.150
Na_2O	0.496	0.428	0.508	0.352	0.455	0.492	0.510	0.220
Cr_2O	0.030	0.000	0.000	0.000	0.000	0.012	0.000	0.010
TiO_2	0.345	0.362	0.257	0.220	0.393	0.379	0.286	0.390
MnO	0.171	0.188	0.220	0.218	0.170	0.148	0.185	0.410
Total	100.000	100.000	100.000	100.000	100.000	99.999	100.000	95.050
Si(T)	1.932	1.939	1.942	1.941	1.909	1.899	1.928	1.887
Al(T)	0.068	0.061	0.058	0.059	0.091	0.101	0.072	0.086
Al(M)	0.017	0.023	0.010	0.004	0.007	0.013	0.014	
Cr(M)	0.001	0.000	0.000	0.000	0.000	0.001	0.000	0.000
Fe^{3+}	0.043	0.026	0.049	0.052	0.071	0.077	0.056	0.000
Fe^{2+}	0.254	0.271	0.246	0.220	0.241	0.208	0.232	0.299

Ti	0.014	0.015	0.010	0.009	0.016	0.015	0.011	0.012
Mn	0.007	0.008	0.009	0.009	0.007	0.006	0.007	0.014
Mg	0.820	0.824	0.812	0.856	0.831	0.832	0.816	0.893
Ca	0.825	0.817	0.844	0.837	0.809	0.828	0.844	0.859
Na	0.020	0.017	0.020	0.014	0.018	0.020	0.020	0.017
K	0.000	0.000	0.000	0.000	0.000	0.000	0.000	0.000

Formation	**Pilaló**						**Pilaló**	
Sample	**00RS34**						**03CV223**	
Lithology	**Sandstone**						**Sandstone**	
UTM	**0769357 / 0000702**						**740717 / 9805993**	
Grain	1.20	1.30	1.40	1.50	1.60	1.70	1.10	1.20
$Si0_2$	50.870	49.230	45.190	50.560	51.700	49.380	48.470	48.378
Al_2O_3	1.620	1.280	7.660	1.490	0.750	1.710	1.860	1.775
CaO	21.140	20.830	10.940	20.960	20.690	21.140	20.444	20.301
K	0.010	0.010	0.440	0.000	0.000	0.010	0.000	0.010
FeO	8.490	9.310	14.130	9.050	8.550	9.080	9.070	8.677
Fe_2O_3	0.000	0.000	0.000	0.000	0.000	0.000		
MgO	14.520	14.020	13.800	14.490	15.410	14.150	19.298	20.077
Na_2O	0.310	0.280	1.330	0.310	0.170	0.330	0.433	0.376
Cr_2O	0.000	0.000	0.000	0.000	0.010	0.010	0.017	0.001
TiO_2	0.350	0.230	1.320	0.250	0.190	0.330	0.215	0.207
MnO	0.360	0.400	0.690	0.490	0.540	0.370	0.193	0.199
Total	97.670	95.580	95.510	97.590	98.000	96.510	100.000	100.000
Si(T)	1.942	1.935	1.782	1.939	1.964	1.921	1.939	1.935
Al(T)	0.073	0.059	0.356	0.068	0.033	0.078	0.061	0.065
Al(M)							0.013	0.006
Cr(M)	0.000	0.000	0.000	0.000	0.000	0.000	0.001	0.000
Fe^{3+}	0.000	0.000	0.000	0.000	0.000	0.000	0.048	0.058
Fe^{2+}	0.271	0.306	0.466	0.290	0.272	0.295	0.315	0.289
Ti	0.010	0.007	0.039	0.007	0.005	0.010	0.009	0.008
Mn	0.012	0.013	0.023	0.016	0.017	0.012	0.008	0.008
Mg	0.826	0.821	0.811	0.828	0.872	0.821	0.772	0.803
Ca	0.865	0.877	0.462	0.861	0.842	0.881	0.818	0.812
Na	0.023	0.021	0.102	0.023	0.012	0.025	0.017	0.015
K	0.000	0.000	0.022	0.000	0.000	0.001	0.000	0.000

Formation	**Pilaló**							
Sample	**03CV223**							
Lithology	**Sandstone**							
UTM	**740717 / 9805993**							
Grain	1.30	1.40	1.50	1.60	1.70	1.80	1.90	1.10
$Si0_2$	48.367	47.651	48.598	48.671	48.229	48.211	49.271	46.810
Al_2O_3	2.415	2.977	1.859	1.387	1.950	1.837	1.025	2.473
CaO	21.351	21.659	20.486	20.457	20.847	20.364	20.355	18.141
K	0.000	0.000	0.016	0.019	0.012	0.010	0.000	0.018

FeO	3.862	5.246	8.555	10.042	8.330	8.827	11.145	14.705
MgO	23.316	21.945	19.620	18.583	19.778	19.984	17.335	16.969
Na_2O	0.205	0.236	0.418	0.309	0.517	0.338	0.375	0.364
Cr_2O	0.323	0.078	0.000	0.003	0.000	0.045	0.000	0.041
TiO_2	0.109	0.103	0.228	0.209	0.140	0.203	0.162	0.161
MnO	0.053	0.105	0.221	0.319	0.197	0.182	0.333	0.318
Total	100.000	100.000	100.000	99.999	100.000	99.999	100.000	100.000
Si(T)	1.935	1.906	1.944	1.947	1.929	1.928	1.971	1.872
Al(T)	0.065	0.094	0.056	0.053	0.071	0.072	0.029	0.099
Al(M)	0.031	0.025	0.018	0.002	0.007	0.002	0.012	0.000
Cr(M)	0.013	0.003	0.000	0.000	0.000	0.002	0.000	0.002
Fe^{3+}	0.021	0.067	0.037	0.047	0.074	0.066	0.019	0.157
Fe^{2+}	0.134	0.143	0.305	0.355	0.260	0.288	0.426	0.431
Ti	0.004	0.004	0.009	0.008	0.006	0.008	0.007	0.006
Mn	0.002	0.004	0.009	0.013	0.008	0.007	0.013	0.013
Mg	0.933	0.878	0.785	0.743	0.791	0.799	0.693	0.679
Ca	0.854	0.866	0.819	0.818	0.834	0.815	0.814	0.726
Na	0.008	0.009	0.017	0.012	0.021	0.014	0.015	0.015
K	0.000	0.000	0.001	0.001	0.000	0.000	0.000	0.001

Formation	**Pilaló**							
Sample	**03CV223**							
Lithology	**Sandstone**							
UTM	**740717 / 9805993**							
Grain	1.11	1.12	1.13	1.14	1.15	1.16	1.17	1.18
$Si0_2$	49.097	48.912	48.865	48.436	49.049	48.842	48.947	48.443
Al_2O_3	1.208	1.160	1.343	1.796	1.207	1.167	1.184	1.732
CaO	20.744	20.483	20.909	21.339	20.638	20.393	20.355	20.678
K	0.000	0.011	0.006	0.000	0.000	0.000	0.006	0.003
FeO	8.807	10.581	8.716	7.343	9.680	10.772	10.579	8.401
MgO	19.216	17.892	19.289	20.158	18.506	17.871	17.994	20.037
Na_2O	0.407	0.418	0.384	0.570	0.423	0.372	0.383	0.321
Cr_2O	0.026	0.000	0.000	0.000	0.000	0.013	0.000	0.021
TiO_2	0.180	0.186	0.197	0.178	0.161	0.197	0.187	0.182
MnO	0.316	0.359	0.290	0.178	0.335	0.374	0.366	0.184
Total	100.000	99.999	99.999	99.999	100.000	100.000	100.000	100.000
Si(T)	1.964	1.957	1.955	1.937	1.962	1.954	1.958	1.938
Al(T)	0.036	0.044	0.045	0.063	0.038	0.046	0.042	0.062
Al(M)	0.012	0.003	0.008	0.009	0.010	0.000	0.005	0.007
Cr(M)	0.001	0.000	0.000	0.000	0.000	0.001	0.000	0.001
Fe^{3+}	0.025	0.043	0.037	0.062	0.032	0.045	0.038	0.053
Fe^{2+}	0.327	0.380	0.312	0.232	0.355	0.386	0.386	0.283
Ti	0.007	0.007	0.008	0.007	0.007	0.008	0.008	0.007
Mn	0.013	0.014	0.012	0.007	0.013	0.015	0.015	0.007
Mg	0.769	0.716	0.772	0.806	0.740	0.715	0.720	0.802
Ca	0.830	0.819	0.836	0.854	0.826	0.816	0.814	0.827

Na	0.016	0.017	0.015	0.023	0.017	0.015	0.015	0.013
K	0.000	0.000	0.000	0.000	0.000	0.000	0.000	0.000

Formation	**Pilaló**		**Silante**					
Sample	**03CV223**		**02CV56**					
Lithology	**Sandstone**		**Sandstone**					
UTM	**740717 / 9805993**		**765766 / 2296**					
Grain	1.19	1.20	1.10	1.20	1.30	1.40	1.50	1.60
$Si0_2$	47.851	48.051	47.491	47.336	47.801	48.094	48.243	48.361
Al_2O_3	2.348	2.270	3.099	2.999	2.285	2.196	2.267	2.062
CaO	20.264	20.586	20.345	19.833	20.390	19.967	20.067	20.787
K	0.000	0.000	0.000	0.005	0.000	0.003	0.000	0.011
FeO	7.303	8.583	6.670	7.234	7.364	6.351	5.562	7.037
MgO	21.432	19.697	21.500	21.554	21.048	22.436	23.075	20.668
Na_2O	0.414	0.323	0.507	0.460	0.569	0.480	0.333	0.524
Cr_2O	0.107	0.000	0.008	0.019	0.000	0.012	0.183	0.055
TiO_2	0.178	0.235	0.257	0.418	0.356	0.330	0.172	0.311
MnO	0.103	0.255	0.124	0.142	0.188	0.131	0.099	0.184
Total	99.999	100.000	100.000	99.999	100.000	100.000	100.000	100.000
Si(T)	1.914	1.922	1.900	1.893	1.912	1.924	1.930	1.934
Al(T)	0.086	0.078	0.100	0.107	0.088	0.076	0.070	0.066
Al(M)	0.008	0.013	0.024	0.013	0.003	0.012	0.020	0.017
Cr(M)	0.004	0.000	0.000	0.001	0.000	0.001	0.007	0.002
Fe^{3+}	0.076	0.059	0.076	0.078	0.079	0.057	0.042	0.043
Fe^{2+}	0.216	0.284	0.191	0.212	0.216	0.197	0.180	0.239
Ti	0.007	0.009	0.010	0.017	0.014	0.013	0.007	0.013
Mn	0.004	0.010	0.005	0.006	0.008	0.005	0.004	0.007
Mg	0.857	0.788	0.860	0.862	0.842	0.897	0.923	0.827
Ca	0.811	0.823	0.814	0.793	0.816	0.799	0.803	0.832
Na	0.017	0.013	0.020	0.018	0.023	0.019	0.013	0.021
K	0.000	0.000	0.000	0.000	0.000	0.000	0.000	0.000

Formation	**Silante**							
Sample	**02CV56**							
Lithology	**Sandstone**							
UTM	**765766 / 2296**							
Grain	1.70	1.80	1.90	1.10	1.11	1.12	1.13	1.14
$Si0_2$	48.497	48.591	46.104	47.894	48.315	47.685	48.611	48.388
Al_2O_3	2.128	1.477	4.751	2.537	1.721	2.527	1.521	1.399
CaO	21.431	20.201	21.185	19.544	19.531	20.372	21.182	21.813
K	0.017	0.000	0.000	0.003	0.003	0.014	0.006	0.000
FeO	6.818	7.001	5.538	5.199	7.107	7.097	6.565	6.636
MgO	19.894	21.731	21.247	23.854	22.460	21.185	21.126	20.752
Na_2O	0.862	0.517	0.561	0.440	0.411	0.564	0.539	0.618
Cr_2O	0.001	0.009	0.175	0.259	0.000	0.000	0.000	0.039
TiO_2	0.173	0.279	0.378	0.167	0.267	0.364	0.245	0.176

MnO	0.179	0.194	0.061	0.103	0.185	0.192	0.207	0.178
Total	100.000	99.999	100.000	100.000	100.000	100.000	100.000	99.999
Si(T)	1.940	1.944	1.844	1.916	1.933	1.907	1.944	1.936
Al(T)	0.060	0.056	0.156	0.084	0.067	0.093	0.056	0.056
Al(M)	0.025	0.003	0.034	0.017	0.001	0.009	0.005	0.000
Cr(M)	0.000	0.000	0.007	0.010	0.000	0.000	0.000	0.002
Fe^{3+}	0.056	0.052	0.107	0.061	0.061	0.078	0.053	0.082
Fe^{2+}	0.216	0.228	0.115	0.147	0.223	0.206	0.210	0.183
Ti	0.007	0.011	0.015	0.007	0.011	0.015	0.010	0.007
Mn	0.007	0.008	0.003	0.004	0.007	0.008	0.008	0.007
Mg	0.796	0.869	0.850	0.954	0.898	0.847	0.845	0.830
Ca	0.857	0.808	0.847	0.782	0.781	0.815	0.847	0.873
Na	0.035	0.021	0.022	0.018	0.016	0.023	0.022	0.025
K	0.001	0.000	0.000	0.000	0.000	0.001	0.000	0.000

Formation	**Silante**				**Silante**			
Sample	**02CV56**				**02CV99**			
Lithology	**Sandstone**				**Sandstone**			
UTM	**765766 / 2296**				**782581 / 30669**			
Grain	1.15	1.16	1.17	1.18	1.10	1.20	1.30	1.40
$Si0_2$	47.815	46.159	47.276	49.013	51.030	51.220	51.900	52.770
Al_2O_3	2.182	4.316	3.558	1.396	1.960	2.100	1.590	2.030
CaO	21.403	19.280	21.430	22.047	21.230	20.700	20.940	20.160
K	0.006	0.015	0.000	0.000	0.010	0.010	0.020	0.020
FeO	7.347	7.105	4.386	6.285	8.400	9.970	9.080	89.230
Fe_2O_3					0.000	0.000	0.000	0.000
MgO	20.132	21.741	22.512	20.382	15.040	14.490	14.830	16.640
Na_2O	0.695	0.742	0.262	0.485	0.310	0.370	0.290	0.570
Cr_2O	0.000	0.000	0.312	0.032	0.000	0.030	0.040	0.000
TiO_2	0.252	0.458	0.207	0.157	0.430	0.400	0.310	0.220
MnO	0.167	0.184	0.059	0.204	0.320	0.470	0.460	0.340
Total	99.999	99.999	100.000	100.000	98.730	99.760	99.460	181.970
Si(T)	1.913	1.846	1.891	1.961	1.926	1.925	1.947	1.369
Al(T)	0.087	0.154	0.109	0.040	0.087	0.093	0.070	0.062
Al(M)	-0.000	0.019	0.033	0.016				
Cr(M)	0.000	0.000	0.012	0.001	0.000	0.001	0.001	0.000
Fe^{3+}	0.095	0.128	0.057	0.029	0.000	0.000	0.000	0.000
Fe^{2+}	0.199	0.156	0.118	0.223	0.265	0.313	0.285	1.935
Ti	0.010	0.018	0.008	0.006	0.012	0.011	0.009	0.004
Mn	0.007	0.007	0.002	0.008	0.010	0.015	0.015	0.008
Mg	0.805	0.870	0.901	0.815	0.846	0.811	0.829	0.643
Ca	0.856	0.771	0.857	0.882	0.859	0.834	0.842	0.560
Na	0.028	0.030	0.011	0.019	0.023	0.027	0.021	0.029
K	0.000	0.001	0.000	0.000	0.000	0.001	0.001	0.001

Formation	**Silante**							**Silante**
Sample	**02CV99**							**00RS26**
Lithology	**Sandstone**							
UTM	**782581 / 30669**							
Grain	1.50	1.60	1.70	1.80	1.90	1.10	1.11	1.10
$Si0_2$	51.560	50.800	49.070	48.870	50.440	50.520	50.410	51.070
Al_2O_3	1.730	2.680	2.510	2.550	2.220	1.460	2.420	1.720
CaO	20.950	20.890	20.040	19.690	20.790	20.110	20.960	21.170
K	0.000	0.000	0.010	0.010	0.010	0.000	0.000	0.000
FeO	9.390	9.100	10.790	10.800	9.670	8.800	9.070	6.350
Fe_2O_3	0.000	0.000	0.000	0.000	0.000	0.000	0.000	0.000
MgO	14.480	14.990	13.520	14.340	14.540	15.900	14.980	16.550
Na_2O	0.410	0.340	0.470	0.430	0.410	0.220	0.320	0.290
Cr_2O	0.020	0.030	0.000	0.020	0.030	0.000	0.000	0.320
TiO_2	0.280	0.400	0.380	0.520	0.470	0.330	0.530	0.230
MnO	0.410	0.260	0.460	0.360	0.340	0.360	0.360	0.190
Total	99.240	99.500	97.240	97.580	98.910	97.700	99.050	97.900
Si(T)	1.943	1.907	1.904	1.889	1.912	1.928	1.904	1.927
Al(T)	0.077	0.119	0.115	0.116	0.099	0.066	0.108	0.076
Al(M)								
Cr(M)	0.001	0.001	0.000	0.001	0.001	0.000	0.000	0.010
Fe^{3+}	0.000	0.000	0.000	0.000	0.000	0.000	0.000	0.000
Fe^{2+}	0.296	0.286	0.350	0.349	0.307	0.281	0.286	0.201
Ti	0.008	0.011	0.011	0.015	0.014	0.010	0.015	0.007
Mn	0.013	0.008	0.015	0.012	0.011	0.012	0.012	0.006
Mg	0.813	0.838	0.782	0.826	0.822	0.904	0.843	0.931
Ca	0.846	0.840	0.833	0.815	0.844	0.822	0.848	0.856
Na	0.030	0.025	0.035	0.032	0.030	0.016	0.024	0.021
K	0.000	0.000	0.001	0.000	0.000	0.000	0.000	0.000

Formation	**Silante**							
Sample	**00RS26**							
Lithology	**Pepperite breccia**							
UTM	**0745856 / 9953698**							
Grain	1.20	1.30	1.40	1.50	1.60	1.70	1.80	1.90
$Si0_2$	51.280	51.030	48.940	50.390	49.570	46.620	50.260	51.750
Al_2O_3	1.510	2.250	2.120	2.040	2.000	2.190	2.400	2.830
CaO	20.930	20.740	18.050	20.240	17.760	20.100	20.970	22.170
K	0.010	0.000	0.000	0.010	0.010	0.020	0.010	0.010
FeO	8.610	9.800	8.010	6.870	7.950	9.530	8.400	6.520
Fe_2O_3	0.000	0.000	0.000	0.000	0.000	0.000	0.000	0.000
MgO	15.330	14.930	15.070	15.080	14.380	14.740	15.420	15.900
Na_2O	0.380	0.480	0.400	0.330	0.390	0.310	0.390	0.460
Cr_2O	0.000	0.000	0.010	0.120	0.010	0.000	0.000	0.080
TiO_2	0.440	0.500	0.470	0.360	0.320	0.630	0.650	0.250
MnO	0.370	0.290	0.220	0.210	0.310	0.340	0.270	0.120

Total	98.860	100.010	93.300	95.650	92.700	94.490	98.760	100.100
Si(T)	1.934	1.912	1.939	1.945	1.971	1.863	1.899	1.912
Al(T)	0.067	0.100	0.099	0.093	0.094	0.103	0.107	0.123
Cr(M)	0.000	0.000	0.000	0.004	0.000	0.000	0.000	0.002
Fe^{3+}	0.000	0.000	0.000	0.000	0.000	0.000	0.000	0.000
Fe^{2+}	0.272	0.307	0.266	0.222	0.264	0.319	0.265	0.201
Ti	0.012	0.014	0.014	0.011	0.010	0.019	0.018	0.007
Mn	0.012	0.009	0.008	0.007	0.010	0.012	0.009	0.004
Mg	0.862	0.834	0.890	0.867	0.852	0.878	0.868	0.876
Ca	0.846	0.832	0.766	0.837	0.757	0.861	0.849	0.877
Na	0.028	0.035	0.031	0.024	0.030	0.024	0.029	0.033
K	0.000	0.000	0.000	0.001	0.000	0.001	0.001	0.001

Formation	**Silante**			**Silante**				
Sample	**00RS26**			**00RS35**				
Lithology	**Pepperite breccia**			**Volcanic Breccia**				
UTM	**0745856 / 9953698**			**0768146 / 0000692**				
Grain	1.10	1.11	1.12	1.10	1.20	1.30	1.40	1.50
$Si0_2$	48.190	50.800	50.680	47.070	47.570	47.980	44.690	51.620
Al_2O_3	3.250	1.340	2.660	1.400	1.790	1.540	1.310	1.300
CaO	19.690	20.840	20.820	18.050	19.710	18.890	18.250	21.350
K	0.010	0.000	0.000	0.000	0.020	0.000	0.010	0.020
FeO	6.340	7.380	8.420	8.690	10.750	9.630	10.930	10.560
Fe_2O_3	0.000	0.000	0.000	0.000	0.000	0.000	0.000	0.000
MgO	15.190	15.150	15.390	13.580	14.500	14.270	14.190	14.200
Na_2O	0.290	0.310	0.360	0.230	0.260	0.300	0.200	0.280
Cr_2O	0.280	0.100	0.060	0.010	0.050	0.000	0.050	0.000
TiO_2	0.380	0.280	0.440	0.160	0.120	0.150	0.160	0.160
MnO	0.150	0.260	0.210	0.290	0.350	0.300	0.330	0.340
Total	93.770	96.450	99.060	89.480	95.110	93.070	90.130	99.820
Si(T)	1.896	1.953	1.905	1.959	1.893	1.932	1.884	1.945
Al(T)	0.151	0.061	0.118	0.069	0.084	0.073	0.065	0.058
Cr(M)	0.009	0.003	0.002	0.000	0.002	0.000	0.002	0.000
Fe^{3+}	0.000	0.000	0.000	0.000	0.000	0.000	0.000	0.000
Fe^{2+}	0.209	0.237	0.265	0.303	0.358	0.324	0.385	0.333
Ti	0.011	0.008	0.013	0.005	0.003	0.005	0.005	0.004
Mn	0.005	0.008	0.007	0.010	0.012	0.010	0.012	0.011
Mg	0.891	0.868	0.862	0.842	0.860	0.856	0.892	0.798
Ca	0.830	0.858	0.838	0.805	0.840	0.815	0.824	0.862
Na	0.022	0.023	0.026	0.019	0.020	0.024	0.016	0.020
K	0.000	0.000	0.000	0.000	0.001	0.000	0.001	0.001

Formation	**Sanguangal**
Sample	**00RS39**
Lithology	**Breccia**
UTM	**0725862 / 9988704**

Grain	1.10	1.20	1.30	1.40	1.50	1.60	1.70	1.80
$Si0_2$	50.980	51.020	50.860	51.110	51.420	51.190	51.340	52.890
Al_2O_3	1.960	1.910	2.550	2.580	1.830	1.740	1.760	1.900
CaO	19.530	19.580	20.690	20.680	19.220	19.460	19.380	19.420
K	0.000	0.020	0.000	0.020	0.010	0.010	0.010	0.020
FeO	11.170	11.260	9.320	9.410	11.610	10.940	11.190	8.500
Fe_2O_3	0.000	0.000	0.000	0.000	0.000	0.000	0.000	0.000
MgO	15.220	15.370	15.430	15.270	14.980	15.150	15.180	17.340
Na_2O	0.270	0.260	0.250	0.240	0.340	0.310	0.300	0.230
Cr_2O	0.010	0.000	0.000	0.010	0.000	0.030	0.030	0.090
TiO_2	0.500	0.530	0.750	0.540	0.530	0.510	0.510	0.330
MnO	0.390	0.360	0.340	0.290	0.420	0.420	0.350	0.210
Total	99.640	99.950	100.190	100.140	100.360	99.760	100.050	100.930
Si(T)	1.915	1.912	1.897	1.906	1.926	1.926	1.926	1.936
Al(T)	0.087	0.084	0.112	0.113	0.081	0.077	0.078	0.082
Al(M)								
Cr(M)	0.000	0.000	0.000	0.000	0.000	0.001	0.001	0.003
Fe^{3+}	0.000	0.000	0.000	0.000	0.000	0.000	0.000	0.000
Fe^{2+}	0.351	0.353	0.291	0.294	0.364	0.344	0.351	0.260
Ti	0.014	0.015	0.021	0.015	0.015	0.015	0.014	0.009
Mn	0.012	0.011	0.011	0.009	0.013	0.013	0.011	0.006
Mg	0.852	0.859	0.858	0.849	0.836	0.850	0.849	0.946
Ca	0.786	0.786	0.827	0.826	0.771	0.784	0.779	0.762
Na	0.020	0.019	0.018	0.018	0.025	0.023	0.022	0.016
K	0.000	0.001	0.000	0.001	0.001	0.001	0.001	0.001

Formation	**Sanguangal**							**Pilatón**
Sample	**00RS39**							**02CV72**
Lithology	**Breccia**							**Sandstone**
UTM	**0725862 / 9988704**							
Grain	1.90	1.10	1.11	1.12	1.13	1.14	1.15	1.00
$Si0_2$	50.020	51.600	52.000	51.340	51.170	50.120	50.950	49.970
Al_2O_3	1.700	2.170	1.470	1.590	1.250	1.960	1.410	2.380
CaO	17.900	19.530	19.710	19.140	19.560	19.070	19.130	18.790
K	0.020	0.010	0.000	0.000	0.020	0.020	0.010	0.000
FeO	10.280	10.590	11.650	12.240	12.170	10.500	11.840	10.460
Fe_2O_3	0.000	0.000	0.000	0.000	0.000	0.000	0.000	0.000
MgO	14.730	15.500	14.530	14.580	14.000	14.620	14.450	15.560
Na_2O	0.290	0.280	0.320	0.320	0.310	0.340	0.320	0.190
Cr_2O	0.010	0.020	0.000	0.000	0.000	0.020	0.000	0.010
TiO_2	0.460	0.540	0.420	0.470	0.430	0.500	0.480	0.380
MnO	0.380	0.270	0.660	0.520	0.590	0.410	0.540	0.310
Total	95.810	100.520	100.770	100.190	99.490	97.550	99.130	98.050
Si(T)	1.947	1.920	1.943	1.932	1.943	1.926	1.937	1.907
Al(T)	0.078	0.095	0.065	0.071	0.056	0.089	0.063	0.107
Cr(M)	0.000	0.001	0.000	0.000	0.000	0.001	0.000	0.000

Fe^{3+}	0.000	0.000	0.000	0.000	0.000	0.000	0.000	0.000
Fe^{2+}	0.335	0.330	0.364	0.385	0.386	0.337	0.376	0.334
Ti	0.013	0.015	0.012	0.013	0.012	0.015	0.014	0.011
Mn	0.013	0.009	0.021	0.017	0.019	0.013	0.017	0.010
Mg	0.855	0.860	0.809	0.818	0.793	0.837	0.819	0.885
Ca	0.747	0.779	0.789	0.772	0.796	0.785	0.779	0.768
Na	0.022	0.020	0.023	0.023	0.023	0.025	0.024	0.014
K	0.001	0.001	0.000	0.000	0.001	0.001	0.001	0.000

Formation	**Pilatón**							
Sample	**02CV72**							
Lithology	**Sandstone**							
UTM	**804076 / 85924**							
Grain	1.10	1.20	1.30	1.40	1.50	1.60	1.70	1.80
$Si0_2$	49.990	50.480	50.400	50.640	50.220	51.070	52.540	51.340
Al_2O_3	2.730	2.200	2.620	1.760	2.990	2.010	1.750	2.790
CaO	20.600	22.230	21.020	20.110	19.900	19.870	22.100	22.260
K	0.010	0.000	0.000	0.010	0.010	0.010	0.010	0.010
FeO	8.400	5.070	7.860	10.100	10.730	10.390	5.120	5.870
Fe_2O_3	0.000	0.000	0.000	0.000	0.000	0.000	0.000	0.000
MgO	15.400	16.730	15.830	15.130	14.410	15.030	16.950	16.220
Na_2O	0.180	0.100	0.170	0.240	0.200	0.170	0.080	0.160
Cr_2O	0.060	0.110	0.040	0.000	0.000	0.000	0.290	0.260
TiO_2	0.440	0.190	0.300	0.340	0.470	0.370	0.150	0.250
MnO	0.260	0.100	0.230	0.440	0.300	0.330	0.130	0.120
Total	98.070	97.210	98.460	98.760	99.250	99.260	99.110	99.280
Si(T)	1.898	1.912	1.902	1.922	1.899	1.926	1.944	1.907
Al(T)	0.122	0.098	0.117	0.079	0.133	0.089	0.076	0.122
Cr(M)	0.002	0.003	0.001	0.000	0.000	0.000	0.008	0.008
Fe^{3+}	0.000	0.000	0.000	0.000	0.000	0.000	0.000	0.000
Fe^{2+}	0.267	0.161	0.248	0.321	0.339	0.328	0.158	0.182
Ti	0.013	0.005	0.008	0.010	0.013	0.010	0.004	0.007
Mn	0.008	0.003	0.007	0.014	0.010	0.011	0.004	0.004
Mg	0.872	0.944	0.890	0.856	0.812	0.845	0.935	0.898
Ca	0.838	0.902	0.850	0.818	0.806	0.803	0.876	0.886
Na	0.014	0.008	0.012	0.018	0.015	0.013	0.005	0.011
K	0.000	0.000	0.000	0.000	0.001	0.000	0.000	0.001

Formation	**Pilatón**							
Sample	**02CV72**							
Lithology	**Sandstone**							
UTM	**804076 / 85924**							
Grain	1.90	1.10	1.11	1.12	1.13	1.14	1.15	1.16
$Si0_2$	51.330	48.520	48.140	48.090	48.350	48.140	46.440	50.590
Al_2O_3	1.590	2.030	2.130	1.480	1.860	1.300	2.720	2.030
CaO	19.880	19.940	21.750	19.410	20.100	20.850	21.280	19.840

K	0.010	0.010	0.010	0.020	0.000	0.000	0.010	0.020
FeO	10.730	8.450	5.470	10.430	10.390	9.630	6.580	10.400
Fe_2O_3	0.000	0.000	0.000	0.000	0.000	0.000	0.000	0.000
MgO	14.850	15.870	16.680	15.310	14.890	14.280	15.290	14.990
Na_2O	0.230	0.130	0.100	0.220	0.210	0.280	0.150	0.250
Cr_2O	0.000	0.030	0.130	0.020	0.010	0.020	0.090	0.020
TiO_2	0.330	0.270	0.140	0.330	0.300	0.270	0.250	0.340
MnO	0.410	0.300	0.120	0.470	0.370	0.330	0.150	0.330
Total	99.360	95.540	94.680	95.790	96.480	95.120	92.950	98.800
Si(T)	1.938	1.896	1.883	1.895	1.891	1.910	1.864	1.920
Al(T)	0.071	0.094	0.098	0.069	0.086	0.061	0.128	0.091
Cr(M)	0.000	0.001	0.004	0.001	0.000	0.001	0.003	0.001
Fe^{3+}	0.000	0.000	0.000	0.000	0.000	0.000	0.000	0.000
Fe^{2+}	0.339	0.276	0.179	0.344	0.340	0.319	0.221	0.330
Ti	0.009	0.008	0.004	0.010	0.009	0.008	0.008	0.010
Mn	0.013	0.010	0.004	0.016	0.012	0.011	0.005	0.011
Mg	0.836	0.924	0.973	0.899	0.868	0.844	0.914	0.848
Ca	0.804	0.835	0.912	0.819	0.843	0.886	0.915	0.807
Na	0.017	0.010	0.008	0.017	0.016	0.022	0.011	0.019
K	0.000	0.000	0.001	0.001	0.000	0.000	0.001	0.001

Formation	**Pilatón**	**Mulaute**						
Sample	**02CV72**	**02CV130**						
Lithology	**Sandstone**	**Basalt**						
UTM		**739121 / 9962111**						
Grain	1.17	1.1	1.2	1.3	1.4	1.5	1.6	1.7
$Si0_2$	50.530	48.471	48.353	47.743	48.182	47.779	48.373	48.369
Al_2O_3	2.590	1.694	2.130	3.052	2.523	2.620	2.143	2.038
CaO	21.830	18.798	18.796	22.128	21.618	22.492	19.561	18.777
K	0.000	0.001	0.011	0.006	0.018	0.002	0.001	0.000
FeO	6.720	7.021	6.134	4.054	4.567	3.684	9.301	7.446
MgO	16.350	23.417	23.853	22.427	22.452	22.561	20.078	22.700
Na_2O	0.080	0.227	0.324	0.112	0.261	0.179	0.210	0.295
Cr_2O	0.070	0.077	0.100	0.308	0.168	0.457	0.000	0.051
TiO_2	0.230	0.152	0.166	0.109	0.128	0.147	0.167	0.154
MnO	0.180	0.139	0.134	0.062	0.085	0.078	0.167	0.169
Total	98.590	99.999	100.000	100.000	100.000	100.000	100.000	100.000
Si(T)	1.899	1.939	1.934	1.910	1.927	1.911	1.935	1.935
Al(T)	0.115	0.061	0.066	0.090	0.073	0.089	0.065	0.065
Al(M)		0.007	0.019	0.032	0.028	0.016	0.021	0.016
Cr(M)	0.002	0.003	0.004	0.012	0.007	0.018	0.000	0.002
Fe^{3+}	0.000	0.049	0.043	0.042	0.039	0.050	0.040	0.046
Fe^{2+}	0.211	0.232	0.203	0.120	0.144	0.097	0.333	0.252
Ti	0.006	0.006	0.007	0.004	0.005	0.006	0.007	0.006
Mn	0.006	0.006	0.005	0.003	0.003	0.003	0.007	0.007
Mg	0.916	0.937	0.954	0.897	0.898	0.902	0.803	0.908

Ca	0.879	0.752	0.752	0.885	0.865	0.900	0.782	0.751
Na	0.006	0.009	0.013	0.005	0.010	0.007	0.008	0.012
K	0.000	0.000	0.000	0.000	0.001	0.000	0.000	0.000

Formation	**Mulaute**							
Sample	**02CV130**							
Lithology	**Basalt**							
UTM	**739121 / 9962111**							
Grain	1.8	1.9	1.10	1.11	1.12	1.13	1.14	1.15
$Si0_2$	47.902	48.237	48.022	48.104	48.687	47.674	48.190	48.177
Al_2O_3	2.669	2.468	2.691	2.416	1.905	2.937	2.581	2.391
CaO	21.347	20.890	21.734	19.677	18.740	19.463	18.625	18.770
K	0.006	0.000	0.013	0.000	0.003	0.000	0.005	0.000
FeO	4.772	5.036	4.074	5.916	7.427	5.438	6.265	7.560
MgO	22.660	22.598	22.924	23.146	22.538	23.526	23.494	22.426
Na_2O	0.251	0.289	0.143	0.266	0.331	0.304	0.344	0.285
Cr_2O	0.142	0.228	0.221	0.159	0.079	0.436	0.218	0.040
TiO_2	0.148	0.128	0.108	0.194	0.159	0.128	0.187	0.211
MnO	0.103	0.128	0.067	0.122	0.130	0.093	0.092	0.141
Total	99.999	100.000	99.999	100.000	100.000	100.000	100.000	100.000
Si(T)	1.916	1.930	1.921	1.924	1.948	1.907	1.928	1.927
Al(T)	0.084	0.071	0.079	0.076	0.053	0.093	0.072	0.073
Al(M)	0.023	0.028	0.029	0.021	0.024	0.025	0.031	0.023
Cr(M)	0.006	0.009	0.009	0.006	0.003	0.017	0.009	0.002
Fe^{3+}	0.054	0.035	0.039	0.044	0.026	0.053	0.032	0.043
Fe^{2+}	0.137	0.167	0.124	0.193	0.271	0.165	0.219	0.259
Ti	0.006	0.005	0.004	0.008	0.006	0.005	0.008	0.008
Mn	0.004	0.005	0.003	0.005	0.005	0.004	0.004	0.006
Mg	0.906	0.904	0.917	0.926	0.902	0.941	0.940	0.897
Ca	0.854	0.836	0.869	0.787	0.750	0.779	0.745	0.751
Na	0.010	0.012	0.006	0.011	0.013	0.012	0.014	0.011
K	0.000	0.000	0.001	0.000	0.000	0.000	0.000	0.000

Formation	**Mulaute**		**Pilatón**					
Sample	**02CV130**		**02CV131**					
Lithology	**Basalt**		**Sandstone**					
UTM	**739121 / 9962111**		**741445 / 9958359**					
Grain	1.16	1.17	1.10	1.20	1.30	1.40	1.50	1.60
$Si0_2$	48.520	48.388	46.663	48.168	46.427	47.527	47.055	47.131
Al_2O_3	1.810	1.709	4.313	3.194	4.473	2.821	3.559	3.523
CaO	18.077	18.326	20.477	22.234	22.382	20.545	20.145	22.152
K	0.009	0.000	0.008	0.000	0.000	0.000	0.011	0.006
FeO	8.089	7.530	6.460	2.938	4.448	5.753	5.479	3.790
MgO	22.735	23.292	21.048	22.815	21.470	22.527	22.742	22.457
Na_2O	0.381	0.286	0.508	0.129	0.272	0.313	0.316	0.296
Cr_2O	0.050	0.088	0.068	0.366	0.159	0.172	0.359	0.418

TiO_2	0.199	0.210	0.333	0.132	0.283	0.235	0.236	0.181
MnO	0.130	0.171	0.122	0.023	0.086	0.107	0.098	0.045
Total	100.000	100.000	99.999	99.999	99.999	99.999	99.999	99.999
Si(T)	1.941	1.936	1.867	1.927	1.857	1.901	1.882	1.885
Al(T)	0.059	0.065	0.134	0.073	0.143	0.099	0.118	0.115
Al(M)	0.013	0.004	0.039	0.055	0.036	0.014	0.025	0.026
Cr(M)	0.002	0.004	0.003	0.015	0.006	0.007	0.014	0.017
Fe^{3+}	0.044	0.052	0.086	0.000	0.089	0.072	0.073	0.070
Fe^{2+}	0.280	0.250	0.173	0.118	0.089	0.158	0.146	0.082
Ti	0.008	0.008	0.013	0.005	0.011	0.009	0.009	0.007
Mn	0.005	0.007	0.005	0.001	0.003	0.004	0.004	0.002
Mg	0.909	0.932	0.842	0.913	0.859	0.901	0.910	0.898
Ca	0.723	0.733	0.819	0.889	0.895	0.822	0.806	0.886
Na	0.015	0.011	0.020	0.005	0.011	0.013	0.013	0.012
K	0.000	0.000	0.000	0.000	0.000	0.000	0.000	0.000

Formation	**Pilatón**							
Sample	**02CV131**							
Lithology	**Sandstone**							
UTM	**741445 / 9958359**							
Grain	1.70	1.80	1.90	1.10	1.11	1.12	1.13	1.14
$Si0_2$	46.782	46.409	46.781	47.222	47.524	46.929	46.883	46.858
Al_2O_3	4.414	4.514	3.941	3.593	2.707	3.830	4.511	4.461
CaO	22.026	21.757	21.578	20.615	21.061	22.000	22.823	22.767
K	0.015	0.006	0.001	0.007	0.001	0.000	0.000	0.010
FeO	4.980	5.810	5.554	5.458	5.737	4.209	4.013	3.901
MgO	20.970	20.728	21.218	22.175	22.210	22.161	21.068	21.205
Na_2O	0.282	0.309	0.374	0.366	0.310	0.379	0.251	0.248
Cr_2O	0.196	0.110	0.155	0.200	0.085	0.180	0.189	0.244
TiO_2	0.263	0.247	0.296	0.281	0.247	0.243	0.214	0.248
MnO	0.072	0.110	0.100	0.083	0.117	0.068	0.049	0.058
Total	100.000	99.999	99.999	100.000	99.999	100.000	100.000	99.999
Si(T)	1.871	1.856	1.871	1.889	1.901	1.877	1.875	1.874
Al(T)	0.129	0.144	0.129	0.111	0.099	0.123	0.125	0.126
Al(M)	0.048	0.037	0.029	0.033	0.009	0.030	0.056	0.053
Cr(M)	0.008	0.004	0.006	0.008	0.003	0.007	0.008	0.010
Fe^{3+}	0.064	0.095	0.085	0.063	0.079	0.081	0.054	0.054
Fe^{2+}	0.135	0.137	0.137	0.155	0.150	0.087	0.106	0.102
Ti	0.011	0.010	0.012	0.011	0.010	0.010	0.009	0.010
Mn	0.003	0.004	0.004	0.003	0.005	0.003	0.002	0.002
Mg	0.839	0.829	0.849	0.887	0.888	0.886	0.843	0.848
Ca	0.881	0.870	0.863	0.825	0.842	0.880	0.913	0.911
Na	0.011	0.012	0.015	0.015	0.012	0.015	0.010	0.010
K	0.001	0.000	0.000	0.000	0.000	0.000	0.000	0.000

Formation	**Pilatón**					**Yunguilla**		
Sample	**02CV131**					**02CV122**		
Lithology	**Sandstone**					**Coarse-grained sandstone**		
UTM	**741445 / 9958359**					**734821 / 9823121**		
Grain	1.15	1.16	1.17	1.18	1.19	1.10	1.20	1.30
$Si0_2$	47.357	47.067	48.103	48.469	47.102			
Al_2O_3	3.187	3.628	2.789	1.940	4.079			
CaO	20.666	20.480	21.141	22.515	22.738			
K	0.004	0.000	0.008	0.005	0.001			
FeO	6.063	6.827	4.462	2.518	3.706			
Fe_2O_3								
MgO	21.728	21.064	22.688	23.935	21.393			
Na_2O	0.457	0.389	0.213	0.226	0.227			
Cr_2O	0.129	0.032	0.299	0.247	0.531			
TiO_2	0.293	0.385	0.214	0.116	0.174			
MnO	0.117	0.128	0.082	0.029	0.050			
Total	100.000	100.000	99.999	99.999	99.999			
Si(T)	1.894	1.883	1.924	1.939	1.884	1.911	1.918	1.892
Al(T)	0.106	0.117	0.076	0.061	0.116	0.076	0.067	0.099
Al(M)	0.022	0.028	0.036	0.016	0.047			
Cr(M)	0.005	0.001	0.012	0.010	0.021	0.010	0.000	0.000
Fe^{3+}	0.074	0.073	0.020	0.035	0.043	0.101	0.101	0.124
Fe^{2+}	0.169	0.200	0.159	0.066	0.106	0.098	0.169	0.179
Ti	0.012	0.015	0.009	0.005	0.007	0.007	0.012	0.014
Mn	0.005	0.005	0.003	0.001	0.002	0.006	0.012	0.009
Mg	0.869	0.843	0.908	0.957	0.856	0.923	0.855	0.825
Ca	0.827	0.819	0.846	0.901	0.910	0.849	0.839	0.824
Na	0.018	0.016	0.009	0.009	0.009	0.021	0.028	0.035
K	0.000	0.000	0.000	0.000	0.000	0.000	0.000	0.000

Formation	**Yunguilla**							
Sample	**02CV122**							
Lithology	**Coarse-grained sandstone**							
UTM	**734821 / 9823121**							
Grain	1.40	1.50	1.60	1.70	1.80	1.90	1.10	1.11
Si(T)	1.933	1.940	1.977	1.827	1.878	1.895	1.885	1.943
Al(T)	0.099	0.093	0.094	0.101	0.106	0.122	0.150	0.060
Cr(M)	0.000	0.004	0.000	0.000	0.000	0.002	0.009	0.003
Fe^{3+}	0.038	0.027	0.000	0.233	0.131	0.106	0.072	0.058
Fe^{2+}	0.227	0.194	0.265	0.080	0.132	0.094	0.135	0.178
Ti	0.014	0.011	0.010	0.019	0.018	0.007	0.011	0.008
Mn	0.007	0.007	0.011	0.011	0.008	0.004	0.005	0.008
Mg	0.887	0.865	0.854	0.861	0.859	0.868	0.885	0.864
Ca	0.764	0.835	0.759	0.844	0.839	0.870	0.825	0.854
Na	0.031	0.024	0.030	0.024	0.028	0.033	0.022	0.023
K	0.000	0.001	0.000	0.001	0.001	0.001	0.000	0.000

Formation	**Yunguilla**	**Pilaló**						
Sample	**02CV122**	**03CV172**						
Lithology		**Andesite**						
UTM		**771610 / 9996629**						
Grain	1.12	1.10	1.20	1.30	1.40	1.50	1.60	1.70
$Si0_2$		48.384	48.052	48.127	49.794	48.395	48.568	48.723
Al_2O_3		2.106	2.621	2.357	1.970	2.615	1.391	1.542
CaO		20.395	20.172	20.139	19.902	20.830	20.222	19.856
K		0.000	0.011	0.029	0.000	0.000	0.015	0.000
FeO		8.329	8.679	8.993	6.553	5.593	9.760	9.971
MgO		19.997	19.593	19.430	20.933	21.991	19.214	18.959
Na_2O		0.353	0.391	0.491	0.423	0.225	0.356	0.490
Cr_2O		0.024	0.039	0.051	0.097	0.074	0.003	0.000
TiO_2		0.240	0.238	0.196	0.158	0.180	0.210	0.231
MnO		0.173	0.204	0.187	0.172	0.097	0.261	0.229
Total		99.999	100.000	100.000	100.000	100.000	99.999	100.000
Si(T)	1.888	1.935	1.922	1.925	1.992	1.936	1.943	1.949
Al(T)	0.117	0.065	0.078	0.075	0.008	0.064	0.056	0.051
Al(M)		0.020	0.027	0.019	0.071	0.040	0.000	0.011
Cr(M)	0.002	0.001	0.002	0.002	0.004	0.003	0.000	0.000
Fe^{3+}	0.107	0.039	0.046	0.059	0.000	0.015	0.057	0.042
Fe^{2+}	0.156	0.294	0.301	0.301	0.262	0.208	0.333	0.357
Ti	0.012	0.010	0.010	0.008	0.006	0.007	0.008	0.009
Mn	0.007	0.007	0.008	0.008	0.007	0.004	0.011	0.009
Mg	0.855	0.800	0.784	0.777	0.837	0.880	0.769	0.758
Ca	0.831	0.816	0.807	0.806	0.796	0.833	0.809	0.794
Na	0.026	0.014	0.016	0.020	0.017	0.009	0.014	0.020
K	0.000	0.000	0.000	0.001	0.000	0.000	0.001	0.000

Formation	**Pilaló**						**Rio Cala**	
Sample	**03CV172**						**02CV104**	
Lithology	**Andesite**						**Basalt**	
UTM	**771610 / 9996629**						**786921 / 2743**	
Grain	1.80	1.90	1.10	1.11	1.12	1.13	1.10	1.20
$Si0_2$	48.871	47.915	47.907	47.470	48.865	48.563	48.150	46.942
Al_2O_3	1.481	2.682	2.583	3.090	1.578	1.842	2.092	3.505
CaO	20.181	20.382	20.714	19.912	20.451	20.683	22.609	22.150
K	0.000	0.000	0.000	0.003	0.011	0.002	0.000	0.005
FeO	9.339	7.381	5.017	5.931	9.640	8.824	3.044	4.962
MgO	19.258	20.980	22.930	22.784	18.606	19.387	23.200	21.660
Na_2O	0.431	0.263	0.265	0.254	0.415	0.275	0.292	0.326
Cr_2O	0.020	0.040	0.405	0.278	0.000	0.000	0.405	0.054
TiO_2	0.213	0.217	0.106	0.170	0.210	0.218	0.147	0.309
MnO	0.207	0.140	0.075	0.110	0.225	0.206	0.062	0.088
Total	100.000	100.000	100.000	100.000	99.999	99.999	100.000	100.000
Si(T)	1.955	1.917	1.916	1.899	1.955	1.943	1.926	1.878

Al(T)	0.045	0.083	0.084	0.101	0.045	0.058	0.074	0.122
Al(M)	0.014	0.024	0.020	0.022	0.018	0.016	0.010	0.018
Cr(M)	0.001	0.002	0.016	0.011	0.000	0.000	0.016	0.002
Fe^{3+}	0.031	0.051	0.050	0.064	0.028	0.035	0.048	0.091
Fe^{2+}	0.343	0.244	0.151	0.173	0.358	0.318	0.074	0.108
Ti	0.009	0.009	0.004	0.007	0.008	0.009	0.006	0.012
Mn	0.008	0.006	0.003	0.004	0.009	0.008	0.003	0.004
Mg	0.770	0.839	0.917	0.911	0.744	0.776	0.928	0.866
Ca	0.807	0.815	0.829	0.797	0.818	0.827	0.904	0.886
Na	0.017	0.011	0.011	0.010	0.017	0.011	0.012	0.013
K	0.000	0.000	0.000	0.000	0.000	0.000	0.000	0.000

Formation	**Rio Cala**							
Sample	**02CV104**							
Lithology	**Basalt**							
UTM	**786921 / 2743**							
Grain	1.30	1.40	1.50	1.60	1.70	1.80	1.90	1.10
$Si0_2$	47.491	46.554	47.930	47.991	47.796	46.474	47.896	47.715
Al_2O_3	2.969	3.843	2.213	2.058	2.355	3.639	2.424	3.000
CaO	22.376	22.249	22.467	22.554	21.435	22.021	22.590	22.162
K	0.005	0.000	0.000	0.006	0.000	0.012	0.003	0.000
FeO	4.237	6.059	3.525	3.330	4.399	5.713	3.586	4.288
MgO	22.339	20.504	23.306	23.343	23.398	21.216	22.938	22.180
Na_2O	0.239	0.415	0.178	0.316	0.226	0.352	0.298	0.309
Cr_2O	0.078	0.004	0.141	0.164	0.096	0.089	0.032	0.004
TiO_2	0.199	0.275	0.188	0.169	0.206	0.384	0.178	0.291
MnO	0.067	0.097	0.051	0.068	0.090	0.099	0.055	0.052
Total	100.000	100.000	100.000	99.999	100.000	99.999	99.999	100.000
Si(T)	1.900	1.862	1.917	1.920	1.912	1.859	1.916	1.909
Al(T)	0.100	0.138	0.083	0.080	0.088	0.141	0.084	0.091
Al(M)	0.018	0.016	0.006	0.002	0.006	0.005	0.013	0.029
Cr(M)	0.003	0.000	0.006	0.007	0.004	0.004	0.001	0.000
Fe^{3+}	0.073	0.116	0.064	0.071	0.071	0.117	0.068	0.052
Fe^{2+}	0.097	0.126	0.078	0.062	0.105	0.112	0.076	0.120
Ti	0.008	0.011	0.008	0.007	0.008	0.015	0.007	0.012
Mn	0.003	0.004	0.002	0.003	0.004	0.004	0.002	0.002
Mg	0.894	0.820	0.932	0.934	0.936	0.849	0.918	0.887
Ca	0.895	0.890	0.899	0.902	0.857	0.881	0.904	0.887
Na	0.010	0.017	0.007	0.013	0.009	0.014	0.012	0.012
K	0.000	0.000	0.000	0.000	0.000	0.000	0.000	0.000

Formation	**Rio Cala**
Sample	**02CV104**
Lithology	**Basalt**
UTM	**786921 / 2743**

Grain	1.11	1.12	1.13	1.14	1.15	1.16	1.17
$Si0_2$	48.460	48.237	47.166	48.010	46.730	47.974	48.178
Al_2O_3	1.996	2.136	3.163	2.364	3.663	2.608	2.198
CaO	22.599	22.478	21.387	22.509	22.060	22.527	22.501
K	0.000	0.000	0.000	0.004	0.000	0.000	0.008
FeO	3.137	3.499	6.339	3.782	5.139	3.635	3.412
MgO	23.030	23.082	21.027	22.715	21.694	22.695	23.018
Na_2O	0.250	0.209	0.457	0.276	0.275	0.243	0.240
Cr_2O	0.249	0.115	0.007	0.087	0.039	0.082	0.167
TiO_2	0.210	0.181	0.346	0.185	0.324	0.191	0.205
MnO	0.070	0.065	0.107	0.068	0.076	0.045	0.073
Total	100.000	100.000	99.999	99.999	100.000	100.000	100.000
Si(T)	1.938	1.930	1.887	1.920	1.869	1.919	1.927
Al(T)	0.062	0.071	0.113	0.080	0.131	0.081	0.073
Al(M)	0.018	0.015	0.013	0.015	0.016	0.023	0.015
Cr(M)	0.010	0.005	0.000	0.003	0.002	0.003	0.007
Fe^{3+}	0.027	0.045	0.091	0.058	0.099	0.049	0.045
Fe^{2+}	0.099	0.095	0.163	0.094	0.107	0.097	0.092
Ti	0.008	0.007	0.014	0.007	0.013	0.008	0.008
Mn	0.003	0.003	0.004	0.003	0.003	0.002	0.003
Mg	0.921	0.923	0.841	0.909	0.868	0.908	0.921
Ca	0.904	0.899	0.856	0.900	0.882	0.901	0.900
Na	0.010	0.008	0.018	0.011	0.011	0.010	0.010
K	0.000	0.000	0.000	0.000	0.000	0.000	0.000

Formation	**Pallatanga**							
Sample	**02CV120**							
Lithology	**Basalt**							
UTM	**734152 / 9822302**							
Grain	1.10	1.20	1.30	1.40	1.50	1.60	1.70	1.80
$Si0_2$	47.946	47.464	46.627	47.222	46.991	47.539	48.161	47.066
Al_2O_3	2.708	2.974	3.929	3.691	4.095	3.167	2.528	4.041
CaO	20.579	20.811	20.939	21.064	20.663	20.836	20.186	20.568
K	0.015	0.012	0.000	0.022	0.000	0.000	0.000	0.000
FeO	4.405	4.318	4.570	4.108	4.507	4.258	4.550	4.652
MgO	23.106	23.069	22.294	22.380	22.115	22.819	23.382	22.014
Na_2O	0.264	0.410	0.412	0.327	0.413	0.324	0.318	0.382
Cr_2O	0.693	0.584	0.680	0.829	0.789	0.666	0.535	0.861
TiO_2	0.243	0.295	0.473	0.315	0.370	0.324	0.273	0.357
MnO	0.039	0.062	0.077	0.041	0.057	0.067	0.067	0.060
Total	99.999	100.000	100.000	99.999	99.999	100.000	100.000	100.000
Si(T)	1.918	1.899	1.865	1.889	1.880	1.902	1.926	1.883
Al(T)	0.082	0.101	0.135	0.111	0.120	0.099	0.074	0.117
Al(M)	0.026	0.018	0.022	0.037	0.044	0.028	0.028	0.044
Cr(M)	0.028	0.023	0.027	0.033	0.032	0.027	0.021	0.034
Fe^{3+}	0.020	0.054	0.064	0.030	0.032	0.031	0.016	0.025

Fe^{2+}	0.156	0.119	0.119	0.134	0.148	0.140	0.167	0.161
Ti	0.010	0.012	0.019	0.013	0.015	0.013	0.011	0.014
Mn	0.002	0.003	0.003	0.002	0.002	0.003	0.003	0.002
Mg	0.924	0.923	0.892	0.895	0.885	0.913	0.935	0.881
Ca	0.823	0.832	0.838	0.843	0.827	0.833	0.807	0.823
Na	0.011	0.016	0.017	0.013	0.017	0.013	0.013	0.015
K	0.001	0.000	0.000	0.001	0.000	0.000	0.000	0.000

Formation	**Pallatanga**							
Sample	**02CV120**							
Lithology	**Basalt**							
UTM	**734152 / 9822302**							
Grain	1.90	1.10	1.11	1.12	1.13	1.14	1.15	1.16
$Si0_2$	47.079	46.579	46.845	47.074	47.176	47.217	47.940	47.559
Al_2O_3	3.971	4.015	4.162	3.469	3.324	3.430	2.599	2.839
CaO	20.457	21.170	20.637	21.081	20.641	20.941	20.644	20.885
K	0.010	0.028	0.005	0.000	0.000	0.025	0.001	0.001
FeO	4.619	4.525	4.555	5.036	4.793	4.040	4.457	4.258
MgO	22.321	22.034	22.102	22.088	22.570	22.790	23.069	23.157
Na_2O	0.381	0.362	0.399	0.391	0.334	0.417	0.401	0.347
Cr_2O	0.745	0.883	0.804	0.388	0.780	0.853	0.565	0.620
TiO_2	0.351	0.338	0.427	0.392	0.327	0.272	0.282	0.286
MnO	0.066	0.067	0.063	0.081	0.056	0.016	0.042	0.047
Total	100.000	99.999	100.000	99.999	100.000	100.000	100.000	99.999
Si(T)	1.883	1.863	1.874	1.883	1.887	1.889	1.918	1.902
Al(T)	0.117	0.137	0.126	0.117	0.113	0.111	0.082	0.098
Al(M)	0.042	0.024	0.040	0.022	0.020	0.026	0.022	0.016
Cr(M)	0.030	0.035	0.032	0.016	0.031	0.034	0.023	0.025
Fe^{3+}	0.033	0.066	0.036	0.064	0.049	0.047	0.032	0.048
Fe^{2+}	0.152	0.115	0.147	0.137	0.143	0.114	0.147	0.122
Ti	0.014	0.014	0.017	0.016	0.013	0.011	0.011	0.012
Mn	0.003	0.003	0.003	0.003	0.002	0.001	0.002	0.002
Mg	0.893	0.881	0.884	0.884	0.903	0.912	0.923	0.926
Ca	0.818	0.847	0.826	0.843	0.826	0.838	0.826	0.835
Na	0.015	0.015	0.016	0.016	0.013	0.017	0.016	0.014
K	0.000	0.001	0.000	0.000	0.000	0.001	0.000	0.000

Formation	**Pallatanga**	
Sample	**02CV120**	
Lithology	**Basalt**	
UTM	**734152 / 9822302**	
Grain	1.17	1.18
$Si0_2$	47.417	46.660
Al_2O_3	2.780	4.024
CaO	21.100	20.214
K	0.000	0.000

FeO	4.341	4.727
MgO	23.052	22.851
Na_2O	0.366	0.335
Cr_2O	0.572	0.752
TiO_2	0.339	0.389
MnO	0.034	0.048
Total	100.000	100.000
Si(T)	1.897	1.866
Al(T)	0.103	0.134
Al(M)	0.008	0.027
Cr(M)	0.023	0.030
Fe^{3+}	0.060	0.058
Fe^{2+}	0.114	0.131
Ti	0.014	0.016
Mn	0.001	0.002
Mg	0.922	0.914
Ca	0.844	0.809
Na	0.015	0.013
K	0.000	0.000

APPENDIX 8: Trace elements composition of clinopyroxenes from the Western Cordillera.

Formation	Macuchi (Las Juntas turbidites)							
Sample	02CV197							
Grain	1	2	3	4	5	6	7	8
Sc	142.432	129.050	236.638	172.839	104.545	163.769	175.143	148.132
V	310.377	282.001	235.707	294.596	212.879	325.899	314.803	362.134
Cr	27.101	1188.939	13.758	23.78	5241.574	66.376	147.964	157.985
Sr	15.686	16.085	12.236	15.394	16.847	17.967	15.17	16.688
Y	26.888	17.245	30.359	34.279	5.596	32.647	29.637	23.107
Zr	10.252	7.588	7.242	12.569	2.97	12.671	11.484	10.934
Nb	<0.011	<0.016	<0.014	<0.015	0.011	<0.024	<0.013	<0.014
Ba	<0.045	0.473	<0.057	0.328	0.148	<0.073	0.188	0.127
La	1.067	0.439	0.289	1.35	0.338	1.176	0.895	0.83
Ce	4.132	2.192	1.461	5.989	1.116	4.841	4.02	3.534
Nd	7.665	4.287	3.891	9.777	1.621	8.821	7.248	6.525
Sm	3.126	1.788	2.15	3.842	0.699	3.766	3.224	2.615
Eu	0.896	0.519	0.635	0.961	0.23	1.022	0.868	0.784
Dy	5.034	3.234	5.996	6.287	1.092	6.248	5.52	4.378
Er	2.792	1.85	3.189	3.322	0.606	3.973	3.414	2.672
Yb	2.891	1.733	3.269	3.464	0.638	3.413	3.348	2.543
Lu	0.388	0.259	0.453	0.488	0.088	0.436	0.467	0.34
Hf	0.513	0.489	0.331	0.545	0.212	0.549	0.658	0.597
Ti	2332.051	1906.407	1804.492	1978.347	1270.938	2787.670	2212.151	2487.921
Th	0.014	0.014	<0.008	0.083	0.013	0.026	0.022	0.059

Formation	Macuchi		Silante				Silante	
Sample	02CV197		00RS26				02CV56	
Grain	9	10	1	2	3	4	1	2
Sc	212.592	231.805	84.09	97.47	123.3	101.2	141.556	175.950
V	267.153	197.002	175.87	269.2	252.67	207.41	168.894	205.379
Cr	44.376	10.868	49.47	286.53	22.91	237.11	10.731	29.834
Sr	15.803	13.138	29.58	37.27	31.67	32.97	22.286	25.82
Y	47.372	79.984	18.16	15.07	26.75	22.56	30.31	45.872
Zr	14.106	22.838	22.14	18.62	23.07	20.8	16.085	44.053
Nb	0.015	<0.016	0.03	0.02	0.04	0.01	0.024	0.039
Ba	0.131	0.126	0.4	0.12	0.19	0.18	1.895	7.637
La	2.05	2.49	1.9	1.71	1.68	1.59	1.459	2.133
Ce	7.655	10.692	7.39	6.11	7	6.86	5.869	10.03
Nd	12.791	20.183	9.83	8.62	10.69	10.94	9.255	16.159
Sm	6.033	8.267	3.15	4.12	4.48	4.08	3.796	6.911
Eu	1.313	1.503	0.86	0.92	1.2	1.03	1.015	1.515
Dy	8.885	15.659	3.3	3.66	5.47	4.84	5.787	9.501
Er	5.595	8.854	1.69	1.72	2.91	2.19	3.415	5.249
Yb	5.041	8.887	1.87	1.34	2.32	2.31	3.221	5.163
Lu	0.675	1.263	0.28	0.17	0.27	0.28	0.452	0.67
Hf	0.776	1.14	0.94	1.2	1.04	1.04	0.736	2.06
Ti	2110.236	1306.908	1918.077	2937.055	2877.115	2277.716	2056.282	1234.968
Th	0.015	0.026					0.012	0.037

Formation	Silante							
Sample	02CV56							
Grain	3	4	5	6	7	8	9	10
Sc	116.375	138.586	142.517	90.863	121.378	109.702	128.882	178.720
V	209.745	167.886	304.951	268.042	172.024	212.824	180.568	164.062
Cr	18.787	4.441	25.989	393.015	37.479	19.448	21.322	71.582
Sr	26.263	23.235	26.069	23.765	19.806	29.07	23.106	19.356
Y	27.96	29.808	28.058	9.513	23.791	24.487	34.248	42.236
Zr	19.985	16.537	21.358	7.818	14.468	21.275	33.928	24.902
Nb	<0.014	0.029	0.022	0.006	<0.026	0.025	<0.015	<0.014
Ba	0.634	0.768	0.071	0.034	<0.111	0.034	10.632	0.146
La	0.999	1.874	1.382	0.34	1.053	0.831	2.305	2.289
Ce	4.566	6.737	5.776	1.509	4.27	3.75	10.707	10.713
Nd	8.481	10.32	10.034	2.624	5.789	6.706	17.229	16.652
Sm	3.454	3.995	4.405	1.102	2.986	3.49	6.559	7.14
Eu	1.109	1.125	1.319	0.426	0.943	1.074	1.225	1.19
Dy	5.091	6.179	5.751	2.019	4.455	4.879	6.943	8.512
Er	3.199	3.158	3.179	0.984	2.294	2.827	3.671	4.749
Yb	2.893	2.96	2.737	0.938	2.682	2.581	4.135	4.482
Lu	0.38	0.425	0.363	0.116	0.334	0.349	0.574	0.66
Hf	0.997	0.85	1.188	0.41	0.581	1.127	2.092	1.207
Ti	2715.730	2104.241	3375.179	2194.166	1924.392	3129.385	1582.677	1061.113

Th	0.01	0.032	0.011	0.004	<0.016	<0.018	<0.009	0.015

Formation	Pilaló						Silante	
Sample	03CV172						02CV99	
Grain	1	2	3	4	5	6	1	2
Sc	222.188	209.247	201.539	202.487	176.391	182.665	122.19	170.36
V	165.344	383.996	204.495	206.203	372.746	251.354	148.89	286.63
Cr	11.962	88.062	65.279	54.113	416.572	286.509	38.75	240.96
Sr	9.17	34.547	9.539	9.449	9.669	11.831	22.12	24.23
Y	31.868	31.96	29.118	26.84	20.502	21.879	28.54	34.11
Zr	10.503	19.417	10.599	10.056	13.886	9.536	17.65	23.91
Nb	<0.013	<0.029	<0.012	<0.005	<0.067	0.012	0.01	0.01
Ba	0.112	142.582	1.281	0.938	0.33	5.02	0.06	0.02
La	0.523	1.419	0.509	0.484	0.627	0.437	1.66	1.52
Ce	2.443	4.076	2.483	2.322	2.244	2.051	6.26	6.11
Nd	5.062	5.46	5.039	4.617	4.128	3.923	9.41	9.69
Sm	2.988	2.871	2.505	2.469	2.326	1.891	4.18	4.68
Eu	0.67	0.742	0.619	0.577	0.41	0.551	1.08	1.18
Dy	6.079	6.382	5.571	5.274	3.633	3.706	5.9	6.67
Er	3.612	3.184	3.517	3.126	2.24	2.568	3.43	3.94
Yb	3.721	3.835	3.356	3.095	1.924	2.508	2.92	3.65
Lu	0.565	0.56	0.524	0.387	0.334	0.373	0.39	0.5
Hf	0.527	0.597	0.44	0.445	0.607	0.365	0.94	1.22
Ti	1480.763	1492.753	1516.732	1342.878	2344.041	1600.662	1918.397	2457.946

Formation	Silante			Pilaló				
Sample	02CV99			03CV223				
Grain	3	4	5	1	2	3	4	5
Sc	134.49	134.63	155.91	122.053	186.144	341.409	372.299	249.627
V	244.3	191.49	236.51	284.851	198.378	83.901	74.305	110.279
Cr	32.32	99.83	58.17	1027.83	8.314	<4.472	3.925	<4.399
Sr	25.99	20.31	22.1	16.804	13.928	13.458	12.905	13.471
Y	34.58	33.95	43.51	11.536	23.396	51.971	58.237	40.64
Zr	28.04	37.77	32.58	6.597	8.605	14.369	14.928	12.057
Nb	0.02	0.05	0.03	<0.007	<0.010	<0.026	<0.012	<0.024
Ba	0.26	-0.02	0.14	0.042	<0.031	<0.111	<0.049	<0.100
La	2.01	2.41	1.98	0.297	0.55	1.008	1.134	0.919
Ce	8.23	8.73	8.51	1.457	2.655	5.704	5.996	4.92
Nd	11.88	13.9	14.14	2.497	4.849	10.961	12.037	9.34
Sm	4.34	4.59	6.27	1.193	2.506	5.554	5.453	3.735
Eu	1.27	1.13	1.38	0.395	0.626	1	0.763	0.713
Dy	7.28	6.52	8.77	2.2	4.6	10.573	11.448	7.939
Er	3.81	3.35	4.57	1.22	2.76	6.012	6.866	4.892
Yb	3.56	3.47	4.24	1.307	3.058	6.031	7.448	4.241
Lu	0.49	0.53	0.59	0.191	0.405	0.977	1.025	0.731
Hf	1.48	1.55	1.66	0.391	0.517	0.872	0.596	0.377

Ti	2817.645	1918.397	2278.096	1246.958	1354.868	1300.913	1151.038	1169.023

Formation	Pilaló							Sanguangal
Sample	03CV223							00RS39
Grain	6	7	8	9	10	11	12	1
Sc	220.026	192.643	278.031	376.962	77.357	186.538	160.928	129.05
V	133.050	132.824	97.240	72.401	154.219	225.379	322.393	154.18
Cr	<4.610	9.394	3.219	4.593	3300.9	15.247	272.026	8.3
Sr	13.276	13.653	13.877	14.482	12.815	13.634	6.706	15.84
Y	25.56	26.452	49.596	64.373	2.382	25.295	4.526	41.75
Zr	7.064	7.148	14.422	14.935	0.667	9.59	1.431	18.33
Nb	<0.083	<0.032	<0.016	<0.013	<0.007	<0.015	<0.024	0.04
Ba	<0.088	1.104	0.287	0.563	<0.042	0.137	<0.101	1.12
La	0.617	0.649	1.267	2.182	0.06	0.569	0.08	1.93
Ce	2.712	2.853	5.934	8.829	0.231	2.716	0.39	7.54
Nd	5.094	6.374	10.29	14.709	0.46	5.176	0.625	12.08
Sm	2.765	3.018	5.214	6.765	0.184	2.488	0.456	4.83
Eu	0.759	0.541	0.905	0.919	0.093	0.611	0.133	1.06
Dy	5.402	5.063	10.003	12.257	0.364	5.091	0.936	7.82
Er	2.757	3.096	5.522	7.579	0.2	2.606	0.496	4.59
Yb	3.15	3.336	6.052	7.547	0.273	2.743	0.648	4.81
Lu	0.447	0.434	0.878	1.16	0.035	0.383	0.07	0.72
Hf	0.311	0.411	0.792	0.723	0.049	0.555	0.115	80%
Ti	1037.133	1007.158	1342.878	1121.063	539.549	1378.848	869.274	2037.957

Formation	Sanguangal					Pilatón		
Sample	00RS39					02CV131		
Grain	2	3	4	5	6	1	2	3
Sc	176.17	137.64	137.22	152.04	144.86	150.820	110.734	84.350
V	142.28	266.4	272.39	204.22	244.06	442.901	284.303	115.792
Cr	8.02	29.33	33.78	7.73	46.07	712.18	2598.829	2381.549
Sr	18.1	16.75	17.03	21.55	17.03	16.864	22.98	16.937
Y	54.62	33.98	34.08	44.59	37.93	13.255	7.549	2.578
Zr	21.87	16.71	17.43	20.26	17.41	8.478	5.252	0.956
Nb	0.03	0.04	0.07	0.04	0.02	<0.013	<0.016	<0.025
Ba	0.17	0.19	0.13	0.87	0.16	<0.026	0.246	<0.102
La	2.3	1.6	1.51	2	1.47	0.366	0.357	0.074
Ce	9.68	6.12	6.21	8.19	6.49	1.653	1.441	0.327
Nd	15.91	10.06	9.92	13.37	10.45	3.023	2.572	0.76
Sm	6.72	4.68	4.25	5.49	4.37	1.527	1.051	0.24
Eu	1.48	1.04	1.1	1.23	1.1	0.546	0.41	0.121
Dy	10.61	6.49	6.5	7.82	6.81	2.642	1.65	0.386
Er	6.58	3.69	3.7	4.97	4.09	1.375	0.651	0.225
Yb	6.31	3.69	3.73	5.1	4.06	1.348	0.811	0.308
Lu	0.88	0.52	0.56	0.75	0.59	0.186	0.123	0.032
Hf	103%	84%	81%	101%	74%	0.431	0.21	0.097

Ti	2337.656	2757.235	2817.175	2457.536	2637.356	2589.836	1666.607	653.454

Formation	Pilatón							
Sample	02CV131							
Grain	4	5	6	7	8	9	10	11
Sc	121.262	167.213	128.378	112.220	109.632	123.490	109.559	117.195
V	227.757	421.848	392.243	246.103	249.439	274.768	279.015	283.630
Cr	4166.461	238.066	1863.042	2275.54	1344.574	1706.488	2091.6	1482.82
Sr	19.727	20.676	18.489	21.246	25.111	20.223	19.179	20.469
Y	5.532	15.021	10.337	4.895	5.609	5.95	6.858	6.789
Zr	4.176	8.033	5.444	3.942	5.548	3.84	3.639	5.365
Nb	<0.008	<0.009	0.008	<0.009	<0.009	0.014	0.01	<0.007
Ba	0.075	<0.063	<0.055	<0.039	<0.036	0	<0.030	0.036
La	0.184	0.382	0.271	0.166	0.3	0.149	0.173	0.172
Ce	0.854	2.036	1.519	0.947	1.431	0.785	0.981	0.962
Nd	1.405	4.074	2.556	1.633	2.03	1.675	2.105	1.804
Sm	0.756	1.9	1.298	0.784	0.871	0.713	0.914	0.887
Eu	0.235	0.622	0.406	0.262	0.31	0.335	0.314	0.376
Dy	1.057	3.108	2.066	0.921	1.102	1.156	1.416	1.27
Er	0.537	1.706	0.945	0.503	0.594	0.627	0.865	0.739
Yb	0.539	1.589	1.084	0.45	0.59	0.587	0.733	0.632
Lu	0.076	0.191	0.16	0.069	0.075	0.074	0.115	0.092
Hf	0.191	0.464	0.332	0.254	0.231	0.157	0.24	0.26
Ti	1534.717	2859.610	2182.176	1642.627	1876.432	1870.437	1552.702	2134.216

Formation	Pilatón	Mulaute						
Sample	02CV131	02CV130						
Grain	12	1	2	3	4	5	6	7
Sc	105.240	111.331	118.047	106.641	101.555	106.920	95.638	103.928
V	200.739	328.167	381.798	318.389	257.910	216.455	215.352	167.414
Cr	3128.098	720.611	456.26	665.214	1134.887	2040.322	2468.555	4212.229
Sr	12.96	9.517	9.073	7.543	8.838	11.115	10.397	11.69
Y	3.356	9.268	10.263	7.778	8.099	4.872	4.576	3.269
Zr	1.782	2.428	2.719	1.679	1.894	1.682	1.296	1.307
Nb	<0.027	<0.005	0.008	<0.006	<0.006	<0.006	<0.005	0.014
Ba	<0.154	0.066	0.059	<0.034	0.095	0.199	0.119	0.16
La	0.095	0.126	0.133	0.124	0.14	0.076	0.057	0.071
Ce	0.425	0.653	0.606	0.455	0.531	0.382	0.306	0.247
Nd	0.674	1.421	1.427	1.005	1.067	0.762	0.703	0.533
Sm	0.21	0.73	0.722	0.556	0.675	0.473	0.399	0.287
Eu	0.094	0.221	0.271	0.207	0.25	0.175	0.168	0.125
Dy	0.813	1.68	1.838	1.345	1.565	0.842	0.846	0.657
Er	0.487	0.965	1.171	0.914	0.849	0.521	0.47	0.365
Yb	0.299	1.033	1.17	0.957	0.8	0.522	0.569	0.378
Lu	0.069	0.155	0.176	0.14	0.134	0.076	0.062	0.051
Hf	0.11	0.138	0.132	0.114	0.106	0.058	0.08	0.076

Ti	845.294	1354.868	1318.898	977.183	1001.163	1031.138	773.354	899.249

Formation	Mulaute			Rio Cala				
Sample	02CV130			02CV104				
Grain	8	9	10	1	2	3	4	5
Sc	148.554	101.493	109.404	102.823	134.431	98.164	91.963	117.127
V	370.194	200.649	227.320	152.050	312.079	127.592	136.046	161.160
Cr	495.141	1245.257	1733.131	706.621	73.986	638.293	2246.873	413.713
Sr	6.638	13.572	12.141	42.87	54.868	59.25	51.961	47.742
Y	5.107	5.44	5.554	5.376	13.409	5.418	4.568	6.37
Zr	1.417	1.707	1.737	5.74	16.624	7.864	5.178	9.37
Nb	<0.005	<0.006	0.008	0.006	0.01	<0.007	0.007	0.014
Ba	0.089	<0.026	0.056	0.354	0.596	0.185	0.022	0.389
La	0.067	0.094	0.094	0.817	2.25	1.224	0.786	1.165
Ce	0.292	0.444	0.445	3.212	8.027	4.814	3.234	4.391
Nd	0.49	0.957	0.899	3.918	10.933	6.15	4.493	5.295
Sm	0.327	0.475	0.535	1.398	3.657	2.11	1.377	1.717
Eu	0.122	0.258	0.178	0.441	1.126	0.628	0.434	0.571
Dy	0.957	0.87	1.054	1.213	2.998	1.328	1.002	1.392
Er	0.608	0.614	0.628	0.482	1.347	0.535	0.434	0.672
Yb	0.564	0.663	0.62	0.489	1.207	0.421	0.375	0.57
Lu	0.098	0.091	0.088	0.064	0.181	0.061	0.045	0.073
Hf	0.036	0.1	0.102	0.3	0.881	0.354	0.246	0.427
Ti	917.233	1019.148	1001.163	1588.672	2841.625	1444.793	1384.843	1822.477
Th				0.005	0.021	0.01	0.004	0.009

Formation	Rio Cala	Pallatanga					
Sample	02CV104	02CV120					
Grain	6	1	2	3	4	5	6
Sc	117.101	76.374	73.094	70.499	72.898	85.134	81.368
V	310.564	353.048	346.043	332.666	308.491	428.179	389.501
Cr	951.885	5726.177	5237.139	4997.449	6229.575	7001.438	2738.672
Sr	52.099	10.867	10.909	10.163	11.013	11.955	10.917
Y	10.521	6.358	5.836	5.55	5.578	7.785	7.15
Zr	12.997	6.156	5.523	5.204	5.204	8.789	7.972
Nb	0.019	0.039	0.024	0.02	0.023	0.026	0.012
Ba	0.07	0.654	0.45	0.853	0.675	0.906	0.794
La	1.428	0.225	0.185	0.18	0.167	0.276	0.203
Ce	5.586	0.846	0.743	0.774	0.761	1.007	0.921
Nd	7.276	1.385	1.446	1.251	1.341	1.937	1.691
Sm	2.578	0.779	0.731	0.77	0.803	0.916	0.953
Eu	0.785						
Dy	2.209	1.374	1.224	1.111	1.168	1.658	1.476
Er	1.045	0.568	0.589	0.646	0.59	0.796	0.703
Yb	0.921	0.484	0.47	0.505	0.461	0.648	0.571
Lu	0.149	0.08	0.063	0.063	0.065	0.098	0.077

Hf	0.636	0.335	0.312	0.278	0.303	0.434	0.409
Ti	2823.640	2242.126	2194.166	2074.267	2134.216	2745.705	2493.916
Th	0.015						

APPENDIX 9 Analytical procedures U/Pb SHRIMP dating and $^{40}Ar/^{39}Ar$ analyses

U/Pb SHRIMP dating

The zircons analyzed in this study were recovered after rock crushing and sieving to a size of < 300 µm, followed by a coarse scale density separation and cleaning step using a wilfley table. Magnetite was removed using a hand magnet, and the subsequent residue was passed through a Frantz magnetic separator. The non-magnetic fraction was placed in di-iodomethane at a density of 3.3 g/cm^3 and the fraction that sank was dominated by zircons and pyrite. Individual zircons were separated from the pyrite by hand picking under a petrographic binocular, and washed in de-ionized water in an ultrasonic bath for one minute. The zircon separates were sent to the Australian National University to be analyzed in the SHRIMP ion microprobe under the supervision of Mark Fanning. Euhedral zircon selections for each sample were mounted in epoxy resin together with chips of the FC1 reference zircons, sectioned approximately in half and polished. Reflected and transmitted light photomicrographs and cathodoluminescence SEM images were prepared for all zircons, to assess the internal structure of the unknown zircons and to target specific areas within the zircons. Dating of the zircons was carried out using SHRIMP-1 with each analysis consisting of four scans through the mass range. The data were reduced in a manner similar to that described by Williams (1998), using the SQUID Excel macro of Ludwig (2000). The Pb/U ratios have been normalised relative to a value of 0.1859 for the $^{206}Pb/^{238}U$ ratio of the FC1 reference zircons, equivalent to an age of 1099 Ma (Paces & Miller 1993). Uncertainties given for individual analyses (ratios and ages) are at the 1σ level. The Tera–Wasserburg concordia plots (Tera and Wasserburg, 1972) and probability density plots with stacked histograms were carried out using ISOPLOT / EX (Ludwig 2001). The error in the FC1 reference zircon calibration was 0.31% for the analytical session (not included in above errors but required when comparing data from different mounts). f_{206} % denotes the percentage of ^{206}Pb that is common Pb. The correction for common Pb was made using the measured $^{238}U/^{206}Pb$ and $^{207}Pb/^{206}Pb$ ratios following Tera and Wasserburg (1972), as outlined in Williams (1998).

$^{40}Ar/^{39}Ar$ analyses

Rock samples for $^{40}Ar/^{39}Ar$ analysis were crushed following the method outlined by Koppers et al. (2000), which consists of continuous grinding and sieving to below 500 µm until 90% of the rock powder is reduced to <250 µm. The remaining 10% corresponds to the fraction between 250-500 µm, and include the hardest components, and is considered as the freshest material.

For groundmass separation, rock crushing, sieving was followed by removal of phenocrysts fraction and hand-picking under the binocular microscope. Hand picking was followed by acid leaching using HNO_3 (5%) in an ultrasonic bath at 50° C during 5 minutes. The grains were then washed in de-ionised water, dried and hand picked, selecting the freshest fragments.

Hornblende, pyroxene and plagioclase separates were obtained from the 250-500 and 125-250 µm rock fractions.

Hornblende and pyroxene crystals sank during heavy liquid separation using bromoform (ρ = 2.8 g/cm^3), and they were subsequently hand picked from the heavy fraction and washed in deionized water in an ultrasonic bath. Plagioclase separates were obtained from the light fraction after heavy liquid separation and a Frantz magnetic separation. Great care was taken to separate unaltered and inclusion free plagioclase grains. In the case of fine grained samples, plagioclase concentrates were purified by separating it from quartz using a ρ = 2.6 g/ cm^3 bromoform/acetone mixture The plagioclase grains were cleaned in 5% HNO_3 for 5 minutes, and washed in de-ionized water in an ultrasonic bath for 20 seconds, and then hand picked. The groundmass and mineral separates were wrapped in Cu-foil, labeled and stored in sealed quartz tubes for high energy neutron irradiation. The samples were irradiated at the Oregon State University TRIGA reactor (CLICIT facility, 1MW) for 9 hours, 30 minutes. Fish Canyon Tuff sanidine standards were placed 1cm apart along the quartz tube to allow the neutron fluence to be monitored via the measurement of J-values. The J-values ranged between 0.002277 and 0.002391.

Laser incremental heating technique

Argon extraction by the incremental heating was performed at the Department of Mineralogy, University of Geneva, Switzerland, using an automated, ultra-high vacuum, stainless steel, gas extraction line. The samples were heated using a Merchantek/New Wave floating, 30W continuous wave IR (CO_2) laser (model MIR10). The laser system allows the user to peform step-heating of one or more grains.

The groundmass, plagioclase, pyroxene and hornblende separates were spread out thinly in isolated cylindrical depressions that have a diameter of 13 mm (groundmass and pyroxene), and 3mm (plagioclase, hornblende and pyroxene), within a copper planchette. The laser beam as defocused using a 4 by 4 faceted lens, and the sample was heated homogeneously by rastering the laser across the sample following a specified grid pattern. Blanks were measured either before every second (groundmass and pyroxene) or third step (hornblende and plagioclase) incremental heating experiment. An extended low temperature heating schedule was applied during step heating, particularly for groundmass separates (e.g. Koppers et al., 2000), to provide greater resolution in the region of the age spectrum, which might be influenced by excess ^{40}Ar. The gas fractions were purified for seven minutes using one hot ST707 getter (0.45A), and one hot AP10 getter (1.45A). The purified gas was then allowed to diffuse for 50 seconds into the static vacuum, GV Instruments ARGUS mass spectrometer, equipped with a Nier-Bright source, prior to data collection. The mass spectrometer is a multi-collector machine, equipped with four high-gain (1E12Ω) Faraday collectors (^{36}Ar, ^{37}Ar, ^{38}Ar and ^{39}Ar) and one normal-gain (1E11Ω) Faraday collector (^{40}Ar). Baseline measurements using Faraday collectors are extremely stable over a period of several months, and hence they were not measured during each blank or sample analysis. Isotopic mass/charge abundances were collected using twelve cycles, which were then regressed to determine the abundances of each Ar isotope prior to fractionation in the source unit. The source consumption rate is ~3%/min, and hence the regressions are exponential. The multi-collector facility precludes the necessity for peak-hopping. The data was corrected for mass discrimination (measured using a cleaned air-standard) and blanks.

References

Koppers, A.A.P., Staudigel, H. and Wijbrans, J.R., 2000. Dating Crystalline Groundmass separates of Altered Cretaceous Seamount Basalts by the ^{40}Ar/^{39}Ar Incremental Heating Technique. Chemical Geology, v. 166,

p. 139-158.

Ludwig, K.R., 2001. Isoplot, v 2.49. Berkeley Geochronology Center Special Publ. 1a.

Ludwig, K.R. 2000. SQUID 1.00: a user's manual. Berkeley Geochronology Center Spec. Publ. 2, Berkeley, 17 p.

Paces, J.B., and Miller, J.D., 1993, Precise U-Pb age of Duluth Complex and related mafic intrusions, northeastern Minnesota: Geochronological insights into physical, petrogenetic, paleomagnetic, and tectonomagmatic processes associated with the 1.1 Ga midcontintent rift system: Journal of Geophysical Research, v.98, p.13,997-14,013.

Tera, F., Wasserburg, G. 1972. U-Th-Pb systematics in three Apollo 14 basalts and the problem of initial Pb in lunar rocks: Earth and Planetary Science Letters, v. 14, p. 281-304.

Williams, I.S., 1998. U–Th –Pb Geochronology by Ion Microprobe. In: McKibben, M.A., Shanks III, W.C., Ridley, W.I. (Eds.), Applications of Microanalytical Techniques to Understanding Mineralizing Processes. Rev. Econ. Geol., vol. 7, pp. 1 – 35.

APPENDIX 10: U-Pb results by the LA-ICPMS method

Saguangal Formation, sandstone, sample 03CV137; UTM: 747194/10023517

	$^{206}Pb/^{238}u$		$^{207}Pb/^{235}U$		$^{206}Pb/^{238}U$		$^{207}Pb/^{235}U$	
Number	Ratio	±% (1σ)	Ratio	±% (1σ)	AGE (Ma)	±2σ	AGE (Ma)	±2σ
1	0.015	1.60%	0.103	4.54%	96	3	99	9
2	0.016	1.33%	0.116	3.14%	104	3	111	7
3	0.010	2.38%	0.068	10.99%	62	3	67	14
4	0.009	5.72%	0.081	25.23%	57	7	79	38
5	0.009	2.94%	0.062	10.96%	56	3	61	13
6	0.012	2.43%	0.088	6.74%	77	4	85	11
7	0.011	2.04%	0.086	9.68%	71	3	83	15
8	0.012	2.21%	0.081	7.68%	75	3	79	12
9	0.037	1.38%	0.262	3.34%	237	6	236	14
10	0.036	1.18%	0.257	4.05%	229	5	233	17
11	0.132	1.01%	1.230	1.98%	797	15	814	22
12	0.012	1.67%	0.088	5.12%	75	2	86	8
13	0.346	1.00%	5.967	1.16%	1914	33	1971	20
14	0.011	2.46%	0.080	7.01%	72	4	78	10
15	0.274	1.25%	5.283	1.60%	1563	35	1866	27
16	0.242	1.46%	4.429	1.62%	1395	37	1718	27
17	0.012	3.70%	0.095	12.89%	76	6	93	23
18	0.100	1.55%	1.201	2.30%	617	18	801	25
19	0.052	1.54%	0.356	4.82%	327	10	309	26
20	0.323	0.86%	4.390	1.34%	1804	27	1710	22
21	0.123	2.56%	1.166	6.83%	748	36	785	75
22	0.109	1.45%	0.913	5.20%	665	18	658	50
23	0.113	1.24%	0.946	3.43%	690	16	676	34

24	0.336	0.90%	4.793	1.31%	1868	29	1784	22
25	0.1	0.92%	0.865	1.87%	614	11	633	18
26	0.109	0.85%	0.890	1.54%	666	11	646	15
27	0.065	1.26%	0.501	3.74%	403	10	412	25
28	0.075	1.30%	0.552	3.21%	467	12	447	23
29	0.056	2.28%	0.402	4.94%	350	16	343	29
30	0.106	0.97%	0.887	2.33%	651	12	645	22
31	0.095	1.27%	0.788	4.01%	587	14	590	36
32	0.293	0.90%	3.919	1.24%	1657	26	1618	20
33	0.146	2.28%	1.693	3.77%	881	37	1006	48
34	0.333	1.00%	5.839	1.43%	1853	32	1952	25
35	0.103	1.47%	0.872	3.82%	629	18	636	36
36	0.100	1.19%	0.843	2.31%	611	14	621	21
37	0.338	1.01%	5.754	1.29%	1877	33	1940	22
38	0.092	1.56%	0.822	7.55%	567	17	609	69
39	0.116	0.96%	1.264	3.69%	709	13	830	42
40	0.136	1.76%	1.245	3.54%	822	27	821	40
41	0.187	0.89%	1.877	1.40%	1107	18	1073	19
42	0.100	2.68%	0.859	6.20%	612	31	630	58
43	0.119	3.44%	1.137	4.67%	723	47	771	50
44	0.095	1.79%	0.747	3.43%	582	20	567	30
45	0.100	2.71%	0.853	5.63%	617	32	626	53
46	0.122	3.52%	1.144	4.70%	743	49	774	51
47	0.095	1.86%	0.752	3.51%	586	21	569	31
48	0.017	5.85%	0.141	8.46%	110	13	134	21
49	0.010	7.83%	0.063	15.33%	66	10	62	18
50	0.014	4.14%	0.083	7.39%	86	7	81	11
51	0.097	7.80%	0.794	10.12%	594	89	593	91
52	0.015	5.81%	0.119	10.77%	96	11	114	23
53	0.136	1.62%	1.216	2.84%	824	25	808	32
54	0.476	1.83%	10.901	1.98%	2509	76	2515	37
55	0.195	2.00%	1.971	3.21%	1151	42	1106	43
56	0.171	1.59%	1.660	2.13%	1017	30	993	27
57	0.077	1.91%	0.536	4.63%	478	18	436	33
58	0.307	2.19%	5.146	2.64%	1725	66	1844	45

Yunguilla Formation, sandstone, sample 00RS33; UTM: 771490/10001497

	$^{206}Pb/^{238}u$		$^{207}Pb/^{235}U$		$^{206}Pb/^{238}U$		$^{207}Pb/^{235}U$	
Number	Ratio	±% (1σ)	Ratio	±% (1σ)	AGE (Ma)	±2σ	AGE (Ma)	±2σ
1	0.164	2.15	1.736	3.75	978	39	1022	48
2	0.195	1.42	2.178	2.59	1149	30	1174	36
3	0.098	1.36	0.804	3.34	604	16	599	30

4	0.011	6.43	0.068	14.39	69	9	66	18
5	0.320	3.04	4.750	5.11	1789	95	1776	86
6	0.104	1.11	0.889	2.46	639	13	646	24
7	0.016	7	0.117	19.1	104	14	112	41
8	0.079	2.39	0.681	7.42	491	23	527	61
9	0.152	1.09	1.507	2.13	910	19	933	26
10	0.336	1.02	5.187	1.6	1867	33	1851	27
11	0.013	4.04	0.086	14.18	84	7	83	23
12	0.221	1.31	2.532	2.81	1285	30	1281	41
13	0.015	5.36	0.285	9.26	94	10	255	42
14	0.061	1.97	0.447	5.87	384	15	375	37
15	0.192	2.06	2.093	3.7	1133	43	1147	51
16	0.227	1.6	2.583	3.11	1318	38	1296	46
17	0.011	2	0.083	6.11	71	3	81	9
18	0.016	3.75	0.266	10.14	100	7	240	43
19	0.092	1.11	0.800	2.56	568	12	597	23
20	0.102	1.64	0.863	2.49	624	20	632	23
21	0.325	1	5.169	1.74	1812	32	1848	30
22	0.507	1.33	12.199	1.86	2642	58	2620	35
23	0.011	2.28	0.073	6.83	72	3	71	9
24	0.124	1.17	1.170	2.16	755	17	786	24
25	0.188	1.29	2.334	2.91	1112	26	1223	41

APPENDIX 11: Summary of SHRIMP U-Pb zircon results from rocks of the Western Cordillera, Ecuador.

Notes:

1) Samples measured by Mark Fanning at the SHRIMP facilities of the Australian National Uni.versity

2) Uncertainties given at the one σ level.

3) Error in FC1 reference zircon calibration was 0.31% for the analytical session (not included in above errors but required when comparing data from different mounts).

4) f_{206} % denotes the percentage of ^{206}Pb that is common Pb.

5) Correction for common Pb made using the measured $^{238}U/^{206}Pb$ and $^{207}Pb/^{206}Pb$ ratios following Tera and Wasserburg (1972) as outlined in Williams (1998).

Granite - Pujili Unit - Sample 03CV258 - UTM: 755300/9898600

Grain. spot	U (ppm)	Th (ppm)	Th/U	$^{206}Pb^{*}$ (ppm)	$^{204}Pb/^{206}Pb$	f_{206} %	Total Radiogenetic Age							
							$^{238}U/^{206}Pb$	±	$^{207}Pb/^{206}Pb$	±	$^{206}Pb/^{238}U$	±	$^{206}Pb/^{238}U$	±
1.1	214	81	0.38	14.0	-	0.80	74.72	1.10	0.054	0.002	0.013	0.000	85.0	1.3
2.1	156	49	0.31	18.3	0.001	0.96	73.39	1.21	0.055	0.002	0.013	0.000	86.4	1.4
3.1	105	27	0.26	26.6	0.004	2.49	73.89	1.36	0.067	0.003	0.013	0.000	84.5	1.6
4.1	288	108	0.37	19.7	0.000	1.04	74.73	1.02	0.056	0.002	0.013	0.000	84.8	1.2
5.1	67	19	0.29	13.5	0.001	5.21	72.24	1.66	0.089	0.004	0.013	0.000	84.0	2.1
6.1	416	287	0.69	37.1	-	0.55	75.14	1.09	0.052	0.001	0.013	0.000	84.8	1.2
7.1	474	208	0.44	4.1	0.000	0.63	74.24	0.92	0.053	0.001	0.013	0.000	85.7	1.1
8.1	121	45	0.37	15.4	0.002	1.72	75.61	1.34	0.061	0.004	0.013	0.000	83.3	1.5
9.1	201	57	0.28	24.9	0.000	1.18	73.85	1.13	0.057	0.002	0.013	0.000	85.7	1.3
10.1	183	80	0.44	31.8	0.002	1.39	74.75	1.16	0.059	0.002	0.013	0.000	84.5	1.3
11.1	538	501	0.93	14.2	0.001	0.51	74.03	0.91	0.052	0.001	0.013	0.000	86.1	1.1
11.2	222	176	0.80	51.8	0.001	1.16	73.97	1.37	0.057	0.002	0.013	0.000	85.6	1.6
12.1	160	48	0.30	31.6	-	1.82	75.22	1.26	0.062	0.003	0.013	0.000	83.6	1.4
13.1	82	21	0.26	31.7	0.001	2.20	72.55	1.48	0.065	0.004	0.013	0.000	86.3	1.8
14.1	452	246	0.54	12.9	0.000	0.83	72.56	0.91	0.054	0.001	0.014	0.000	87.5	1.1
15.1	26	5	0.18	8.6	0.014	8.38	68.60	2.21	0.114	0.011	0.013	0.001	85.5	3.2
16.1	66	20	0.30	79.0	0.002	3.17	69.21	1.51	0.073	0.004	0.014	0.000	89.6	2.0
17.1	198	132	0.67	37.8	0.001	1.26	73.42	1.14	0.058	0.003	0.013	0.000	86.1	1.4

Age	± no std	± include std
85.5	0.6	0.7

Gabbro - San Juan Unit - Sample 02CV34 - UTM:759961/9967463

Grain. spot	U (ppm)	Th (ppm)	Th/U	$^{206}Pb^{*}$ (ppm)	$^{204}Pb/^{206}Pb$	f_{206} %	Total Radiogenetic Age $^{238}U/^{206}Pb$	±	$^{207}Pb/^{206}Pb$	±	$^{206}Pb/^{238}U$	±	$^{206}Pb/^{238}U$	±
1.1	336	262	0.78	3.9	0.000	0.60	73.67	0.98	0.052	0.001	0.013	0.000	86.4	1.2
2.1	480	760	1.58	5.6	0.000	0.58	73.37	0.90	0.052	0.001	0.014	0.000	86.8	1.1
3.1	218	137	0.63	2.6	0.002	1.22	73.37	1.07	0.057	0.002	0.013	0.000	86.2	1.3
4.1	366	408	1.12	4.3	0.001	0.53	72.95	1.04	0.052	0.001	0.014	0.000	87.3	1.3
5.1	225	102	0.45	2.6	0.000	0.82	74.12	1.09	0.054	0.002	0.013	0.000	85.7	1.3
6.1	48	19	0.39	0.6	0.003	4.11	70.72	1.77	0.080	0.009	0.014	0.000	86.8	2.5
7.1	324	461	1.42	3.7	0.000	0.35	75.40	1.03	0.050	0.002	0.013	0.000	84.6	1.2
8.1	364	394	1.08	4.4	0.000	0.27	71.78	0.93	0.050	0.001	0.014	0.000	88.9	1.2
9.1	676	785	1.16	7.8	0.000	0.23	74.43	0.87	0.050	0.001	0.013	0.000	85.8	1.0
10.1	310	292	0.94	3.7	0.001	0.70	72.92	0.99	0.053	0.002	0.014	0.000	87.2	1.2
10.2	377	425	1.13	4.5	0.000	0.64	71.74	0.99	0.053	0.001	0.014	0.000	88.7	1.2
11.1	98	70	0.72	1.1	-	1.47	72.99	1.35	0.059	0.003	0.014	0.000	86.4	1.6
12.1	154	105	0.68	1.9	0.002	1.18	71.70	1.15	0.057	0.002	0.014	0.000	88.2	1.4
13.1	464	492	1.06	5.6	0.000	0.48	71.47	0.91	0.052	0.001	0.014	0.000	89.1	1.1
13.2	249	178	0.71	3.0	0.000	1.35	71.26	1.06	0.059	0.002	0.014	0.000	88.6	1.3

Age	± no std	± include std
87.1	1	0.83

APPENDIX 12: $^{40}Ar/^{39}Ar$ data

03CV165, J=0.002388, basalt:
Groundmass

Step	$^{36}Ar(a)$	$^{37}Ar(Ca)$	$^{39}Ar(k)$	$^{40}Ar(r)$	$^{40}Ar^*/^{39}Ar(k)$	^{40}Ar (r) (%)	$^{39}Ar(k)$ (%)	K/Ca ± 2σ		Age ± 2σ (Ma)	
1	0.0	0	0.0	0.0	4.660	60.361	33.047	0	0	19.96	± 2.80
2	0.0	0	0.0	0.0	4.757	63.616	20.129	0	0	20.38	± 4.58
3	0.0	0	0.0	0.0	5.615	65.540	15.904	0	0	24.03	± 5.71
4	0	0.0	0.0	0.0	11.693	99.991	13.686	0.001	0.005	49.68	± 59.60
5	0	0.0	0.0	0.0	24.367	99.996	13.676	0.000	0.000	102.04	± 112.48
6	0	0.0	0.0	0.0	98.654	99.999	3.558	0.000	0.000	381.64	± 1538.45

plateau steps: 1-3

03CV263, J=0.002315, diorite
Plagioclase

Step	$^{36}Ar(a)$	$^{37}Ar(Ca)$	$^{39}Ar(k)$	$^{40}Ar(r)$	$^{40}Ar^*/^{39}Ar(k)$	^{40}Ar (r) (%)	$^{39}Ar(k)$ (%)	K/Ca ± 2σ		Age ± 2σ (Ma)	
1	0	0.0	0.0	0.0	258.098	100.000	0.077	0.000	0.001	845.10	±
2	0	0.0	0.0	0.0	71.625	99.999	9.718	0.000	0.000	276.78	± 281.42
3	0	0.0	0.0	0.0	20.470	99.995	20.179	0.001	0.001	83.53	± 12.87
4	0.0	0.0	0.0	0.0	14.705	81.711	9.529	0.115	0.231	60.39	± 4.14
5	0.0	0.0	0.0	0.0	21.202	92.325	25.459	0.010	0.050	86.45	± 67.74
6	0.0	0.0	0.0	0.0	22.983	99.312	16.636	0.007	0.032	93.52	± 95.18
7	0	0.0	0.0	0.0	28.558	99.996	15.200	0.001	0.001	115.49	± 24.21
8	0	0.0	0.0	0.0	142.475	99.999	0.701	0.000	0.000	514.25	± 1681.98
9	0	0.0	0.0	0.0	118.960	99.999	0.862	0.000	0.000	438.85	± 864.68
10	0	0.0	0.0	0.0	116.904	99.999	1.639	0.000	0.000	432.10	± 460.41

plateau steps: 3-7

02CV67, J=0.00227, basaltic andesite
Groundmass

Step	$^{36}Ar(a)$	$^{37}Ar(ca)$	$^{39}Ar(k)$	$^{40}Ar(r)$	$^{40}Ar^*/^{39}Ar(k)$	^{40}Ar (r) (%)	$^{39}Ar(k)$ (%)	K/Ca ± 2σ		Age ± 2σ (Ma)	
1	0.0	0	0.0	0.0	8.695	78.707	15.707	0	0	35.37	± 2.68
2	0.0	0	0.0	0.0	8.367	74.381	19.495	0	0	34.05	± 2.16
3	0.0	0	0.0	0.0	8.568	63.688	19.740	0	0	34.86	± 2.13
4	0.0	0	0.0	0.0	9.657	58.333	11.240	0	0	39.24	± 4.05
5	0.0	0	0.0	0.0	11.245	47.724	9.950	0	0	45.61	± 4.57
6	0.0	0	0.0	0.0	11.244	44.414	8.754	0	0	45.61	± 5.28
7	0.0	0	0.0	0.0	13.282	37.215	3.605	0	0	53.75	± 12.47
8	0.0	0	0.0	0.0	14.970	33.928	2.795	0	0	60.47	± 16.16
9	0.0	0	0.0	0.0	15.512	32.207	2.985	0	0	62.62	± 15.20
10	0.0	0	0.0	0.0	15.291	29.751	1.048	0	0	61.75	± 39.61
11	0.0	0	0.0	0.0	17.712	28.653	2.022	0	0	71.33	± 21.03
12	0.0	0	0.0	0.0	16.770	27.755	2.659	0	0	67.60	± 15.84

plateau steps: 1-4

02CV126, J=0.00239, basaltic andesite

Plagioclase

Step	^{36}Ar(a)	^{37}Ar(ca)	^{39}Ar(k)	^{40}Ar(r)	^{40}Ar*/ ^{39}Ar(k)	^{40}Ar (r) (%)	^{39}Ar(k) (%)	K/Ca ± 2σ		Age ± 2σ (Ma)	
1	0.0	0.0	0.0	0.0	19.401	20.098	9.482	0.021	0.003	81.80	± 2.02
2	0.0	0.0	0.0	0.0	12.582	35.945	9.225	0.022	0.004	53.47	± 1.65
3	0.0	0.0	0.0	0.0	12.452	52.430	6.884	0.018	0.003	52.93	± 1.70
4	0.0	0.0	0.0	0.0	10.048	46.559	13.085	0.043	0.006	42.83	± 0.84
5	0.0	0.0	0.0	0.0	9.561	57.149	10.923	0.040	0.006	40.78	± 0.90
6	0.0	0.0	0.0	0.0	10.628	63.128	7.370	0.028	0.004	45.27	± 1.60
7	0.0	0.0	0.0	0.0	9.974	54.770	9.828	0.030	0.005	42.52	± 1.22
8	0.0	0.0	0.0	0.0	9.888	48.865	7.746	0.025	0.004	42.16	± 2.08
9	0.0	0.0	0.0	0.0	10.480	49.131	7.930	0.028	0.004	44.65	± 1.35
10	0.0	0.0	0.0	0.0	12.276	49.555	5.226	0.015	0.002	52.19	± 2.34
11	0.0	0.0	0.0	0.0	11.514	47.626	5.838	0.016	0.002	49.00	± 2.13
12	0.0	0.0	0.0	0.0	12.973	38.574	6.462	0.022	0.003	55.11	± 1.81

plateau steps: 4-9

03CV162, J=0.00229, basaltic andesite

Groundmass

Step	^{36}Ar(a)	^{37}Ar(ca)	^{39}Ar(k)	^{40}Ar(r)	^{40}Ar*/ ^{39}Ar(k)	^{40}Ar (r) (%)	^{39}Ar(k) (%)	K/Ca ± 2σ		Age ± 2σ (Ma)	
1	0.0	0.0	0.0	0.0	14.925	85.915	35.186	397.737	619.810	60.81	± 1.06
2	0.0	0.0	0.0	0.0	14.946	81.111	15.459	112.723	109.231	60.90	± 2.46
3	0.0	0.0	0.0	0.0	14.929	77.491	14.030	119.480	147.335	60.83	± 2.76
4	0.0	0.0	0.0	0.0	14.761	69.188	21.050	128.142	92.046	60.16	± 1.83
5	0.0	0.0	0.0	0.0	15.825	66.353	14.276	230.574	374.697	64.41	± 2.73

plateau steps: 1-5

02CV104, J=0,002386, basaltic andesite

Pyroxene

Step	^{36}Ar (a)	^{37}Ar (ca)	^{39}Ar (k)	^{40}Ar (r)	^{40}Ar*/ ^{39}Ar(k)	^{40}Ar (r) (%)	^{39}Ar(k) (%)	K/Ca ± 2σ		Age ± 2σ (Ma)	
1	0.0	0.0	0.0	0.0	13.312	79.865	16.833	0.020	0.040	56.41	± 16.02
2	0.0	0.0	0.0	0.0	16.576	81.769	11.881	0.014	0.028	69.98	± 23.00
3	0.0	0.0	0.0	0.0	15.747	85.033	17.376	0.020	0.041	66.54	± 15.74
4	0.0	0.0	0.0	0.0	13.993	80.677	15.952	0.019	0.038	59.25	± 16.51
5	0.0	0.0	0.0	0.0	14.836	83.363	13.272	0.015	0.031	62.76	± 19.82
6	0	0.0	0.0	0.0	18.379	99.995	5.518	0.006	0.013	77.43	± 12.04
7	0.0	0.0	0.0	0.0	3.709	18.456	12.243	0.014	0.029	15.89	± 21.33
8	0	0.0	0.0	0.0	52.291	99.998	6.925	0.000	0.000	212.11	± 537.98

plateau steps: 1-6

03CV144, J=0,002362, andesite

Hornblende

Step	^{36}Ar (a)	^{37}Ar (ca)	^{39}Ar (k)	^{40}Ar (r)	^{40}Ar*/ ^{39}Ar(k)	^{40}Ar (r) (%)	^{39}Ar(k) (%)	K/Ca ± 2σ		Age ± 2σ (Ma)	
1	0.0	0	0.0	0.0	19.701	19.631	1.557	0	0	82.02	± 18.68

2	0.0	0	0.0	0.0	8.885	29.295	1.937	0	0	37.45	± 14.89
3	0.0	0	0.0	0.0	7.715	45.069	3.923	0	0	32.57	± 7.18
4	0.0	0.0	0.0	0.0	6.035	63.996	13.766	1.093		25.52	± 2.34
5	0.0	0	0.0	0.0	6.288	53.677	14.141	0	0	26.59	± 2.27
6	0.0	0	0.0	0.0	5.944	55.608	20.909	0	0	25.14	± 1.55
7	0.0	0	0.0	0.0	6.199	49.768	11.191	0.000	0	26.21	± 2.77
8	0.0	0	0.0	0.0	5.580	48.437	9.800	0.000	0	23.61	± 3.20
9	0.0	0.0	0.0	0.0	6.107	79.787	22.776	0.082	0.039	25.83	± 1.35

plateau steps: 4-9

03CV234, J=0,00239, amphibolite

Hornblende

Step	^{36}Ar (a)	^{37}Ar (ca)	^{39}Ar (k)	^{40}Ar (r)	^{40}Ar*/ ^{39}Ar(k)	^{40}Ar (r) (%)	^{39}Ar(k) (%)	K/Ca ± 2σ		Age ± 2σ (Ma)	
1	0.0	0.0	0.0	0.0	77.013	30.349	2.584	0.016	0.026	304.80	± 30.31
2	0.0	0.0	0.0	0.0	19.958	55.217	21.706	0.010	0.002	84.06	± 2.99
3	0.0	0.0	0.0	0.0	20.469	69.079	38.250	0.008	0.001	86.17	± 3.75
4	0.0	0.0	0.0	0.0	19.746	59.652	36.191	0.010	0.002	83.19	± 6.56
5	0.0	0	0.0	0.0	67.522	19.008	0.691	0.000	0	269.90	± 144.24
6	0.0	0.0	0.0	0.0	4.307	1.758	0.577	0.002	0.001	18.48	± 118.62

plateau steps: 2-4

02CV75, J=0,002372, andesite

Hornblende

Step	^{36}Ar (a)	^{37}Ar (ca)	^{39}Ar (k)	^{40}Ar (r)	^{40}Ar*/ ^{39}Ar(k)	^{40}Ar (r) (%)	^{39}Ar(k) (%)	K/Ca ± 2σ		Age ± 2σ (Ma)	
1	0.0	0.0	0.0	0.0	10.956	34.814	0.568	0.002	0.001	46.29	± 60.90
2	0.0	0.0	0.0	0.0	20.047	82.621	0.379	0.001	0.001	83.81	± 78.51
3	0.0	0.0	0.0	0.0	8.187	92.759	10.921	0.020	0.005	34.70	± 2.65
4	0.0	0.0	0.0	0.0	7.701	94.724	43.455	0.061	0.016	32.66	± 0.78
5	0.0	0.0	0.0	0.0	7.815	93.700	20.576	0.049	0.018	33.14	± 1.47
6	0.0	0.0	0.0	0.0	7.899	92.764	16.906	0.044	0.020	33.49	± 1.86
7	0.0	0.0	0.0	0.0	7.206	88.218	7.195	0.203	0.826	30.58	± 4.04

plateau steps: 3-7

03CV185, J=0,002389, andesite

Hornblende

Step	^{36}Ar(a)	^{37}Ar(Ca)	^{39}Ar(k)	^{40}Ar(r)	^{40}Ar*/ ^{39}Ar(k)	^{40}Ar (r) (%)	^{39}Ar(k) (%)	K/Ca ± 2σ		Age ± 2σ (Ma)	
1	0.0	0.0	0.0	0.0	18.209	17.327	7.506	0.059	0.085	76.82	± 6.64
2	0.0	0	0.0	0.0	9.430	66.727	13.437	0.0	0	40.19	± 3.46
3	0.0	0	0.0	0.0	10.451	53.819	13.346	0.0	0	44.49	± 3.38
4	0.0	0.0	0.0	0.0	7.310	24.135	5.935	0.026	0.017	31.24	± 5.32
5	0.0	0.0	0.0	0.0	5.322	34.175	5.251	0.045	0.062	22.79	± 6.56
6	0.0	0.0	0.0	0.0	6.604	34.028	5.633	0.032	0.025	28.24	± 6.22
7	0.0	0.0	0.0	0.0	8.740	56.823	8.216	0.024	0.013	37.28	± 5.29
8	0.0	0.0	0.0	0.0	7.685	45.088	5.249	0.273	2.454	32.82	± 8.85

9	0.0	0.0	0.0	0.0	8.145	41.349	4.680	0.089	0.359	34.77	± 9.96
10	0.0	0	0.0	0.0	7.179	43.853	4.665	0	0	30.68	± 7.45
11	0.0	0	0.0	0.0	8.162	35.196	26.082	0	0	34.84	± 1.44

plateau steps: 7-11

03CV232, J=0,00239, andesite

Groundmass

Step	^{36}Ar(a)	^{37}Ar(Ca)	^{39}Ar(k)	^{40}Ar(r)	^{40}Ar*/ ^{39}Ar(k)	^{40}Ar (r) (%)	^{39}Ar(k) (%)	K/Ca ± 2σ		Age ± 2σ (Ma)	
1	0	0.0	0.0	0.0	3.597	99.972	26.094	0.006	0.026	15.44	± 3.41
2	0	0.0	0.0	0.0	3.798	99.973	9.922	0.014	0.069	16.30	± 1.74
3	0	0.0	0.0	0.0	4.027	99.975	15.388	0.016	0.059	17.28	± 1.09
4	0.0	0.0	0.0	0.0	2.586	60.756	14.154	0.471	3.771	11.12	± 2.45
5	0.0	0.0	0.0	0.0	2.600	57.295	15.526	0.516	4.133	11.17	± 2.24
6	0.0	0.0	0.0	0.0	3.013	40.090	2.944	0.096	0.772	12.94	± 11.97
7	0.0	0.0	0.0	0.0	3.259	34.426	7.224	0.237	1.893	14.00	± 4.88
8	0.0	0.0	0.0	0.0	4.508	31.838	6.404	0.209	1.676	19.33	± 5.49
9	0.0	0.0	0.0	0.0	5.596	34.752	2.345	0.077	0.613	23.97	± 14.97

plateau steps: 1-3

02CV55, J=0,002376, basaltic andesite

Groundmass

Step	^{36}Ar(a)	^{37}Ar(Ca)	^{39}Ar(k)	^{40}Ar(r)	^{40}Ar*/ ^{39}Ar(k)	^{40}Ar (r) (%)	^{39}Ar(k) (%)	K/Ca ± 2σ		Age ± 2σ (Ma)	
1	0.0	0.0	0.0	0.0	13.318	89.165	52.176	0.419	0.846	56.20	± 4.81
2	0.0	0.0	0.0	0.0	13.984	87.424	19.730	0.157	0.316	58.97	± 2.36
3	0.0	0.0	0.0	0.0	13.436	83.509	11.160	0.089	0.179	56.69	± 4.73
4	0.0	0.0	0.0	0.0	18.159	73.003	3.480	0.028	0.056	76.21	± 13.65
5	0.0	0.0	0.0	0.0	21.005	80.331	3.031	0.024	0.048	87.86	± 16.84
6	0.0	0.0	0.0	0.0	21.233	82.835	3.874	0.031	0.062	88.80	± 13.95
7	0.0	0.0	0.0	0.0	18.039	63.061	6.549	0.049	0.099	75.71	± 7.64

plateau steps: 1-3

03CV174, J=0,002369, basalt

Groundmass

Step	^{36}Ar(a)	^{37}Ar(ca)	^{39}Ar(k)	^{40}Ar(r)	^{40}Ar*/ ^{39}Ar(k)	^{40}Ar (r) (%)	^{39}Ar(k) (%)	K/Ca ± 2σ		Age ± 2σ (Ma)	
1	0	0.0	0.0	0.0	33.646	99.997	14.278	0.001	0.001	138.35	± 46.40
2	0.0	0.0	0.0	0.0	15.642	64.652	34.037	0.152	0.608	65.64	± 6.52
3	0.0	0.0	0.0	0.0	15.842	62.300	25.339	0.113	0.452	66.47	± 9.18
4	0.0	0.0	0.0	0.0	15.534	57.371	26.346	0.117	0.470	65.20	± 7.57

plateau steps: 2-4

03CV172, J = 0.003181, andesite

Pyroxene

Step	Power	Ca/K	$^{36}Ar/^{39}Ar$	$\%^{36}Ar$ (Ca)b	$^{40}Ar^*/^{39}Ar$	^{39}Ar	$\%^{39}Arc$	Cum. $\%^{39}Ar$	$\%^{40}Ar^*d$	Age	$\pm 2\sigma$ (Ma)
	(W)					(Mol-14)				(Ma)	
1	•3.9	2.353	0.029	1.1	11.408	3.943	36.6	36.6	56.9	64.308	0.254
2	•4.2	4.124	0.043	1.3	11.494	4.285	39.8	76.5	47.8	64.784	0.321
3	•4.3	11.166	0.020	7.4	11.354	1.397	13	89.4	67	64.006	0.256
4	4.5	37.164	0.029	17.4	10.222	0.657	6.1	95.5	59	57.729	0.380
5	8	529.326	0.132	53.9	9.403	0.480	4.5	100	30	53.170	1.179

plateau steps; 1-3